Physics Reports 894 (2021) 1–116

Contents lists available at ScienceDirect

Physics Reports

journal homepage: www.elsevier.com/locate/physrep

The Alpha Magnetic Spectrometer (AMS) on the international space station: Part II — Results from the first seven years

M. Aguilar [31], L. Ali Cavasonza [1], G. Ambrosi [37], L. Arruda [29], N. Attig [24], F. Barao [29], L. Barrin [15], A. Bartoloni [43], S. Başeğmez-du Pree [18,a], J. Bates [21], R. Battiston [40,41], M. Behlmann [10], B. Beischer [1], J. Berdugo [31], B. Bertucci [37,38], V. Bindi [20], W. de Boer [25], K. Bollweg [21], B. Borgia [43,44], M.J. Boschini [33], M. Bourquin [16], E.F. Bueno [18], J. Burger [10], W.J. Burger [40], S. Burmeister [26], X.D. Cai [10], M. Capell [10], J. Casaus [31], G. Castellini [14], F. Cervelli [39], Y.H. Chang [48,49], G.M. Chen [6,7], H.S. Chen [6,7], Y. Chen [16], L. Cheng [22], H.Y. Chou [49], S. Chouridou [1], V. Choutko [10], C.H. Chung [1], C. Clark [10,21], G. Coignet [3], C. Consolandi [20], A. Contin [8,9], C. Corti [20], Z. Cui [22,23], K. Dadzie [10], Y.M. Dai [5], C. Delgado [31], S. Della Torre [33], M.B. Demirköz [2], L. Derome [17], S. Di Falco [39], V. Di Felice [45,b], C. Díaz [31], F. Dimiccoli [40], P. von Doetinchem [20], F. Dong [35], F. Donnini [45,b], M. Duranti [37], A. Egorov [10], A. Eline [10], J. Feng [10], E. Fiandrini [37,38], P. Fisher [10], V. Formato [45,b], C. Freeman [20], Y. Galaktionov [10], C. Gámez [31], R.J. García-López [27,28], C. Gargiulo [15], H. Gast [1], I. Gebauer [25], M. Gervasi [33,34], F. Giovacchini [31], D.M. Gómez-Coral [20], J. Gong [35], C. Goy [3], V. Grabski [32], D. Grandi [33,34], M. Graziani [37,38], K.H. Guo [19], S. Haino [48], K.C. Han [30], R.K. Hashmani [2], Z.H. He [19], B. Heber [26], T.H. Hsieh [10], J.Y. Hu [6,7], Z.C. Huang [19], W. Hungerford [21], M. Incagli [39], W.Y. Jang [13], Yi Jia [10], H. Jinchi [30], K. Kanishev [40], B. Khiali [45,b], G.N. Kim [13], Th. Kirn [1], M. Konyushikhin [10], O. Kounina [10], A. Kounine [10], V. Koutsenko [10], A. Kuhlman [20], A. Kulemzin [10], G. La Vacca [33,34], E. Laudi [15], G. Laurenti [8], I. Lazzizzera [40,41], A. Lebedev [10], H.T. Lee [47], S.C. Lee [48], C. Leluc [16], J.Q. Li [35], M. Li [1], Q. Li [35], S. Li [1], T.X. Li [19], Z.H. Li [6], C. Light [20], C.H. Lin [48], T. Lippert [24], Z. Liu [16], S.Q. Lu [19], Y.S. Lu [6], K. Luebelsmeyer [1], J.Z. Luo [35], S.S. Lyu [19], F. Machate [1], C. Mañá [31], J. Marín [31], J. Marquardt [26], T. Martin [10,21], G. Martínez [31], N. Masi [8,9], D. Maurin [17], A. Menchaca-Rocha [32], Q. Meng [35], D.C. Mo [19], M. Molero [31], P. Mott [10,21], L. Mussolin [37,38], J.Q. Ni [19], N. Nikonov [1], F. Nozzoli [40], A. Oliva [8], M. Orcinha [29], M. Palermo [20], F. Palmonari [8,9], M. Paniccia [16], A. Pashnin [10], M. Pauluzzi [37,38], S. Pensotti [33,34], H.D. Phan [10], V. Plyaskin [10], M. Pohl [16], S. Porter [21], X.M. Qi [19], X. Qin [10], Z.Y. Qu [48], L. Quadrani [8,9], P.G. Rancoita [33], D. Rapin [16], A. Reina Conde [27,28], S. Rosier-Lees [3], A. Rozhkov [10], D. Rozza [33,34], R. Sagdeev [11], S. Schael [1], S.M. Schmidt [24], A. Schulz von Dratzig [1], G. Schwering [1], E.S. Seo [12], B.S. Shan [4], J.Y. Shi [35], T. Siedenburg [1], C. Solano [10], J.W. Song [23], R. Sonnabend [1], Q. Sun [23], Z.T. Sun [6,7], M. Tacconi [33,34], X.W. Tang [6], Z.C. Tang [6], J. Tian [37,38],

https://doi.org/10.1016/j.physrep.2020.09.003

Samuel C.C. Ting [10,15,*], S.M. Ting [10], N. Tomassetti [37,38], J. Torsti [50], C. Tüysüz [2], T. Urban [10,21], I. Usoskin [36], V. Vagelli [42,37], R. Vainio [50], E. Valente [43,44], E. Valtonen [50], M. Vázquez Acosta [27,28], M. Vecchi [18], M. Velasco [31], J.P. Vialle [3], L.Q. Wang [23], N.H. Wang [23], Q.L. Wang [5], S. Wang [20], X. Wang [10], Z.X. Wang [19], J. Wei [16], Z.L. Weng [10], H. Wu [35], R.Q. Xiong [35], W. Xu [22,23], Q. Yan [10], Y. Yang [46], H. Yi [35], Y.J. Yu [5], Z.Q. Yu [6], M. Zannoni [33,34], C. Zhang [6], F. Zhang [6], F.Z. Zhang [6,7], J.H. Zhang [35], Z. Zhang [10], F. Zhao [6,7], Z.M. Zheng [4], H.L. Zhuang [6], V. Zhukov [1], A. Zichichi [8,9], N. Zimmermann [1], P. Zuccon [40,41], AMS Collaboration

[1] *I. Physics Institute and JARA-FAME, RWTH Aachen University, 52056 Aachen, Germany*
[2] *Department of Physics, Middle East Technical University (METU), 06800 Ankara, Turkey*
[3] *Univ. Grenoble Alpes, Univ. Savoie Mont Blanc, CNRS, LAPP-IN2P3, 74000 Annecy, France*
[4] *Beihang University (BUAA), Beijing, 100191, China*
[5] *Institute of Electrical Engineering (IEE), Chinese Academy of Sciences, Beijing, 100190, China*
[6] *Institute of High Energy Physics (IHEP), Chinese Academy of Sciences, Beijing, 100049, China*
[7] *University of Chinese Academy of Sciences (UCAS), Beijing, 100049, China*
[8] *INFN Sezione di Bologna, 40126 Bologna, Italy*
[9] *Università di Bologna, 40126 Bologna, Italy*
[10] *Massachusetts Institute of Technology (MIT), Cambridge, MA 02139, USA*
[11] *East–West Center for Space Science, University of Maryland, College Park, MD 20742, USA*
[12] *IPST, University of Maryland, College Park, MD 20742, USA*
[13] *CHEP, Kyungpook National University, 41566, Daegu, Korea*
[14] *CNR–IROE, 50125 Firenze, Italy*
[15] *European Organization for Nuclear Research (CERN), 1211 Geneva 23, Switzerland*
[16] *DPNC, Université de Genève, 1211 Genève 4, Switzerland*
[17] *Univ. Grenoble Alpes, CNRS, Grenoble INP, LPSC-IN2P3, 38000 Grenoble, France*
[18] *Kapteyn Astronomical Institute, University of Groningen, P.O. Box 800, 9700 AV Groningen, The Netherlands*
[19] *Sun Yat–Sen University (SYSU), Guangzhou, 510275, China*
[20] *Physics and Astronomy Department, University of Hawaii, Honolulu, HI 96822, USA*
[21] *National Aeronautics and Space Administration Johnson Space Center (JSC), Houston, TX 77058, USA*
[22] *Shandong Institute of Advanced Technology (SDIAT), Jinan, Shandong, 250100, China*
[23] *Shandong University (SDU), Jinan, Shandong, 250100, China*
[24] *Jülich Supercomputing Centre and JARA-FAME, Research Centre Jülich, 52425 Jülich, Germany*
[25] *Institut für Experimentelle Teilchenphysik, Karlsruhe Institute of Technology (KIT), 76131 Karlsruhe, Germany*
[26] *Institut für Experimentelle und Angewandte Physik, Christian-Alberts-Universität zu Kiel, 24118 Kiel, Germany*
[27] *Instituto de Astrofísica de Canarias (IAC), 38205 La Laguna, Spain*
[28] *Departamento de Astrofísica, Universidad de La Laguna, 38206 La Laguna, Tenerife, Spain*
[29] *Laboratório de Instrumentação e Física Experimental de Partículas (LIP), 1649-003 Lisboa, Portugal*
[30] *National Chung–Shan Institute of Science and Technology (NCSIST), Longtan, Tao Yuan, 32546, Taiwan*
[31] *Centro de Investigaciones Energéticas, Medioambientales y Tecnológicas (CIEMAT), 28040 Madrid, Spain*
[32] *Instituto de Física, Universidad Nacional Autónoma de México (UNAM), Ciudad de México, 01000, Mexico*
[33] *INFN Sezione di Milano–Bicocca, 20126 Milano, Italy*
[34] *Università di Milano–Bicocca, 20126 Milano, Italy*
[35] *Southeast University (SEU), Nanjing, 210096, China*
[36] *Sodankylä Geophysical Observatory and Space Physics and Astronomy Research Unit, University of Oulu, 90014 Oulu, Finland*
[37] *INFN Sezione di Perugia, 06100 Perugia, Italy*
[38] *Università di Perugia, 06100 Perugia, Italy*
[39] *INFN Sezione di Pisa, 56100 Pisa, Italy*
[40] *INFN TIFPA, 38123 Povo, Trento, Italy*
[41] *Università di Trento, 38123 Povo, Trento, Italy*
[42] *Agenzia Spaziale Italiana (ASI), 00133 Roma, Italy*
[43] *INFN Sezione di Roma 1, 00185 Roma, Italy*
[44] *Università di Roma La Sapienza, 00185 Roma, Italy*
[45] *INFN Sezione di Roma Tor Vergata, 00133 Roma, Italy*
[46] *National Cheng Kung University, Tainan, 70101, Taiwan*
[47] *Academia Sinica Grid Center (ASGC), Nankang, Taipei, 11529, Taiwan*
[48] *Institute of Physics, Academia Sinica, Nankang, Taipei, 11529, Taiwan*
[49] *Physics Department and Center for High Energy and High Field Physics, National Central University (NCU), Tao Yuan, 32054, Taiwan*
[50] *Space Research Laboratory, Department of Physics and Astronomy, University of Turku, 20014 Turku, Finland*

* Corresponding author at: Massachusetts Institute of Technology (MIT), Cambridge, MA 02139, USA.
E-mail address: Samuel.Ting@cern.ch (S.C.C. Ting).
[a] Also at Nikhef, 1098 XG Amsterdam, Netherlands.
[b] Also at ASI Space Science Data Center (SSDC), 00133 Roma, Italy.

ARTICLE INFO

Article history:
Received 5 September 2020
Accepted 9 September 2020
Available online 19 September 2020
Editor: Jonathan L. Feng

Keywords:
Cosmic ray composition & spectra
Cosmic ray acceleration
Cosmic ray propagation
Cosmic ray sources
Particle astrophysics
Particle dark matter
Cosmic ray detectors
Alpha Magnetic Spectrometer
International space station

ABSTRACT

The Alpha Magnetic Spectrometer (AMS) is a precision particle physics detector on the International Space Station (ISS) conducting a unique, long-duration mission of fundamental physics research in space. The physics objectives include the precise studies of the origin of dark matter, antimatter, and cosmic rays as well as the exploration of new phenomena. Following a 16-year period of construction and testing, and a precursor flight on the Space Shuttle, AMS was installed on the ISS on May 19, 2011. In this report we present results based on 120 billion charged cosmic ray events up to multi-TeV energies. This includes the fluxes of positrons, electrons, antiprotons, protons, and nuclei. These results provide unexpected information, which cannot be explained by the current theoretical models. The accuracy and characteristics of the data, simultaneously from many different types of cosmic rays, provide unique input to the understanding of origins, acceleration, and propagation of cosmic rays.

Contents

0. Introduction

The Alpha Magnetic Spectrometer (AMS) is a precision particle physics detector on the International Space Station (ISS) conducting a unique, long-duration mission of fundamental physics research in space. The physics objectives include precise studies of the origins of dark matter, antimatter, and cosmic rays as well as the exploration of new phenomena. Prior to the main mission, a precursor flight of AMS, AMS-01, was flown on the Space Shuttle Discovery in June 1998. AMS-01 results were published in Physics Reports, "The Alpha Magnetic Spectrometer (AMS) on the International Space Station: Part I – results from the test flight on the space shuttle" [1]. With the experience accumulated from AMS-01, a new state of the art detector, known as AMS-02 or AMS on the ISS, was built and launched on the Space Shuttle Endeavour and installed on the ISS on May 19, 2011 (see Fig. 1). The ISS is orbiting the Earth at an altitude of $\sim$ 410 km with an orbit inclination of 52 degrees.

There are two kinds of cosmic rays in space:

1. Neutral cosmic rays (light rays and neutrinos) that have been studied by many satellite (COBE [2], EGRET [3], WMAP [4], Planck [5], ROSAT [6], Fermi [7], AGILE [8], Chandra [9], INTEGRAL [10], the Hubble Space Telescope [11] and the coming James Webb Telescope [12], etc.) and ground based (ARGO-YBJ [13], HAWC [14], H.E.S.S. [15], MAGIC [16], IceCube [17], Tibet ASgamma [18], LHAASO [19], etc.) experiments. Studies of neutral cosmic rays have provided fundamental information about the universe;
2. Charged cosmic rays are absorbed in the Earth's atmosphere and therefore, in the energy range up to multi-TeV, their properties such as charge magnitude and sign, mass, and rigidity can only be studied in space. In the past there have been many excellent experiments with balloons (ATIC [20], BESS [21], CAPRICE/WiZard [22], CREAM [23], etc.) and with satellites (CRIS [24], HEAO [25], PAMELA [26], etc.). Recently, precision non-magnetic, calorimeter experiments in space (CALET [27], ISS-CREAM [28], and DAMPE [29]) have also begun to provide important results.

There are excellent ongoing and proposed experiments that study cosmic rays at the highest energies. This includes innovative experiments EUSO-SPB [30] and POEMMA [31], as well as ground-based experiments — the Pierre Auger Observatory [32], H.E.S.S. [15], LHAASO [19], KASCADE-Grande [33], TA [34], CTA [35], and others.

AMS is the first long duration (about two 11-year solar cycles), large acceptance precision magnetic spectrometer to measure the sign and value of the charge, the momentum, the rigidity, and the flux of elementary particles (positrons, electrons, antiprotons, protons), nuclei, and anti-nuclei directly in space.

1. AMS on the ISS

As seen in Fig. 2, the AMS detector [36] consists of a permanent magnet and an array of particle detectors to measure the velocity $\beta = v/c$, momentum P, charge Z, and rigidity $R = P/Z$ of traversing particles and nuclei. Within the magnet bore and above and below the magnet are a total of 9 precision silicon tracker layers, L1 to L9. The Transition Radiation Detector (TRD) is located at the top of the AMS. Above the magnet bore are two orthogonal planes of Time of Flight counters (TOF), the Upper TOF, and below the bore are another two orthogonal planes, the Lower TOF. The Anti-Coincidence Counters (ACC or Veto), surround the tracker within the magnet bore. Below the Lower TOF is the Ring Imaging Cherenkov counter (RICH) and below that the Electromagnetic Calorimeter (ECAL). Each of these detector elements is described below.

The separation of the TRD and the ECAL by a magnetic field ensures that most of the secondary particles generated in the TRD are swept away by the magnet and do not enter into the ECAL. In this way, the rejection powers of the TRD and the ECAL are independent.

Before launch to the ISS, AMS was tested extensively at the CERN test beam with electrons, positrons, protons, and pions. Pion beams were used to simulate transition radiation effects in the TRD for high energy protons. In total, more than 2000 combinations of particles, energies, incident angles, and locations were tested.

AMS on the ISS has functioned reliably and the properties of the detector are continuously monitored. Minute changes compared to the original calibration at the CERN accelerator before launch are corrected in the data analysis. This ensures the quality and accuracy of the data.

During more than 10 years of AMS construction, a large international group of physicists have developed a comprehensive Monte Carlo simulation program for AMS. This program is based on the GEANT4 package [37] and it is constantly being improved with the AMS data obtained on the ISS. This Monte Carlo program simulates electromagnetic, hadronic, and nuclear interactions of particles and nuclei in the material of AMS, namely:

Fig. 1. AMS is a unique precision magnetic spectrometer on the ISS. AMS will operate on the ISS for the Station's lifetime. It is mounted on the ISS with a 12 degree angle to the zenith to prevent that the rotating ISS solar arrays are in the AMS field of view.

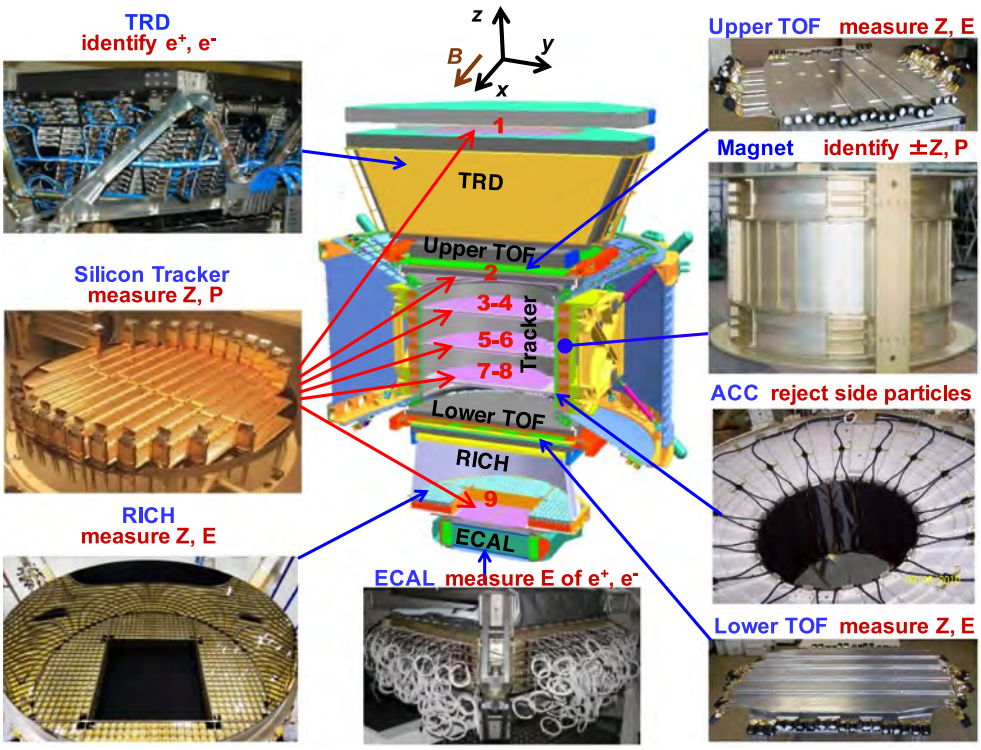

Fig. 2. The AMS detector showing the main elements and their functions. AMS is a TeV precision, multipurpose particle physics magnetic spectrometer. It identifies particles and nuclei by their charge (Z), energy (E) and momentum (P) or rigidity ($R = P/Z$), which are measured independently by the Tracker, TOF, RICH and ECAL. The ACC counters, located in the magnet bore, are used to reject particles entering AMS from the side. The AMS coordinate system, concentric with the magnet, is also shown. The x axis is parallel to the main component of the magnetic field and the z axis is pointing vertically.

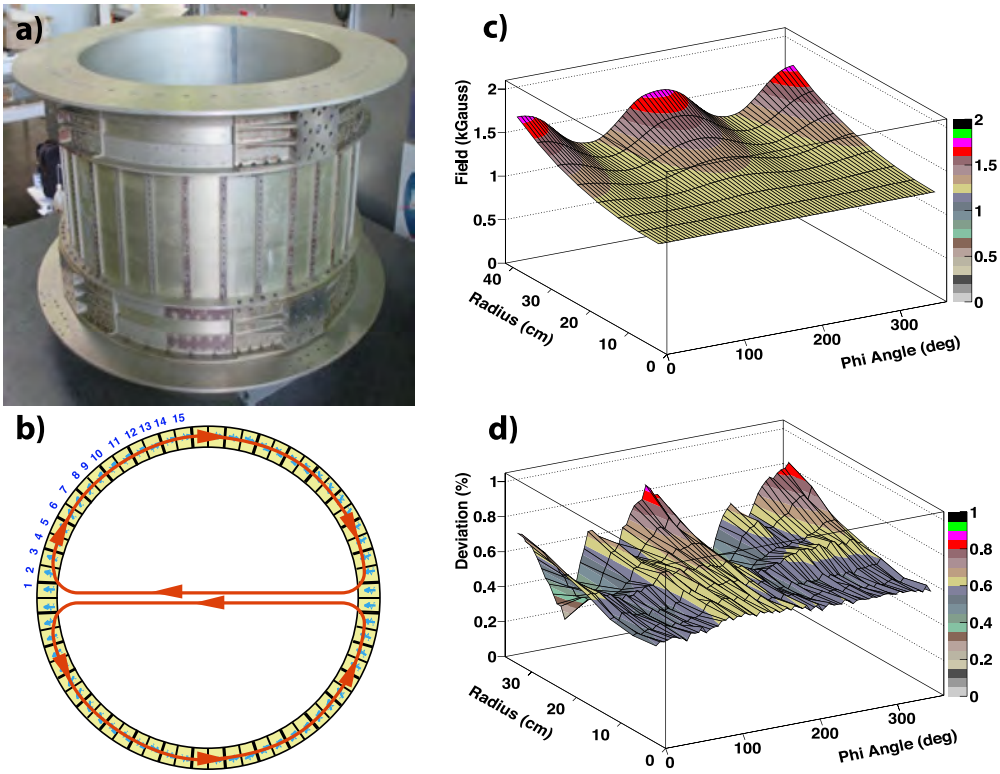

Fig. 3. (a) The magnet being prepared for the AMS mission on the ISS. The magnet is 800 mm long with an inner diameter of 1115 mm. (b) The arrangement of the AMS magnet showing the field directions of the 64 permanent magnet sectors resulting in negligible dipole moment and field leakage outside the magnet. (c) The magnet field measured in 2010 at $z = 0$. (d) The deviation between the field measurements in 1997 and 2010. The Radius and Phi Angle are cylindrical coordinates in the x–y plane, such that Phi=0 corresponds to the x-axis.

1. Electromagnetic interactions including
   - Ionization losses
   - Bremsstrahlung
   - Pair Production
   - Multiple and single Coulomb scattering
2. X-ray generation for the TRD detector
3. Cherenkov photon generation and propagation for the RICH detector
4. Elastic hadronic and nuclear scattering including
   - Hadron elastic scattering
   - Elastic nuclear scattering for ions
5. Inelastic hadronic and nuclear interactions from theoretical models tuned according to our nuclear cross section measurements (see Section 7).

The trigger conditions and digitization of the signals are simulated according to the measured characteristics of the electronics. The simulated events then undergo the same reconstruction as used for the data.

The AMS coordinate system is concentric with the center of the magnet. The x-axis is parallel to the main component of the magnetic field and the z-axis is parallel to the magnet bore. The $(y - z)$ plane is the bending plane.

The usual ISS attitude has the velocity vector roughly parallel to the AMS y-axis. As shown in Fig. 1, AMS is mounted on the ISS with a 12-degree angle to the zenith to prevent that the rotating ISS solar arrays are in the AMS field of view.

1.1. Permanent magnet

The permanent magnet [38], shown in Fig. 3a, was flown on the AMS engineering flight in 1998 and was described in detail in the AMS-01 Physics Report [1]. It is made of 64 high-grade Nd-Fe-B sectors assembled in a cylindrical shell 800 mm long with an inner diameter of 1115 mm. This configuration produces a field of 1.4 kG at the center of the magnet

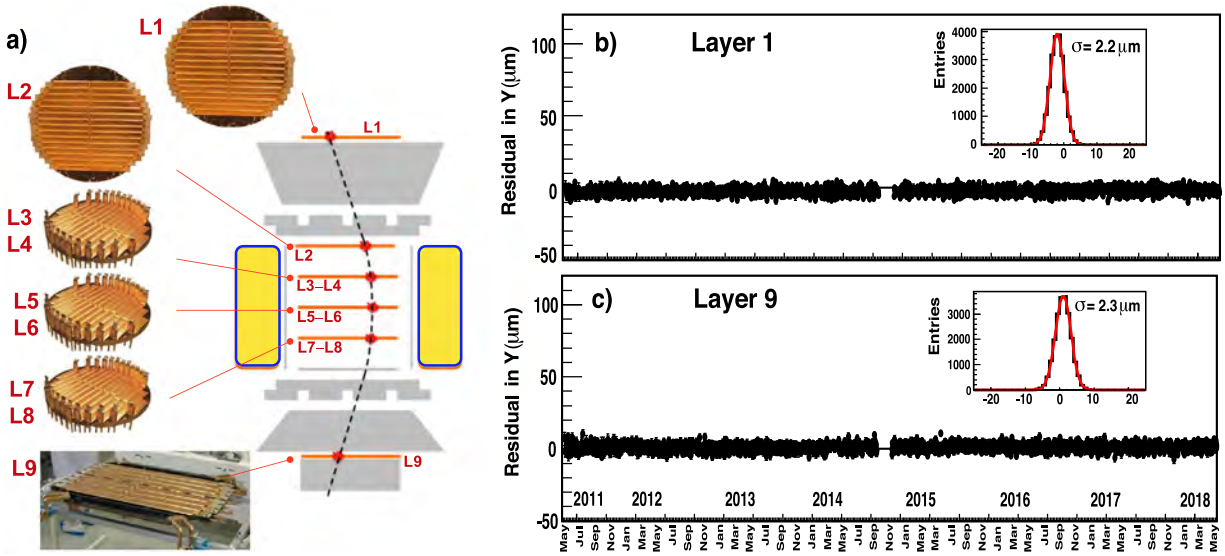

Fig. 4. (a) The 9 layers of the AMS silicon tracker and their locations within the detector. The alignment stability of (b) Layer 1 and (c) Layer 9 over seven years.

and negligible dipole moment and field leakage outside the magnet (see Fig. 3b). This is important in order to eliminate the effect of torque on the ISS and to ensure safety of astronauts. The detailed 3-dimensional field of the magnet was mapped in 2010 and is shown in Fig. 3c. The field was measured in 120,000 locations to an accuracy of better than 1%. Comparison with the measurements performed with the same magnet in 1997, before the engineering flight AMS-01, shows that the field did not change within 1%, limited by the accuracy of the 1997 measurement, as shown in Fig. 3d.

On the ISS, slight temperature induced changes in the field are constantly monitored and corrected in the analysis.

1.2. Tracker

The tracker, together with the magnet, accurately determines the trajectory and charge Z of cosmic rays by multiple measurements of the coordinates (x and y) and energy loss. It is composed of 192 ladders, each containing double-sided silicon sensors, readout electronics, and mechanical support [38,39]. The AMS tracker has nine layers, L1–L9, and 196,608 readout channels. As shown in Fig. 4a, three planes of aluminum honeycomb with carbon fiber skins are equipped with ladders on both sides. The layers on these planes are numbered L3–L8. Another three planes are equipped with one layer of ladders each, numbered L1, L2, and L9. As also indicated in Fig. 4a, L1 is located on top of the TRD, L2 is above the magnet, and L9 is between the RICH and the ECAL. L9 covers the ECAL acceptance. L2–L8 constitute the inner tracker. The total lever arm of the tracker from L1 to L9 is 3.0 m. From the trajectory and the magnetic field map, the tracker measurement directly yields the rigidity or momentum per unit charge, $R = P/Z$.

Positions of the planes of the inner tracker are held stable by a special carbon fiber structure [1]. It is monitored using 20 IR laser beams, which penetrate through all planes of the inner Tracker and provide micron level accuracy position measurements. The positions of L1 and L9 are aligned using cosmic ray protons every 2 min. As seen in Figs. 4b and 4c, they are stable to 2–3 μm.

1.2.1. Tracker coordinate measurements

The tracker independently measures the x and y coordinates. The y strips have a much finer implantation pitch of 27.5 μm (with 110 μm readout pitch) compared to the x strips (implantation pitch of 104 μm and readout pitch of 208 μm) to provide better accuracy of the coordinate measurement in the bending direction, which is important for the determination of the rigidity (or momentum) [40]. This provides spatial resolution of $5 - 10$ μm in the bending plane and $13 - 20$ μm in the non-bending plane.

We present the method of determination of the y coordinate. The method of determination of the x coordinate is similar.

When a charged particle crosses a layer of the silicon tracker, its coordinate d (either in x or y) is determined by taking the ratio between the signals induced on the two strips between which the particle passed (see Fig. 5).

The amplitude of the induced signals should be proportional to Z^2. For high Z, the amplitudes gradually saturate and become non-linear. This causes coordinate resolution degradation.

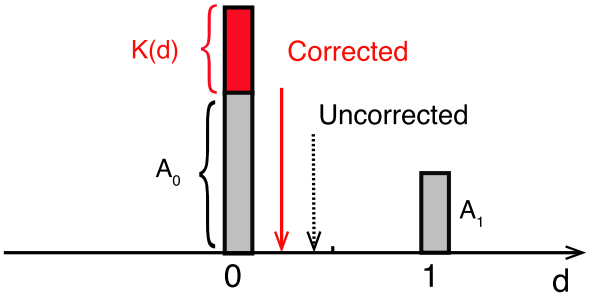

Fig. 5. Schematic of particle coordinate measurement in the silicon tracker. The solid red arrow indicates the point where the particle intersected the silicon sensor, the two adjacent strips are positioned at 0 and 1 in "strip" units. The maximum amplitude is defined as A_0 (at 0) and the next largest adjacent strip as A_1 (at 1). For an ideal tracker, the ratio between amplitude A_0 and A_1 gives the particle coordinate, $d = 1/(1 + A_0/A_1)$. To correct for the non-linear effect, the correction function $K(d)$ is added to the measured non-linear amplitude A_0. The dashed arrow shows the uncorrected coordinate measurement. The corrected coordinate is at its true position within the measured accuracy of few microns.

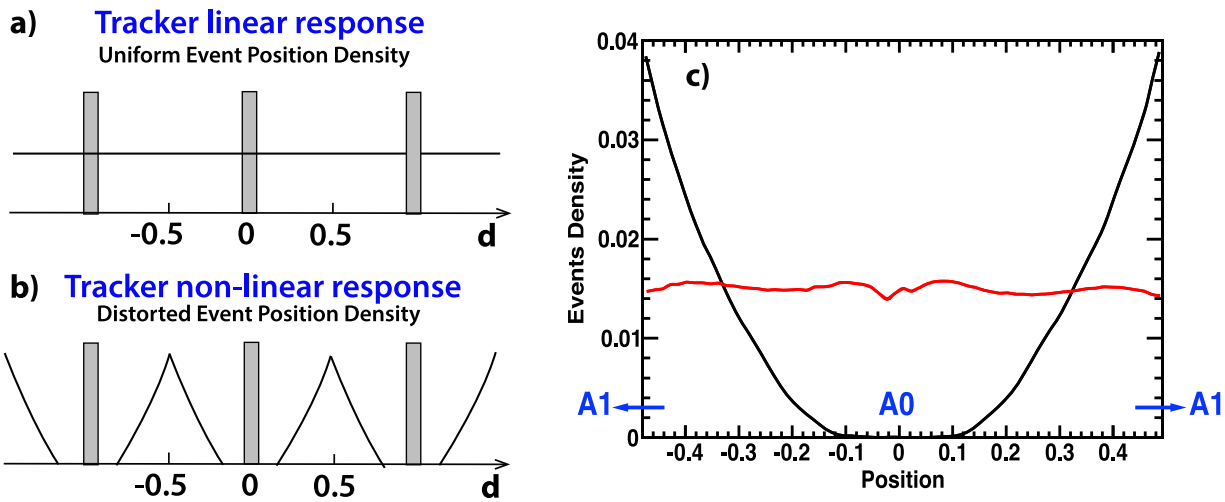

Fig. 6. (a) The uniform event position density for an ideal tracker. (b) The distorted event position density for the tracker with non-linear amplitude response. (c) The event position density before correction (black curve) and after correction (red curve) for carbon. The strips are positioned at 0 for the strip with the amplitude A_0, and at 1 or -1 for A_1.

We have developed an optimal technique to correct for the non-linear effect. As illustrated in Fig. 5, we identify a function $K(d)$ which will restore the linearity of the amplitudes by taking into account measured amplitudes A_0, A_1 and the corrected position d:

$$d = 1/(1 + (A_0 + K(d))/A_1). \tag{1}$$

To determine $K(d)$, we used the fact that cosmic rays are uniform and isotropic, so for an ideal tracker, without nonlinearity, we should see a uniform event position density (see Fig. 6a), while in the non-linear case the event density is distorted (see Fig. 6b).

The function $K(d)$ was found to be different for different Z. Fig. 6c shows the event position density distribution for carbon nuclei before and after correction. With this correction, the observed coordinate accuracy in the bending plane is 6.5 μm for helium, 5.1 μm for carbon, and 6.3 μm for oxygen.

Fig. 7 shows the coordinate measurement accuracy for nuclei from $Z = 2$ to $Z = 26$ for two different track geometries: L1–L9 and L1–L8. Note that, the L1–L9 geometry has tracks with almost normal incidence and therefore has the best coordinate resolution, while the L1–L8 geometry has tracks with larger inclination angles. Due to the design of the tracker readout amplifier, the maximum non-linearity occurs for $Z \sim 9$.

1.2.2. Tracker rigidity measurement

Together, the tracker and the magnet determine the rigidity R of charged cosmic rays by measuring the particle trajectory in the magnetic field. To find the particle trajectory we use a track-finding algorithm based on cellular

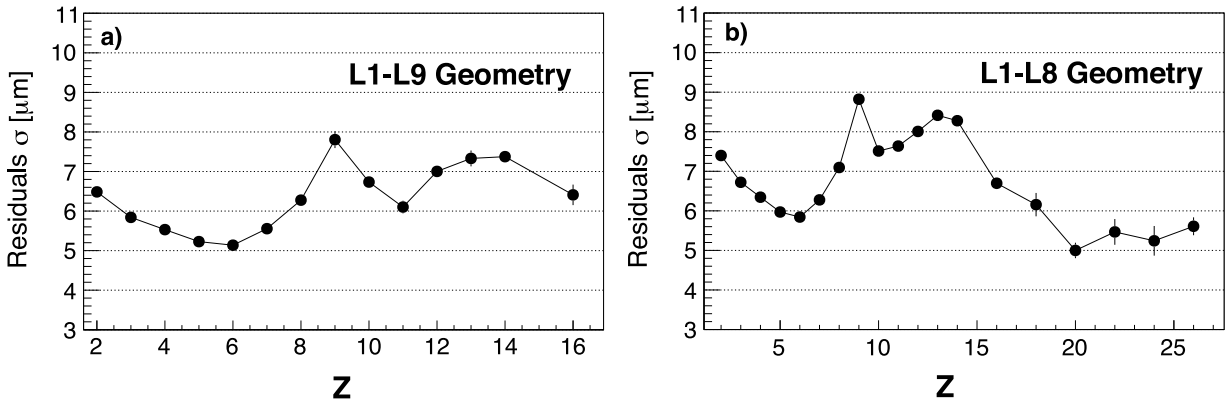

Fig. 7. AMS tracker residuals σ as functions of nuclei charge Z for (a) the L1–L9 geometry and (b) the L1–L8 geometry. The residuals were obtained by comparison of the differences of the coordinates measured in layers L3 or L5 to those obtained from the track fit using the measurements from L1, L2, L4, L6, L7, and L8 in the rigidity range $R > 50$ GV. Due to the design of the tracker readout amplifier, the maximum non-linearity occurs for $Z \sim 9$.

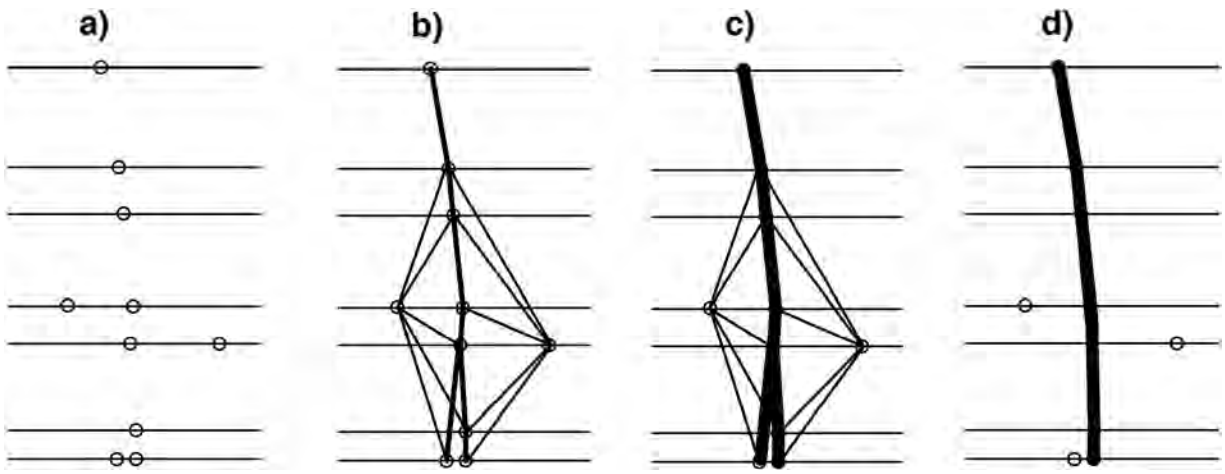

Fig. 8. Schematics of the track-finding algorithm. (a) Event with original hits. (b) Event with all track segments. (c) Correct segments chosen based on minimization of angles between segments. (d) Chose one track as the result of using a χ^2-like track quality estimator.

automaton for finding the track segments and then constructing the track, as illustrated in Fig. 8. This improves the track finding efficiency and rejection of spurious hits in the detector [41].

This algorithm is particularly important for heavy nuclei events, in which additional hits or track segments are often present due to delta-ray generation and nuclei interactions with the tracker materials.

Once a track has been found, its rigidity is determined using a track-fitting algorithm based on the Kalman filtering technique. It accurately accounts for energy losses and multiple scattering by charged particles [42]. For low rigidities ($<$ 20 GV) the $\Delta R/R$ is 0.1. This is particularly important for the measurements of nuclear isotopes. The maximum detectable rigidity (MDR) with this algorithm is 2.0 TV for protons, 3.2 TV for helium, 3.7 TV for carbon, 3.4 TV for oxygen, and 3.7 TV for iron.

Test beam data are important in understanding the tracker performance. Fig. 9a shows the comparison between data and the Monte Carlo simulation of the inverse rigidity measured by the tracker for 400 GeV/c protons from the CERN test beam. As seen, the Monte Carlo simulation describes not only detector resolution effects (the central part of the distribution) but also the effects of interactions with the detector materials including multiple, large angle, elastic, and quasi-elastic scattering (the tails of the distribution). Fig. 9 shows that the agreement between the data and the Monte Carlo simulation extends over five orders of magnitude. To study the tracker performance beyond the test beam momentum (400 GeV/c proton beam), we used the data from the ISS to compare the rigidity measured using the upper layers of the tracker, layers L1 to L8, with the rigidity measured with the lower layers, L2 to L9. Fig. 9b shows that the difference of these inverse rigidities is centered at zero and in good agreement with the Monte Carlo simulation for the rigidity range [1130-1800] GV.

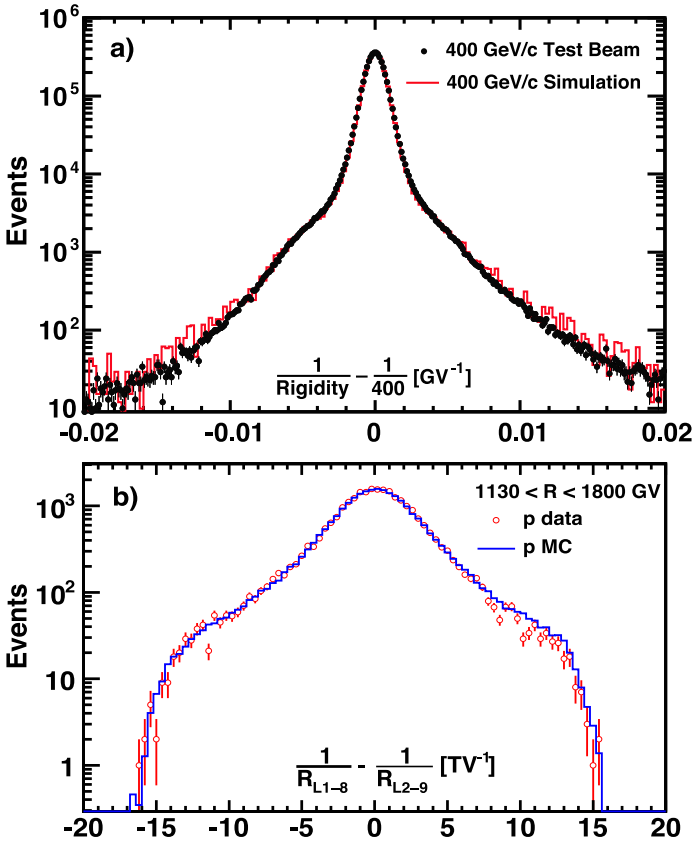

Fig. 9. (a) Comparison between data and the Monte Carlo simulation of the inverse rigidity measured by the tracker for 400 GV test beam protons. As seen, the agreement between the data and the Monte Carlo simulation extends over five orders of magnitude. (b) The difference of the inverse rigidities measured with the upper (Layers L1–L8) and the lower (Layers L2–L9) parts of the tracker for the cosmic ray proton data collected on the ISS and for the Monte Carlo simulation in the rigidity range [1130-1800] GV.

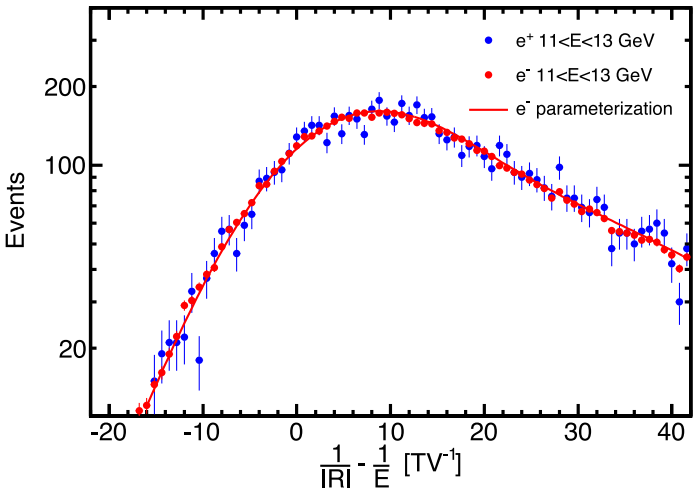

Fig. 10. The $1/|R| - 1/E$ distribution for the energy bin 11 to 13 GeV for electrons (red data points) and positrons (blue data points). The distribution for electrons is parametrized by the sum (red curve) of a Gaussian and an exponentially modified Gaussian with a $\chi^2/\text{d.o.f.} = 65/68$.

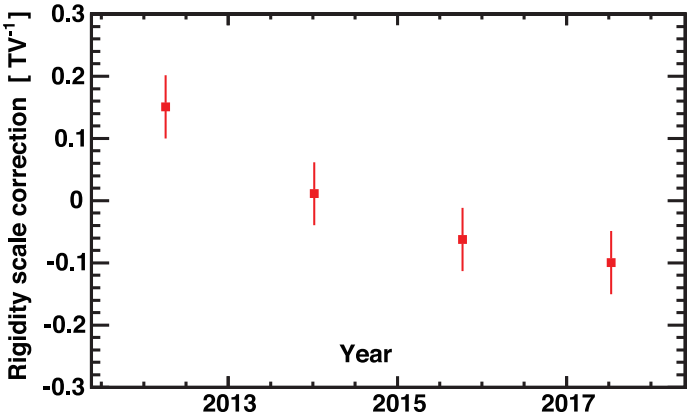

Fig. 11. The time dependence of the rigidity scale correction for the period from May 2011 to May 2018.

1.2.3. Determination of tracker absolute rigidity scale and alignment

In AMS, for all Z, the largest systematic error in the determination of the fluxes at the highest energies is due to the uncertainty of the absolute rigidity scale. The AMS tracker alignment and the absolute rigidity scale determination were performed before launch using the CERN test beam data, as shown in Fig. 9a. Vibrations and accelerations on the ISS due to movement of solar arrays, the attitude change, docking and undocking of the visiting vehicles, astronaut activities, and during the AMS launch into space as well as outgassing of the carbon fiber supporting structure in vacuum, may change the ladder positions of the inner tracker at the sub-micron level, and therefore cause shifts in the absolute rigidity scale. Note, a coherent shift in the inner tracker layers of less than 0.5 μm is sufficient to create an absolute rigidity scale shift of 10% at 1 TV.

The in-flight rigidity scale shift s and its uncertainty were obtained by the comparison of the inverse absolute rigidity $1/|R|$, measured by the tracker, with the inverse energy $1/E$, measured by the electromagnetic calorimeter, for positron events and electron events [43].

- First, the electron events and positron events were split into 72 energy bins from 2 to 300 GeV, with bin widths chosen according to the calorimeter energy resolution.
- Next, probability density function (PDF) for each bin were calculated from the $1/|R| - 1/E$ electron distributions. Fig. 10 shows the $1/|R| - 1/E$ distribution for electron events and its parametrization together with the positron events in the 11 to 13 GeV bin.
- Each PDF is then parametrized by the sum of a Gaussian function and an exponentially modified Gaussian function.
- The bin-by-bin PDF distributions are parametrized as functions of energy.
- The resulting energy dependent PDF, $f(1/|R| - 1/E, E)$, is then used in an unbinned likelihood fit of the rigidity scale shift parameters, namely s^+ for positrons and s^- for electrons.
- The likelihood is defined as $\sum^+ \log f(1/|R| + s^+ - 1/E, E) + \sum^- \log f(1/|R| + s^- - 1/E, E)$, where the summations include all positron events or electron events, respectively.
- The absolute rigidity scale shift is then evaluated as $s = (s^+ - s^-)/2$.

As mentioned above, various effects at launch and in space may modify rigidity scale and bias flux measurements. To determine the time-dependent rigidity shift correction, the electron–positron data from the first 7 years of operations is divided into four time intervals. Fig. 11 shows the time dependence of the rigidity scale correction for the period from May 2011 to May 2018. With this time dependent correction, the accuracy of the rigidity scale shift is found to be within 0.033 TV^{-1} or 3% at 1 TV, limited mostly by available positron statistics.

The positions of L1 and L9 are dynamically aligned every 2 min according to extrapolations from the inner tracker (layers L2 to L8). Therefore, the rigidity scale of the full span tracker with layers from L1 to L9 follows the rigidity scale of the inner tracker. To verify this, the difference in the rigidity scale shifts between the full span tracker and the inner tracker, $s(1/R_{19}) - s(1/R_{28})$, has been estimated using high energy cosmic ray proton and helium events. Both proton and helium samples yield similar results. The difference is found to be $s(1/R_{19}) - s(1/R_{28}) = -0.019 \pm 0.011$ TV^{-1} independent of rigidity [43]. The corresponding small shifts in the L1 and L9 positions were corrected and the error of 0.011 TV^{-1} is added in quadrature to the total error of the rigidity scale.

Overall, the tracker rigidity scale was measured with an accuracy of ± 0.034 TV^{-1} (i.e. quadratic sum of 0.033 TV^{-1} and 0.011 TV^{-1}). This corresponds to the determination of a coherent displacement of layers L2–L8 by less than 0.2 μm.

To verify that after these corrections rigidity scale is time independent, we have studied the time dependence of the measured fluxes. Fig. 12 shows the ratio of the proton and helium fluxes measured using data from each 21-month period to the fluxes measured over the complete 7 years. As seen, at high rigidities (>100 GV), where the solar effects

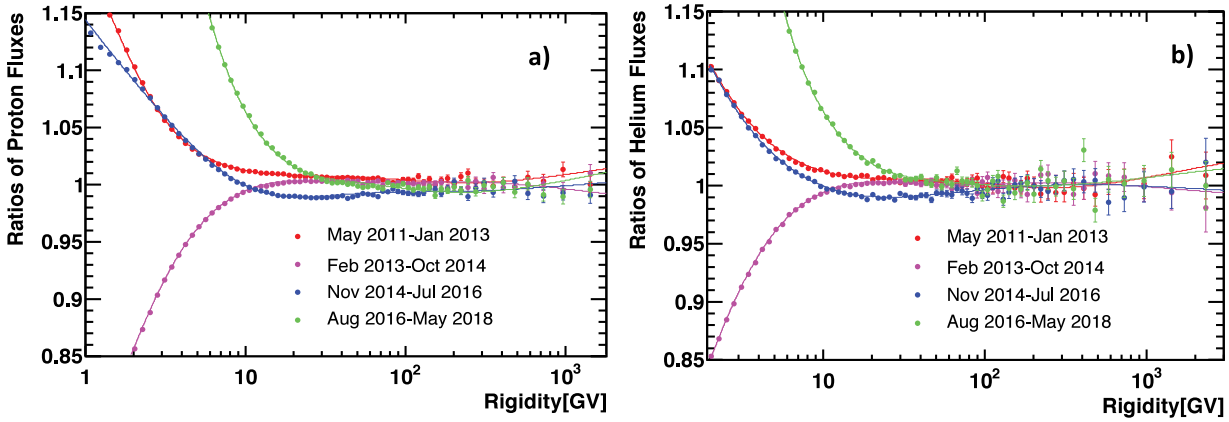

Fig. 12. The ratios of the (a) proton and (b) helium fluxes measured for each of the four 21-month periods to the flux measured over 7 years. At low rigidities, the fluxes are time dependent due to solar modulation. At high rigidities, above 100 GV, the fluxes are consistent within measurement errors.

are negligible, the fluxes for different time periods are consistent within the measurement errors both for protons and helium.

1.2.4. Charge-sign identification

Charge-sign identification is a critical property of the spectrometer. It allows AMS to distinguish negatively charged cosmic rays from positively charged cosmic rays. It is quantified by the amount of charge confusion. For example, in the analysis of positrons it is important to distinguish positrons from charge-confusion electrons, i.e. those electrons reconstructed with the positive charge sign due to the finite tracker resolution or interactions in the detector materials. To this end, a charge confusion estimator $\Lambda^e_{\rm CC}$ is defined using the Boosted Decision Trees technique [44,45]. The estimator combines several measurements: the ratio of the energy from the calorimeter to the momentum from the tracker, E/p, the track χ^2/d.o.f., momenta reconstructed with different combinations of tracker layers, the number of hits in the vicinity of the track, and the charge measurements in the TOF and in the tracker. With this method, positrons, which have $\Lambda^e_{\rm CC} \sim +1$, are efficiently separated from charge confusion electrons, which have $\Lambda^e_{\rm CC} \sim -1$.

After selection of a sample of positron and electron events with the TRD and ECAL, the charge confusion in data is obtained using the template fitting technique with the $\Lambda^e_{\rm CC}$ distribution [45]. From the fit to the positive rigidity sample, we obtain the number of positron N_{e^+} events, charge confusion electron background $N^{c.c.}_{e^-}$ events, and proton background events. From the fit to the negative rigidity sample, we obtain the number of electron N_{e^-} events, charge confusion positron background $N^{c.c.}_{e^+}$ events, and proton background events. The charge confusion fraction in the electron data is calculated as $N^{c.c.}_{e^-}/(N^{c.c.}_{e^-} + N_{e^-})$ and similarly for positrons.

The charge confusion in the Monte Carlo simulation is directly calculated as the fraction of electrons being reconstructed with positive rigidity after the same selection cuts as used in data. As an illustration, the comparison between the electron charge confusion fraction in the data and in the Monte Carlo simulation is presented in Fig. 13. As seen, the charge confusion is well reproduced by the Monte Carlo simulation. The charge confusion fraction is <8% in the energy range up to 1 TeV.

Similar methods are used to differentiate antiprotons and anti-deuterons from proton and deuteron backgrounds.

1.2.5. Tracker charge measurement

The nine tracker layers independently measure the charge $|Z|$ of cosmic rays. The ionization energy losses deposited in the silicon are proportional to Z^2 and they are measured with strips on both the x and y sides of a silicon sensor.

The energy loss deposition is collected by several strips on both x and y sides. The relative signal on either side is related to the transverse distance d between the nearest strip and the location where the particle crosses the silicon, as shown in Fig. 14. The strip amplitudes are first corrected for electronics gain factors and then for the dependence on the particle position d and inclination angle θ. Details of this technique as well as the effects of non-linear electronics response for high Z nuclei are described in Ref. [46].

The charge measurement is obtained by combining the charge determined by both x and y strips. Fig. 15 shows the charge resolution of tracker layers L2–L8 for nuclei from $Z = 1$ to $Z = 28$. This resolution enables us to perform the precision measurement of all nuclei fluxes up to and beyond nickel ($Z = 28$).

Fig. 16 shows the charge measured simultaneously by the TOF (see Section 1.4) and the tracker.

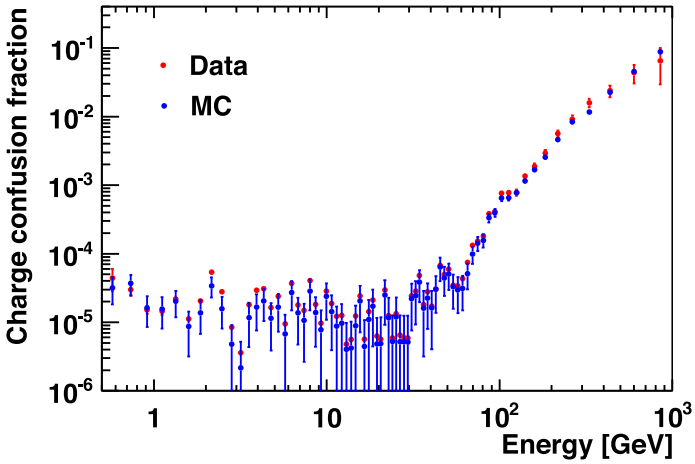

Fig. 13. The charge confusion fraction as a function of energy measured with electrons. The charge confusion fraction is <8% in the energy range up to 1 TeV. As seen, the charge confusion is well reproduced by the Monte Carlo simulation.

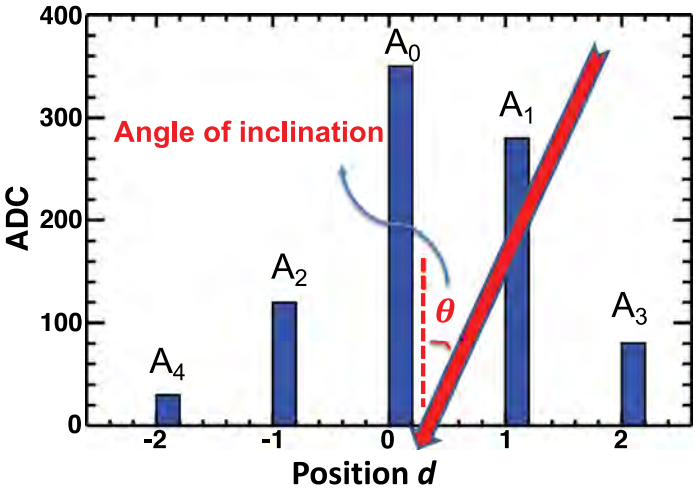

Fig. 14. Schematic of ionization energy deposition signals per strip, in ADC counts, at the incident particle position d (defined in Eq. (1), see also Fig. 5) and the inclination angle θ of the particle (red arrow). A_0 is the strip with the highest amplitude (that is, the strip nearest to the crossing point), the next highest adjacent strip A_1, the other adjacent strip A_2, etc.

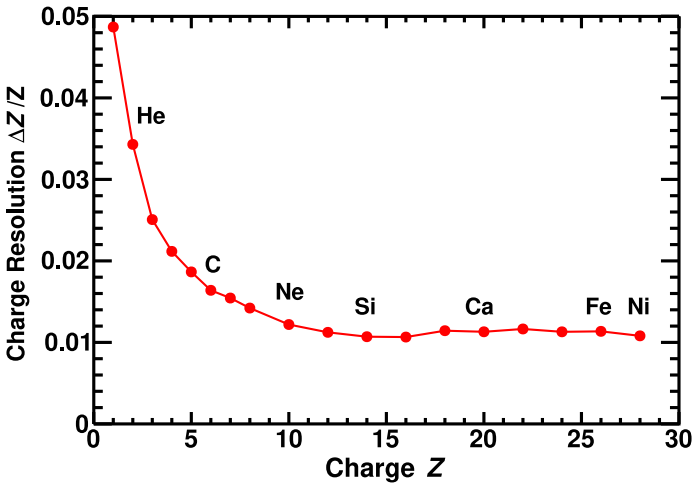

Fig. 15. The inner tracker (layers L2–L8 combined) charge resolution $\Delta Z/Z$. The solid line is to guide the eye.

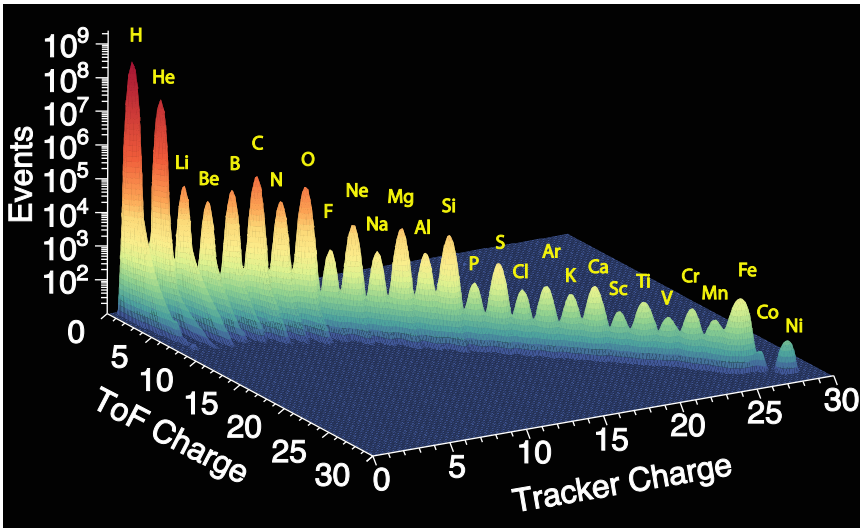

Fig. 16. The charge measurement by the TOF (see Fig. 22) and the tracker.

1.3. Transition Radiation Detector (TRD)

The Transition Radiation Detector (TRD) [47] is located at the top of the AMS as shown in Fig. 2. Its main purpose is to identify electrons and positrons by transition radiation while rejecting protons at a level of 10^3. The TRD also provides an independent tracking capability and determination of the charge value of the nuclei by measuring their rate of energy loss (dE/dx).

The TRD consists of 5248 proportional tubes of 6 mm diameter with a maximum length of 2 m arranged side-by-side in 16-tube modules. The 328 modules are mounted in 20 layers. As shown in Fig. 17a, the assembly of the TRD layers is supported in a tapered octagonal carbon fiber structure with a very low coefficient of thermal expansion. Such a structure ensures the minimum relative movement of the TRD elements with the variation of the ambient temperature.

As shown in Fig. 17b, each layer is interleaved with a 20 mm thick fiber fleece radiator, LRP375BK, with a density of 0.06 g/cm^3. There are twelve layers of proportional tubes along the y axis located in the middle of the TRD and, along the x axis, four layers located on top and four on the bottom. The tubes are filled with a 90:10 Xe:CO_2 gas mixture. Xenon efficiently captures the transition radiation X-rays generated in the radiator layers. CO_2 ensures stable operation of the proportional tubes. An anode wire in each straw tube measures the signal from the resulting ionization due to the captures of the transition radiation photons as well as the ionization signal of the traversing charged particle (see Fig. 17c).

Experience over the first 7 years of operations on the ISS shows a negligible, diffusion dominated leak rate of CO_2. The measured leak rate during the first seven years of operations is stable and amounts to 0.47 g/day on average. The onboard gas supplies contained 49 kg of Xe and 5 kg of CO_2 at launch, which ensures ∼30 years of steady TRD operations in space.

In order to differentiate between $e^{\pm}$ and protons, signals from the 20 layers are combined in a TRD estimator, Λ_{TRD}, formed from the ratio of the log-likelihood probability of the $e^{\pm}$ hypothesis to that of the proton hypothesis. The Λ_{TRD} distributions for cosmic ray protons and electrons in the rigidity range 10–100 GV are shown in Fig. 18 together with the Monte Carlo simulation [48]. As seen, positrons and electrons have a TRD estimator value ∼0.4 and protons ∼1. This allows the efficient discrimination of the proton background. By varying the position of the cut on the TRD estimator, we can achieve better purity with the corresponding reduction of the efficiency of the electron signal (see Fig. 18).

Fig. 19 shows the proton rejection power of the TRD estimator measured on orbit at 90% $e^{\pm}$ efficiency. As seen, the proton rejection power can be further improved by tightening the $e^{\pm}$ efficiency to 65%.

1.4. Time of Flight Counters (TOF)

Time of Flight counters (TOF) provide a charged particle trigger to AMS, determine the direction and velocity of incoming particles, and measure their charge via dE/dx.

Two planes of scintillation counters are located above and two planes below the magnet, see Figs. 20a and 20b. Each plane contains 8 or 10 scintillating paddles. Each paddle is equipped with 2 or 3 PMTs on each end for efficient detection of traversing particles. The coincidence of signals from all four planes provides a charged particle trigger, see Section 1.8. The detailed description of TOF detector is presented in Ref. [49].

The average time resolution of each counter has been measured to be $\Delta = 160$ picoseconds for $Z = 1$ nuclei. The timing resolution improves with increasing magnitude of the charge to a limit of $\Delta = 50$ ps for $Z > 6$ nuclei. This corresponds

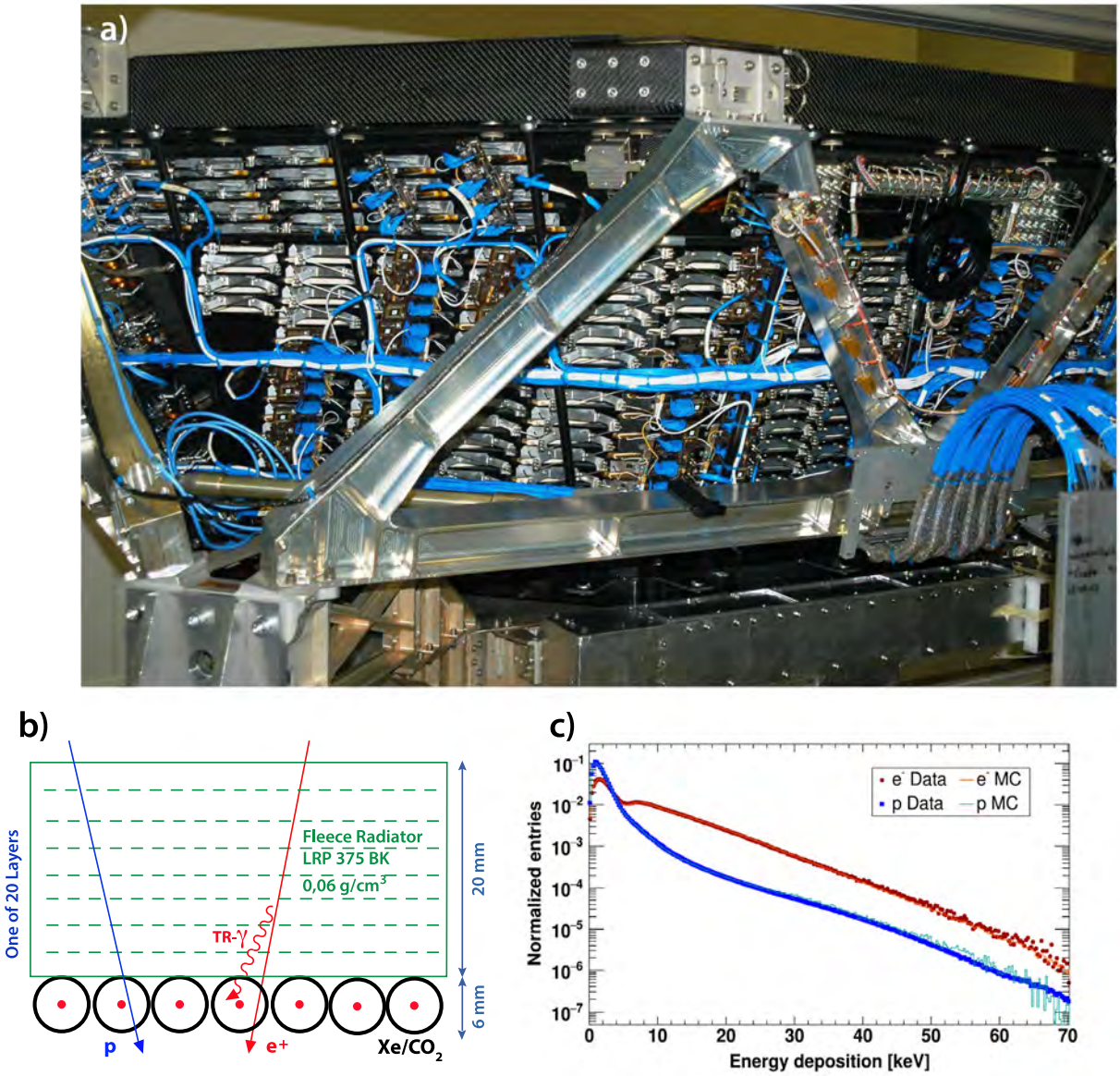

Fig. 17. (a) The Transition Radiation Detector. (b) Schematic of the detection of ionization losses from charged particles, for example protons (blue arrow) compared to positrons (red arrow) and transition radiation photons (red curved arrow, TR-γ) in one of the twenty TRD layers. (c) The energy deposition spectra of cosmic ray protons (blue data points) and electrons (red data points) in the rigidity range 10–100 GV together with the Monte Carlo simulation (light blue and red histograms, respectively). A significant difference in the shape of the proton and electron spectra is used in the likelihood function to separate these two species of cosmic rays.

to an overall velocity ($\beta = v/c$) resolution $\Delta(1/\beta) = 4\%$ for $Z = 1$, $\Delta(1/\beta) = 2\%$ for $Z = 2$ and $\Delta(1/\beta) = 1\%$ for $Z > 6$ nuclei. Figs. 20c and 20d show the measured velocity resolution for $Z = 2$ and $Z = 6$, respectively.

The TOF also discriminates between upward- and downward-going particles, see Fig. 21. The measured direction confusion probability is about 10^{-9}.

The TOF charge resolution is shown in Fig. 22 for $Z = 6$ and $Z = 26$ for a single TOF counter. Fig. 16 shows the combined charge determination by the tracker (see Section 1.2) and the TOF.

1.5. Anticoincidence counters (ACC)

The Anticoincidence (or veto) counters (ACC) [50] surround the tracker inside the magnet bore. Their purpose is to reject particles that enter or exit the tracker volume transversely. As shown in Fig. 23, the ACC consists of sixteen

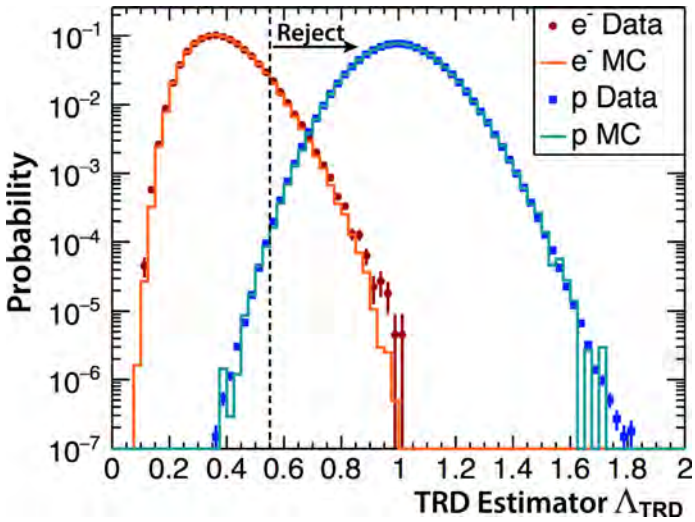

Fig. 18. The Λ_{TRD} distributions for cosmic ray protons (blue) and electrons (red) in the rigidity range 10–100 GV together with the Monte Carlo simulation. As seen, the simulation describes the data over six orders of magnitude. The vertical dashed line shows the position of the cut corresponding to 90% efficiency of the electron signal. By tightening this cut (i.e. moving the dashed line to the left) we can achieve better purity of the electron signal with the corresponding reduction of the signal efficiency.

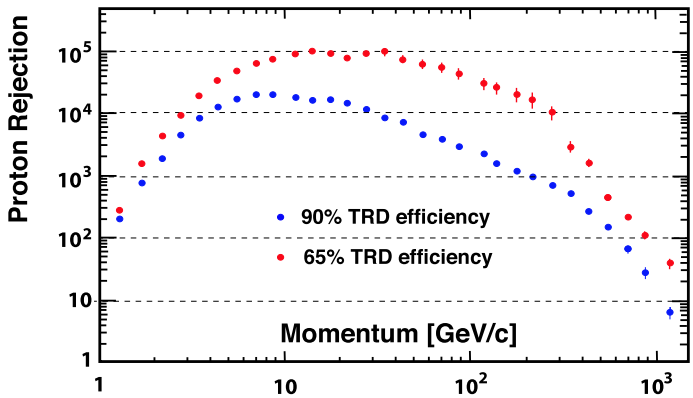

Fig. 19. Proton rejection power of the TRD measured from ISS data at 90% and 65% electron and positron efficiency. At 90% $e^{\pm}$ efficiency, the measured proton rejection is above 1000 in the energy range 2–200 GeV/c. At higher rigidities, the rejection power can be improved by tightening the $e^{\pm}$ selection.

curved scintillator panels of 800 mm length, instrumented with embedded wavelength shifting fibers to collect the light efficiently. The light from the two ends of the fibers from two adjacent panels are routed to two photo-multiplier tubes. To maintain the hermeticity of the ACC cylinder, the counters have a tongue and a groove along the vertical edges such that particles crossing this area are detected simultaneously in two panels. Long duration tests of the counters show they have an efficiency of 0.99999.

1.6. Ring Imaging Cherenkov counter (RICH)

Ring Imaging Cherenkov counter (RICH) [51] measures the velocity and charge of passing particles. Both are calculated from the geometrical shapes, circles or rings, generated by the Cherenkov effect. The opening angle θ of the cone of photons generated in the radiator yields a measurement of the velocity $\beta = v/c$ and the number of photons is proportional to Z^2. As shown in Fig. 24a, the RICH has three main components — a radiator plane, an expansion volume, and a photo-detection plane. The radiator plane consists of a central radiator formed by 16 sodium fluoride, NaF, tiles each $85 \times 85 \times 5\,\mathrm{mm}^3$ with a refractive index $n = 1.33$. These are surrounded by 92 tiles each $113 \times 113 \times 25\,\mathrm{mm}^3$ of silica aerogel with a refractive index $n = 1.05$. This allows the detection of particles with velocities $\beta > 0.75$ with the NaF radiator and $\beta > 0.953$ with the aerogel radiator. The expansion volume extends 470 mm in z and is surrounded by a conical reflector. The photo-detection plane (see Fig. 24b) is composed of 680 sixteen-pixel photo-multiplier tubes,

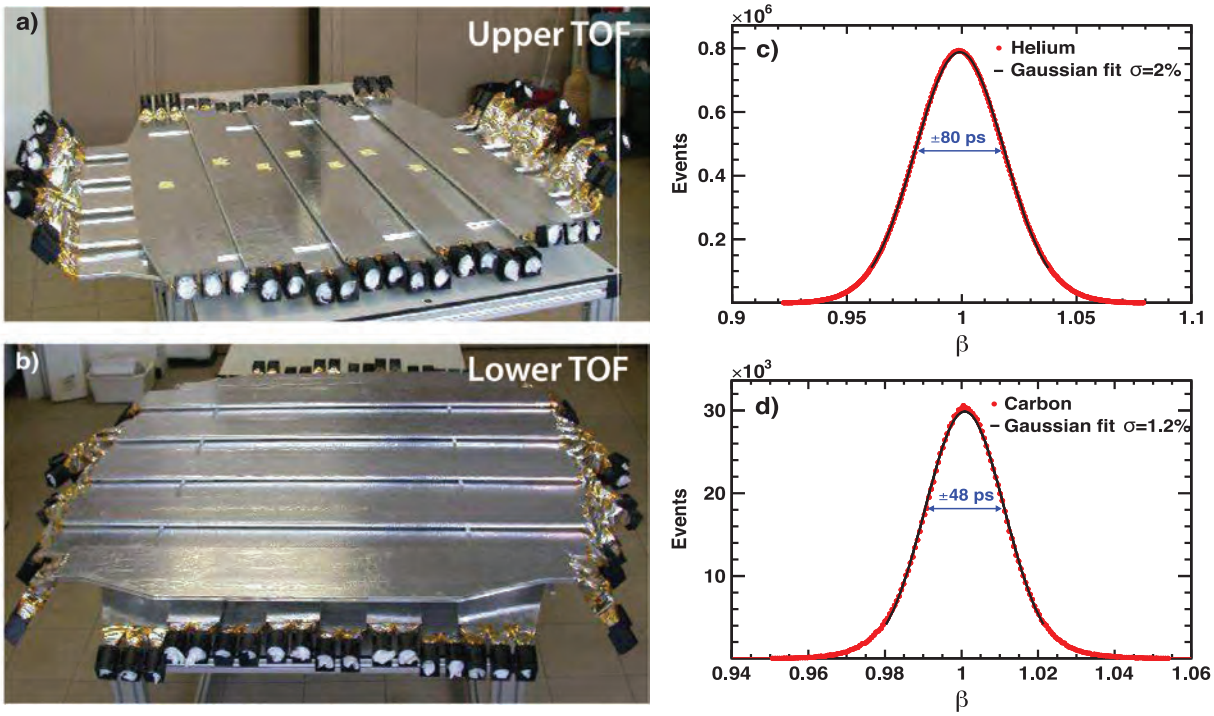

Fig. 20. (a) The upper TOF counters. (b) The lower TOF counters. Location of the counters is shown in Fig. 2. The measured TOF velocity distribution for (c) $Z = 2$ (He) and (d) $Z = 6$ (C) nuclei with rigidity > 20 GV. The solid black lines are Gaussian fits with standard deviations of σ=2% for helium and σ=1.2% for carbon. This corresponds to TOF time resolution of 80 ps and 48 ps, respectively.

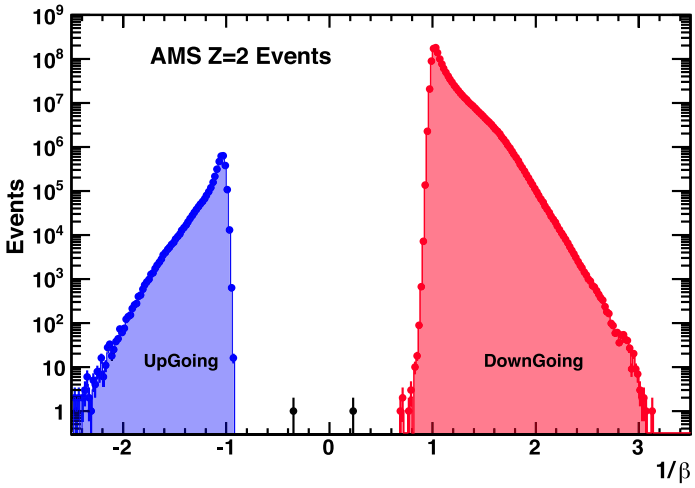

Fig. 21. The $1/\beta$ distribution for 1.2 billion $Z = 2$ nuclei measured by AMS. The measured direction confusion probability is about 10^{-9}.

for a total of 10,880 pixels. Figs. 24c and 24d show the RICH velocity (σ_β, in units of β) and charge (σ_Z, in charge units) resolution as functions of Z. The velocity resolution for $|Z| > 1$ is better than 0.1% at $\beta \sim 1$.

1.7. Electromagnetic Calorimeter (ECAL)

The Electromagnetic Calorimeter, ECAL, is located at the bottom of AMS as shown in Fig. 2. The assembled ECAL is presented in Fig. 25a. It is a 3-dimensional imaging instrument providing a shower measurement over 17 radiation lengths X_0 [52].

ECAL is the key detector for measurements of electrons and positrons in AMS. It consists of a multilayer sandwich of lead foils and ∼50,000 scintillating fibers with an active area of 648 × 648 mm^2 and a thickness of 166.5 mm. The calorimeter is composed of 9 superlayers, each 18.5 mm thick and made of 11 grooved, 1 mm thick lead foils interleaved

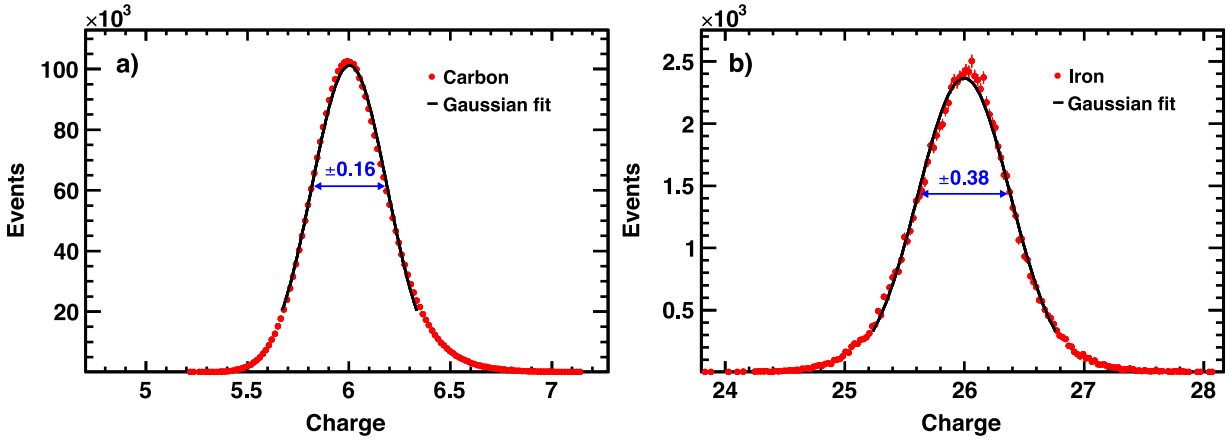

Fig. 22. Distribution of the TOF charge Z for (a) carbon ($Z = 6$) and (b) iron ($Z = 26$) nuclei for a single TOF counter. The solid black lines are Gaussian fits with standard deviations of 0.16 and 0.38 charge units, respectively.

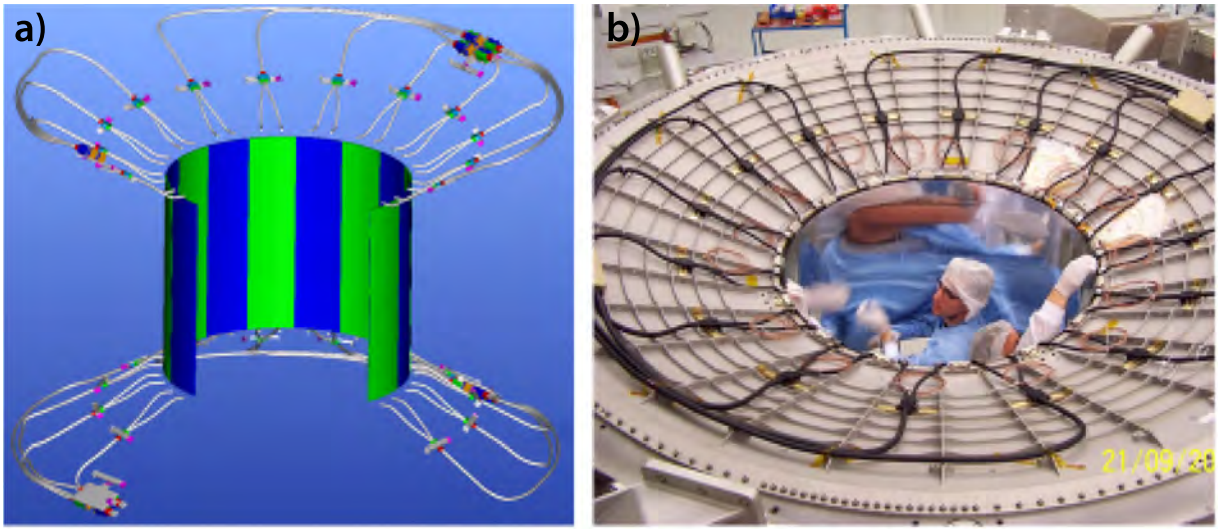

Fig. 23. (a) Cutaway view of the ACC counters (blue and green colored panels) and their fiber light guide collection system and (b) installation of the ACC in the magnet bore. The fiber light guide collection system (black cables) is also shown.

with 10 layers of 1 mm diameter scintillating fibers. In each superlayer, the fibers run in one direction only. The 3D imaging capability of the detector is obtained by stacking alternate superlayers with fibers parallel to the x and y axes (5 and 4 superlayers, respectively).

All fibers are read out on one end only by 324 photomultiplier tubes (PMT). Each PMT has four anodes and is surrounded by a magnetic shield which covers light guides, the PMT base and the frontend electronics. Each anode has an active area of $9 \times 9\,\mathrm{mm}^2$, corresponding to about 35 fibers, defined as a cell. Fig. 25b schematically shows the ECAL structure and Fig. 25c the optical face of one superlayer of the lead-fiber matrix, against which a grid of PMTs is mounted. Fig. 25d illustrates the locations of optical fibers within a cell. In total there are 1296 cells segmented into 18 layers longitudinally, two per superlayer, with 72 transverse cells in each layer providing a fine granularity sampling of the shower in three dimensions. The signals are processed over a wide dynamic range, from a minimum ionizing particle, which produces about 10 photoelectrons per cell, up to the 60,000 photoelectrons produced in one cell near the shower maximum for a 1 TeV electron, corresponding to a deposited energy of 60 GeV.

1.7.1. ECAL shower reconstruction

Reconstruction of the showers from electrons and positrons in the calorimeter uses a 3-dimensional parametrization, which accounts for the detector specifics: the finite size of the calorimeter, the non-uniform efficiency of the signal collection, and saturation effects due to the electronics and due to large energy deposition in calorimeter cells.

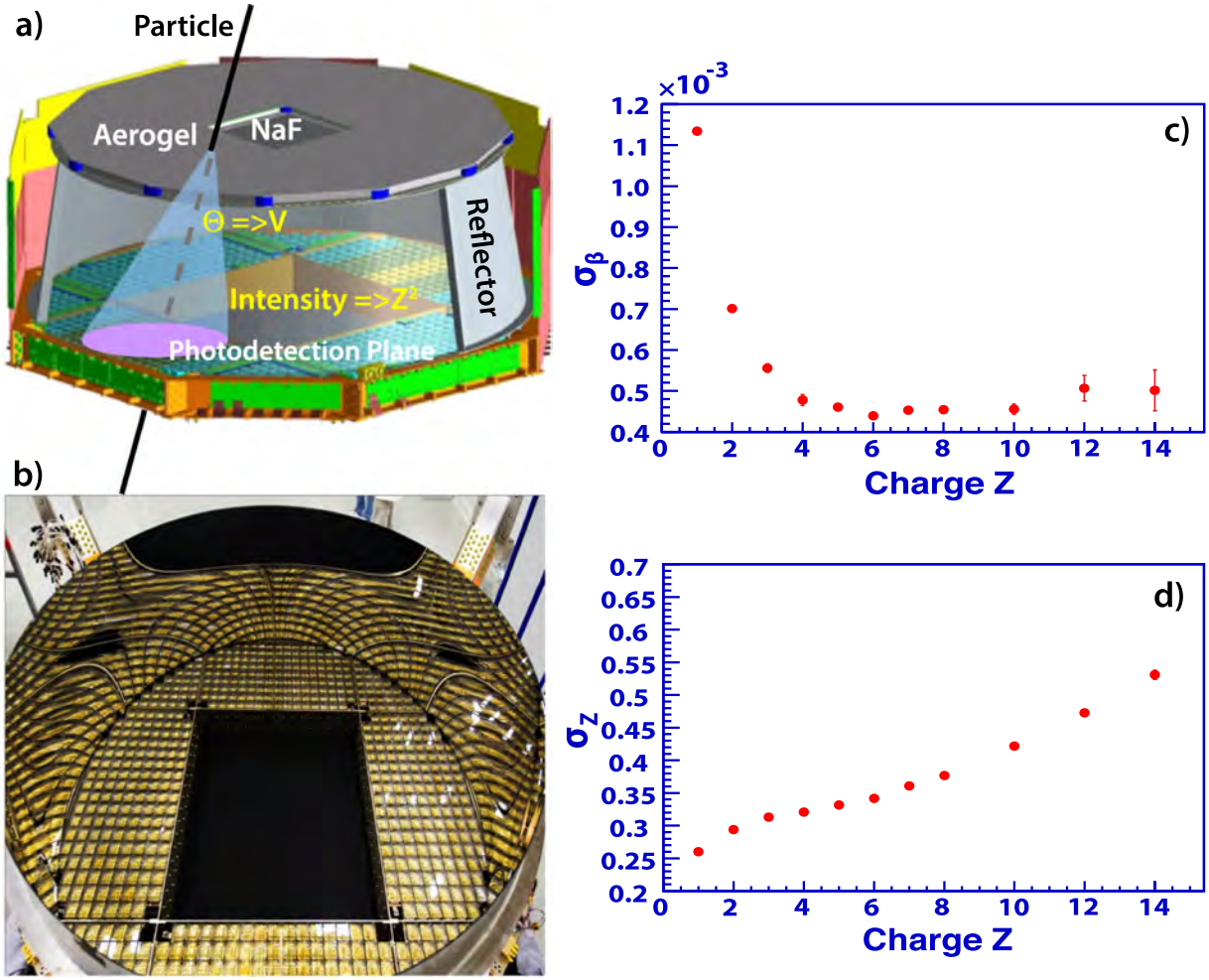

Fig. 24. (a) Schematic of the RICH. (b) The RICH reflector and photo-detection plane. (c) The RICH velocity and (d) charge resolution vs charge Z for the aerogel radiator.

An electromagnetic shower is described by seven parameters, which fully determine the measured pattern of energy depositions in the calorimeter cells [53]: the shower energy (E_0); the 3-dimensional spatial point (x_0, y_0, z_0) corresponding to the location of the shower maximum; the two angles (K_X, K_Y), which together with the spatial point, define the shower axis; and the location (T_0) of the shower maximum on the shower axis. This is a minimal parameter set, which allows accurate shower parametrization without introducing correlation between these parameters.

The longitudinal shower profile in terms of the depth t in the calorimeter (in units of radiation lengths) is described by an empirical parametrization [54]:

$$\frac{dE}{dt}(t) = E_0 \frac{(bt)^{bT_0} b e^{-bt}}{\Gamma(bT_0 + 1)}, \tag{2}$$

using the parameters described above and the scale parameter b, which depends on the specific construction and materials of the calorimeter. In the AMS ECAL, we found that the scale parameter b is constant ($b = 0.65$). The individual shower parameters E_0 and T_0 are obtained from a fit to observed energy depositions in the ECAL cells of each shower. This provides a good description of the energy evolution of the shower shape in the energy range up to a few TeV [53].

1.7.2. ECAL energy reconstruction

The saturation in the electronics is insignificant over the energy range of interest, the remaining saturation is in the calorimeter fibers. It is related to conversion of ionization to light. As illustrated in Fig. 26, the effect is maximal near the shower peak, whereas for the rest of the shower, the cells are not affected. Using non-saturated cells allows an accurate accounting for the amount of saturation.

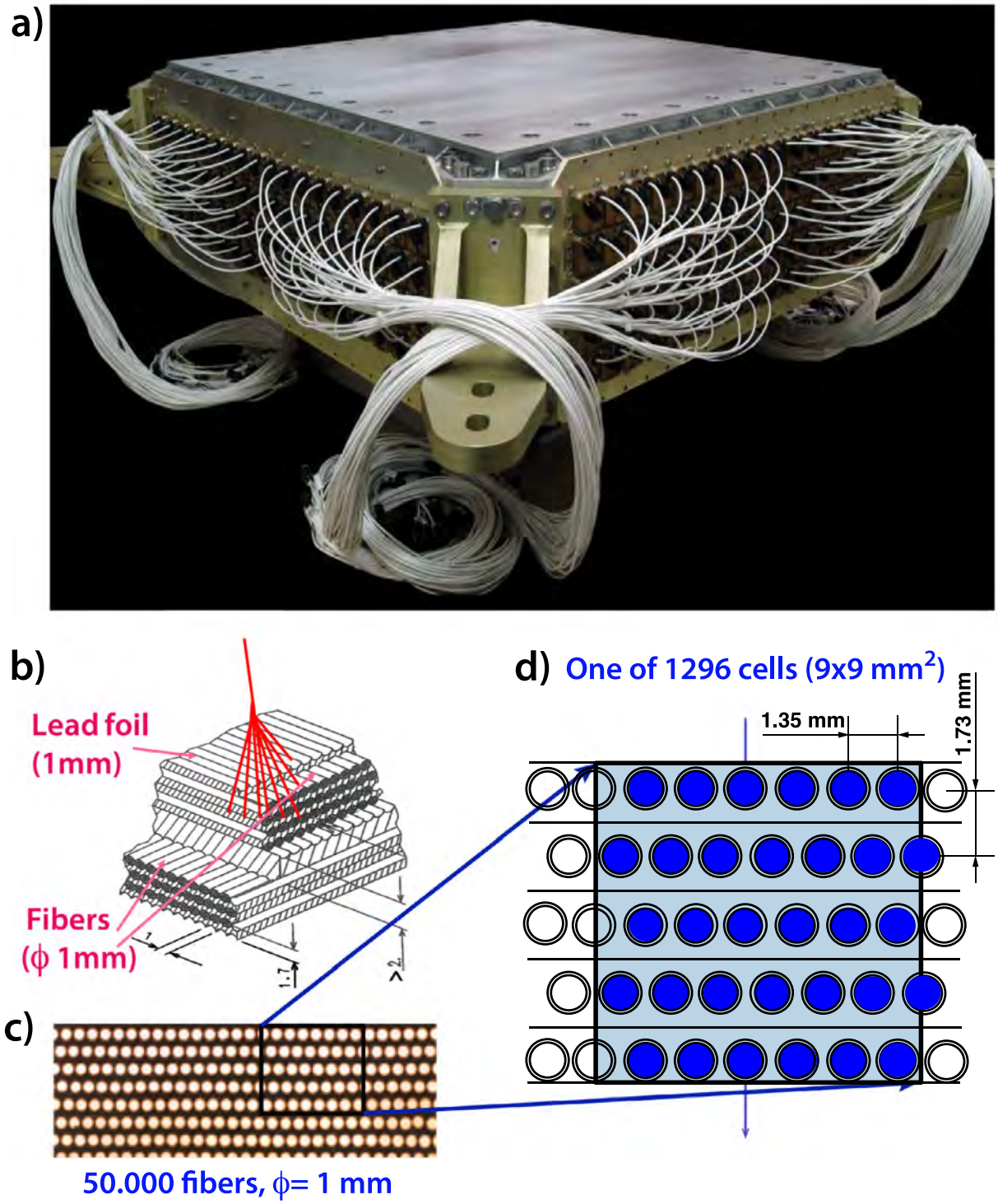

Fig. 25. (a) The Electromagnetic Calorimeter, ECAL, has ∼50,000 scintillating fibers sandwiched with 1 mm lead foils, covers an active area of 648 × 648 mm^2, measures electromagnetic showers over 17 radiation lengths and weighs 640 kg. (b) The ECAL structure. (c) The optical face of one superlayer. (d) The ECAL lead-fiber matrix corresponding to a single cell. Optical fibers of 1 mm diameter are embedded in lead with 1.35 mm horizontal pitch. Adjacent rows of fibers are shifted by half a pitch. The distance between fiber rows is 1.73 mm.

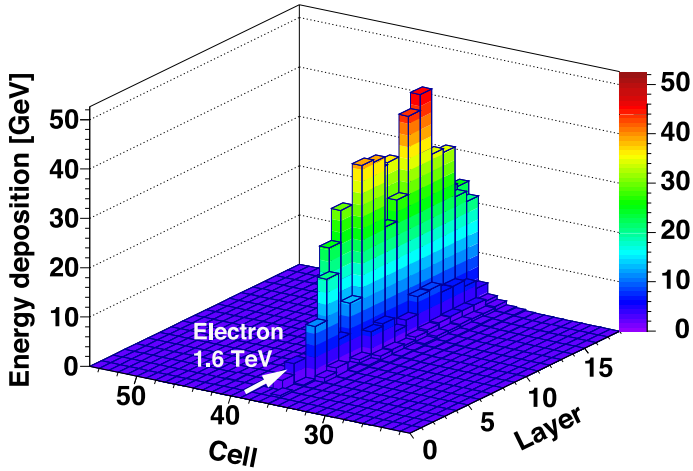

Fig. 26. Example of a 1.6 TeV electron shower in the ECAL. Most of the shower energy is deposited along the shower axis near the shower maximum. For high energy showers (> 500 GeV), some of the amplitudes are saturated, for example, those shaded in red.

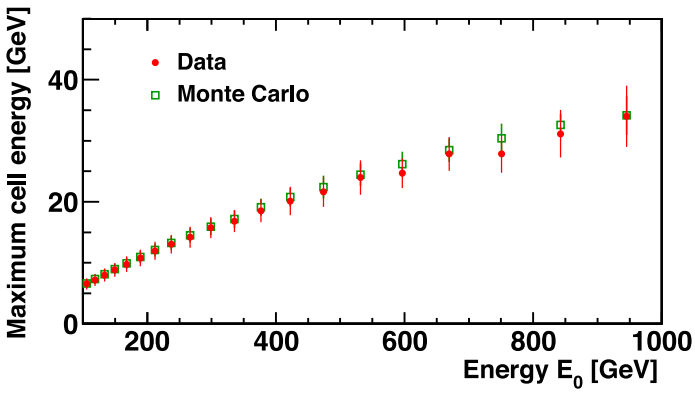

Fig. 27. The maximum cell energy in a shower as a function of the reconstructed shower energy E_0 for the data from a sample of cosmic ray electrons (red data points) and the Monte Carlo simulation with the saturation effects in fibers (open green squares). The Monte Carlo simulation that takes into account saturation effects is in good agreement with the data.

The saturation effect is taken into account [53] using the energy dependence of the maximum cell amplitude in the shower. This is illustrated in Fig. 27 using a sample of high-energy electrons. There is good agreement between the data and the Monte Carlo simulation when saturation effects are accounted. Note that if saturation effects are not included in the Monte Carlo simulation, its prediction is significantly above the observation [53].

The techniques outlined above provide AMS with a precision energy measurement of electrons and positrons up to multi-TeV as well as a coordinate resolution of ∼200 μm and an angular resolution of 0.3 degrees at 1 TeV [53]. The ECAL energy resolution is measured using the beam test data in the energy range from 10 to 300 GeV and the Monte Carlo simulation beyond this range. Fig. 28 shows the ECAL energy resolution as a function of the $e^{\pm}$ energy compared with the Monte Carlo simulation.

1.7.3. Proton rejection using ECAL

ECAL is used to separate electrons and positrons from protons using the same shower parametrization as used for the energy reconstruction. This is achieved by using an ECAL estimator Λ_{ECAL}. The estimator includes variables which measure the compatibility of energy depositions in the calorimeter cells with that of an electromagnetic shower. It also includes variables that measure the consistency of the shower parameter values (like z_0 and T_0) with those expected for an electromagnetic shower of energy E_0. Altogether, there are 16 variables included in the definition of Λ_{ECAL} [53].

The proton rejection power, which combines the Λ_{ECAL} with the energy–momentum matching ($E/p > 0.7$), is evaluated as a function of rigidity as shown in Fig. 29. As seen, the proton rejection can be further increased with a tighter Λ_{ECAL} cut. With the tighter Λ_{ECAL} cut the electron and positron selection efficiency is reduced correspondingly.

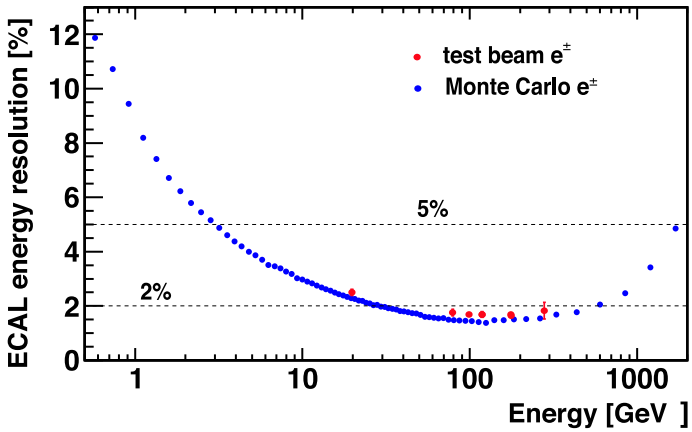

Fig. 28. The ECAL energy resolution for electrons and positrons averaged over the ECAL acceptance. Beam test measurements (red data points) and results of the Monte Carlo simulation (blue data points) are shown.

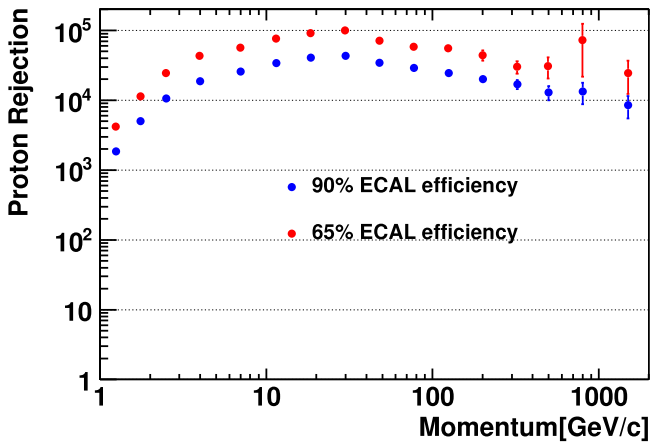

Fig. 29. Comparison of the measured proton rejection for 90% (blue data points) and 65% (red data points) $e^{\pm}$ selection efficiencies. A total of 1.03 billion proton events are used in the momentum range [1–2000] GeV/c in this analysis. The tighter cut further reduces the proton background by a factor of ∼3. This is independent of the rejection power of the TRD shown in Fig. 19.

1.8. Trigger and data acquisition

In AMS, signals from the 300,000 data acquisition channels are only digitized in response to a two-level trigger (fast trigger and level-1 trigger) which detects that a cosmic ray of interest may have passed through the detector. The fast trigger is formed from the logical OR of three inputs:

1. for all cosmic rays: the coincidence within 240 ns of signals in any three of the four TOF planes each with a pulse height greater than 0.5 times that deposited by a $Z = 1$ minimum-ionizing particle (MIP);
2. for electrons, positrons and photons: an energy deposition in the ECAL consistent with an electromagnetic particle of energy greater than 1 GeV;
3. for slow particles: the coincidence within 640 ns of signals from four TOF planes each with a pulse height greater than 3.5 times a MIP.

When a fast trigger occurs, further information from the ACC and the ECAL is gathered to form the level-1 trigger within 1 μs. For $Z = 1$ particles four TOF signals with no ACC signals are required. For electrons and positrons a coincidence of four TOF signals and total ECAL energy trigger is required. Level-1 trigger efficiency is measured using three out of four TOF signal coincidence versus the corresponding level-1 trigger. Fig. 30 shows the overall measured efficiency for electrons as a function of energy. As seen, at energies above 3 GeV the trigger efficiency reaches 100%.

The physics performance for each of the detectors described above requires that electronics be designed, produced, tested, and qualified for operation in space to process a total of ∼300,000 electronic signals. Dedicated circuits were implemented for each detector – the tracker, TRD, TOF+ACC, RICH, and ECAL – to collect and digitize the signals. When a trigger occurs, the data volume of ∼3.6 Mbit per event is processed.

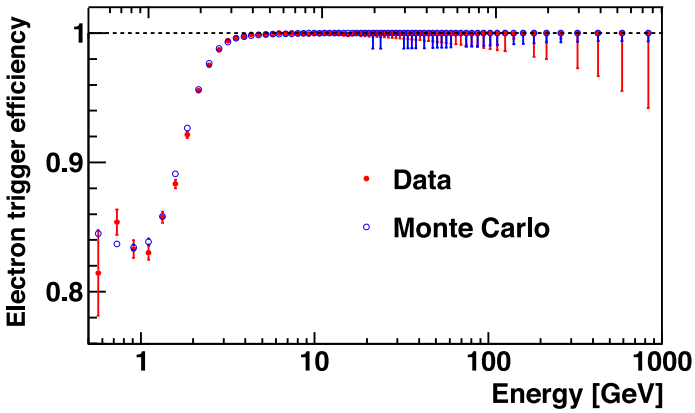

Fig. 30. The trigger efficiency for electrons as a function of energy for data (red data points) and the Monte Carlo simulation (blue data points) with a dashed line at unity to guide the eye. As seen, the Monte Carlo simulation agrees well with the data.

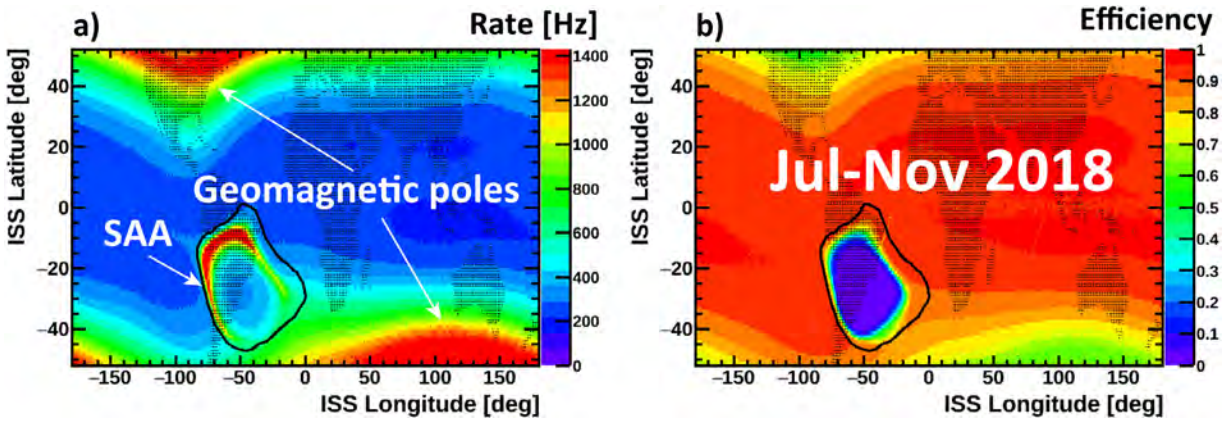

Fig. 31. For a typical data taking period, July–November 2018, (a) the average event acquisition rate in Hz and (b) the data acquisition efficiency as a function of latitude and longitude. The South Atlantic Anomaly (SAA) is indicated by the black curve. Within the SAA the trigger saturates but the detectors are unaffected. The geomagnetic poles are also indicated.

On the ISS, the trigger rates vary from 200 Hz near the Equator to a maximum of ∼2000 Hz near the Earth's magnetic poles, see Fig. 31. The dead time due to the digitization leads to an additional inefficiency which is accounted in the analysis. Within the South Atlantic Anomaly (SAA), the trigger saturates and the event rate drops but the detectors are unaffected. These data are not used in the analysis. Overall, the average data acquisition efficiency is 86% resulting in an average event acquisition rate of ∼600 Hz.

Fig. 32 shows the data flow between the ISS and the AMS Payload Operation and Control Center (POCC) at CERN and then to the AMS Asia POCC in Taiwan. Data from AMS are transmitted at an average rate of 10 Mbit/s from the ISS to a geosynchronous Tracking and Data Relay System (TDRS) satellite and down to the White Sands Ground Terminal in New Mexico. To cover the ISS orbit, there are several TDRS satellites in use sequentially. From White Sands the data are directed over NASA networks to dedicated AMS ground support computers located at the Marshall Space Flight Center (MSFC), Huntsville, Alabama, where the raw data are written on disk. Then the data are copied to the AMS POCC at CERN over the Internet. Commands from the POCC to AMS follow the same path in reverse. A dedicated AMS Laptop is located in the astronaut quarters onboard the ISS which archives all AMS data for up to two months. Whenever there is a dropout anywhere along the chain between the ISS and the POCC, the missing data are recovered later from this AMS Laptop.

The AMS Flight Simulator Laboratory at CERN includes a duplicate of the AMS flight electronics, the ISS avionics, and the AMS Laptop. It is used to qualify AMS software and procedures before they are sent to AMS on the ISS.

2. Origins of cosmic positrons

Studies of light cosmic ray antimatter species, such as positrons, are crucial for the understanding of new phenomena in the cosmos, since the yield of these particles from cosmic ray collisions with the interstellar medium is small.

Fig. 32. World map showing the location of the ISS and the flow of AMS data on May 20, 2020 (day of year 141) at 12:21 GMT including the radio links (orange) from the ISS to the T174 W TDRS satellite and from T174 W to the White Sands ground terminal, the NASA internal network (yellow) connecting White Sands to the Marshall Space Flight Center (MSFC), and the Internet connection (red) from MSFC to the AMS POCC at CERN. The AMS data are re-transmitted over the Internet to the AMS Asia POCC in Taiwan. The ground track of the ISS for three orbits is indicated (white sinusoidal curves). The locations of the other two TDRS satellites active on this ISS orbit are shown (T041 W, T275 W). The day–night boundary is also indicated (dark yellow boundary of dark and light regions). The "staple" shapes along the orbital ground track indicate the location of the ISS where the Sun will rise and set. Latitude and longitude are indicated by the grid pattern.

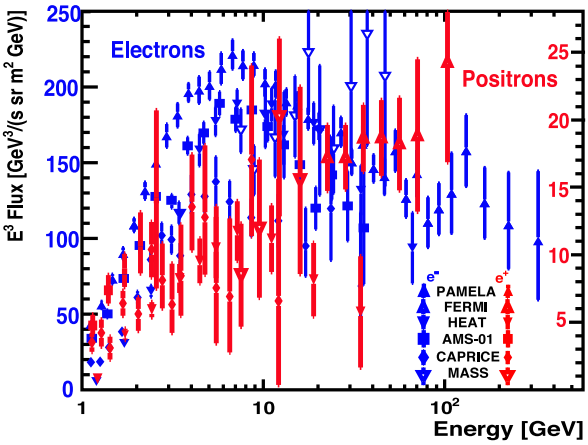

Fig. 33. The electron and positron spectra before AMS, $E^3\Phi_{e^-}$ (electrons, blue data points and left axis) and $E^3\Phi_{e^+}$ (positrons, red data points and right axis) are shown as a function of energy. As seen, although these were the best measurements, the data have large errors and are not always consistent with each other.

Over the last fifty years, there have been many measurements of the fluxes of cosmic ray electrons and positrons. In Fig. 33, we summarize some of the most recent measurements before AMS. As seen, the data have large errors and are not always consistent with each other. Note that traditionally, for display purposes, the electron and positron fluxes, Φ_{e^-} and Φ_{e^+}, are presented scaled by E^3 and called electron and positron spectra, $E^3\Phi_{e^-}$ and $E^3\Phi_{e^+}$.

We present our latest data on the precise measurements of positrons up to 1 TeV and analyze the observation of changing behavior of the cosmic ray positron flux (Table 1). These experimental results are crucial for understanding the origin of high energy positrons in the cosmos. The measurement is based on 1.9 million positrons [45].

Our published data [44,45,55,56] have generated widespread interest and discussions of the observed excess of high energy positrons. The explanations of these results included three classes of models: production of high energy positrons in the interactions of cosmic ray nuclei with interstellar medium [57], acceleration of positrons to high energies in astrophysical objects [58–60] such as pulsars, and annihilation of dark matter particles [61,62]. Most of these explanations differ in their predictions for the behavior of cosmic ray positrons at high energies.

As discussed in Section 1, the combination of information from the TRD, tracker, and ECAL enables the efficient separation of the positron events from background sources [45]. First, an energy dependent cut on Λ_{ECAL} is applied to

Table 1
The positron flux Φ_{e^+} as a function of the energy E at the top of AMS in units of $[\mathrm{m}^2\,\mathrm{sr}\,\mathrm{s}\,\mathrm{GeV}]^{-1}$. Characteristic energy $\tilde{E}$ (i.e. spectrally weighted mean energy in the bin) is given with its systematic error from the energy scale uncertainty. The number of positron events before unfolding, N_{e^+}, is given together with its statistical error from the fit. σ_{stat} is the statistical error. $\sigma_{\mathrm{syst}}^{\mathrm{tmpl}}$ is the systematic error from the definition of templates. $\sigma_{\mathrm{syst}}^{\mathrm{c.c.}}$ is the systematic error from the charge confusion. $\sigma_{\mathrm{syst}}^{\mathrm{eff}}$ is the systematic error from the efficiency corrections. $\sigma_{\mathrm{syst}}^{\mathrm{unf}}$ is the systematic error from the unfolding. σ_{syst} is the total systematic error, which is equal to the sum of $\sigma_{\mathrm{syst}}^{\mathrm{tmpl}}$, $\sigma_{\mathrm{syst}}^{\mathrm{c.c.}}$, $\sigma_{\mathrm{syst}}^{\mathrm{eff}}$, and $\sigma_{\mathrm{syst}}^{\mathrm{unf}}$ in quadrature. $\sigma_{\mathrm{syst}}^{\mathrm{eff}}$ includes the correlated systematic error on the flux normalization of 1%. Note that this 1% error is subtracted in quadrature from the total systematic error for all the fits to the positron data in this Report.

E [GeV]	$\tilde{E}$ [GeV]	N_{e^+}	Φ_{e^+}	σ_{stat}	$\sigma_{\mathrm{syst}}^{\mathrm{tmpl}}$	$\sigma_{\mathrm{syst}}^{\mathrm{c.c.}}$	$\sigma_{\mathrm{syst}}^{\mathrm{eff}}$	$\sigma_{\mathrm{syst}}^{\mathrm{unf}}$	σ_{syst}
0.50–0.65	0.57 ± 0.02	1149 ± 47	(2.669	0.109	0.075	0.000	0.107	0.053	0.141) $\times 10^{0}$
0.65–0.82	0.73 ± 0.02	12911 ± 144	(2.576	0.029	0.046	0.000	0.083	0.044	0.105) $\times 10^{0}$
0.82–1.01	0.91 ± 0.03	26583 ± 192	(2.272	0.016	0.022	0.000	0.060	0.031	0.071) $\times 10^{0}$
1.01–1.22	1.11 ± 0.03	40179 ± 225	(1.929	0.011	0.013	0.000	0.043	0.019	0.049) $\times 10^{0}$
1.22–1.46	1.33 ± 0.03	54417 ± 254	(1.528	0.007	0.009	0.000	0.027	0.014	0.032) $\times 10^{0}$
1.46–1.72	1.58 ± 0.04	74795 ± 293	(1.196	0.005	0.006	0.000	0.018	0.009	0.021) $\times 10^{0}$
1.72–2.00	1.85 ± 0.04	94015 ± 326	(9.239	0.032	0.038	0.002	0.120	0.059	0.139) $\times 10^{-1}$
2.00–2.31	2.15 ± 0.05	109166 ± 349	(7.003	0.022	0.028	0.002	0.084	0.035	0.095) $\times 10^{-1}$
2.31–2.65	2.47 ± 0.05	117702 ± 363	(5.341	0.016	0.022	0.001	0.059	0.025	0.068) $\times 10^{-1}$
2.65–3.00	2.82 ± 0.06	113376 ± 357	(3.983	0.013	0.016	0.001	0.043	0.017	0.049) $\times 10^{-1}$
3.00–3.36	3.17 ± 0.06	106314 ± 345	(3.024	0.010	0.012	0.001	0.032	0.012	0.036) $\times 10^{-1}$
3.36–3.73	3.54 ± 0.07	98881 ± 334	(2.338	0.008	0.010	0.001	0.024	0.009	0.028) $\times 10^{-1}$
3.73–4.12	3.92 ± 0.08	92976 ± 323	(1.809	0.006	0.007	0.001	0.019	0.007	0.021) $\times 10^{-1}$
4.12–4.54	4.32 ± 0.08	87849 ± 315	(1.389	0.005	0.006	0.000	0.015	0.005	0.016) $\times 10^{-1}$
4.54–5.00	4.76 ± 0.09	84539 ± 308	(1.069	0.004	0.004	0.000	0.011	0.004	0.013) $\times 10^{-1}$
5.00–5.49	5.24 ± 0.10	79695 ± 300	(8.208	0.031	0.034	0.003	0.088	0.028	0.099) $\times 10^{-2}$
5.49–6.00	5.74 ± 0.11	72564 ± 287	(6.278	0.025	0.026	0.002	0.068	0.021	0.076) $\times 10^{-2}$
6.00–6.54	6.26 ± 0.12	67597 ± 276	(4.923	0.020	0.021	0.002	0.054	0.015	0.060) $\times 10^{-2}$
6.54–7.10	6.81 ± 0.13	60745 ± 261	(3.890	0.017	0.017	0.001	0.043	0.012	0.048) $\times 10^{-2}$
7.10–7.69	7.39 ± 0.14	53538 ± 246	(3.018	0.014	0.013	0.001	0.034	0.009	0.037) $\times 10^{-2}$
7.69–8.30	7.99 ± 0.15	47132 ± 230	(2.406	0.012	0.010	0.001	0.027	0.006	0.030) $\times 10^{-2}$
8.30–8.95	8.62 ± 0.16	42041 ± 218	(1.900	0.010	0.008	0.001	0.022	0.005	0.024) $\times 10^{-2}$
8.95–9.62	9.28 ± 0.18	36843 ± 203	(1.530	0.008	0.007	0.001	0.018	0.004	0.019) $\times 10^{-2}$
9.62–10.32	9.96 ± 0.19	32889 ± 193	(1.242	0.007	0.005	0.000	0.015	0.003	0.016) $\times 10^{-2}$
10.32–11.04	10.67 ± 0.20	28518 ± 179	(1.007	0.006	0.004	0.000	0.012	0.002	0.013) $\times 10^{-2}$
11.04–11.80	11.41 ± 0.22	25852 ± 170	(8.302	0.055	0.037	0.003	0.100	0.017	0.108) $\times 10^{-3}$
11.80–12.59	12.19 ± 0.23	23378 ± 162	(6.918	0.048	0.031	0.002	0.084	0.014	0.090) $\times 10^{-3}$
12.59–13.41	12.99 ± 0.25	20709 ± 152	(5.668	0.042	0.025	0.002	0.069	0.011	0.075) $\times 10^{-3}$
13.41–14.25	13.82 ± 0.26	18103 ± 142	(4.643	0.037	0.021	0.002	0.057	0.009	0.061) $\times 10^{-3}$
14.25–15.14	14.69 ± 0.28	16624 ± 137	(3.864	0.032	0.017	0.001	0.048	0.008	0.051) $\times 10^{-3}$
15.14–16.05	15.59 ± 0.29	15015 ± 130	(3.262	0.028	0.015	0.001	0.041	0.007	0.044) $\times 10^{-3}$
16.05–17.00	16.52 ± 0.31	13638 ± 124	(2.718	0.025	0.012	0.001	0.034	0.005	0.037) $\times 10^{-3}$
17.00–17.98	17.48 ± 0.33	12414 ± 118	(2.293	0.022	0.011	0.001	0.029	0.005	0.031) $\times 10^{-3}$
17.98–18.99	18.48 ± 0.35	11371 ± 113	(1.933	0.019	0.009	0.001	0.025	0.004	0.026) $\times 10^{-3}$
18.99–20.04	19.51 ± 0.37	10708 ± 110	(1.666	0.017	0.008	0.001	0.021	0.003	0.023) $\times 10^{-3}$
20.04–21.13	20.58 ± 0.39	9985 ± 106	(1.454	0.015	0.007	0.000	0.019	0.003	0.020) $\times 10^{-3}$
21.13–22.25	21.68 ± 0.41	8861 ± 100	(1.214	0.014	0.006	0.000	0.016	0.002	0.017) $\times 10^{-3}$
22.25–23.42	22.83 ± 0.43	7974 ± 95	(1.018	0.012	0.005	0.000	0.013	0.002	0.014) $\times 10^{-3}$
23.42–24.62	24.01 ± 0.45	7434 ± 91	(9.031	0.111	0.043	0.003	0.118	0.018	0.127) $\times 10^{-4}$
24.62–25.90	25.25 ± 0.48	6859 ± 88	(7.647	0.098	0.037	0.002	0.100	0.015	0.108) $\times 10^{-4}$
25.90–27.25	26.56 ± 0.50	6516 ± 86	(6.757	0.089	0.033	0.002	0.089	0.014	0.096) $\times 10^{-4}$
27.25–28.68	27.95 ± 0.53	5881 ± 82	(5.747	0.080	0.028	0.002	0.076	0.011	0.082) $\times 10^{-4}$
28.68–30.21	29.43 ± 0.56	5541 ± 79	(5.063	0.072	0.025	0.001	0.067	0.010	0.072) $\times 10^{-4}$
30.21–31.82	31.00 ± 0.59	4902 ± 75	(4.273	0.065	0.022	0.001	0.057	0.009	0.061) $\times 10^{-4}$
31.82–33.53	32.66 ± 0.62	4487 ± 72	(3.681	0.059	0.019	0.001	0.049	0.007	0.053) $\times 10^{-4}$
33.53–35.36	34.43 ± 0.65	4059 ± 68	(3.126	0.052	0.016	0.001	0.042	0.006	0.045) $\times 10^{-4}$
35.36–37.31	36.32 ± 0.69	3810 ± 66	(2.754	0.048	0.015	0.001	0.037	0.006	0.040) $\times 10^{-4}$
37.31–39.39	38.33 ± 0.72	3423 ± 63	(2.328	0.043	0.013	0.001	0.031	0.005	0.034) $\times 10^{-4}$
39.39–41.61	40.48 ± 0.77	3142 ± 60	(2.004	0.038	0.011	0.001	0.027	0.004	0.030) $\times 10^{-4}$
41.61–44.00	42.78 ± 0.81	2897 ± 58	(1.723	0.034	0.010	0.000	0.023	0.003	0.026) $\times 10^{-4}$
44.00–46.57	45.26 ± 0.86	2607 ± 55	(1.446	0.030	0.009	0.000	0.020	0.003	0.022) $\times 10^{-4}$
46.57–49.33	47.92 ± 0.91	2558 ± 54	(1.323	0.028	0.009	0.000	0.018	0.003	0.020) $\times 10^{-4}$
49.33–52.33	50.80 ± 0.96	2155 ± 50	(1.029	0.024	0.007	0.000	0.014	0.002	0.016) $\times 10^{-4}$
52.33–55.58	53.92 ± 1.02	2005 ± 48	(8.860	0.214	0.063	0.002	0.121	0.018	0.137) $\times 10^{-5}$
55.58–59.13	57.32 ± 1.08	1864 ± 47	(7.558	0.189	0.056	0.002	0.103	0.015	0.118) $\times 10^{-5}$
59.13–63.02	61.03 ± 1.16	1645 ± 44	(6.115	0.164	0.047	0.001	0.084	0.012	0.097) $\times 10^{-5}$

(*continued on next page*)

Table 1 (*continued*).

E [GeV]	$\tilde{E}$ [GeV]	N_{e^+}	Φ_{e^+}	$\sigma_{\rm stat}$	$\sigma_{\rm syst}^{\rm tmpl}$	$\sigma_{\rm syst}^{\rm c.c.}$	$\sigma_{\rm syst}^{\rm eff}$	$\sigma_{\rm syst}^{\rm unf}$	$\sigma_{\rm syst}$
63.02–67.30	65.11 ± 1.23	1626 ± 44	(5.502	0.149	0.044	0.001	0.075	0.011	0.088) $\times 10^{-5}$
67.30–72.05	69.62 ± 1.32	1427 ± 41	(4.367	0.126	0.036	0.001	0.060	0.009	0.071) $\times 10^{-5}$
72.05–77.37	74.65 ± 1.41	1399 ± 41	(3.826	0.111	0.033	0.001	0.052	0.008	0.062) $\times 10^{-5}$
77.37–83.36	80.29 ± 1.52	1234 ± 38	(3.013	0.094	0.027	0.001	0.041	0.006	0.050) $\times 10^{-5}$
83.36–90.19	86.69 ± 1.64	1168 ± 38	(2.511	0.081	0.024	0.002	0.034	0.005	0.042) $\times 10^{-5}$
90.19–98.08	94.02 ± 1.78	1090 ± 36	(2.037	0.068	0.020	0.001	0.028	0.004	0.035) $\times 10^{-5}$
98.1–107.3	102.6 ± 1.9	913 ± 37	(1.461	0.059	0.015	0.002	0.020	0.003	0.025) $\times 10^{-5}$
107.3–118.4	112.7 ± 2.1	871 ± 36	(1.173	0.048	0.012	0.001	0.016	0.002	0.020) $\times 10^{-5}$
118.4–132.1	125.0 ± 2.4	789 ± 34	(8.677	0.376	0.090	0.014	0.120	0.017	0.151) $\times 10^{-6}$
132.1–148.8	140.1 ± 2.7	741 ± 32	(6.998	0.303	0.075	0.012	0.099	0.014	0.125) $\times 10^{-6}$
148.8–169.9	158.9 ± 3.0	613 ± 30	(4.595	0.221	0.051	0.012	0.065	0.009	0.084) $\times 10^{-6}$
169.9–197.7	183.1 ± 3.5	556 ± 28	(3.201	0.163	0.037	0.011	0.046	0.006	0.060) $\times 10^{-6}$
197.7–237.2	216.2 ± 4.2	405 ± 24	(1.871	0.111	0.022	0.012	0.029	0.004	0.039) $\times 10^{-6}$
237.2–290.0	261.8 ± 5.1	330 ± 22	(1.158	0.077	0.014	0.012	0.019	0.002	0.026) $\times 10^{-6}$
290.0–370.0	326.8 ± 6.4	214 ± 18	(5.773	0.496	0.071	0.089	0.097	0.012	0.150) $\times 10^{-7}$
370.0–500.0	428.5 ± 8.6	146 ± 17	(2.491	0.286	0.031	0.072	0.045	0.005	0.091) $\times 10^{-7}$
500.0–700.0	588.8 ± 12.2	71 ± 14	(8.312	1.675	0.548	0.512	0.175	0.017	0.770) $\times 10^{-8}$
700.0–1000.0	832.3 ± 18.3	23 ± 13	(1.927	1.087	0.258	0.358	0.049	0.004	0.444) $\times 10^{-8}$

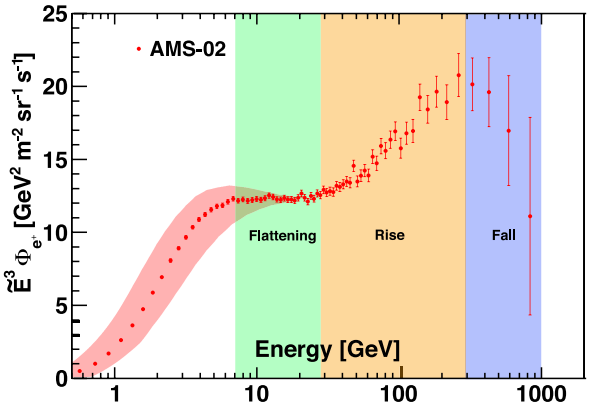

Fig. 34. The AMS positron spectrum, $\tilde{E}^3\Phi_{e^+}$ (red data points) is shown as a function of energy. $\tilde{E}$ is the spectrally weighted mean energy for a flux proportional to E^{-3}. The time variation of the flux at low energies due to solar modulation is indicated by the red band (see Section 16). To guide the eye, the vertical color bands indicate the energy ranges corresponding to changing behavior of the spectrum: flattening, rising, and falling.

remove the bulk of the proton background (see Section 1.7). Then the charge confusion estimator $\Lambda^e_{\rm CC}$ is used to distinguish positrons from charge confusion electrons (see Section 1.2).

The isotropic positron flux for the energy bin E_i of width ΔE_i is given by:

$$\Phi_{e^+,i} = \frac{N_i}{A_i(1+\delta_i)T_i\Delta E_i}, \tag{3}$$

where the energy is defined at the top of AMS. N_i is the number of e^+ in bin i corrected for the small bin-to-bin migration using the unfolding procedure described in Ref. [63]. A_i is the corresponding effective acceptance that includes geometric acceptance, and the trigger and selection efficiencies. It is calculated from Monte Carlo simulation. δ_i is a small correction estimated by comparing the efficiencies in data and MC simulation of every selection cut using information from the detectors unrelated to that cut. T_i is the data collection time. The systematic errors on $\Phi_{e^+,i}$ are extensively discussed in Ref. [45,55].

The detector performance has been studied in-depth for this analysis, as reported in Section 1. These studies include the tracker resolution at rigidities close to the maximum detectable rigidity of 2 TV, charge confusion studies, reconstruction of electromagnetic showers in the TeV energy range, and proton rejection with the electromagnetic calorimeter.

Fig. 34 shows the measured positron spectrum, $\tilde{E}^3\Phi_{e^+}$. The data are placed at $\tilde{E}$, which is the spectrally weighted mean energy for a flux proportional to E^{-3} in each bin [64]. In this and the subsequent figures, the error bars correspond to the quadratic sum of statistical and systematic errors. As seen, the positron spectrum exhibits complex energy dependence. At low energies, the spectrum varies due to solar modulation (see Section 16). At higher energies, the vertical color bands indicate the energy ranges corresponding to changing behavior of the spectrum: flattening, rising, and falling.

As discussed in the following, the positron flux distinctive properties are:

- a significant excess starting from 25.2 ± 1.8 GeV compared to the lower-energy, power-law trend;

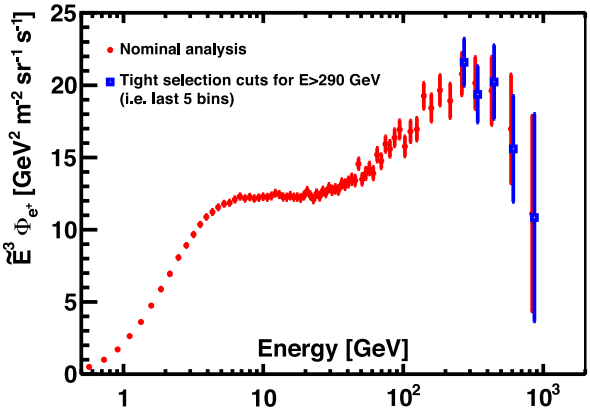

Fig. 35. Comparison of the nominal analysis (red data points) with the results of the tight cut on the positron selection. In the tight cut analysis (using the tighter cut on the ECAL) the proton rejection is increased by a factor ∼3 compared to the nominal one, resulting in a signal efficiency of 65% (blue open squares) instead of the nominal 90% (see Fig. 29). For display purposes, the results of the tight cut analysis are slightly offset horizontally. Note, the tight selection cuts increase the statistical error on the flux in the last bin from 56% to 61%.

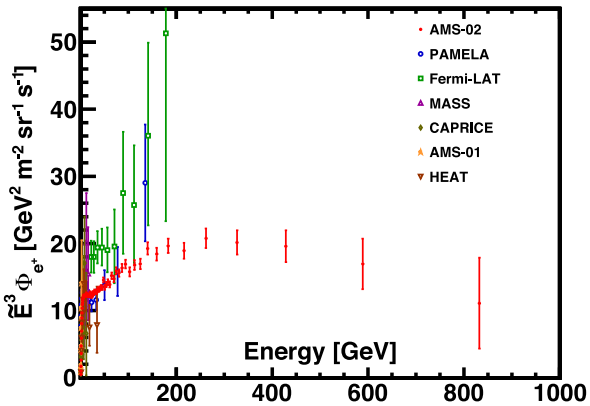

Fig. 36. The AMS positron spectrum ($\tilde{E}^3\Phi_{e^+}$) together with earlier measurements.

- a sharp drop-off above 284^{+91}_{-64} GeV;
- in the entire energy range the positron flux is well described by the sum of a term associated with the positrons produced in the collision of cosmic rays, which dominates at low energies, and a new source term of positrons, which dominates at high energies;
- a finite energy cutoff of the source term of $E_s = 810^{+310}_{-180}$ GeV is established with a significance of more than 4σ.

These experimental data on cosmic ray positrons show that, at high energies, they predominantly originate either from astrophysical sources or from dark matter annihilation as opposed to the secondary production in the interstellar medium.

In addition to the studies presented in Section 1, exhaustive verifications of the results were performed including different analysis methods and by tightening the selection criteria that allow us to achieve a high purity positron sample. An example of the stability of the results is demonstrated with an analysis which aims at a higher signal/background ratio using a tighter cut on the ECAL information. In this analysis the proton rejection is increased by a factor ∼3 (see Fig. 29) compared to the nominal analysis. This tight-cut analysis has a signal efficiency of 65% instead of the nominal 90%. The results of this tight selection analysis do not alter the flux value as presented in Fig. 35 for the last five energy bins.

Fig. 36 shows the AMS result together with earlier experiments: PAMELA, Fermi-LAT, MASS, CAPRICE, AMS-01, and HEAT [65–70] . The new AMS data significantly extend the measurements into an uncharted high energy region.

To examine the changing behavior of the positron spectrum, highlighted in Fig. 34 by the vertical color bands, we use a power law approximation with spectral index γ below a characteristic transition energy E_0 and $\gamma + \Delta\gamma$ above E_0:

$$\Phi_{e^+}(E) = \begin{cases} C(E/55.58\,\text{GeV})^{\gamma}, & E \le E_0; \\ C(E/55.58\,\text{GeV})^{\gamma}(E/E_0)^{\Delta\gamma}, & E > E_0. \end{cases} \tag{4}$$

Fits to data are performed in two energy ranges: $[7.10 - 55.58]$ GeV and $[55.58 - 1000]$ GeV. The first range corresponds to the increase of the spectrum (hardening), while the second range corresponds to the spectrum decrease (softening). The

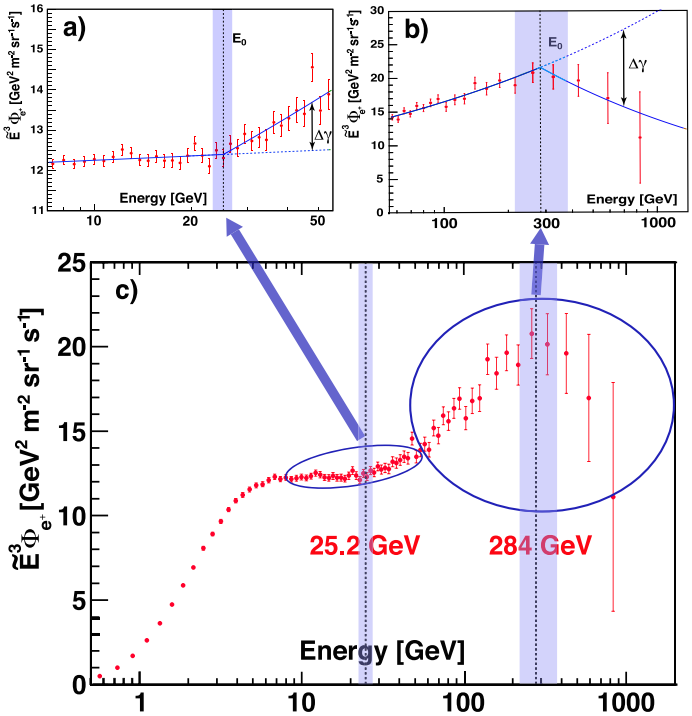

Fig. 37. Fits of Eq. (4) to the positron flux in the energy ranges $[7.10 - 55.58]$ GeV and $[55.58 - 1000]$ GeV. The fitted functions are represented by the blue lines in the upper two graphs (a) and (b). The vertical dashed lines correspond to the values of the energy E_0 where the changes of the spectral index occur and the corresponding bands to their errors. The dashed blue lines are the extrapolations of the power law from below E_0 into the higher energy regions. $\Delta\gamma$ is the magnitude of the spectral index change. The lower graph (c) is for illustration of this changing behavior.

results are presented in Fig. 37. Note that the choice of the constant 55.58 GeV, corresponding to the fit range boundary, defines only the flux normalization C. It does not affect the fitted values of γ and $\Delta\gamma$.

The fit in the range $[7.10 - 55.58]$ GeV yields

$$\begin{aligned} C &= (7.29 \pm 0.08) \times 10^{-5}\,\mathrm{m^{-2}sr^{-1}s^{-1}GeV^{-1}}, \\ \gamma &= -2.988 \pm 0.007, \\ \Delta\gamma &= 0.14 \pm 0.02, \\ E_0 &= 25.2 \pm 1.8\,\mathrm{GeV}, \\ \text{with } \chi^2/\text{d.o.f.} &= 22.8/31. \end{aligned}$$

If $\Delta\gamma$ is fixed to 0 in the fit, the χ^2/d.o.f. increases to 67.2/33. Thus the significance of this increase is established at more than 6σ.

The fit in the energy range $[55.58 - 1000]$ GeV yields

$$\begin{aligned} C &= (8.26 \pm 0.12) \times 10^{-5}\,\mathrm{m^{-2}sr^{-1}s^{-1}GeV^{-1}}, \\ \gamma &= -2.744 \pm 0.025, \\ \Delta\gamma &= -0.61^{+0.27}_{-0.32}, \\ E_0 &= 284^{+91}_{-64}\,\mathrm{GeV}, \\ \text{with } \chi^2/\text{d.o.f.} &= 12.9/16, \end{aligned}$$

for the parameters C and γ, the change of the spectral index $\Delta\gamma$, and the energy at which the spectrum begins to decrease. If $\Delta\gamma$ is fixed to 0 in the fit, the χ^2/d.o.f. increases to 24.9/16. Thus, the significance of this decrease is established at more than 3σ.

The complex behavior of the positron flux (as illustrated in Fig. 37) is consistent with the existence of a new source of high energy positrons, whether of new astrophysical or dark matter origin. It is not consistent with the exclusive secondary production of positrons in collisions of cosmic rays.

There are many models predicting the flux of secondary positrons [71–76], such as GALPROP [71], DRAGON [74], and USINE [75]. They differ in their underlying assumptions and the predictions for the positron flux. Among these models,

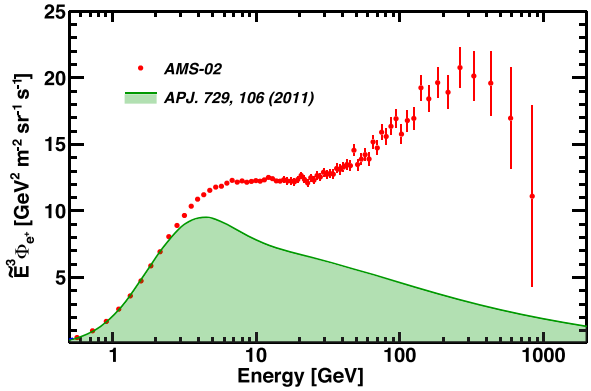

Fig. 38. Comparison of the AMS data (red data points) with a GALPROP model prediction [72] for the secondary positron spectrum (green shaded area).

GALPROP is widely regarded as a standard framework for prediction of fluxes of secondaries based on the data from accelerator experiments and from cosmic-ray studies. The GALPROP prediction for the secondary positron production [72] is compared with the data in Fig. 38. The model prediction below 3 GeV is in good agreement with data, followed by a peak in the spectrum of secondary positrons below 10 GeV and then a steady decrease with increasing energy. As seen in Fig. 38, this is in sharp contrast with the observed data behavior. This shows that the rise of the spectrum at 25.2 GeV, the maximum at 284 GeV, and the subsequent fall of the observed positron spectrum at higher energies contradicts with the GALPROP model predictions for secondary production of cosmic ray positrons.

The accuracy of the AMS data allows for a detailed study of the properties of the new source of positrons. We present the analysis of the positron flux using the simplest model, in which the positron flux is parametrized as the sum of a "diffuse" term, and a source term

$$\Phi_{e^+}(E) = \frac{E^2}{\hat{E}^2}[C_d\,(\hat{E}/E_1)^{\gamma_d} \;+\; C_s\,(\hat{E}/E_2)^{\gamma_s}\exp(-\hat{E}/E_s)]\,. \tag{5}$$

The "diffuse" term describes the low energy part of the flux dominated by the positrons produced in the collisions of ordinary cosmic rays with the interstellar medium. It is characterized by a normalization factor C_d and a spectral index γ_d. The source term has an exponential cutoff, which describes the high energy part of the flux dominated by a source. It is characterized by a cutoff energy E_s, a normalization factor C_s, and a spectral index γ_s. In order to account for solar modulation effects, the force-field approximation [77] is used, with the energy of particles in the interstellar space $\hat{E} = E + \varphi_{e^+}$, where the effective solar potential φ_{e^+} accounts for the solar modulation effects. The constant E_1 is chosen to be 7.0 GeV to minimize the correlation between parameters C_d and γ_d; and the constant E_2 is chosen to be 60.0 GeV to minimize the correlation between the parameters C_s and γ_s. The choice of these constants does not affect the shapes nor the magnitudes of the "diffuse" and the source terms. The fit to the measured flux yields

$$\begin{aligned}
1/E_s &= 1.23 \pm 0.34\,\mathrm{TeV}^{-1},\\
C_s &= (6.80 \pm 0.15) \times 10^{-5}\,\mathrm{m}^{-2}\,\mathrm{sr}^{-1}\,\mathrm{s}^{-1}\,\mathrm{GeV}^{-1},\\
\gamma_s &= -2.58 \pm 0.05,\\
C_d &= (6.51 \pm 0.14) \times 10^{-2}\,\mathrm{m}^{-2}\,\mathrm{sr}^{-1}\,\mathrm{s}^{-1}\,\mathrm{GeV}^{-1},\\
\gamma_d &= -4.07 \pm 0.06,\\
\varphi_{e^+} &= 1.10 \pm 0.03\,\mathrm{GeV},\\
\text{with } \chi^2/\mathrm{d.o.f.} &= 50/68.
\end{aligned}$$

The fitted value of the inverse cutoff energy, $1/E_s$, corresponds to $E_s = 810^{+310}_{-180}$ GeV. The result of the fit is presented in Fig. 39. Note that the fitted value of the effective solar potential φ_{e^+} is higher than the average value ($\sim$ 0.62 GeV) from the analysis of neutron monitor data during this period [78].

As seen in Fig. 39, the "diffuse" term dominates at low energies and then gradually vanishes with increasing energy. The source term dominates the positron spectrum at high energies. It is the contribution of the source term that leads to the observed excess of the positron flux above 25.2 ± 1.8 GeV. The drop-off of the flux above 284^{+91}_{-64} GeV is very well described by the sharp exponential cutoff of the source term.

To study the significance of the cutoff energy E_s, we varied all six fit parameters of Eq. (5), C_d, γ_d, C_s, γ_s, E_s, and φ_{e^+}, to find the regions in the 6D parameter space corresponding to the confidence levels from 1 to 5σ with a step of 0.01σ. As an example, Fig. 40 shows projections of the 6D regions of 1σ (black line, 68.26% C.L.), 2σ (green line, 95.54% C.L.),

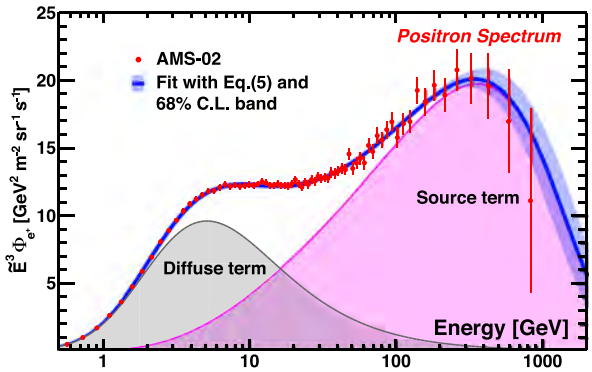

Fig. 39. The fit of Eq. (5) (blue line) to the positron flux in the energy range [0.5 − 1000] GeV together with the 68% C.L. interval (blue band). The exponential cutoff of the source term is determined from the fit to be 810^{+310}_{-180} GeV. The red data points represent the measured positron spectrum. The source term contribution is represented by the magenta area, and the "diffuse" term contribution by the gray area.

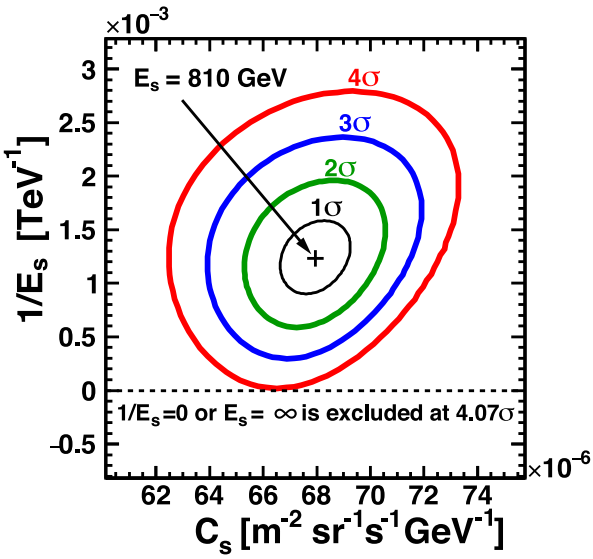

Fig. 40. The projections of the regions of 1σ (black contour), 2σ (green contour), 3σ (blue contour), and 4σ (red contour) significance of the $1/E_s$ measurement onto the plane of parameters $1/E_s - C_s$.

3σ (blue line, 99.74% C.L.), and 4σ (red line, 99.99% C.L.) onto the plane of parameters $1/E_s - C_s$. Detailed analysis shows that a point where the parameter $1/E_s$ reaches 0 corresponds to the confidence level of 4.07σ, i.e., the significance of the source term energy cutoff is established at more than 4σ, or at the 99.99% C.L.

Analysis of the individual components, namely the "diffuse" term and the source term, is presented in Figs. 41 and 42. To perform this study we subtract from the data either the source term (in Fig. 41) or the "diffuse" term (in Fig. 42) using the parameters of these two terms defined from the fit of Eq. (5) to data. As seen in Fig. 41, the positron "diffuse" term data vanish at high energies. At low energies, they are in good qualitative agreement with the GALPROP model predictions for the secondary positron spectrum from the collision of ordinary cosmic rays.

The source term data with a sharp drop-off above 284 GeV dominates at high energies, as seen in Fig. 42.

The experimental data on cosmic ray positrons show that, at high energies, positrons predominantly originate either from dark matter annihilation or from other astrophysical sources. As an example, Fig. 43 shows the comparison of AMS data with a dark matter model based on Ref. [62] with a mass of 1.2 TeV together with the contribution from cosmic ray collisions [72]. This good agreement needs to be verified with more statistics at high energies.

The study of the rate at which the positron spectrum falls beyond the turning point continues. Fig. 44 shows the current and projected results for the positron spectrum from AMS through 2028. By then we will have collected 5 million positron events. With the increase in statistics, we will extend the measurement up to 2 TeV, which will enable us to determine the origin of the positron excess, i.e. to distinguish the dark matter origin of the excess from other, new astrophysical explanations such as high energy positrons originating from pulsars (see Section 6). It should be noted that we are still awaiting other astrophysics models that (a) can explain our positron data, (b) can explain our antiproton data (Section 5),

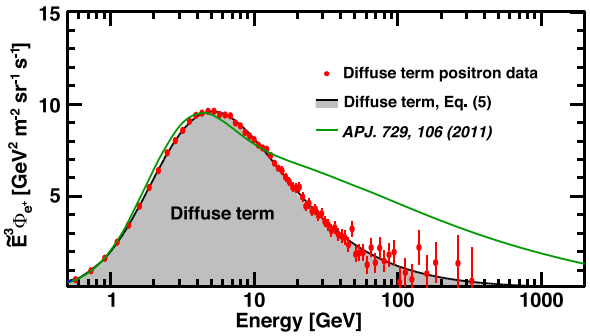

Fig. 41. Analysis of the positron "diffuse" term. The low energy positron "diffuse" term data (i.e. the positron data minus the source term contribution, red data points) together with the "diffuse" term of Eq. (5) (black curve and gray shading). As seen, the "diffuse" term data at low energies are consistent with the GALPROP predictions for the secondary positron spectrum (green curve).

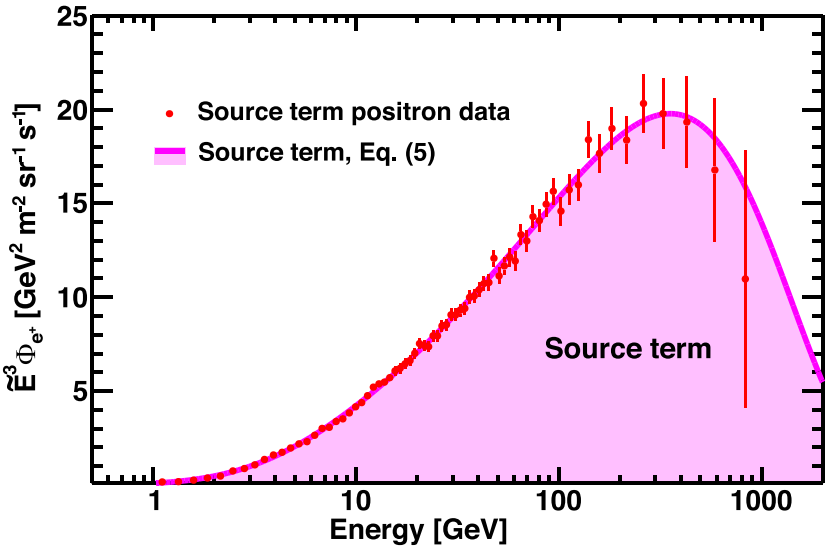

Fig. 42. Analysis of the positron source term. The high energy source term data (i.e. the positron data minus the "diffuse" term contribution, red data points) together with the source term of Eq. (5) (magenta curve and shading).

and (c) are in agreement with our accurate measurements of cosmic rays such as the Be/C, B/C, Be/O, and B/O ratios (Section 10).

Astrophysical point sources like pulsars will imprint a higher anisotropy on the arrival directions of energetic positrons [59,60] than a smooth dark matter halo. If the excess of positrons has a dark matter origin, it should be isotropic. The dipole anisotropy is given by $\delta = 3(C_1/4\pi)^{1/2}$, where C_1 is the dipole moment (see Ref. [55], Eqs. (3) and (4) for the details of the analysis). A similar analysis [79] was performed using the positron data from this Report in the energy range above 16 GeV (see Fig. 45). The positron flux is found to be consistent with isotropy and our upper limit on the amplitude of the positron dipole anisotropy for any axis in galactic coordinates is $\delta < 0.019$ at the 95% C.L.

3. Origins of cosmic electrons

We present the precision measurement of the electron flux based on 28.1 million electron events collected by AMS (Table 2). Analysis of the data is similar to the analysis of positrons in Section 2 and is described in detail in Ref. [80]. These precision results on cosmic-ray electrons up to 1.4 TeV reveal new features. Fig. 46 shows the latest AMS results on the precision measurements of the electron spectrum together with the GALPROP prediction for the secondary electrons from collision of cosmic rays [71,72]. As seen, the contribution of the collision of cosmic rays to the electron spectrum is negligible in the entire energy range.

Our data on cosmic-ray electrons and positrons are crucial for providing insights into their origins.

We found that, over the entire energy range, the electron and positron spectra have distinctly different magnitudes and energy dependences. The electron flux exhibits a significant excess starting from $42.1^{+5.4}_{-5.2}$ GeV compared to the lower

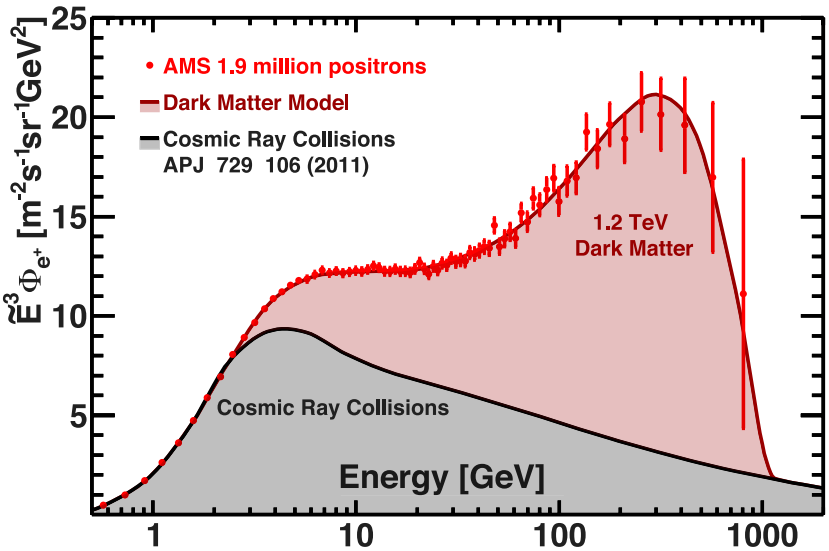

Fig. 43. Comparison of the AMS data (red data points) with predictions of a dark matter model based on Ref. [62] with $M_\chi = 1.2$ TeV (brown curve and shading). Also shown is a model prediction of cosmic ray collisions [72] (black curve and shading).

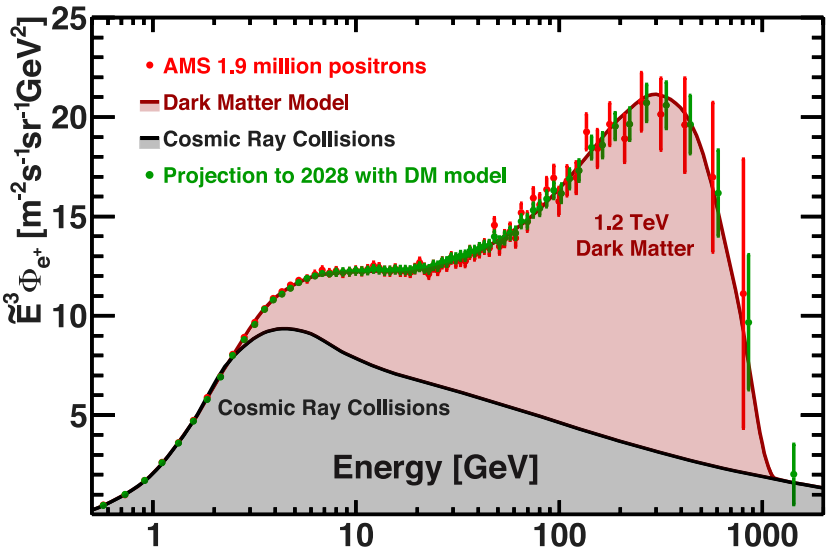

Fig. 44. Comparison of the current AMS positron spectrum (red data points) with the projected spectrum measurement to 2028 (green data points). By then we will have collected 5 million positron events. The results are compared with the same predictions as in Fig. 43 with $M_\chi = 1.2$ TeV. The projection is based on the models [62,72].

energy trends, but the nature of this excess is different from the positron flux excess above 25.2 ± 1.8 GeV. Contrary to the positron flux, which has an exponential energy cutoff of 810^{+310}_{-180} GeV, at the 5σ level the electron flux does not have an energy cutoff below 1.9 TeV. In the entire energy range, the electron flux is well described by the sum of two power law components. The different behavior of the cosmic-ray electrons and positrons measured by AMS is clear evidence that most high energy electrons originate from different sources than high energy positrons.

Fig. 47 shows the latest AMS results on the precision measurements of the electron spectrum together with recent measurements from other experiments [66–68,70,81,82].

Similar to the analysis of the positron flux (Eq. (4)), we examine the changing behavior of the electron flux using the power law approximation

$$\Phi_{e^-}(E) = \begin{cases} C\,(E/20.04\,\mathrm{GeV})^{\gamma}, & E \le E_0; \\ C\,(E/20.04\,\mathrm{GeV})^{\gamma}\,(E/E_0)^{\Delta\gamma}, & E > E_0. \end{cases} \tag{6}$$

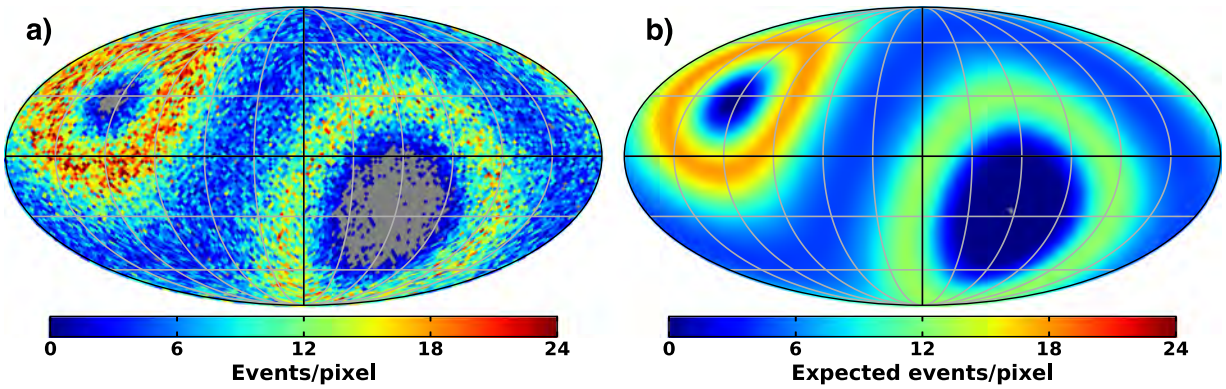

Fig. 45. (a) Map of the incoming positron directions in galactic coordinates observed by AMS on the ISS. (b) Map of the expected positron directions for an isotropic distribution of positrons in galactic coordinates. The dipole anisotropy δ is defined in terms of the dipole moment C_1. Our positron data show that $\delta < 0.019$.

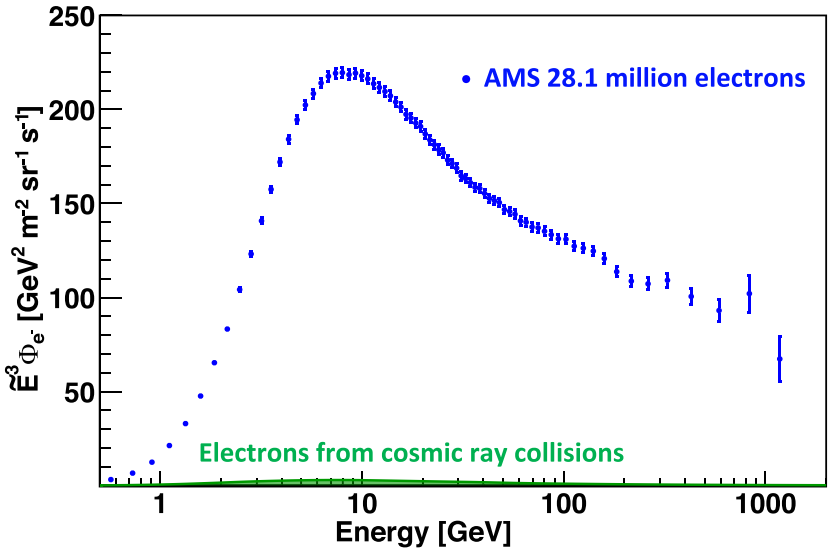

Fig. 46. The AMS electron spectrum ($\tilde{E}^3\Phi_{e^-}$, blue data points) together with the GALPROP prediction for the secondary electrons from collision of cosmic rays [71,72] (green shaded area). As seen, the contribution of the collision of cosmic rays to the electron spectrum is negligible.

A fit to data is performed in the energy range $[20.04 - 1400]$ GeV. The fit energy range is chosen such that the effect of solar modulation is negligible (see Section 16). The results are presented in Fig. 48. The fit yields

$$\begin{aligned} C &= (2.335^{+0.014}_{-0.019}) \times 10^{-2}\,\mathrm{m^{-2}sr^{-1}s^{-1}GeV^{-1}}, \\ \gamma &= -3.280^{+0.014}_{-0.016}, \\ \Delta\gamma &= 0.094 \pm 0.014, \\ E_0 &= 42.1^{+5.4}_{-5.2}\,\mathrm{GeV}, \\ \text{with } \chi^2/\text{d.o.f.} &= 17.9/36, \end{aligned}$$

for the parameters C and γ, the change of the spectral index $\Delta\gamma$, and the energy E_0 where the spectrum increases. The significance of this change is established at 7σ.

To examine the energy dependence of the electron flux, we divide the entire energy range into narrow intervals, assuming that the flux behavior follows a power law function, $\Phi = CE^{\gamma}$, in each of these intervals. The flux spectral index

$$\gamma = d[\log(\Phi)]/d[\log(E)] \tag{7}$$

is calculated over non-overlapping intervals which are chosen to have sufficient sensitivity to the spectral index. The energy interval boundaries are 3.36, 5.00, 7.10, 10.32, 17.98, 27.25, 55.58, 90.19, 148.81, 370, and 1400 GeV. The results

Table 2
The electron flux Φ_{e^-} as a function of the energy E at the top of AMS in units of $[\mathrm{m}^2\,\mathrm{sr\,s\,GeV}]^{-1}$. Characteristic energy $\tilde{E}$ (i.e. spectrally weighted mean energy in the bin) is given with its systematic error from the energy scale uncertainty. The number of electron events before unfolding, N_{e^-}, is given together with its statistical error from the fit. $\sigma^{e^-}_{\mathrm{stat}}$ is the statistical and $\sigma^{e^-}_{\mathrm{syst}}$ is the total systematic error of the electron flux. Similar to positrons (see Table 1), the correlated systematic error of 1% is subtracted in quadrature from the total systematic error for all the fits to the electron data in this Report.

E [GeV]	$\tilde{E}$ [GeV]	N_{e^-}	Φ_{e^-}	$\sigma^{e^-}_{\mathrm{stat}}$	$\sigma^{e^-}_{\mathrm{syst}}$
0.50–0.65	0.57 ± 0.02	7629 ± 91	(1.731	0.021	0.078) $\times 10^{1}$
0.65–0.82	0.73 ± 0.02	86810 ± 301	(1.710	0.006	0.063) $\times 10^{1}$
0.82–1.01	0.91 ± 0.03	197265 ± 451	(1.658	0.004	0.049) $\times 10^{1}$
1.01–1.22	1.11 ± 0.03	328584 ± 579	(1.562	0.003	0.038) $\times 10^{1}$
1.22–1.46	1.33 ± 0.03	494218 ± 709	(1.391	0.002	0.028) $\times 10^{1}$
1.46–1.72	1.58 ± 0.04	748885 ± 872	(1.200	0.001	0.020) $\times 10^{1}$
1.72–2.00	1.85 ± 0.04	1036495 ± 1027	(1.027	0.001	0.015) $\times 10^{1}$
2.00–2.31	2.15 ± 0.05	1302149 ± 1153	(8.403	0.007	0.110) $\times 10^{0}$
2.31–2.65	2.47 ± 0.05	1512278 ± 1243	(6.897	0.006	0.083) $\times 10^{0}$
2.65–3.00	2.82 ± 0.06	1558061 ± 1264	(5.504	0.004	0.064) $\times 10^{0}$
3.00–3.36	3.17 ± 0.06	1540803 ± 1256	(4.405	0.004	0.050) $\times 10^{0}$
3.36–3.73	3.54 ± 0.07	1497077 ± 1236	(3.555	0.003	0.040) $\times 10^{0}$
3.73–4.12	3.92 ± 0.08	1463912 ± 1222	(2.859	0.002	0.032) $\times 10^{0}$
4.12–4.54	4.32 ± 0.08	1437643 ± 1208	(2.279	0.002	0.025) $\times 10^{0}$
4.54–5.00	4.76 ± 0.09	1419809 ± 1200	(1.800	0.002	0.020) $\times 10^{0}$
5.00–5.49	5.24 ± 0.10	1364759 ± 1176	(1.409	0.001	0.016) $\times 10^{0}$
5.49–6.00	5.74 ± 0.11	1273522 ± 1137	(1.104	0.001	0.013) $\times 10^{0}$
6.00–6.54	6.26 ± 0.12	1195202 ± 1103	(8.715	0.008	0.100) $\times 10^{-1}$
6.54–7.10	6.81 ± 0.13	1074027 ± 1043	(6.885	0.007	0.079) $\times 10^{-1}$
7.10–7.69	7.39 ± 0.14	964312 ± 989	(5.439	0.006	0.063) $\times 10^{-1}$
7.69–8.30	7.99 ± 0.15	843948 ± 924	(4.309	0.005	0.051) $\times 10^{-1}$
8.30–8.95	8.62 ± 0.16	755410 ± 874	(3.415	0.004	0.040) $\times 10^{-1}$
8.95–9.62	9.28 ± 0.18	661333 ± 817	(2.747	0.003	0.033) $\times 10^{-1}$
9.62–10.32	9.96 ± 0.19	583806 ± 768	(2.204	0.003	0.026) $\times 10^{-1}$
10.32–11.04	10.67 ± 0.20	504176 ± 712	(1.779	0.003	0.022) $\times 10^{-1}$
11.04–11.80	11.41 ± 0.22	448010 ± 672	(1.438	0.002	0.018) $\times 10^{-1}$
11.80–12.59	12.19 ± 0.23	395528 ± 630	(1.170	0.002	0.014) $\times 10^{-1}$
12.59–13.41	12.99 ± 0.25	349454 ± 593	(9.557	0.016	0.118) $\times 10^{-2}$
13.41–14.25	13.82 ± 0.26	306269 ± 555	(7.849	0.014	0.098) $\times 10^{-2}$
14.25–15.14	14.69 ± 0.28	277278 ± 528	(6.439	0.012	0.081) $\times 10^{-2}$
15.14–16.05	15.59 ± 0.29	244941 ± 496	(5.316	0.011	0.067) $\times 10^{-2}$
16.05–17.00	16.52 ± 0.31	220144 ± 470	(4.382	0.009	0.056) $\times 10^{-2}$
17.00–17.98	17.48 ± 0.33	198307 ± 446	(3.659	0.008	0.047) $\times 10^{-2}$
17.98–18.99	18.48 ± 0.35	180080 ± 425	(3.057	0.007	0.039) $\times 10^{-2}$
18.99–20.04	19.51 ± 0.37	165546 ± 408	(2.573	0.006	0.033) $\times 10^{-2}$
20.04–21.13	20.58 ± 0.39	147538 ± 385	(2.146	0.006	0.028) $\times 10^{-2}$
21.13–22.25	21.68 ± 0.41	131846 ± 364	(1.804	0.005	0.024) $\times 10^{-2}$
22.25–23.42	22.83 ± 0.43	119578 ± 346	(1.524	0.004	0.020) $\times 10^{-2}$
23.42–24.62	24.01 ± 0.45	106414 ± 327	(1.291	0.004	0.017) $\times 10^{-2}$
24.62–25.90	25.25 ± 0.48	98745 ± 315	(1.099	0.004	0.015) $\times 10^{-2}$
25.90–27.25	26.56 ± 0.50	89203 ± 299	(9.236	0.031	0.123) $\times 10^{-3}$
27.25–28.68	27.95 ± 0.53	80344 ± 284	(7.841	0.028	0.105) $\times 10^{-3}$
28.68–30.21	29.43 ± 0.56	72576 ± 270	(6.622	0.025	0.089) $\times 10^{-3}$
30.21–31.82	31.00 ± 0.59	63528 ± 253	(5.530	0.022	0.074) $\times 10^{-3}$
31.82–33.53	32.66 ± 0.62	57191 ± 240	(4.685	0.020	0.063) $\times 10^{-3}$
33.53–35.36	34.43 ± 0.65	51322 ± 227	(3.947	0.017	0.053) $\times 10^{-3}$
35.36–37.31	36.32 ± 0.69	45871 ± 215	(3.311	0.015	0.045) $\times 10^{-3}$
37.31–39.39	38.33 ± 0.72	41312 ± 204	(2.806	0.014	0.038) $\times 10^{-3}$
39.39–41.61	40.48 ± 0.77	36784 ± 192	(2.343	0.012	0.032) $\times 10^{-3}$
41.61–44.00	42.78 ± 0.81	32850 ± 182	(1.951	0.011	0.027) $\times 10^{-3}$
44.00–46.57	45.26 ± 0.86	29514 ± 172	(1.635	0.010	0.022) $\times 10^{-3}$
46.57–49.33	47.92 ± 0.91	26470 ± 163	(1.367	0.008	0.019) $\times 10^{-3}$
49.33–52.33	50.80 ± 0.96	23477 ± 154	(1.119	0.007	0.015) $\times 10^{-3}$
52.33–55.58	53.92 ± 1.02	21067 ± 146	(9.297	0.064	0.128) $\times 10^{-4}$
55.58–59.13	57.32 ± 1.08	18928 ± 138	(7.663	0.056	0.106) $\times 10^{-4}$
59.13–63.02	61.03 ± 1.16	16677 ± 130	(6.191	0.048	0.086) $\times 10^{-4}$
63.02–67.30	65.11 ± 1.23	15006 ± 123	(5.072	0.042	0.070) $\times 10^{-4}$
67.30–72.05	69.62 ± 1.32	13327 ± 116	(4.075	0.035	0.056) $\times 10^{-4}$

(*continued on next page*)

Table 2 (*continued*).

E [GeV]	$\tilde{E}$ [GeV]	N_{e^-}	Φ_{e^-}	$\sigma^{e^-}_{\rm stat}$	$\sigma^{e^-}_{\rm syst}$
72.05–77.37	74.65 ± 1.41	12066 ± 110	(3.296	0.030	0.046) $\times 10^{-4}$
77.37–83.36	80.29 ± 1.52	10716 ± 104	(2.613	0.025	0.036) $\times 10^{-4}$
83.36–90.19	86.69 ± 1.64	9536 ± 98	(2.048	0.021	0.028) $\times 10^{-4}$
90.19–98.08	94.02 ± 1.78	8457 ± 93	(1.579	0.017	0.022) $\times 10^{-4}$
98.1–107.3	102.6 ± 1.9	7589 ± 89	(1.214	0.014	0.017) $\times 10^{-4}$
107.3–118.4	112.7 ± 2.1	6605 ± 82	(8.891	0.111	0.124) $\times 10^{-5}$
118.4–132.1	125.0 ± 2.4	5882 ± 78	(6.460	0.086	0.090) $\times 10^{-5}$
132.1–148.8	140.1 ± 2.7	4805 ± 70	(4.531	0.066	0.065) $\times 10^{-5}$
148.8–169.9	158.9 ± 3.0	4020 ± 64	(3.010	0.048	0.043) $\times 10^{-5}$
169.9–197.7	183.1 ± 3.5	3221 ± 58	(1.853	0.034	0.027) $\times 10^{-5}$
197.7–237.2	216.2 ± 4.2	2331 ± 49	(1.075	0.023	0.017) $\times 10^{-5}$
237.2–290.0	261.8 ± 5.1	1706 ± 43	(5.978	0.149	0.100) $\times 10^{-6}$
290.0–370.0	326.8 ± 6.4	1161 ± 36	(3.129	0.096	0.055) $\times 10^{-6}$
370.0–500.0	428.5 ± 8.6	747 ± 29	(1.278	0.050	0.026) $\times 10^{-6}$
500.0–700.0	588.8 ± 12.2	392 ± 23	(4.560	0.268	0.119) $\times 10^{-7}$
700.0–1000.0	832.3 ± 18.3	214 ± 19	(1.771	0.158	0.063) $\times 10^{-7}$
1000.0–1400.0	1177.7 ± 28.6	68 ± 12	(4.123	0.700	0.220) $\times 10^{-8}$

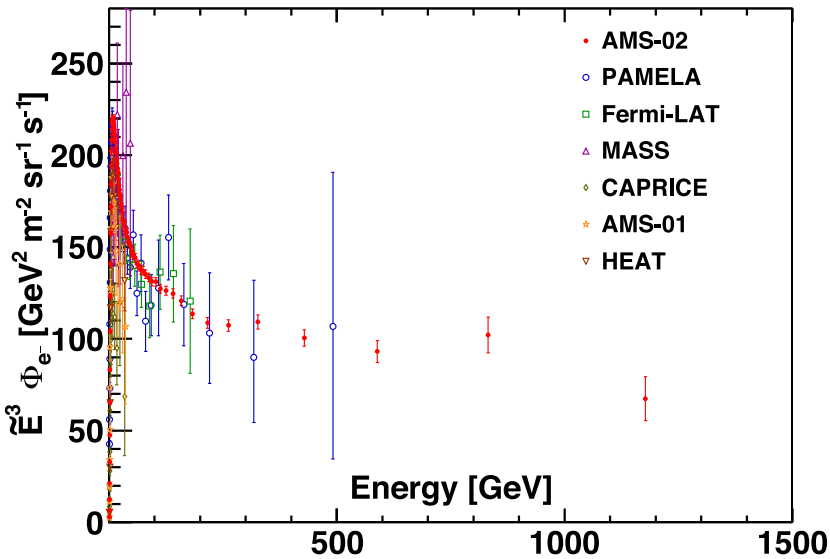

Fig. 47. The AMS cosmic-ray electron spectrum. Recent measurements from PAMELA, Fermi-LAT, MASS, CAPRICE, AMS-01, and HEAT are also shown.

are presented in Fig. 49 together with the positron results. As seen, both the electron and positron indices decrease (soften) rapidly with energy below ∼10 GeV, and then they both start increasing (harden) at > 20 GeV. In particular, the electron spectral index increases from $\gamma = -3.295 \pm 0.026$ in the energy range $[17.98 - 27.25]$ GeV to an average $\gamma = -3.180 \pm 0.008$ in the range $[55.58 - 1400]$ GeV, where it is nearly energy independent.

As seen in Fig. 49, the behavior of the electron and positron spectral indices is distinctly different.

New sources of high energy positrons, such as dark matter, may also produce an equal amount of high energy electrons. We test this hypothesis using the source term from our positron analysis. The electron flux is parametrized as a sum of a power law component and the positron source term with the exponential energy cutoff:

$$\Phi_{e^-}(E) = C_{e^-}\,(E/E_1)^{\gamma_{e^-}} + f_{e^-}\,C_s^{e^+}\,(E/E_2)^{\gamma_s^{e^+}}\,\exp(-E/E_s^{e^+}). \tag{8}$$

The power law component is characterized by the normalization factor C_{e^-} and the spectral index γ_{e^-}. The constant $E_1 = 41.61$ GeV corresponds to the beginning of the fit range, it does not affect the fitted value of γ_{e^-}. The values of the source term parameters $C_s^{e^+} = 6.80 \times 10^{-5}\,\mathrm{m^{-2}\,sr^{-1}\,s^{-1}\,GeV^{-1}}$, $\gamma_s^{e^+} = -2.58$, $E_2 = 60$ GeV, and $E_s^{e^+} = 810$ GeV are taken from the positron data (see Section 2). A fit to the data with the source term normalization f_{e^-} fixed to 1 is performed in the energy range $[41.61 - 1400]$ GeV, where the solar modulation effects are negligible. The fit yields

$$C_{e^-} = (1.965 \pm 0.010) \times 10^{-3}\,\mathrm{m^{-2}\,sr^{-1}\,s^{-1}\,GeV^{-1}},$$
$$\gamma_{e^-} = -3.248 \pm 0.007$$

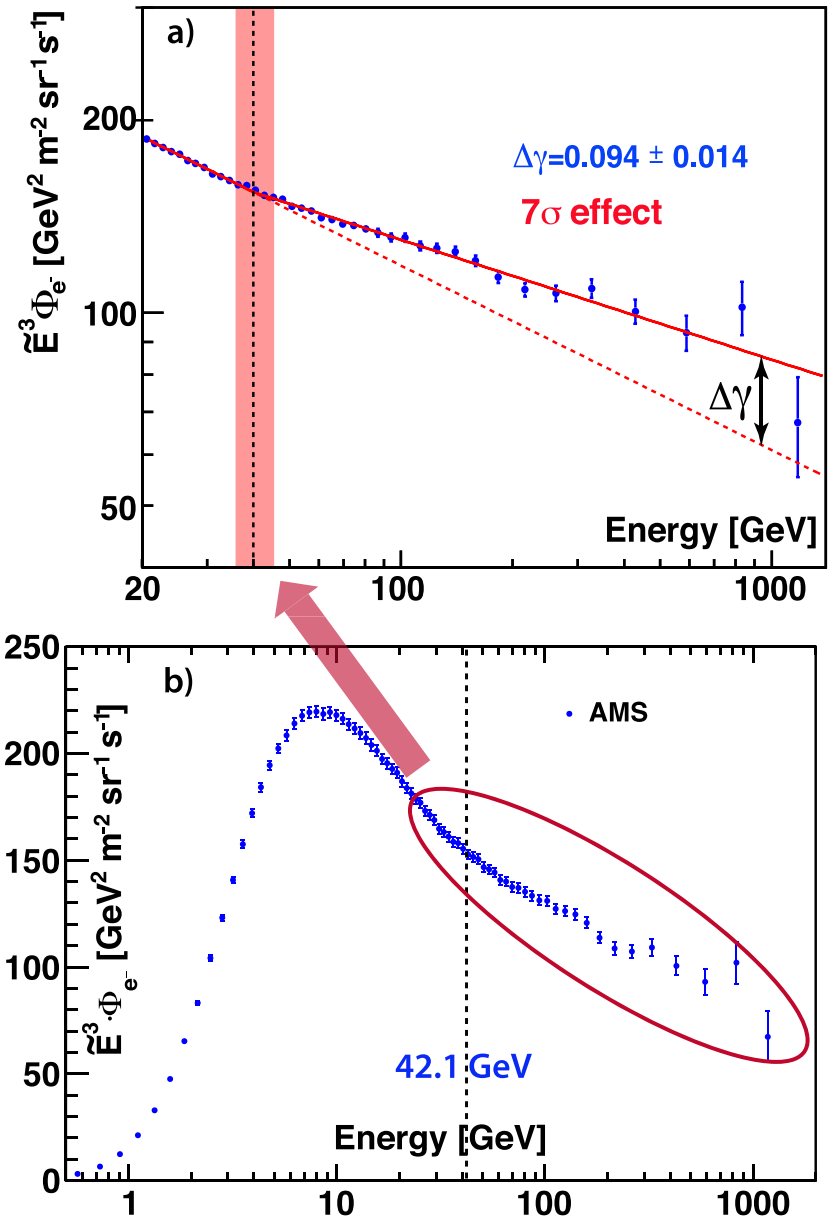

Fig. 48. Fit to the electron flux in the energy range $[20.04 - 1400]$ GeV. The blue data points are the measured electron spectrum. (a) The fitted power law approximation, Eq. (6), is represented by the red line. The vertical dashed line and band correspond to the value and the error of the energy E_0 where the change of the spectrum occurs. The dashed red line is the extrapolation of the power law below E_0 into the higher energy region. $\Delta\gamma$ is the magnitude of the spectral index change (7σ effect). The lower graph (b) is for illustration of this changing behavior.

$$\text{with } \chi^2/\text{d.o.f.} = 15.5/24,$$

for the power law component. The result of the fit is presented in Fig. 50a.

A similar fit of Eq. (8) to data, but with f_{e^-} fixed to 0, yields

$$C_{e^-} = (2.124 \pm 0.010) \times 10^{-3}\,\text{m}^{-2}\,\text{sr}^{-1}\,\text{s}^{-1}\,\text{GeV}^{-1},$$
$$\gamma_{e^-} = -3.186 \pm 0.006$$
$$\text{with } \chi^2/\text{d.o.f.} = 15.2/24.$$

The result of this fit is presented in Fig. 50b. Varying the normalization of the source term f_{e^-} as a free fit parameter does not improve the χ^2 and yields $f_{e^-} = 0.5^{+1.2}_{-0.6}$. As seen in Figs. 50a and 50b, the data are consistent both with the charge symmetric positron source term ($f_{e^-} = 1$ in Eq. (8)) and also with the absence of such a term ($f_{e^-} = 0$). Continuing

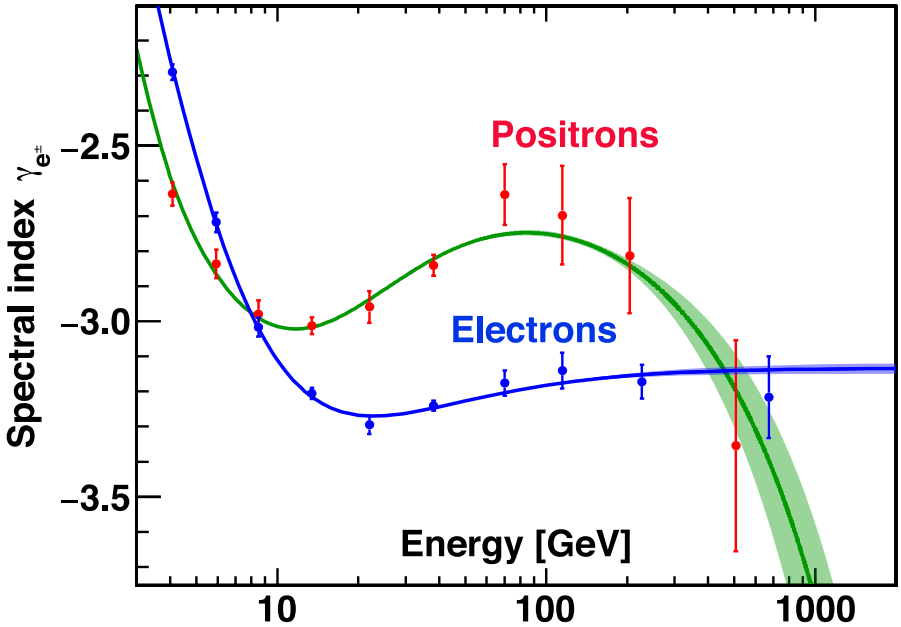

Fig. 49. The spectral indices of the electron flux Φ_{e^-} and of the positron flux Φ_{e^+} as a function of energy. The models (Eqs. (5) and (10)) that fit the positron and electron data are represented by the green line and the blue line, respectively. The corresponding bands are at 68% C.L. of the model parameters.

data taking to 2028 will increase the accuracy and extend the energy range of the measurement. This will enable us to ascertain the existence of the source term contribution to the electron flux.

To investigate the existence of a finite energy cutoff, as seen in the positron flux, the electron flux is fitted with

$$\Phi_{e^-}(E) = C_s\,(E/41.61\,\mathrm{GeV})^{\gamma_s}\,\exp(-E/E_s). \tag{9}$$

A fit to data in the energy range $[41.61 - 1400]$ GeV yields the inverse cutoff energy

$$1/E_s = 0.00^{+0.08}_{-0.00}\,\mathrm{TeV}^{-1}\,,$$
$$C_s = (2.126 \pm 0.010) \times 10^{-3}\,\mathrm{m}^{-2}\mathrm{sr}^{-1}\mathrm{s}^{-1}\mathrm{GeV}^{-1},$$
$$\gamma_s = -3.186^{+0.012}_{-0.006}\,,$$

with $\chi^2/\mathrm{d.o.f.} = 15.2/23$.

A study of the cutoff significance shows that $E_s < 1.9$ TeV is excluded at the 5σ level. These results are presented in Fig. 51.

In addition to a small contribution of secondary electrons produced in the collisions of ordinary cosmic rays with the interstellar medium [71], there could be several astrophysical sources of primary cosmic-ray electrons. It is assumed that there are only a few astrophysical sources of high energy electrons in the vicinity of the solar system each making a power law-like contribution to the electron flux [83,84]. In addition, there are several physics effects which may introduce some spectral features in the original fluxes [85,86]. Therefore, it is important to know the minimal number of distinct power law functions needed to accurately describe the AMS electron flux.

We found that in the entire energy range $[0.5 - 1400]$ GeV the electron flux is well described by the sum of two power law components, a and b, as follows:

$$\Phi_{e^-}(E) = \frac{E^2}{\hat{E}^2}[1 + (\hat{E}/E_t)^{\Delta\gamma_t}]^{-1}[C_a(\hat{E}/E_a)^{\gamma_a} + C_b(\hat{E}/E_b)^{\gamma_b}]. \tag{10}$$

To account for solar modulation effects, the force-field approximation [77] is used, with the energy of particles in the interstellar space $\hat{E} = E + \varphi_{e^-}$, where φ_{e^-} is the effective modulation potential. The additional transition term [86,87], $[1 + (\hat{E}/E_t)^{\Delta\gamma_t}]^{-1}$, has vanishing impact on the flux behavior at energies above E_t (e.g. <0.7% above 40 GeV). The constant E_a is chosen to be 20 GeV to minimize the correlation between parameters C_a and γ_a, and the constant E_b is chosen to be 300 GeV to minimize the correlation between the parameters C_b and γ_b. A fit to the data in the energy range $[0.5 - 1400]$ GeV yields

$$E_t = 3.94 \pm 0.21\,\mathrm{GeV}\,,$$

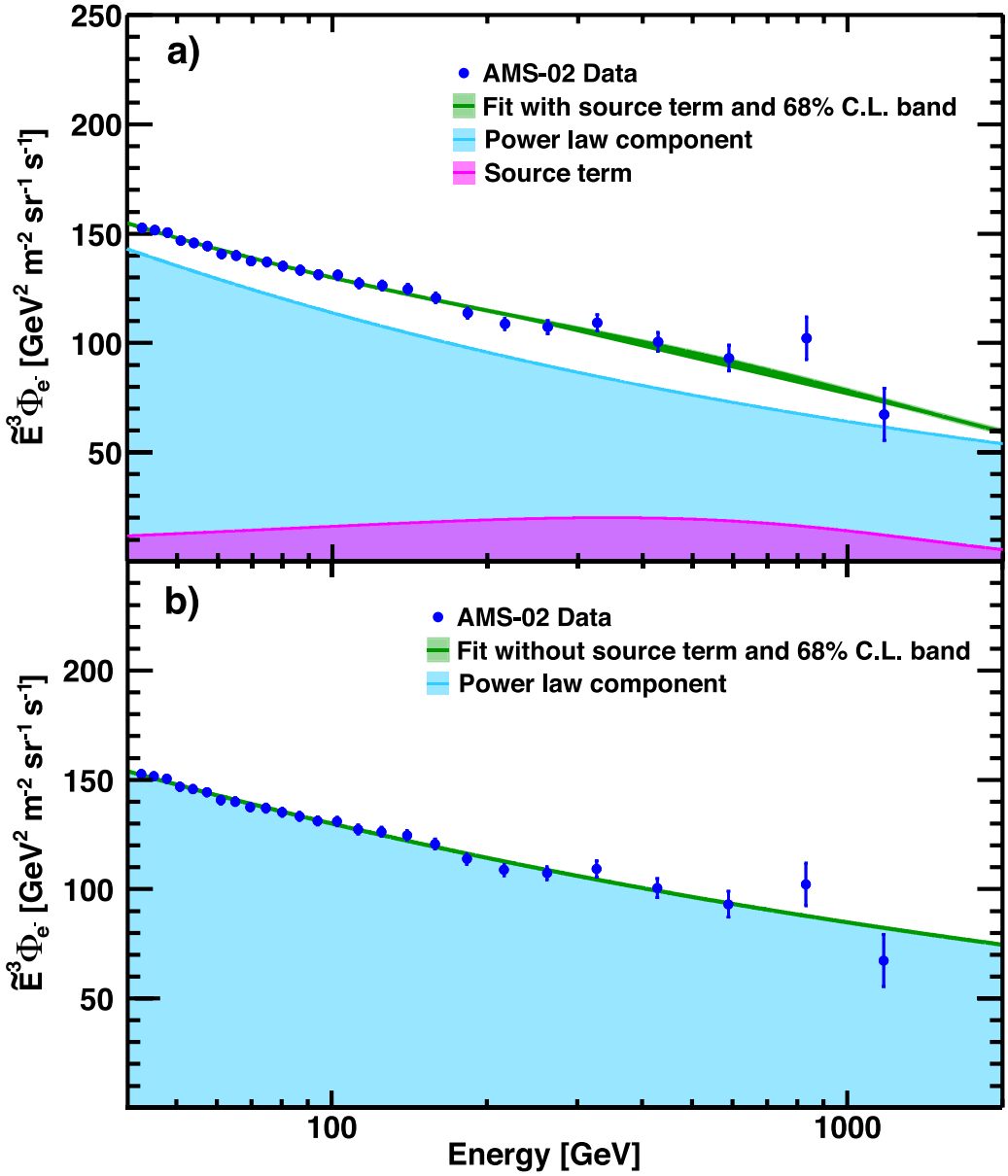

Fig. 50. (a) The fit of a power law plus the positron source term (Eq. (8), $f_{e^-} = 1$) to the electron flux data in the energy range $[41.61 - 1400]$ GeV with the 68% C.L. (green band). The source term contribution, identical to that of positrons, is represented by the magenta area and the power law component by the blue area. (b) The fit of a power law (Eq. (8), $f_{e^-} = 0$) to the electron flux data in the energy range $[41.61 - 1400]$ GeV with the 68% C.L. (green band). The power law component is represented by the blue area.

$$\begin{aligned}
\gamma_t &= -2.14 \pm 0.09\,, \\
C_a &= (1.13 \pm 0.08) \times 10^{-2}\,\mathrm{m^{-2}sr^{-1}s^{-1}GeV^{-1}}, \\
\gamma_a &= -4.31 \pm 0.13\,, \\
C_b &= (3.96 \pm 0.04) \times 10^{-6}\,\mathrm{m^{-2}sr^{-1}s^{-1}GeV^{-1}}, \\
\gamma_b &= -3.14 \pm 0.02\,, \\
\varphi_{e^-} &= 0.87 \pm 0.12\,\mathrm{GeV},
\end{aligned}$$

with $\chi^2/\mathrm{d.o.f.} = 36.5/68$.

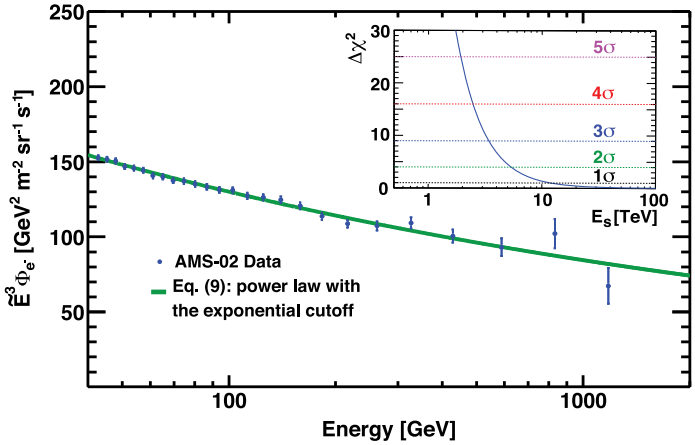

Fig. 51. The fit to the electron flux data in the energy range $[41.61 - 1400]$ GeV. The insert shows the study of the significance of the $1/E_s$ measurement by varying all three fit parameters in Eq. (9) to find the minimal $\Delta\chi^2$ corresponding to E_s values from 1 to 100 TeV. The blue curve shows the dependence of $\Delta\chi^2$ on E_s and the horizontal dashed lines show different significance levels from 1 to 5σ. As seen, E_s values below 1.9 TeV are excluded at the 5σ level.

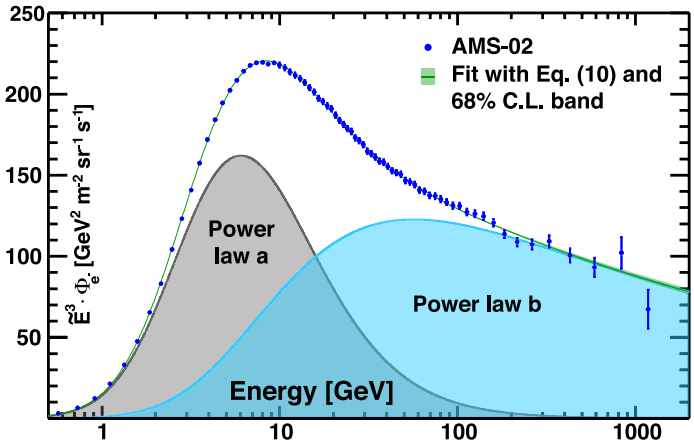

Fig. 52. The two-power law fit (Eq. (10)) to the electron flux data in the energy range $[0.5 - 1400]$ GeV with the 68% C.L. (green band). The two power law components a and b are represented by the gray and blue areas, respectively.

Note that the fitted value of the effective solar potential φ_{e^-} is lower than the value of $\varphi_{e^+} = 1.10 \pm 0.03$ GeV from the fit of Eq. (5) to positron data and higher than the average value (~ 0.62 GeV) from the analysis of neutron monitor data during this period [78].

The fit results are presented in Fig. 52. We conclude that in the energy range $[0.5 - 1400]$ GeV the sum of two power law functions provides an excellent description of the data. Adding a third power law term in Eq. (10) does not improve the χ^2/d.o.f. of the fit to the current data.

An analysis of the individual components in the electron flux, namely the power law a and b terms, is presented in Figs. 53 and 54 together with the corresponding positron data. As seen in Fig. 53, at low energies positrons come from cosmic ray collisions (secondary positrons), while the electron spectrum is dominated by contributions from astrophysical sources [71] (primary electrons).

As shown in Section 2, the positron flux has an exponential energy cutoff of 810^{+310}_{-180} GeV, whereas, for the electron flux, the cutoff energy values $E_s < 1.9$ TeV are excluded at the 5σ level. Fig. 54, shows that the positron and electron spectra have very different behavior at high energies.

In the entire energy range the electron and positron spectra have distinctly different magnitudes and energy dependences. The different behavior of the cosmic-ray electrons and positrons measured by AMS is clear evidence that most high energy electrons originate from different sources than high energy positrons. In particular, the positron flux is well described by the sum of two terms: "diffuse" term associated with the secondary positrons from cosmic ray collisions and the source term associated with dark matter annihilation or a new astrophysical source. In contrast, the electron flux is well described by the sum of two power law functions, which may provide clues to the origin of cosmic ray electrons.

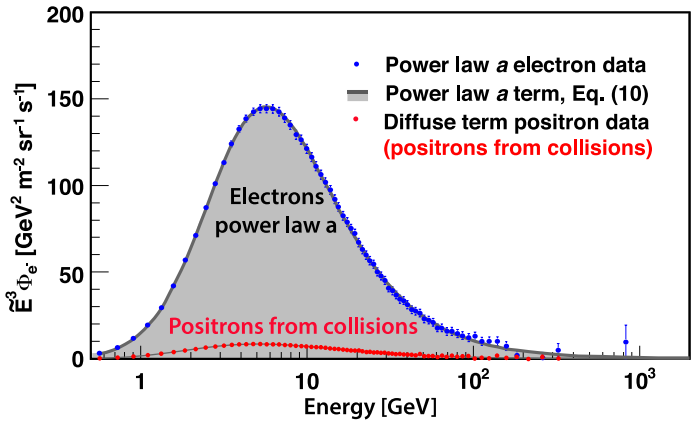

Fig. 53. Analysis of the low energy electron power law *a* data. The difference of the electron data and the power law *b* contribution (blue data points) is shown together with the power law *a* term of Eq. (10) (gray line and shading). For comparison, the positron "diffuse" term data from Fig. 41 is also shown (red data points and black curve).

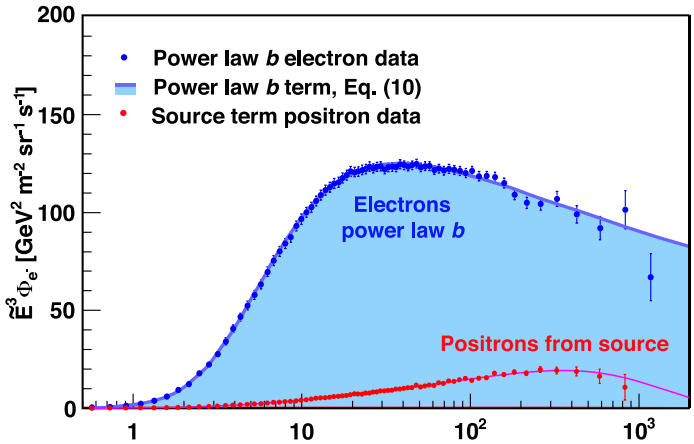

Fig. 54. Analysis of the electron power law *b* data. The difference of the electron data and the power law *a* contribution (blue data points) is shown together with the power law *b* term of Eq. (10) (blue curve and shading). For comparison, the positron source term data from Fig. 42 are also shown (red data points and magenta curve).

Analysis of the electron arrival directions [79], similar to the analysis of positrons described in Section 2, was performed using the data in the energy range above 16 GeV (see Fig. 55). The electron flux is found to be consistent with isotropy and our upper limit on the amplitude of the electron dipole anisotropy for any axis in galactic coordinates is $\delta < 0.005$ at the 95% C.L.

Fig. 56 shows the latest AMS results on the measurement of the positron fraction (i.e. the ratio $\Phi_{e^+}/(\Phi_{e^-} + \Phi_{e^+})$, Table 3) together with the data from other experiments [65–70].

Note that, with precise knowledge of the detector acceptance, the positron flux, Φ_{e^+}, is more sensitive to new physics phenomena than the positron fraction, since it is independent of the energy dependence of electrons.

The AMS data on the combined electron and positron spectrum (Table 4) are presented in Fig. 57 together with other recent measurements that use non-magnetic calorimeters [88–92]. These AMS results on a combined electron and positron flux are obtained using a dedicated analysis [93], which does not use charge sign identification and, therefore, has higher efficiency resulting in more data events. As seen from Fig. 57, the non-magnetic calorimeter measurements often give different results. Note that CALET and HESS results are in agreement with the AMS measurements.

4. Cosmic protons

Protons are the most abundant charged cosmic rays. Knowledge of the rigidity dependence of the proton flux is important in understanding the origin, acceleration, and propagation of cosmic rays [94]. Recent important measurements of the proton flux in cosmic rays have reported different variations of the flux with energy [95–101]. These measurements

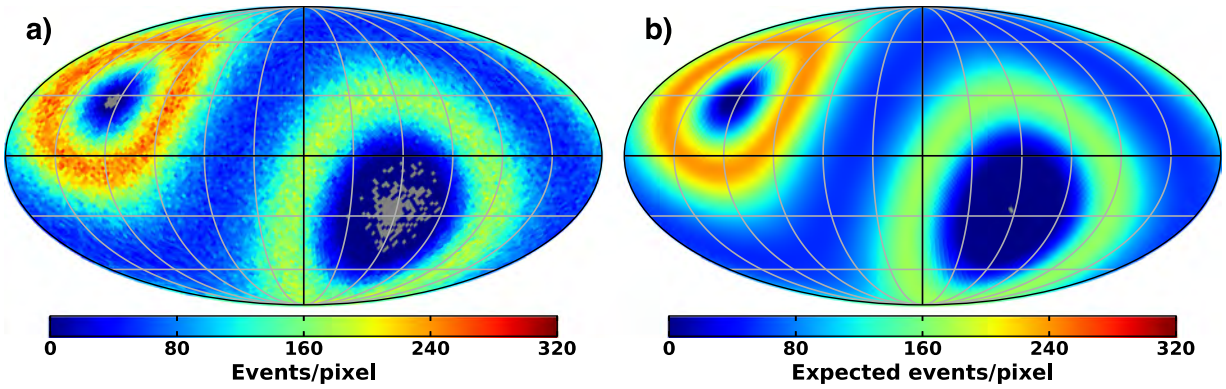

Fig. 55. (a) Map of the incoming electron directions in galactic coordinates observed by AMS on the ISS. (b) Expected map of the incoming electron directions for the isotropic distribution of electrons in galactic coordinates. The electron data show $\delta < 0.005$ at the 95% C.L.

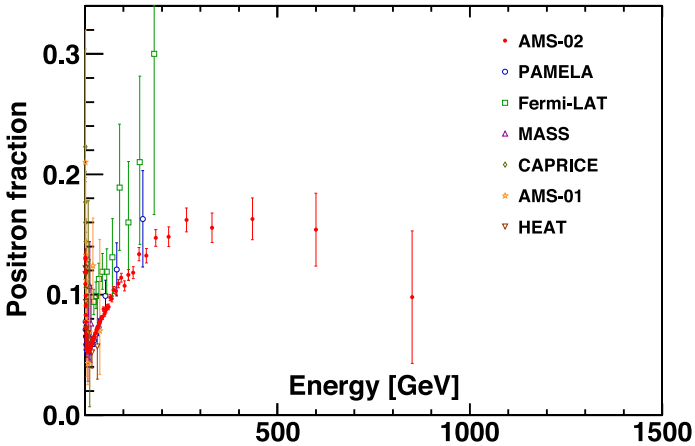

Fig. 56. The AMS positron fraction. Other recent measurements from PAMELA, Fermi-LAT, MASS, CAPRICE, AMS-01, and HEAT are shown for comparison.

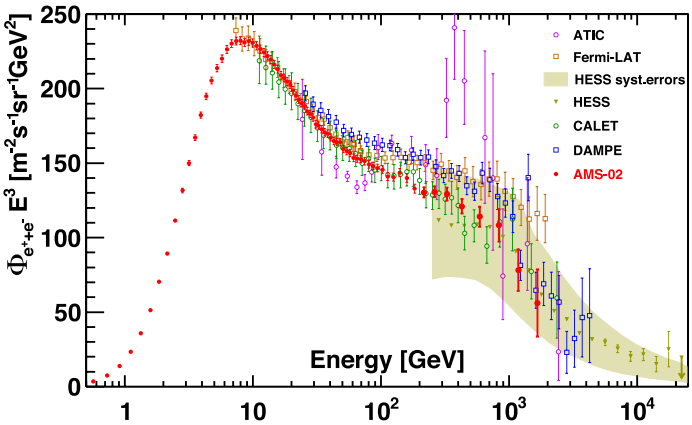

Fig. 57. The AMS combined electron and positron flux, multiplied by E^3, together with the measurements from ATIC [88], HESS [89], Fermi-LAT [90], DAMPE [91], and CALET [92].

Table 3
The positron fraction (PF $= \Phi_{e^+}/(\Phi_{e^-} + \Phi_{e^+})$) as a function of the energy E at the top of AMS. Characteristic energy $\tilde{E}$ (i.e. spectrally weighted mean energy in the bin) is given with its systematic error from the energy scale uncertainty. PF are calculated from the positron and electron fluxes (Sections 2 and 3). $\sigma^{\mathrm{PF}}_{\mathrm{stat}}$ and $\sigma^{\mathrm{PF}}_{\mathrm{syst}}$ are the statistical error and the total systematic error of the positron fraction. The systematic errors of the positron fraction account for correlations related to the calculation of the acceptance.

E [GeV]	$\tilde{E}$ [GeV]	PF	$\sigma^{\mathrm{PF}}_{\mathrm{stat}}$	$\sigma^{\mathrm{PF}}_{\mathrm{syst}}$
0.50–0.65	0.57 ± 0.02	(1.309	0.049	0.033) $\times 10^{-1}$
0.65–0.82	0.73 ± 0.02	(1.295	0.013	0.021) $\times 10^{-1}$
0.82–1.01	0.91 ± 0.03	(1.188	0.008	0.010) $\times 10^{-1}$
1.01–1.22	1.11 ± 0.03	(1.090	0.006	0.007) $\times 10^{-1}$
1.22–1.46	1.33 ± 0.03	(9.919	0.044	0.052) $\times 10^{-2}$
1.46–1.72	1.58 ± 0.04	(9.081	0.034	0.040) $\times 10^{-2}$
1.72–2.00	1.85 ± 0.04	(8.316	0.027	0.030) $\times 10^{-2}$
2.00–2.31	2.15 ± 0.05	(7.735	0.024	0.027) $\times 10^{-2}$
2.31–2.65	2.47 ± 0.05	(7.221	0.021	0.025) $\times 10^{-2}$
2.65–3.00	2.82 ± 0.06	(6.783	0.021	0.023) $\times 10^{-2}$
3.00–3.36	3.17 ± 0.06	(6.455	0.020	0.022) $\times 10^{-2}$
3.36–3.73	3.54 ± 0.07	(6.196	0.020	0.021) $\times 10^{-2}$
3.73–4.12	3.92 ± 0.08	(5.972	0.020	0.020) $\times 10^{-2}$
4.12–4.54	4.32 ± 0.08	(5.759	0.020	0.019) $\times 10^{-2}$
4.54–5.00	4.76 ± 0.09	(5.620	0.020	0.018) $\times 10^{-2}$
5.00–5.49	5.24 ± 0.10	(5.517	0.020	0.018) $\times 10^{-2}$
5.49–6.00	5.74 ± 0.11	(5.391	0.021	0.017) $\times 10^{-2}$
6.00–6.54	6.26 ± 0.12	(5.353	0.021	0.017) $\times 10^{-2}$
6.54–7.10	6.81 ± 0.13	(5.353	0.022	0.017) $\times 10^{-2}$
7.10–7.69	7.39 ± 0.14	(5.260	0.023	0.017) $\times 10^{-2}$
7.69–8.30	7.99 ± 0.15	(5.289	0.025	0.017) $\times 10^{-2}$
8.30–8.95	8.62 ± 0.16	(5.272	0.026	0.017) $\times 10^{-2}$
8.95–9.62	9.28 ± 0.18	(5.277	0.028	0.018) $\times 10^{-2}$
9.62–10.32	9.96 ± 0.19	(5.333	0.030	0.018) $\times 10^{-2}$
10.32–11.04	10.67 ± 0.20	(5.353	0.033	0.019) $\times 10^{-2}$
11.04–11.80	11.41 ± 0.22	(5.456	0.035	0.019) $\times 10^{-2}$
11.80–12.59	12.19 ± 0.23	(5.581	0.037	0.020) $\times 10^{-2}$
12.59–13.41	12.99 ± 0.25	(5.595	0.040	0.020) $\times 10^{-2}$
13.41–14.25	13.82 ± 0.26	(5.581	0.043	0.020) $\times 10^{-2}$
14.25–15.14	14.69 ± 0.28	(5.656	0.045	0.020) $\times 10^{-2}$
15.14–16.05	15.59 ± 0.29	(5.776	0.048	0.021) $\times 10^{-2}$
16.05–17.00	16.52 ± 0.31	(5.833	0.051	0.021) $\times 10^{-2}$
17.00–17.98	17.48 ± 0.33	(5.891	0.054	0.021) $\times 10^{-2}$
17.98–18.99	18.48 ± 0.35	(5.940	0.057	0.021) $\times 10^{-2}$
18.99–20.04	19.51 ± 0.37	(6.075	0.060	0.021) $\times 10^{-2}$
20.04–21.13	20.58 ± 0.39	(6.339	0.065	0.022) $\times 10^{-2}$
21.13–22.25	21.68 ± 0.41	(6.298	0.068	0.022) $\times 10^{-2}$
22.25–23.42	22.83 ± 0.43	(6.252	0.072	0.022) $\times 10^{-2}$
23.42–24.62	24.01 ± 0.45	(6.529	0.077	0.024) $\times 10^{-2}$
24.62–25.90	25.25 ± 0.48	(6.495	0.080	0.024) $\times 10^{-2}$
25.90–27.25	26.56 ± 0.50	(6.808	0.086	0.026) $\times 10^{-2}$
27.25–28.68	27.95 ± 0.53	(6.820	0.091	0.027) $\times 10^{-2}$
28.68–30.21	29.43 ± 0.56	(7.093	0.097	0.029) $\times 10^{-2}$
30.21–31.82	31.00 ± 0.59	(7.164	0.105	0.030) $\times 10^{-2}$
31.82–33.53	32.66 ± 0.62	(7.274	0.111	0.031) $\times 10^{-2}$
33.53–35.36	34.43 ± 0.65	(7.330	0.118	0.032) $\times 10^{-2}$
35.36–37.31	36.32 ± 0.69	(7.669	0.127	0.035) $\times 10^{-2}$
37.31–39.39	38.33 ± 0.72	(7.652	0.134	0.036) $\times 10^{-2}$
39.39–41.61	40.48 ± 0.77	(7.870	0.143	0.038) $\times 10^{-2}$
41.61–44.00	42.78 ± 0.81	(8.105	0.154	0.041) $\times 10^{-2}$
44.00–46.57	45.26 ± 0.86	(8.115	0.163	0.042) $\times 10^{-2}$
46.57–49.33	47.92 ± 0.91	(8.811	0.178	0.047) $\times 10^{-2}$
49.33–52.33	50.80 ± 0.96	(8.406	0.186	0.047) $\times 10^{-2}$
52.33–55.58	53.92 ± 1.02	(8.689	0.199	0.051) $\times 10^{-2}$
55.58–59.13	57.32 ± 1.08	(8.967	0.213	0.054) $\times 10^{-2}$
59.13–63.02	61.03 ± 1.16	(8.978	0.228	0.056) $\times 10^{-2}$
63.02–67.30	65.11 ± 1.23	(9.775	0.249	0.063) $\times 10^{-2}$

(*continued on next page*)

Table 3 (*continued*).

E [GeV]	$\tilde{E}$ [GeV]	PF	σ^{PF}_{stat}	σ^{PF}_{syst}
67.30–72.05	69.62 ± 1.32	(9.670	0.263	0.066) $\times 10^{-2}$
72.05–77.37	74.65 ± 1.41	(1.039	0.028	0.007) $\times 10^{-1}$
77.37–83.36	80.29 ± 1.52	(1.033	0.030	0.008) $\times 10^{-1}$
83.36–90.19	86.69 ± 1.64	(1.091	0.033	0.009) $\times 10^{-1}$
90.19–98.08	94.02 ± 1.78	(1.142	0.036	0.010) $\times 10^{-1}$
98.08–107.3	102.6 ± 1.9	(1.073	0.040	0.009) $\times 10^{-1}$
107.3–118.4	112.7 ± 2.1	(1.165	0.044	0.010) $\times 10^{-1}$
118.4–132.1	125.0 ± 2.4	(1.183	0.047	0.010) $\times 10^{-1}$
132.1–148.8	140.1 ± 2.7	(1.337	0.053	0.012) $\times 10^{-1}$
148.8–169.9	158.9 ± 3.0	(1.323	0.058	0.012) $\times 10^{-1}$
169.9–197.7	183.1 ± 3.5	(1.472	0.068	0.014) $\times 10^{-1}$
197.7–237.2	216.2 ± 4.2	(1.481	0.080	0.017) $\times 10^{-1}$
237.2–290.0	261.8 ± 5.1	(1.621	0.097	0.023) $\times 10^{-1}$
290.0–370.0	326.8 ± 6.4	(1.557	0.120	0.028) $\times 10^{-1}$
370.0–500.0	428.5 ± 8.6	(1.630	0.166	0.050) $\times 10^{-1}$
500.0–700.0	588.8 ± 12.2	(1.541	0.274	0.130) $\times 10^{-1}$
700.0–1000.0	832.3 ± 18.3	(9.802	5.052	2.181) $\times 10^{-2}$

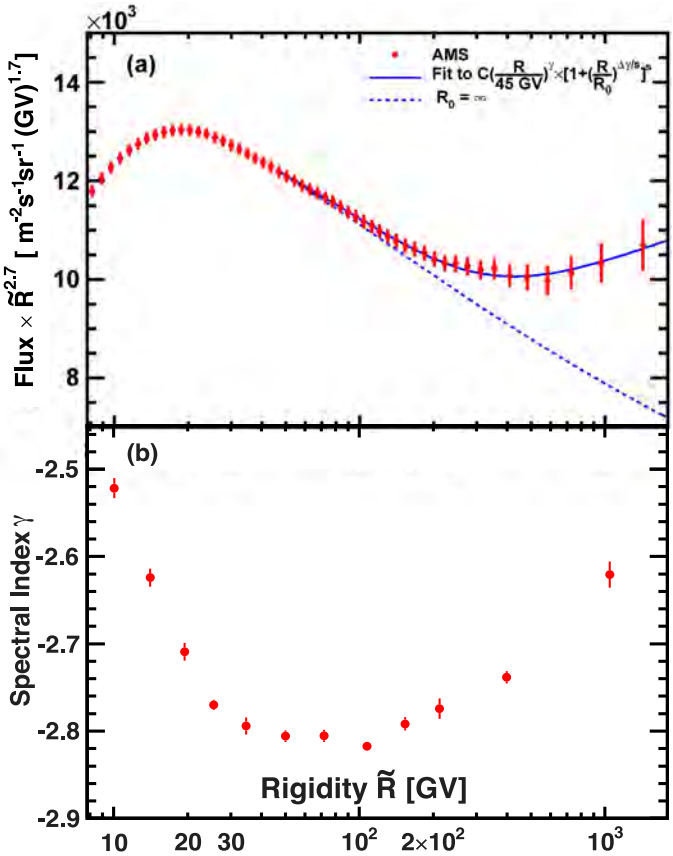

Fig. 58. (a) The AMS proton flux as a function of rigidity $\tilde{R}$ multiplied by $\tilde{R}^{2.7}$. The solid curve indicates the fit of Eq. (12) to the data. For illustration, the dashed curve uses the same fit values but with R_0 set to infinity. (b) The variation of the proton flux spectral index γ on rigidity $\tilde{R}$.

generated widespread interest. In particular, the ATIC-2, CREAM, PAMELA, CALET, and DAMPE experiments showed deviations of the proton flux from a single power law. Many models were proposed to account for the hardening of the flux based on different sources, acceleration mechanisms, diffusive propagation effects, and their superposition [102].

We have reported on the precise measurement of the proton flux in primary cosmic rays in the rigidity range from 1 GV to 1.8 TV based on 300 million proton events. The details of the analysis of the proton flux are given in Ref. [63] including extensive studies of the systematic errors. Our latest measurements of the proton flux from 1 GV to 1.8 TV

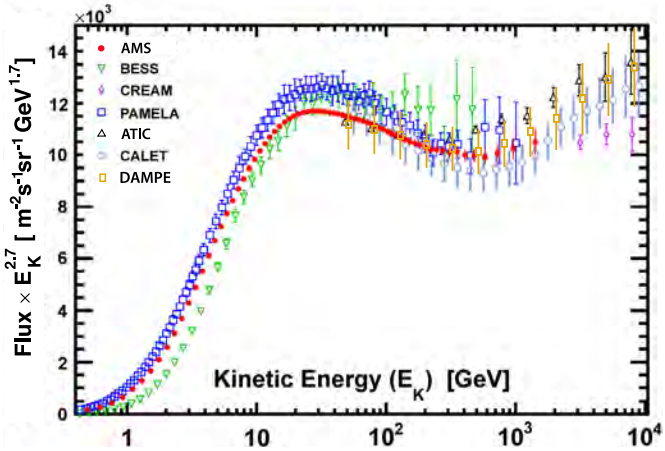

Fig. 59. Latest AMS proton flux multiplied by $E_K^{2.7}$ together with other recent measurements.

are based on 1 billion proton events collected by AMS (Table 5). These new results are in complete agreement with our published data but have smaller errors.

The proton flux measured as a function of rigidity R, multiplied by $R^{2.7}$, is shown in Fig. 58a. A power law with a constant spectral index γ

$$\Phi = CR^{\gamma}\,, \tag{11}$$

where R is in GV and C is a normalization factor, does not fit the measured proton flux in the rigidity range above 45 GV, where the flux time variations due to the solar modulation effects are negligible. We therefore use the function with a varying spectral index

$$\Phi = C\left(\frac{R}{45\,\mathrm{GV}}\right)^{\gamma}\left[1+\left(\frac{R}{R_0}\right)^{\Delta\gamma/s}\right]^{s}\,, \tag{12}$$

where s quantifies the smoothness of the transition of the spectral index from γ for rigidities below the characteristic transition rigidity R_0 to $\gamma+\Delta\gamma$ for rigidities above R_0. Fitting over the range 45 GV to 1.8 TV yields

$$\begin{aligned}
C &= 0.447 \pm 0.0002(\mathrm{fit}) \pm 0.003(\mathrm{sys}) \pm 0.003(\mathrm{sol})\,\mathrm{m}^{-2}\mathrm{sr}^{-1}\mathrm{s}^{-1}\mathrm{GV}^{-1},\\
\gamma &= -2.853^{+0.002}_{-0.003}(\mathrm{fit}) \pm 0.003(\mathrm{sys}) \pm 0.007(\mathrm{sol}),\\
\Delta\gamma &= 0.22^{+0.03}_{-0.02}(\mathrm{fit}) \pm 0.05(\mathrm{sys}) \pm 0.01(\mathrm{sol}),\\
s &= 0.09^{+0.03}_{-0.02}(\mathrm{fit}) \pm 0.02(\mathrm{sys}) \pm 0.01(\mathrm{sol}),\\
R_0 &= 331^{+51}_{-37}(\mathrm{fit})^{+111}_{-96}(\mathrm{sys}) \pm 2(\mathrm{sol})\,\mathrm{GV}\\
\text{with } \chi^2/\mathrm{d.o.f.} &= 25/26.
\end{aligned}$$

The first error quoted (fit) takes into account the statistical and uncorrelated systematic errors. The second (sys) is the error from the remaining systematic errors, namely from the rigidity resolution function and unfolding, and from the absolute rigidity scale, with their bin-to-bin correlations. The third (sol) is the uncertainty due to the variation of the solar potential [77]. The fit confirms that above 45 GV the flux is incompatible with a single spectral index at the 99.9% C.L.

The fit result is presented in Fig. 58a. It shows an excellent agreement with our measurements. The data points in Fig. 58a are placed along the abscissa at $\tilde{R}$ calculated for a flux $\propto R^{-2.7}$ [64]. Fig. 58b presents the proton flux spectral index γ

$$\gamma = d[\log(\Phi)]/d[\log(R)]. \tag{13}$$

It also shows that the proton flux does not follow a single power law (i.e. γ = constant). The spectral index increases progressively above 200 GV, that is, the flux deviates from a single power law and progressively hardens at high rigidities.

Fig. 59 shows the latest AMS proton flux measurement together with the measurements from recent experiments [96–101,103]. As seen, in the entire energy range up to 1800 GeV AMS provides an accurate information on the proton flux.

5. Cosmic antiprotons

There are four charged elementary particles traveling through the cosmos: protons, electrons, positrons, and antiprotons. The experimental data on antiprotons are limited because of low production rate: for each antiproton there are approximately 10^4 protons. Since the observation of antiprotons in cosmic rays [104], many studies of cosmic ray antiprotons have been performed [105–109]. However, to measure the antiproton flux to $\sim$ 3% accuracy requires a separation power of $\sim 10^6$ between the antiproton signal and background from protons. Precision measurements of the cosmic ray antiproton flux are as important as measurements of cosmic ray positrons since both species are antiparticles that have to be created in high-energy processes rather then just being accelerated from the interstellar medium by a passing shock wave.

As discussed in Section 2, AMS has measured the excess in the positron spectrum to 1000 GeV. These data generated many interesting theoretical models including collisions of dark matter particles, astrophysical sources, and collisions of cosmic rays (see Section 2). Some of these models also include specific predictions on the antiproton flux. In this Section we present a comparison of the AMS antiproton results with several theoretical models.

We had reported on the precise measurement of the antiproton flux in primary cosmic rays up to 450 GV using the data sample of 3.5×10^5 antiproton events collected by AMS [44] including extensive studies of the systematic errors. Our latest measurements of the antiproton flux from 1 to 525 GV are based on 5.6×10^5 events collected by AMS (Table 6). These new results agree with our published data [44] but have higher statistics and improved accuracy.

Fig. 60 shows the latest AMS antiproton spectrum together with the measurements from other recent experiments [105,109]. As seen, the AMS results extend the rigidity range with increased precision.

The functional behavior of the antiproton-to-proton flux ratio shows that the antiproton flux is similar to that of protons, as seen in Fig. 61. This result is not expected if cosmic antiprotons are produced only in collisions of cosmic rays with interstellar medium. This generated many theoretical papers examining the observed unusual behavior [110–116].

After the AMS publication on the antiproton flux [44], there were many discussions on the possible contribution of dark matter annihilation to the antiproton spectrum [110]. In the past few years, the accuracy of the calculation of the flux of secondary cosmic ray antiprotons was improved [111], and the discussion on the origin of the high energy antiprotons continues [112–116]. Among many theoretical models we present nine recent models to illustrate qualitatively the current theoretical understanding of AMS results on antiprotons.

Fig. 62 shows the AMS antiproton spectrum and the antiproton-to-proton flux ratio together with five theoretical predictions which take into account only cosmic ray collisions [113,114].

Fig. 63 shows the AMS antiproton spectrum and the antiproton-to-proton flux ratio together with the four recent theoretical predictions for models with dark matter annihilation and cosmic ray collisions [114,115].

As seen from Figs. 62 and 63, the current uncertainties of the modeling need to be further improved before a definitive theoretical interpretation of the origin of cosmic ray antiprotons is possible. As an example, the model [114] shown both in Figs. 62c and 63c exhibits qualitative agreement with the data despite the two different assumptions with or without the contribution from Dark Matter annihilation. This shows the importance of comparing models with all the available AMS data, including also the data on electrons, positrons, protons, and nuclei. The accuracy of theoretical predictions can be improved with the latest AMS results on the fluxes of primary and secondary cosmic rays and their ratios (see Sections 4, 8, 10, and 11) to the models. The continuing AMS measurements of the antiproton spectrum to the highest rigidity with improved accuracy, as well as its detailed time dependent variations, will also provide a crucial input to understanding of the origin of antiprotons in the cosmos.

6. Properties of cosmic elementary particles

With the AMS measurements of the fluxes of all charged cosmic elementary particles, positrons (Section 2), electrons (Section 3), protons (Section 4), and antiprotons (Section 5), we can now study their relative behavior as a function of energy. Comparison of these results, obtained with the same detector, provides precise experimental information over an extended energy range in the study of elementary particles traveling through the cosmos and bring new insights.

As seen from the antiproton-to-proton flux ratio (Fig. 61), the functional behavior of the antiproton flux is similar to that of protons. This observation is surprising if most of the high energy antiprotons are secondary particles produced from collisions of cosmic rays with interstellar medium. This result has generated many theoretical models on the origin of cosmic antiprotons, especially on the existence of the primary component in the antiproton spectrum due to dark matter annihilations [110,114–116].

Electrons and protons are the most abundant elementary particles in the cosmos. Comparison of the energy dependences of their spectra is presented in Fig. 64. As discussed in Sections 3 and 4, these particles are considered primary cosmic rays, but with distinctly different energy dependences. In the entire energy range, the electron energy spectrum is described by a sum of two power law functions (Eq. (10)), and the proton spectrum is described by a power law function with variable spectral index (Eq. (12)) with progressive hardening above 200 GV. As seen in Fig. 64, above $\sim$10 GeV, electrons exhibit much softer energy dependence compared to protons. This is commonly attributed to energy losses by electrons during the propagation in the interstellar medium (including interstellar gas, magnetic fields, and photons) [117].

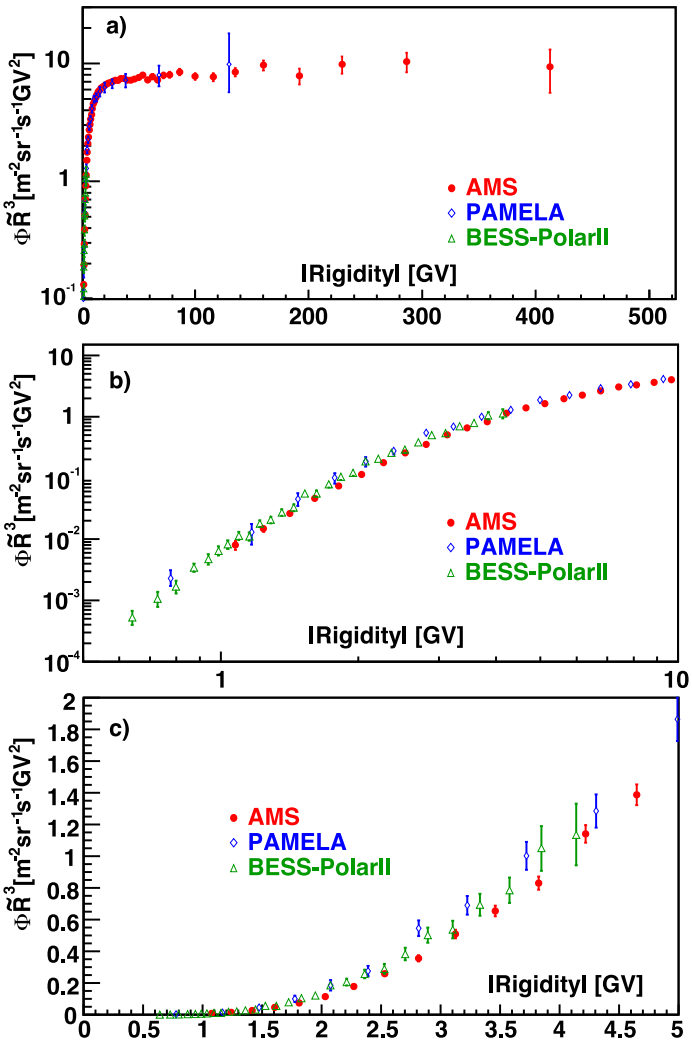

Fig. 60. (a) The measured antiproton spectrum ($\Phi_{\bar{p}}$, red data points). Recent results from BESS [105] and PAMELA [109] are also shown. (b) The measured antiproton spectrum in the low rigidity range, $|R| < 10$ GV. (c) Details of the measured antiproton spectrum in the low rigidity range, $|R| < 5$ GV.

Contrary to electrons, positrons have distinctly different energy dependence in the entire energy range as shown in Fig. 65. This is clear evidence that cosmic ray electrons and positrons originate from completely different sources (see also discussion in Sections 2 and 3).

In Fig. 66, we compare our measured spectra of positrons and protons (see Sections 2 and 4). The two spectra are normalized at 60 GeV. As seen, the positron spectrum $E^3\Phi_{e^+}$ decreases with increasing energy above 284 GeV. This is in contrast with the proton spectrum, which continuously increases in the entire energy range. Another surprising observation is that the positron spectrum is harder then the proton spectrum in the energy range from 60 to ∼260 GeV.

This behavior is illustrated in Fig. 67, which shows the ratio of the positron-to-proton fluxes together with the fit of Eq. (4) in the energy range [55.58 − 1000] GeV. The fit yields

$$\gamma = 0.069 \pm 0.028,$$
$$\Delta\gamma = -0.60^{+0.19}_{-0.42},$$
$$E_0 = 256^{+67}_{-73}\,\text{GeV}$$
$$\text{with } \chi^2/\text{d.o.f.} = 11.3/16.$$

Fitting a constant to the data yields χ^2/d.o.f.= 28.2/19. The difference of these two χ^2 values shows that the flux ratio is not consistent with a constant in this energy range at the 3.4σ level. The fit of Eq. (4) highlights the pronounced change

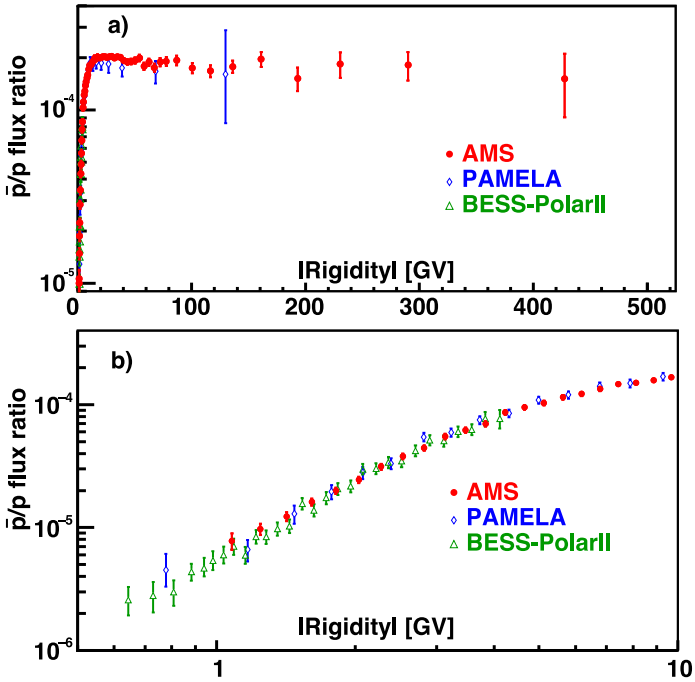

Fig. 61. (a) The antiproton-to-proton ratio. Recent results from BESS [105] and PAMELA [109] are also shown. (b) Behavior of the measured antiproton-to-proton ratio in the low rigidity range (< 10 GV).

in the behavior of the positron-to-proton flux ratio at

$$E_0 = 256^{+67}_{-73}\,\text{GeV}.$$

The value of this transition energy is compatible with the transition energy of 284^{+91}_{-64} GeV from the fit of the power law approximation, Eq. (4), to the positron flux (see Section 2).

It is important to note that positron and antiproton spectra have strikingly similar behavior at high energies, as seen in Fig. 68. This suggests a possible common source of high energy positrons and antiprotons.

To further study the origin of positrons, Fig. 69 shows the positron-to-antiproton flux ratio above 60 GeV. In our first antiproton publication [44], this ratio was found to be consistent with a constant. This is also the case with the latest data for positrons and antiprotons.

Fitting a constant to the flux ratio in the range $[60 - 525]$ GeV, yields

$$\Phi_{e^+}/\Phi_{\bar{p}} = 2.00 \pm 0.035(\text{stat.}) \pm 0.06(\text{syst.})$$
$$\text{with } \chi^2/\text{d.o.f.} = 7.2/12,$$

consistent with a constant. Thus, the antiproton data show nearly identical energy dependence as positrons at high energies.

Antiprotons are not produced by pulsars. The existence of the cutoff in the antiproton energy spectrum is to be expected if high energy antiprotons originate from dark matter annihilation. The continuation of data taking through the lifetime of the ISS will provide an important confirmation of the origin of high energy positrons and antiprotons.

7. Nuclear cross section measurements

To accurately measure the fluxes of cosmic-ray nuclei, we need to know the interaction cross sections of these nuclei with the thin material within AMS. Averaged over path lengths within the AMS acceptance, the material traversed by particles is composed, by mass, of 73% carbon, 17% aluminum, and small amounts of silicon, oxygen, hydrogen, sodium, gold, and other elements. The corresponding inelastic cross sections have only been measured below 10 GV for He and C projectiles [118].

To measure the cosmic nuclear interaction cross sections, we follow the procedure described in detail in Ref. [119]. In particular, the survival probabilities of light nuclei are measured using the data acquired when the ISS attitude was such that AMS is pointing horizontally as shown in Fig. 70a. In these conditions, cosmic nuclei can pass in either direction

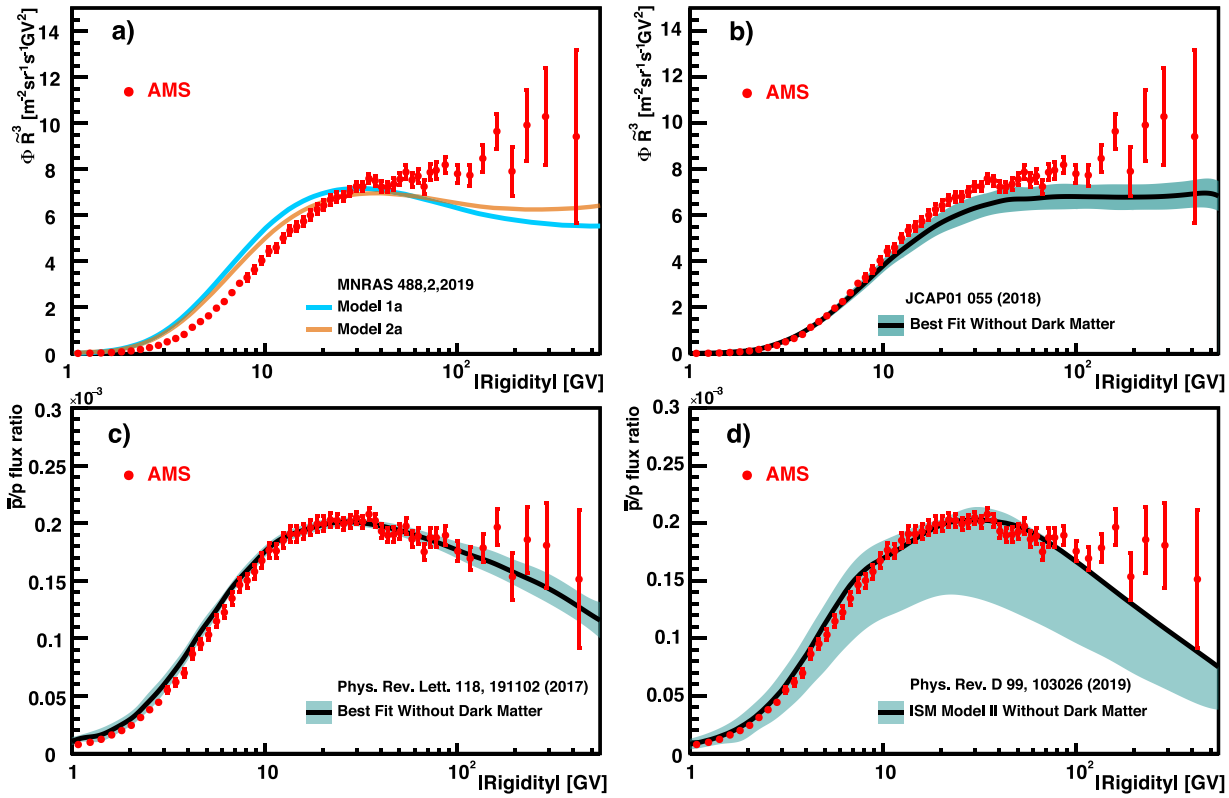

Fig. 62. (a), (b) The AMS antiproton spectrum and (c), (d) the antiproton-to-proton flux ratio (red data points) together with five recent theoretical models that include only collisions of cosmic rays (solid lines) [113,114]. In (a) the orange and blue solid lines show the same model predictions with two different sets of model assumptions. The uncertainties of the models in (b), (c) and (d) are indicated as blue bands.

through AMS, from L8 to L1 as shown in Fig. 70b and from L2 to L9 as shown in Fig. 70c. In either direction, particles were identified by their dE/dx in the seven inner tracker layers L2–L8 and their rigidities measured. The upper TOF and TRD are between L2–L8 and L1, see Fig. 70b. To measure the survival probability for nuclei to traverse this material, the charge distributions in L2–L8 and L1 are compared. Similarly, we measured the survival probability for nuclei to traverse the material from L8 to L9, the lower TOF and RICH, see Fig. 70c. The survival probabilities from L8 to L9 have also been measured during AMS nominal ISS orientation. The small ($<$ 3%) interaction probability between tracker L2 and L8 was calculated by comparing the charge measurements between the upper and the lower TOF. It is combined with survival probabilities from L1 to L2 and from L8 to L9 to obtain the survival probabilities from L1 to L9.

To accurately determine the interaction cross section, dedicated Monte Carlo event samples were simulated with the Glauber–Gribov model inelastic cross sections varied by $\pm$10%. Then, the survival probabilities between L2 and L1 and between L8 and L9 were compared between our measurements and the simulation. The cross section value which agrees best with our measurement was chosen.

The comparison of measured survival probabilities between our measurements and simulations as a function of rigidity is shown in Fig. 71 for He nuclei. As seen, there is a few percent discrepancy between our measurements and simulation survival probabilities at low rigidities, below $\sim$ 30 GV. We have, therefore, additionally modified the GEANT4 Glauber–Gribov model to match the AMS data over the entire rigidity range [119].

Fig. 72 shows the AMS result of the He+C cross section as a function of rigidity together with the original GEANT4 Glauber–Gribov model and measurements from ground-based accelerators.

Similarly, we have measured the survival probabilities for Li, Be, B, C, N, O, Ne, Mg, and Si nuclei. Measurements for other nuclei are in progress. Below 30 GV, the rigidity dependence of the measured He inelastic cross section is used to modify the Glauber–Gribov model for the description of the heavy nuclei inelastic cross sections.

Fig. 73 shows the comparison of the survival probabilities for carbon and oxygen between the simulation and the data. Most importantly, AMS is able to measure interaction cross sections that could not be measured in accelerators.

Fig. 74 shows the measured cross sections of He, Li, Be, B, C, N, O, Ne, Mg, and Si nuclei on carbon averaged from 5 to 100 GV. In this rigidity range the AMS measurements show that the inelastic cross section is constant within our accuracy [119]. Note that, except for the helium-on-carbon and carbon-on-carbon cross sections, no other measurements exist.

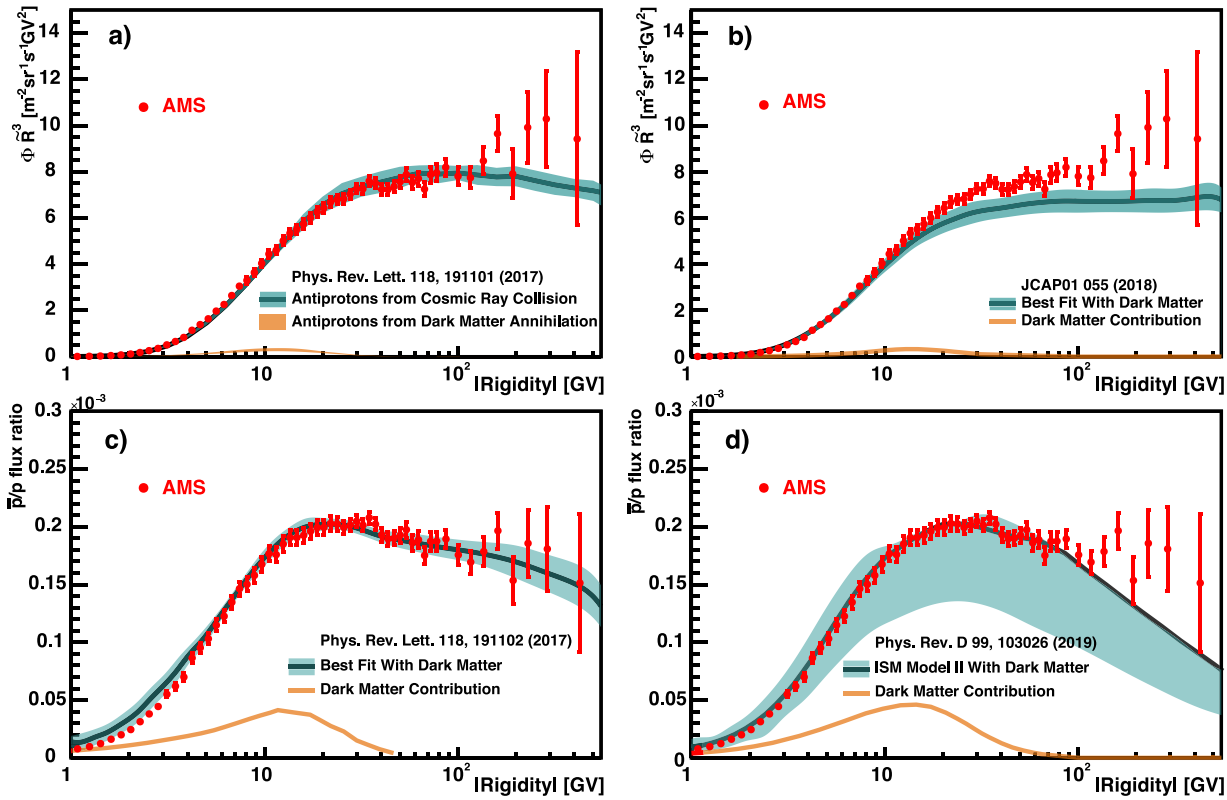

Fig. 63. (a), (b) The AMS antiproton spectrum and (c), (d) the antiproton-to-proton flux ratio (red data points) together with four recent theoretical models (black lines), their uncertainties (blue bands), and the contributions from dark matter annihilation (yellow lines) [114,115].

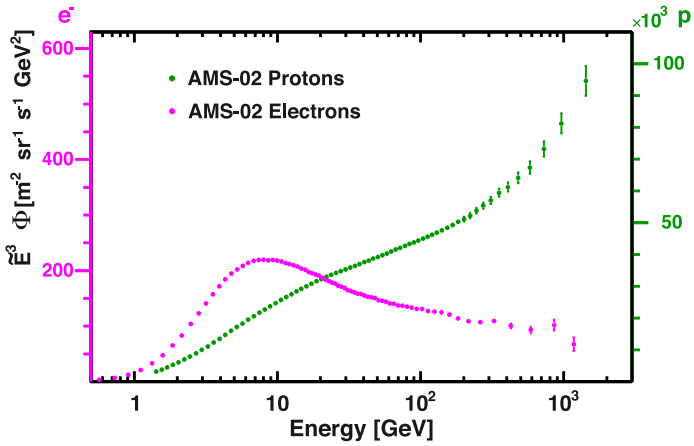

Fig. 64. The measured proton spectrum ($\tilde{E}^3\Phi_p$, green, right axis) compared to the electron spectrum ($\tilde{E}^3\Phi_{e^-}$, purple, left axis) - converted from measured rigidity to total energy for protons. The electron spectrum shows a distinctly different behavior from the proton spectrum over the entire energy range.

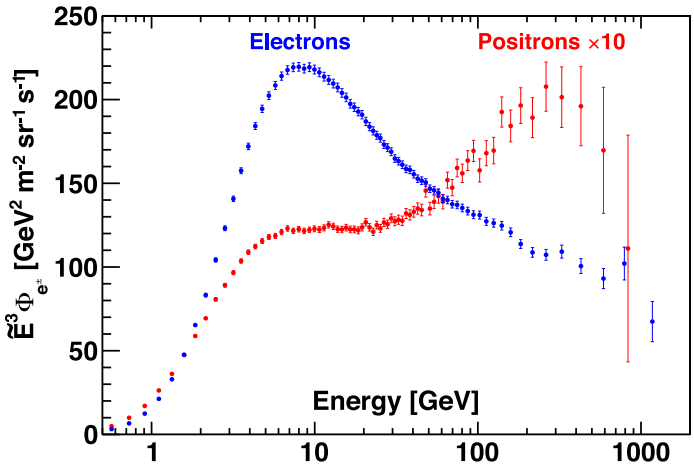

Fig. 65. The measured positron spectrum ($\tilde{E}^3\Phi_{e^+}$, red data points multiplied by 10) compared to the electron spectrum ($\tilde{E}^3\Phi_{e^-}$, blue data points). For display purposes the electron data point at ∼830 GeV is slightly shifted horizontally to avoid overlap with the positron point. As seen, the positron spectrum has distinctly different magnitude and energy dependence compared to that of electrons.

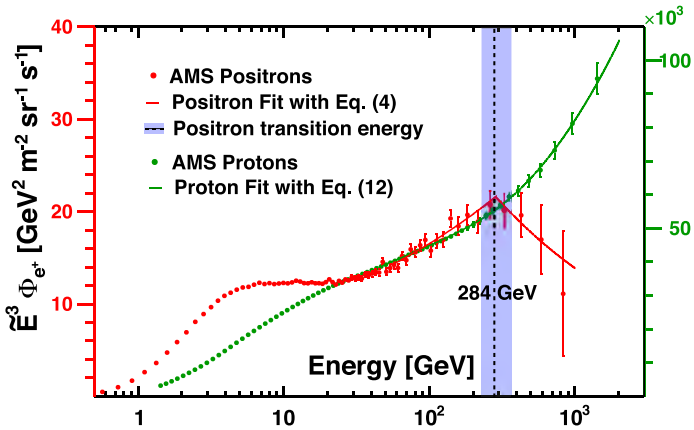

Fig. 66. The positron ($\tilde{E}^3\Phi_{e^+}$, red data points, left axis) and proton ($\tilde{E}^3\Phi_p$, green data points, right axis) spectra. Also shown are the fits of Eq. (4) to positron data and Eq. (12) to proton data. The dashed vertical line and the blue band show the positron transition energy and its uncertainty (see Section 2).

8. Primary helium, carbon, and oxygen fluxes

Primary cosmic rays are believed to be mainly produced by galactic sources such as supernova remnants. Precise knowledge of their spectra in the GV-TV rigidity region provides important information on the origin, acceleration, and subsequent propagation processes of cosmic rays in the Galaxy. Helium, carbon, and oxygen are among the most abundant primary cosmic ray nuclei.

Over the last 30 years, there have been many measurements of helium, carbon and oxygen fluxes. Typically, these measurements have errors larger than 15% at 50 GeV/n. Fig. 75 shows a summary of the most recent measurements before AMS [103]. As seen, the data are not always consistent with each other.

We report the precise measurements of the helium, carbon, and oxygen fluxes in cosmic rays in the rigidity range from 1.9 GV to 3 TV for helium and carbon, and 2.2 GV to 3 TV for oxygen based on data collected by AMS (Tables 7, 8, 9, 10, and 11). The total error is ∼3% at 100 GV for both the carbon and oxygen fluxes and ∼1.5% at 100 GV for the helium flux. The measurements are based on 125 million helium, 14 million carbon and 12 million oxygen nuclei. These new AMS results are consistent with the earlier AMS measurements [120] but have smaller statistical and systematic errors.

Fig. 76 shows the AMS results on the helium, carbon, and oxygen spectra. $\tilde{R}$ is the spectrally weighted mean rigidity for a flux proportional to $R^{-2.7}$. As seen, above 60 GV all the three spectra have identical rigidity dependence. In particular, they all deviate from a single power law and harden progressively from ∼200 GV.

To examine the rigidity dependence of the fluxes, the variation of the flux spectral indices with rigidity was obtained in a model independent way. The flux spectral indices γ were calculated from Eq. (13) over non-overlapping rigidity

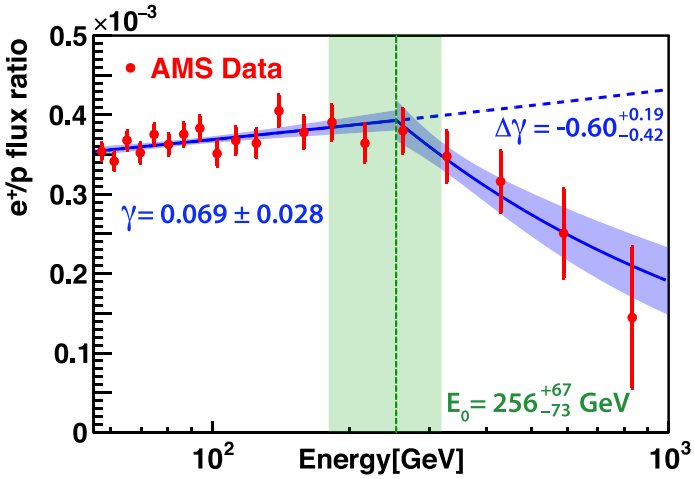

Fig. 67. The ratio of the positron-to-proton fluxes (red data points) together with the fit of Eq. (4) in the energy range [55.58 – 1000] GeV (blue line with 68% C.L. band). As seen, the ratio is rising in the range [55.58 – 256] GeV and decreasing in the range [256 – 1000] GeV. The values of the fit parameters γ and $\Delta\gamma$ are shown in the plot together with the transition energy E_0 and its uncertainty (the vertical green dashed line and the green band). The dashed blue line shows extrapolation of the fitted power law function in the range [55.58 – 256] GeV to higher energies.

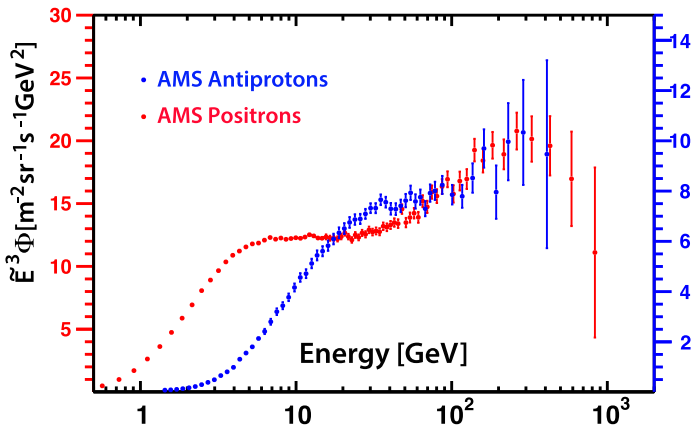

Fig. 68. Comparison of the AMS positron ($\tilde{E}^3\Phi_{e^+}$, red data points, left axis) and antiproton ($\tilde{E}^3\Phi_{\bar{p}}$, blue data points, right axis) spectra. As seen, the AMS antiproton data show nearly identical energy dependence as positrons at high energies.

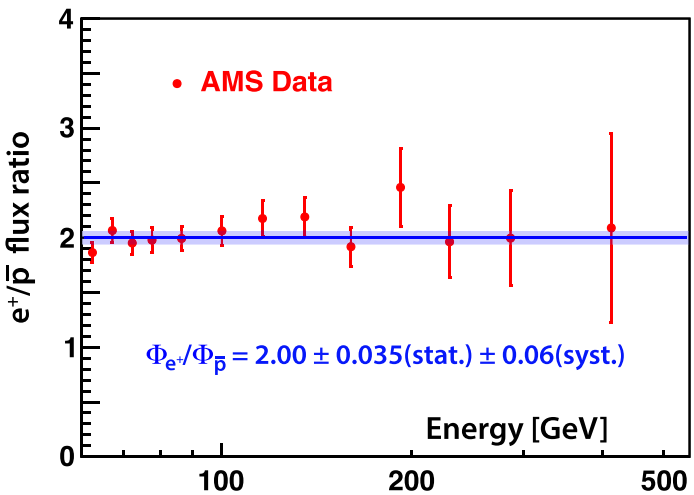

Fig. 69. The ratio of the positron-to-antiproton fluxes (red data points) together with the fit of the constant function to data in the energy range [60 – 525] GeV (blue line with 68% C.L. band).

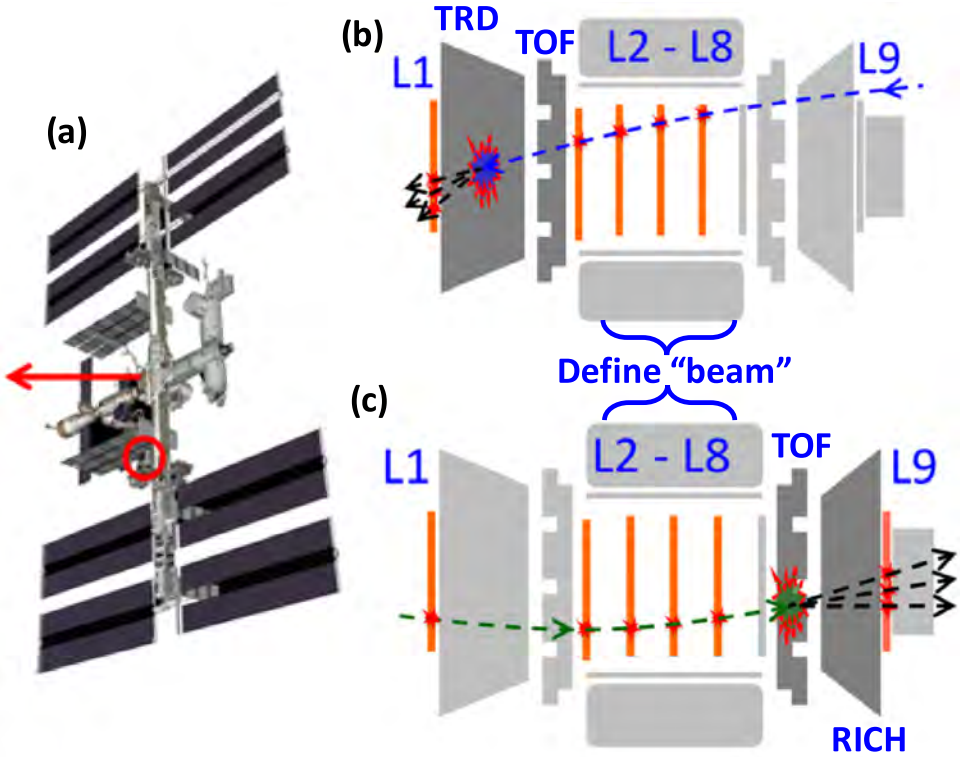

Fig. 70. (a) Schematic of AMS flying horizontally. (b) Illustration of the L2 to L1 nuclei survival probability measurement in the AMS materials of upper TOF and TRD. (c) Illustration of the L8 to L9 nuclei survival probability measurement in the AMS materials of lower TOF and RICH. Note, that both in (b) and (c) we use L2–L8, located inside the magnet and marked "Define beam" in the figures, to identify particles and to measure their rigidities.

intervals above 8.48 GV. The intervals have a variable width to have sufficient sensitivity to determine γ. The results are presented in Fig. 77. As seen, the magnitude and the rigidity dependence of the helium, carbon, and oxygen spectral indices are very similar. In particular, all spectral indices are identical above 60 GV and all spectral indices harden with rigidity above ∼200 GV.

These surprising results are illustrated more clearly in Fig. 78, which shows that the three spectra have identical rigidity dependence above 60 GV. These observations have generated new developments in cosmic ray models [121,122]. The theoretical models have their limitations, as none of them predicted the observed spectral behavior of the cosmic rays presented in this Section.

In conclusion, the high statistics measurements of the helium, carbon, and oxygen fluxes from ∼2 GV to 3 TV show that the fluxes deviate from a single power law. Their spectral indices all progressively harden above 200 GV. Unexpectedly, above 60 GV, the three spectra have identical rigidity dependence.

9. Proton-to-helium flux ratio

Protons and helium are both primary cosmic rays. Traditionally, in models of diffusive-shock-acceleration, they are assumed to be produced in the same sources with the identical power law spectra, so their rigidity dependence should be the same [123]. In absence of the precision data on the proton and helium fluxes, various models of cosmic ray acceleration and diffusion mechanisms were proposed, that lead to different behavior of the proton and helium fluxes [124]. These mechanisms, based on cosmic ray acceleration, predict that the proton-to-helium ratio is decreasing steadily with rigidity, from sub-GV to multi-TV. Other, more complex models [125], predict that the proton-to-helium ratio is decreasing in the range from ∼10 GV to ∼1000 GV and flattens asymptotically above 1000 GV, where the energy losses are negligible.

It is interesting to compare the AMS data, collected at 1 a.u in the solar system, with the Voyager data [126], collected outside the solar system at >100 a.u. Fig. 79 presents both data sets in the rigidity range from 0.1 GV to 2 TV. As seen in Fig. 79 there is a smooth continuation of the ratio measured by AMS in the solar system to the Voyager measurements outside the solar system.

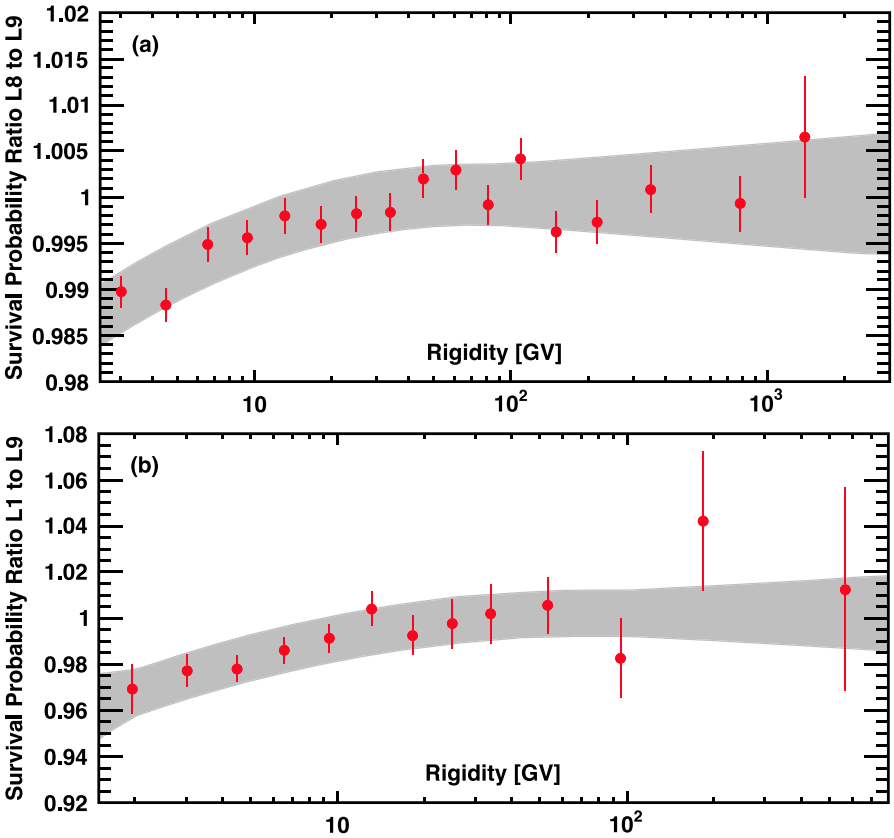

Fig. 71. Rigidity dependence of (a) the ratio of the simulation to the data of the He survival probabilities from L8 to L9 for particles traversing the lower TOF and RICH; (b) the ratio of the He survival probabilities from L1 to L9 for particles traversing the entire detector. In (a) and (b) the gray shaded area indicate the corresponding systematic errors.

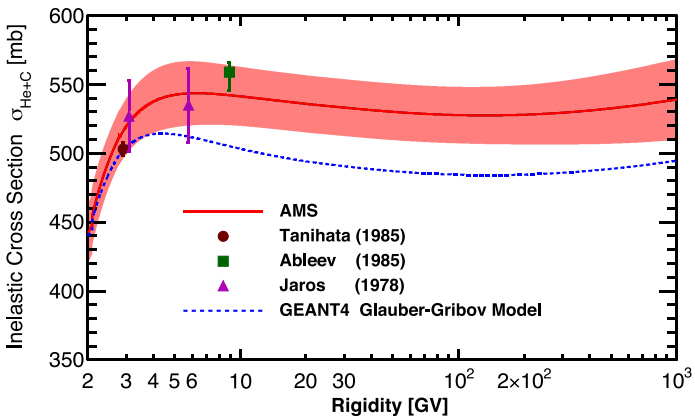

Fig. 72. The He+C cross section measured by AMS on the ISS as a function of rigidity (red curve) and its errors (light red band), together with the original GEANT4 Glauber–Gribov cross section model (blue curve) and measurements from ground-based accelerators (data points) [118].

Table 4
The combined (electron + positron) flux $\Phi_{e^-+e^+}$ in units of $[\mathrm{m}^2\,\mathrm{sr}\,\mathrm{s}\,\mathrm{GeV}]^{-1}$ as a function of the energy E at the top of AMS. Characteristic energy $\tilde{E}$ (i.e. spectrally weighted mean energy in the bin) is given with its systematic error from the energy scale uncertainty. $\sigma_{\mathrm{stat}}^{e^-+e^+}$ and $\sigma_{\mathrm{syst}}^{e^-+e^+}$ are the statistical error and the total systematic error of the combined (electron + positron) flux. The systematic errors account for correlations related to the calculation of the acceptance.

E [GeV]	$\tilde{E}$ [GeV]	$\Phi_{e^++e^-}$	σ_{stat}	σ_{syst}
0.50–0.65	0.57 ± 0.02	(1.945	0.038	0.117) $\times 10^{1}$
0.65–0.82	0.73 ± 0.02	(1.918	0.010	0.085) $\times 10^{1}$
0.82–1.01	0.91 ± 0.03	(1.839	0.006	0.060) $\times 10^{1}$
1.01–1.22	1.11 ± 0.03	(1.712	0.004	0.042) $\times 10^{1}$
1.22–1.46	1.33 ± 0.03	(1.511	0.003	0.029) $\times 10^{1}$
1.46–1.72	1.58 ± 0.04	(1.297	0.002	0.020) $\times 10^{1}$
1.72–2.00	1.85 ± 0.04	(1.106	0.001	0.015) $\times 10^{1}$
2.00–2.31	2.15 ± 0.05	(9.019	0.009	0.111) $\times 10^{0}$
2.31–2.65	2.47 ± 0.05	(7.380	0.007	0.085) $\times 10^{0}$
2.65–3.00	2.82 ± 0.06	(5.884	0.005	0.066) $\times 10^{0}$
3.00–3.36	3.17 ± 0.06	(4.696	0.004	0.052) $\times 10^{0}$
3.36–3.73	3.54 ± 0.07	(3.771	0.003	0.042) $\times 10^{0}$
3.73–4.12	3.92 ± 0.08	(3.029	0.003	0.033) $\times 10^{0}$
4.12–4.54	4.32 ± 0.08	(2.411	0.002	0.027) $\times 10^{0}$
4.54–5.00	4.76 ± 0.09	(1.901	0.002	0.021) $\times 10^{0}$
5.00–5.49	5.24 ± 0.10	(1.488	0.001	0.017) $\times 10^{0}$
5.49–6.00	5.74 ± 0.11	(1.165	0.001	0.013) $\times 10^{0}$
6.00–6.54	6.26 ± 0.12	(9.216	0.009	0.106) $\times 10^{-1}$
6.54–7.10	6.81 ± 0.13	(7.281	0.008	0.084) $\times 10^{-1}$
7.10–7.69	7.39 ± 0.14	(5.755	0.007	0.067) $\times 10^{-1}$
7.69–8.30	7.99 ± 0.15	(4.555	0.006	0.054) $\times 10^{-1}$
8.30–8.95	8.62 ± 0.16	(3.609	0.005	0.043) $\times 10^{-1}$
8.95–9.62	9.28 ± 0.18	(2.904	0.004	0.035) $\times 10^{-1}$
9.62–10.32	9.96 ± 0.19	(2.334	0.003	0.028) $\times 10^{-1}$
10.32–11.04	10.67 ± 0.20	(1.881	0.003	0.023) $\times 10^{-1}$
11.04–11.80	11.41 ± 0.22	(1.524	0.003	0.019) $\times 10^{-1}$
11.80–12.59	12.19 ± 0.23	(1.239	0.002	0.015) $\times 10^{-1}$
12.59–13.41	12.99 ± 0.25	(1.012	0.002	0.013) $\times 10^{-1}$
13.41–14.25	13.82 ± 0.26	(8.313	0.016	0.103) $\times 10^{-2}$
14.25–15.14	14.69 ± 0.28	(6.827	0.014	0.086) $\times 10^{-2}$
15.14–16.05	15.59 ± 0.29	(5.628	0.012	0.071) $\times 10^{-2}$
16.05–17.00	16.52 ± 0.31	(4.640	0.011	0.059) $\times 10^{-2}$
17.00–17.98	17.48 ± 0.33	(3.878	0.009	0.049) $\times 10^{-2}$
17.98–18.99	18.48 ± 0.35	(3.246	0.008	0.042) $\times 10^{-2}$
18.99–20.04	19.51 ± 0.37	(2.731	0.007	0.035) $\times 10^{-2}$
20.04–21.13	20.58 ± 0.39	(2.283	0.006	0.030) $\times 10^{-2}$
21.13–22.25	21.68 ± 0.41	(1.915	0.006	0.025) $\times 10^{-2}$
22.25–23.42	22.83 ± 0.43	(1.620	0.005	0.021) $\times 10^{-2}$
23.42–24.62	24.01 ± 0.45	(1.375	0.004	0.018) $\times 10^{-2}$
24.62–25.90	25.25 ± 0.48	(1.170	0.004	0.015) $\times 10^{-2}$
25.90–27.25	26.56 ± 0.50	(9.860	0.035	0.130) $\times 10^{-3}$
27.25–28.68	27.95 ± 0.53	(8.380	0.031	0.111) $\times 10^{-3}$
28.68–30.21	29.43 ± 0.56	(7.084	0.028	0.094) $\times 10^{-3}$
30.21–31.82	31.00 ± 0.59	(5.910	0.025	0.079) $\times 10^{-3}$
31.82–33.53	32.66 ± 0.62	(5.028	0.022	0.067) $\times 10^{-3}$
33.53–35.36	34.43 ± 0.65	(4.232	0.020	0.057) $\times 10^{-3}$
35.36–37.31	36.32 ± 0.69	(3.564	0.017	0.048) $\times 10^{-3}$
37.31–39.39	38.33 ± 0.72	(3.016	0.015	0.041) $\times 10^{-3}$
39.39–41.61	40.48 ± 0.77	(2.521	0.014	0.034) $\times 10^{-3}$
41.61–44.00	42.78 ± 0.81	(2.105	0.012	0.029) $\times 10^{-3}$
44.00–46.57	45.26 ± 0.86	(1.769	0.011	0.024) $\times 10^{-3}$
46.57–49.33	47.92 ± 0.91	(1.491	0.009	0.020) $\times 10^{-3}$
49.33–52.33	50.80 ± 0.96	(1.216	0.008	0.017) $\times 10^{-3}$
52.33–55.58	53.92 ± 1.02	(1.008	0.007	0.014) $\times 10^{-3}$
55.58–59.13	57.32 ± 1.08	(8.324	0.063	0.113) $\times 10^{-4}$
59.13–63.02	61.03 ± 1.16	(6.752	0.054	0.092) $\times 10^{-4}$
63.02–67.30	65.11 ± 1.23	(5.541	0.047	0.076) $\times 10^{-4}$
67.30–72.05	69.62 ± 1.32	(4.524	0.040	0.062) $\times 10^{-4}$
72.05–77.37	74.65 ± 1.41	(3.637	0.034	0.050) $\times 10^{-4}$

(*continued on next page*)

Table 4 (*continued*).

E [GeV]	$\tilde{E}$ [GeV]	$\Phi_{e^+ + e^-}$	σ_{stat}	σ_{syst}
77.37–83.36	80.29 ± 1.52	(2.883	0.029	0.040) $\times 10^{-4}$
83.36–90.19	86.69 ± 1.64	(2.273	0.024	0.031) $\times 10^{-4}$
90.19–98.08	94.02 ± 1.78	(1.765	0.020	0.024) $\times 10^{-4}$
98.08–107.3	102.6 ± 1.9	(1.349	0.016	0.019) $\times 10^{-4}$
107.3–118.4	112.7 ± 2.1	(9.853	0.124	0.137) $\times 10^{-5}$
118.4–132.1	125.0 ± 2.4	(7.197	0.096	0.100) $\times 10^{-5}$
132.1–148.8	140.1 ± 2.7	(5.220	0.075	0.073) $\times 10^{-5}$
148.8–169.9	158.9 ± 3.0	(3.492	0.055	0.050) $\times 10^{-5}$
169.9–197.7	183.1 ± 3.5	(2.166	0.039	0.029) $\times 10^{-5}$
197.7–237.2	216.2 ± 4.2	(1.289	0.026	0.022) $\times 10^{-5}$
237.2–290.0	261.8 ± 5.1	(7.285	0.166	0.118) $\times 10^{-6}$
290.0–370.0	326.8 ± 6.4	(3.705	0.098	0.076) $\times 10^{-6}$
370.0–500.0	428.5 ± 8.6	(1.539	0.053	0.034) $\times 10^{-6}$
500.0–700.0	588.8 ± 12.2	(5.586	0.273	0.184) $\times 10^{-7}$
700.0–1000.0	832.3 ± 18.3	(1.877	0.144	0.123) $\times 10^{-7}$
1000.0–1400.0	1177.7 ± 28.6	(4.786	0.741	0.437) $\times 10^{-8}$
1400.0–2000.0	1664.5 ± 46.7	(1.216	0.401	0.283) $\times 10^{-8}$

Table 5
The Proton flux Φ_p as a function of rigidity at the top of AMS in units of $[\text{m}^2\,\text{sr}\,\text{s}\,\text{GV}]^{-1}$ including errors due to statistics (σ_{stat}); contributions to the systematic error from the trigger and acceptance (σ_{acc}); the rigidity resolution function and unfolding (σ_{unf}); the absolute rigidity scale (σ_{scale}); and the total systematic error (σ_{syst}). The contribution of individual sources to the systematic error are added in quadrature to arrive at the total systematic error.

Rigidity [GV]	Φ_p	σ_{stat}	σ_{acc}	σ_{unf}	σ_{scale}	σ_{syst}
1.00–1.16	(8.247	0.004	0.091	0.081	0.030	0.125) $\times 10^2$
1.16–1.33	(7.986	0.003	0.087	0.055	0.018	0.105) $\times 10^2$
1.33–1.51	(7.601	0.002	0.082	0.037	0.010	0.090) $\times 10^2$
1.51–1.71	(7.055	0.002	0.076	0.025	0.005	0.080) $\times 10^2$
1.71–1.92	(6.398	0.001	0.068	0.019	0.001	0.071) $\times 10^2$
1.92–2.15	(5.672	0.001	0.060	0.016	0.002	0.062) $\times 10^2$
2.15–2.40	(4.933	0.001	0.052	0.014	0.004	0.054) $\times 10^2$
2.40–2.67	(4.248	0.001	0.044	0.013	0.005	0.046) $\times 10^2$
2.67–2.97	(3.619	0.001	0.037	0.012	0.005	0.040) $\times 10^2$
2.97–3.29	(3.062	0.001	0.031	0.010	0.005	0.033) $\times 10^2$
3.29–3.64	(2.571	0.000	0.026	0.009	0.005	0.028) $\times 10^2$
3.64–4.02	(2.145	0.000	0.022	0.008	0.005	0.023) $\times 10^2$
4.02–4.43	(1.779	0.000	0.018	0.006	0.004	0.019) $\times 10^2$
4.43–4.88	(1.465	0.000	0.015	0.005	0.004	0.016) $\times 10^2$
4.88–5.37	(1.197	0.000	0.012	0.004	0.003	0.013) $\times 10^2$
5.37–5.90	(9.729	0.002	0.094	0.035	0.027	0.104) $\times 10^1$
5.90–6.47	(7.883	0.001	0.075	0.028	0.023	0.084) $\times 10^1$
6.47–7.09	(6.371	0.001	0.060	0.023	0.019	0.067) $\times 10^1$
7.09–7.76	(5.138	0.001	0.048	0.018	0.016	0.054) $\times 10^1$
7.76–8.48	(4.139	0.001	0.038	0.015	0.014	0.043) $\times 10^1$
8.48–9.26	(3.331	0.001	0.030	0.012	0.011	0.034) $\times 10^1$
9.26–10.1	(2.679	0.000	0.023	0.010	0.009	0.027) $\times 10^1$
10.1–11.0	(2.155	0.000	0.018	0.008	0.008	0.021) $\times 10^1$
11.0–12.0	(1.731	0.000	0.014	0.006	0.006	0.017) $\times 10^1$
12.0–13.0	(1.395	0.000	0.011	0.005	0.005	0.014) $\times 10^1$
13.0–14.1	(1.132	0.000	0.009	0.004	0.004	0.011) $\times 10^1$
14.1–15.3	(9.141	0.002	0.070	0.035	0.035	0.086) $\times 10^0$
15.3–16.6	(7.363	0.002	0.054	0.029	0.029	0.068) $\times 10^0$
16.6–18.0	(5.929	0.001	0.042	0.024	0.024	0.054) $\times 10^0$
18.0–19.5	(4.774	0.001	0.032	0.020	0.019	0.042) $\times 10^0$
19.5–21.1	(3.850	0.001	0.026	0.016	0.016	0.034) $\times 10^0$
21.1–22.8	(3.110	0.001	0.021	0.014	0.013	0.028) $\times 10^0$
22.8–24.7	(2.506	0.001	0.017	0.011	0.011	0.023) $\times 10^0$
24.7–26.7	(2.013	0.001	0.013	0.009	0.009	0.018) $\times 10^0$
26.7–28.8	(1.628	0.000	0.011	0.008	0.007	0.015) $\times 10^0$

(*continued on next page*)

Table 5 (*continued*).

Rigidity [GV]	Φ_p	σ_{stat}	σ_{acc}	σ_{unf}	σ_{scale}	σ_{syst}
28.8–31.1	(1.316	0.000	0.009	0.006	0.006	0.012) $\times 10^{0}$
31.1–33.5	(1.066	0.000	0.007	0.005	0.005	0.010) $\times 10^{0}$
33.5–36.1	(8.649	0.003	0.057	0.045	0.038	0.082) $\times 10^{-1}$
36.1–38.9	(7.018	0.003	0.046	0.038	0.031	0.068) $\times 10^{-1}$
38.9–41.9	(5.702	0.002	0.038	0.032	0.026	0.056) $\times 10^{-1}$
41.9–45.1	(4.637	0.002	0.031	0.027	0.021	0.046) $\times 10^{-1}$
45.1–48.5	(3.775	0.002	0.025	0.022	0.017	0.038) $\times 10^{-1}$
48.5–52.2	(3.074	0.002	0.020	0.019	0.014	0.031) $\times 10^{-1}$
52.2–56.1	(2.508	0.001	0.017	0.016	0.012	0.026) $\times 10^{-1}$
56.1–60.3	(2.048	0.001	0.014	0.013	0.010	0.021) $\times 10^{-1}$
60.3–64.8	(1.674	0.001	0.011	0.011	0.008	0.018) $\times 10^{-1}$
64.8–69.7	(1.369	0.001	0.009	0.009	0.007	0.015) $\times 10^{-1}$
69.7–74.9	(1.116	0.001	0.007	0.008	0.005	0.012) $\times 10^{-1}$
74.9–80.5	(9.124	0.007	0.061	0.066	0.045	0.101) $\times 10^{-2}$
80.5–86.5	(7.445	0.006	0.050	0.056	0.037	0.084) $\times 10^{-2}$
86.5–93.0	(6.067	0.005	0.041	0.047	0.031	0.069) $\times 10^{-2}$
93.0–100	(4.951	0.005	0.034	0.039	0.026	0.058) $\times 10^{-2}$
100–108	(4.009	0.004	0.027	0.032	0.021	0.048) $\times 10^{-2}$
108–116	(3.253	0.003	0.022	0.027	0.018	0.039) $\times 10^{-2}$
116–125	(2.647	0.003	0.018	0.023	0.015	0.033) $\times 10^{-2}$
125–135	(2.137	0.003	0.015	0.019	0.013	0.027) $\times 10^{-2}$
135–147	(1.702	0.002	0.012	0.016	0.011	0.022) $\times 10^{-2}$
147–160	(1.341	0.002	0.009	0.013	0.009	0.018) $\times 10^{-2}$
160–175	(1.052	0.001	0.008	0.010	0.007	0.015) $\times 10^{-2}$
175–192	(8.166	0.012	0.059	0.084	0.059	0.118) $\times 10^{-3}$
192–211	(6.269	0.010	0.046	0.068	0.047	0.095) $\times 10^{-3}$
211–233	(4.790	0.008	0.036	0.055	0.038	0.076) $\times 10^{-3}$
233–259	(3.627	0.006	0.027	0.044	0.031	0.061) $\times 10^{-3}$
259–291	(2.674	0.005	0.021	0.035	0.025	0.048) $\times 10^{-3}$
291–330	(1.914	0.004	0.015	0.027	0.019	0.037) $\times 10^{-3}$
330–379	(1.343	0.003	0.011	0.021	0.015	0.028) $\times 10^{-3}$
379–441	(8.957	0.020	0.075	0.157	0.114	0.208) $\times 10^{-4}$
441–525	(5.752	0.014	0.050	0.113	0.083	0.149) $\times 10^{-4}$
525–643	(3.432	0.009	0.031	0.075	0.058	0.100) $\times 10^{-4}$
643–822	(1.905	0.006	0.019	0.046	0.039	0.063) $\times 10^{-4}$
822–1130	(9.068	0.029	0.096	0.236	0.241	0.351) $\times 10^{-5}$
1130–1800	(3.260	0.012	0.039	0.091	0.127	0.160) $\times 10^{-5}$

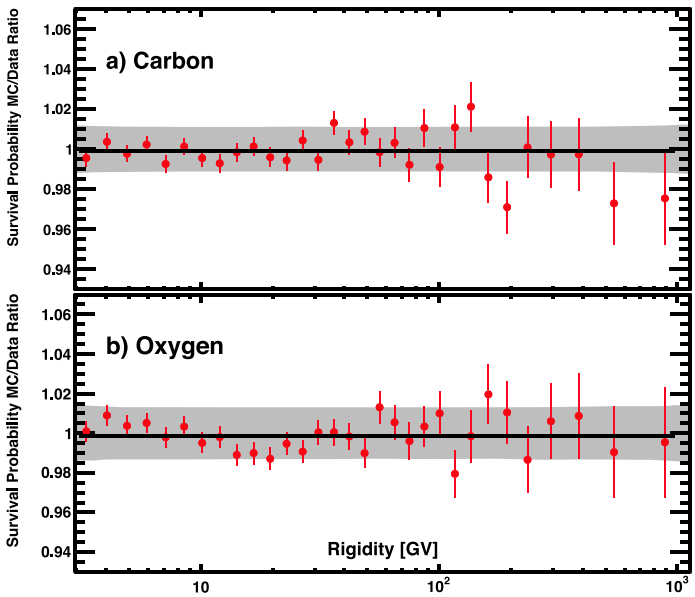

Fig. 73. The survival probability ratio of the Monte Carlo simulation to our measured data for (a) carbon and (b) oxygen when traversing the lower TOF and RICH. The solid black lines show fits to the data points and the gray shaded areas indicate the corresponding systematic error ranges (68% C.L.).

Table 6
The $\bar{p}$ flux $\Phi_{\bar{p}}$ in units of $[\mathrm{m}^2\,\mathrm{sr}\,\mathrm{s}\,\mathrm{GV}]^{-1}$ and the $(\bar{p}/p)$ flux ratio $\Phi_{\bar{p}}/\Phi_p$ as a function of absolute rigidity at the top of AMS. $\tilde{N}_{\bar{p}}$ is the number of antiprotons observed in each rigidity bin rounded to the nearest integer. σ_{stat} and σ_{syst} are the respective statistical and systematic errors.

Rigidity [GV]	$\tilde{N}_{\bar{p}}$	$\Phi_{\bar{p}}$	σ_{stat}	σ_{syst}	$\Phi_{\bar{p}}/\Phi_p$	σ_{stat}	σ_{syst}
1.00–1.16	69	(6.41	0.85	0.57) $\times 10^{-3}$	(7.78	1.04	0.59) $\times 10^{-6}$
1.16–1.33	159	(7.78	0.64	0.61) $\times 10^{-3}$	(9.70	0.80	0.63) $\times 10^{-6}$
1.33–1.51	324	(9.29	0.60	0.63) $\times 10^{-3}$	(1.23	0.08	0.07) $\times 10^{-5}$
1.51–1.71	1027	(1.11	0.04	0.07) $\times 10^{-2}$	(1.61	0.06	0.08) $\times 10^{-5}$
1.71–1.92	1609	(1.25	0.04	0.07) $\times 10^{-2}$	(1.99	0.06	0.10) $\times 10^{-5}$
1.92–2.15	2285	(1.36	0.04	0.07) $\times 10^{-2}$	(2.45	0.07	0.12) $\times 10^{-5}$
2.15–2.40	3185	(1.52	0.04	0.08) $\times 10^{-2}$	(3.13	0.08	0.15) $\times 10^{-5}$
2.40–2.67	4792	(1.60	0.03	0.08) $\times 10^{-2}$	(3.80	0.08	0.19) $\times 10^{-5}$
2.67–2.97	6805	(1.59	0.03	0.08) $\times 10^{-2}$	(4.44	0.08	0.21) $\times 10^{-5}$
2.97–3.29	9281	(1.67	0.03	0.08) $\times 10^{-2}$	(5.50	0.09	0.26) $\times 10^{-5}$
3.29–3.64	10888	(1.58	0.03	0.08) $\times 10^{-2}$	(6.20	0.10	0.29) $\times 10^{-5}$
3.64–4.02	12681	(1.48	0.03	0.07) $\times 10^{-2}$	(6.99	0.13	0.31) $\times 10^{-5}$
4.02–4.43	3553	(1.52	0.03	0.07) $\times 10^{-2}$	(8.64	0.15	0.38) $\times 10^{-5}$
4.43–4.88	4670	(1.38	0.02	0.06) $\times 10^{-2}$	(9.52	0.14	0.41) $\times 10^{-5}$
4.88–5.37	6051	(1.22	0.02	0.05) $\times 10^{-2}$	(1.03	0.01	0.04) $\times 10^{-4}$
5.37–5.90	8541	(1.11	0.01	0.05) $\times 10^{-2}$	(1.15	0.01	0.05) $\times 10^{-4}$
5.90–6.47	9703	(9.57	0.10	0.41) $\times 10^{-3}$	(1.23	0.01	0.05) $\times 10^{-4}$
6.47–7.09	10734	(8.52	0.08	0.36) $\times 10^{-3}$	(1.35	0.01	0.05) $\times 10^{-4}$
7.09–7.76	11154	(7.48	0.07	0.31) $\times 10^{-3}$	(1.46	0.01	0.06) $\times 10^{-4}$
7.76–8.48	12023	(6.18	0.06	0.25) $\times 10^{-3}$	(1.50	0.01	0.06) $\times 10^{-4}$
8.48–9.26	12426	(5.23	0.05	0.21) $\times 10^{-3}$	(1.58	0.01	0.06) $\times 10^{-4}$
9.26–10.1	38386	(4.47	0.02	0.17) $\times 10^{-3}$	(1.67	0.01	0.06) $\times 10^{-4}$
10.1–11.0	37058	(3.79	0.02	0.14) $\times 10^{-3}$	(1.77	0.01	0.06) $\times 10^{-4}$
11.0–12.0	34784	(3.04	0.02	0.11) $\times 10^{-3}$	(1.76	0.01	0.06) $\times 10^{-4}$
12.0–13.0	28535	(2.57	0.02	0.09) $\times 10^{-3}$	(1.85	0.01	0.07) $\times 10^{-4}$
13.0–14.1	26843	(2.15	0.01	0.08) $\times 10^{-3}$	(1.91	0.01	0.07) $\times 10^{-4}$
14.1–15.3	24428	(1.74	0.01	0.06) $\times 10^{-3}$	(1.91	0.01	0.07) $\times 10^{-4}$
15.3–16.6	24120	(1.42	0.01	0.05) $\times 10^{-3}$	(1.93	0.01	0.06) $\times 10^{-4}$
16.6–18.0	23238	(1.16	0.01	0.04) $\times 10^{-3}$	(1.96	0.01	0.06) $\times 10^{-4}$
18.0–19.5	22957	(9.52	0.07	0.32) $\times 10^{-4}$	(1.99	0.01	0.06) $\times 10^{-4}$
19.5–21.1	20227	(7.71	0.06	0.25) $\times 10^{-4}$	(1.99	0.01	0.06) $\times 10^{-4}$
21.1–22.8	19126	(6.33	0.05	0.20) $\times 10^{-4}$	(2.03	0.02	0.06) $\times 10^{-4}$
22.8–24.7	18338	(5.09	0.04	0.15) $\times 10^{-4}$	(2.02	0.02	0.06) $\times 10^{-4}$
24.7–26.7	17664	(4.03	0.03	0.11) $\times 10^{-4}$	(1.99	0.02	0.05) $\times 10^{-4}$
26.7–28.8	14463	(3.30	0.03	0.09) $\times 10^{-4}$	(2.01	0.02	0.05) $\times 10^{-4}$
28.8–31.1	13035	(2.71	0.02	0.07) $\times 10^{-4}$	(2.05	0.02	0.05) $\times 10^{-4}$
31.1–33.5	12207	(2.16	0.02	0.06) $\times 10^{-4}$	(2.01	0.02	0.05) $\times 10^{-4}$
33.5–36.1	11756	(1.81	0.02	0.05) $\times 10^{-4}$	(2.08	0.02	0.05) $\times 10^{-4}$
36.1–38.9	9681	(1.43	0.02	0.04) $\times 10^{-4}$	(2.02	0.02	0.05) $\times 10^{-4}$
38.9–41.9	3477	(1.10	0.02	0.03) $\times 10^{-4}$	(1.93	0.03	0.05) $\times 10^{-4}$
41.9–45.1	3299	(8.80	0.16	0.24) $\times 10^{-5}$	(1.90	0.03	0.05) $\times 10^{-4}$
45.1–48.5	2742	(7.19	0.14	0.20) $\times 10^{-5}$	(1.90	0.04	0.05) $\times 10^{-4}$
48.5–52.2	2341	(5.94	0.13	0.16) $\times 10^{-5}$	(1.93	0.04	0.05) $\times 10^{-4}$
52.2–56.1	2117	(4.97	0.11	0.14) $\times 10^{-5}$	(1.97	0.05	0.05) $\times 10^{-4}$
56.1–60.3	1840	(3.83	0.10	0.11) $\times 10^{-5}$	(1.86	0.05	0.05) $\times 10^{-4}$
60.3–64.8	1606	(3.16	0.08	0.09) $\times 10^{-5}$	(1.89	0.05	0.05) $\times 10^{-4}$
64.8–69.7	1426	(2.39	0.07	0.07) $\times 10^{-5}$	(1.75	0.05	0.05) $\times 10^{-4}$
69.7–74.9	1200	(2.09	0.07	0.06) $\times 10^{-5}$	(1.87	0.06	0.05) $\times 10^{-4}$
74.9–80.5	1133	(1.70	0.06	0.05) $\times 10^{-5}$	(1.87	0.06	0.06) $\times 10^{-4}$
80.5–93.0	1557	(1.27	0.04	0.04) $\times 10^{-5}$	(1.89	0.05	0.06) $\times 10^{-4}$
93–108	1319	(7.77	0.26	0.29) $\times 10^{-6}$	(1.76	0.06	0.06) $\times 10^{-4}$
108–125	1031	(4.94	0.21	0.21) $\times 10^{-6}$	(1.69	0.07	0.07) $\times 10^{-4}$
125–147	890	(3.41	0.17	0.16) $\times 10^{-6}$	(1.79	0.09	0.08) $\times 10^{-4}$
147–175	833	(2.34	0.13	0.13) $\times 10^{-6}$	(1.97	0.11	0.11) $\times 10^{-4}$
175–211	119	(1.12	0.12	0.09) $\times 10^{-6}$	(1.53	0.16	0.13) $\times 10^{-4}$
211–250	84	(8.21	1.04	0.73) $\times 10^{-7}$	(1.86	0.24	0.16) $\times 10^{-4}$
250–330	77	(4.37	0.70	0.55) $\times 10^{-7}$	(1.81	0.29	0.23) $\times 10^{-4}$
330–525	63	(1.33	0.36	0.39) $\times 10^{-7}$	(1.51	0.40	0.44) $\times 10^{-4}$

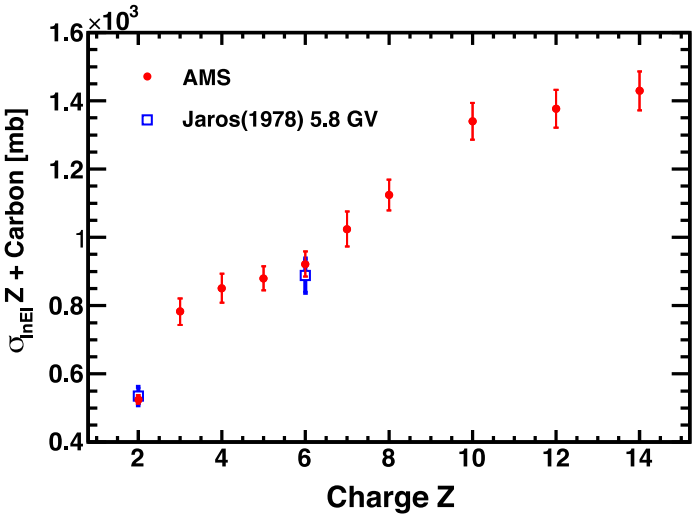

Fig. 74. The AMS measured inelastic cross sections of He, Li, Be, B, C, N, O, Ne, Mg, and Si on carbon averaged from 5 to 100 GV together with the measurements from ground-based accelerators [118].

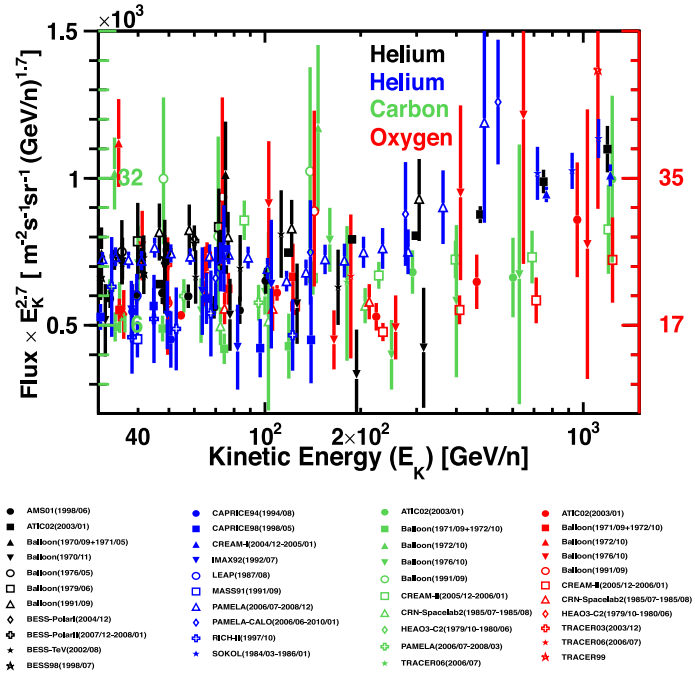

Fig. 75. Flux measurements before AMS of primary cosmic rays He (black and blue, left axis), C (green, left axis), and O (red, right axis) multiplied by $E_K^{2.7}$ as functions of kinetic energy per nucleon.

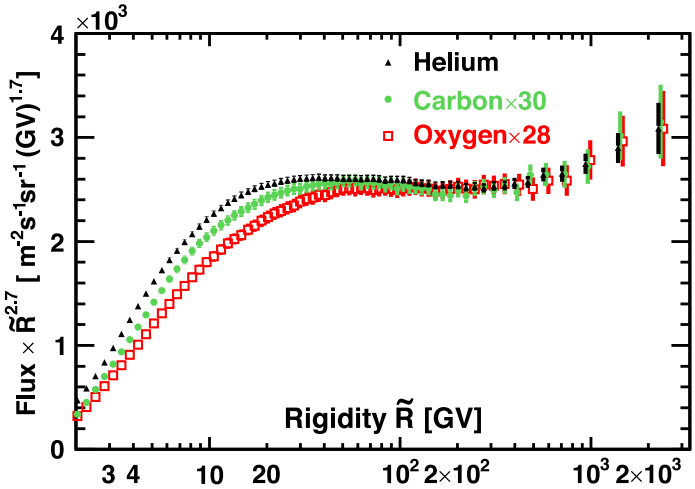

Fig. 76. The AMS measurements of helium (black triangles), carbon (green circles, scaled by 30) and oxygen (red squares, scaled by 28) nuclei fluxes from ∼2 GV to 3.0 TV multiplied by $\tilde{R}^{2.7}$. For clarity, horizontal positions of the helium and oxygen data points above 400 GV are displaced with respect to the carbon. $\tilde{R}$ is the spectrally weighted mean rigidity for a flux proportional to $R^{-2.7}$.

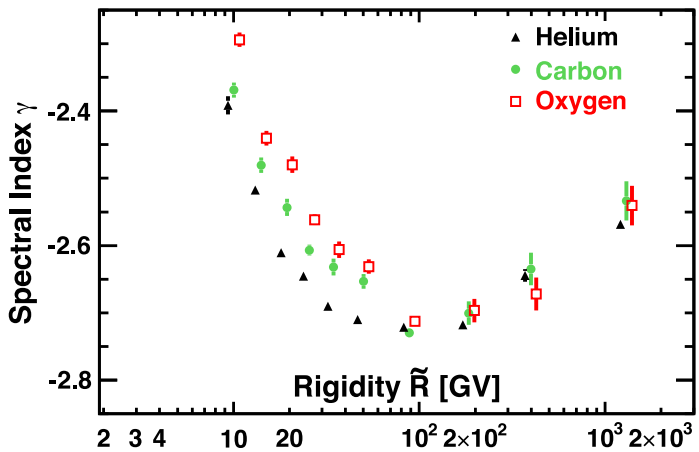

Fig. 77. The dependence of the helium, carbon, and oxygen spectral indices on rigidity. For clarity, the horizontal positions of the helium and oxygen data points are displaced with respect to carbon. As seen, above 60 GV the spectral indices are identical.

Table 7
The Helium flux Φ_{He} as a function of rigidity at the top of AMS in units of $[\mathrm{m}^2\,\mathrm{sr\,s\,GV}]^{-1}$ including errors due to statistics (σ_{stat}); contributions to the systematic error from the trigger, acceptance, and background (σ_{acc}); the rigidity resolution function and unfolding (σ_{unf}); the absolute rigidity scale (σ_{scale}); and the total systematic error (σ_{syst}). The contribution of individual sources to the systematic error are added in quadrature to arrive at the total systematic error.

Rigidity [GV]	Φ_{He}	σ_{stat}	σ_{acc}	σ_{unf}	σ_{scale}	σ_{syst}
1.92–2.15	(6.947	0.004	0.110	0.112	0.018	0.158) $\times 10^{1}$
2.15–2.40	(6.411	0.004	0.089	0.049	0.010	0.102) $\times 10^{1}$
2.40–2.67	(5.751	0.003	0.074	0.034	0.004	0.081) $\times 10^{1}$
2.67–2.97	(5.112	0.003	0.064	0.027	0.001	0.069) $\times 10^{1}$
2.97–3.29	(4.490	0.002	0.057	0.021	0.002	0.060) $\times 10^{1}$
3.29–3.64	(3.890	0.002	0.050	0.016	0.004	0.053) $\times 10^{1}$
3.64–4.02	(3.329	0.002	0.044	0.012	0.005	0.046) $\times 10^{1}$
4.02–4.43	(2.822	0.001	0.038	0.009	0.005	0.040) $\times 10^{1}$
4.43–4.88	(2.368	0.001	0.032	0.007	0.005	0.033) $\times 10^{1}$
4.88–5.37	(1.968	0.001	0.027	0.005	0.004	0.028) $\times 10^{1}$
5.37–5.90	(1.624	0.001	0.022	0.004	0.004	0.023) $\times 10^{1}$
5.90–6.47	(1.334	0.001	0.018	0.003	0.003	0.019) $\times 10^{1}$
6.47–7.09	(1.092	0.000	0.015	0.002	0.003	0.015) $\times 10^{1}$
7.09–7.76	(8.920	0.004	0.117	0.019	0.026	0.121) $\times 10^{0}$
7.76–8.48	(7.278	0.003	0.094	0.015	0.022	0.097) $\times 10^{0}$
8.48–9.26	(5.927	0.003	0.075	0.012	0.019	0.079) $\times 10^{0}$
9.26–10.1	(4.828	0.002	0.061	0.010	0.016	0.064) $\times 10^{0}$
10.1–11.0	(3.927	0.002	0.049	0.008	0.014	0.051) $\times 10^{0}$
11.0–12.0	(3.186	0.002	0.039	0.007	0.011	0.042) $\times 10^{0}$
12.0–13.0	(2.597	0.001	0.032	0.006	0.009	0.034) $\times 10^{0}$
13.0–14.1	(2.122	0.001	0.026	0.005	0.008	0.028) $\times 10^{0}$
14.1–15.3	(1.730	0.001	0.021	0.004	0.007	0.023) $\times 10^{0}$
15.3–16.6	(1.406	0.001	0.017	0.004	0.005	0.018) $\times 10^{0}$
16.6–18.0	(1.141	0.001	0.014	0.003	0.004	0.015) $\times 10^{0}$
18.0–19.5	(9.268	0.006	0.114	0.027	0.036	0.122) $\times 10^{-1}$
19.5–21.1	(7.530	0.005	0.092	0.023	0.030	0.100) $\times 10^{-1}$
21.1–22.8	(6.131	0.004	0.075	0.019	0.024	0.081) $\times 10^{-1}$
22.8–24.7	(4.986	0.004	0.061	0.017	0.020	0.066) $\times 10^{-1}$
24.7–26.7	(4.049	0.003	0.050	0.014	0.016	0.054) $\times 10^{-1}$
26.7–28.8	(3.302	0.003	0.041	0.012	0.013	0.044) $\times 10^{-1}$
28.8–31.1	(2.694	0.002	0.033	0.010	0.011	0.036) $\times 10^{-1}$
31.1–33.5	(2.201	0.002	0.027	0.009	0.009	0.030) $\times 10^{-1}$
33.5–36.1	(1.802	0.002	0.022	0.007	0.007	0.024) $\times 10^{-1}$
36.1–38.9	(1.475	0.001	0.018	0.006	0.006	0.020) $\times 10^{-1}$
38.9–41.9	(1.203	0.001	0.015	0.005	0.005	0.016) $\times 10^{-1}$
41.9–45.1	(9.861	0.011	0.121	0.044	0.041	0.135) $\times 10^{-2}$
45.1–48.5	(8.092	0.009	0.099	0.037	0.034	0.111) $\times 10^{-2}$
48.5–52.2	(6.627	0.008	0.081	0.031	0.028	0.091) $\times 10^{-2}$
52.2–56.1	(5.446	0.007	0.067	0.026	0.023	0.075) $\times 10^{-2}$
56.1–60.3	(4.481	0.006	0.055	0.022	0.019	0.062) $\times 10^{-2}$
60.3–64.8	(3.685	0.005	0.045	0.018	0.016	0.051) $\times 10^{-2}$
64.8–69.7	(3.036	0.005	0.037	0.015	0.013	0.042) $\times 10^{-2}$
69.7–74.9	(2.496	0.004	0.031	0.012	0.011	0.035) $\times 10^{-2}$
74.9–80.5	(2.051	0.004	0.025	0.010	0.009	0.029) $\times 10^{-2}$
80.5–86.5	(1.681	0.003	0.021	0.008	0.008	0.024) $\times 10^{-2}$
86.5–93.0	(1.387	0.003	0.017	0.007	0.006	0.020) $\times 10^{-2}$
93.0–100	(1.140	0.002	0.014	0.006	0.005	0.016) $\times 10^{-2}$
100–108	(9.311	0.020	0.116	0.045	0.045	0.132) $\times 10^{-3}$
108–116	(7.597	0.018	0.095	0.037	0.037	0.108) $\times 10^{-3}$
116–125	(6.186	0.016	0.078	0.030	0.031	0.089) $\times 10^{-3}$
125–135	(5.029	0.013	0.064	0.024	0.026	0.073) $\times 10^{-3}$
135–147	(4.036	0.011	0.051	0.019	0.022	0.059) $\times 10^{-3}$
147–160	(3.187	0.009	0.041	0.015	0.018	0.047) $\times 10^{-3}$

(*continued on next page*)

Table 7 (*continued*).

Rigidity [GV]	Φ_{He}	σ_{stat}	σ_{acc}	σ_{unf}	σ_{scale}	σ_{syst}
160–175	(2.521	0.008	0.033	0.012	0.015	0.038) $\times 10^{-3}$
175–192	(1.972	0.006	0.026	0.009	0.012	0.030) $\times 10^{-3}$
192–211	(1.532	0.005	0.021	0.007	0.010	0.024) $\times 10^{-3}$
211–233	(1.170	0.004	0.016	0.006	0.008	0.019) $\times 10^{-3}$
233–259	(8.895	0.034	0.124	0.044	0.062	0.146) $\times 10^{-4}$
259–291	(6.552	0.026	0.094	0.035	0.048	0.111) $\times 10^{-4}$
291–330	(4.758	0.020	0.070	0.027	0.038	0.084) $\times 10^{-4}$
330–379	(3.339	0.015	0.051	0.021	0.030	0.063) $\times 10^{-4}$
379–441	(2.274	0.011	0.036	0.017	0.023	0.046) $\times 10^{-4}$
441–525	(1.473	0.008	0.024	0.013	0.017	0.032) $\times 10^{-4}$
525–643	(9.095	0.050	0.158	0.093	0.125	0.222) $\times 10^{-5}$
643–822	(4.983	0.030	0.092	0.063	0.087	0.141) $\times 10^{-5}$
822–1130	(2.412	0.016	0.047	0.040	0.057	0.084) $\times 10^{-5}$
1130–1800	(8.831	0.065	0.184	0.216	0.326	0.432) $\times 10^{-6}$
1800–3000	(2.518	0.026	0.055	0.101	0.162	0.199) $\times 10^{-6}$

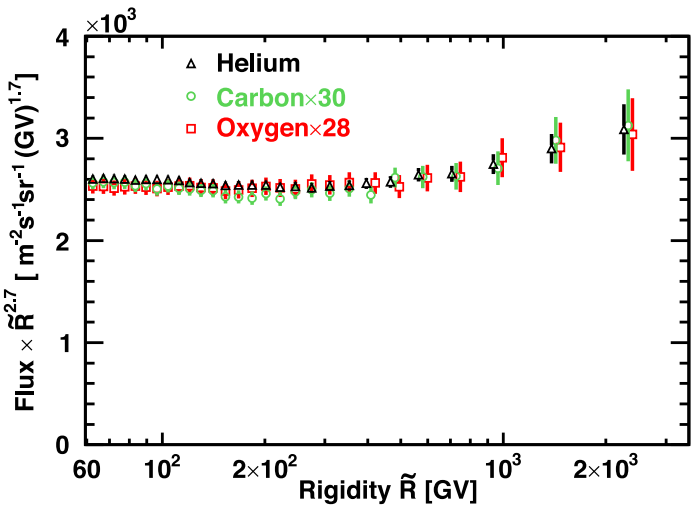

Fig. 78. The rigidity dependence of the helium (black triangles), carbon (green circles, scaled by 30), and oxygen (red squares, scaled by 28) fluxes multiplied by $\tilde{R}^{2.7}$. For clarity, horizontal positions of the helium and oxygen data points above 400 GV are displaced with respect to the carbon points. As seen, above 60 GV the three fluxes have identical rigidity dependence and deviate from the single power law in an identical manner above ∼200 GV.

Table 8
The Carbon flux Φ_C as a function of rigidity at the top of AMS in units of $[\mathrm{m}^2\,\mathrm{sr}\,\mathrm{s}\,\mathrm{GV}]^{-1}$ including errors due to statistics (σ_{stat}); contributions to the systematic error from the trigger, acceptance, and background (σ_{acc}); the rigidity resolution function and unfolding (σ_{unf}); the absolute rigidity scale (σ_{scale}); and the total systematic error (σ_{syst}). The contribution of individual sources to the systematic error are added in quadrature to arrive at the total systematic error.

Rigidity [GV]	Φ_C	σ_{stat}	σ_{acc}	σ_{unf}	σ_{scale}	σ_{syst}
1.92–2.15	(1.626	0.003	0.045	0.033	0.008	0.056) $\times 10^{0}$
2.15–2.40	(1.613	0.003	0.042	0.018	0.005	0.047) $\times 10^{0}$
2.40–2.67	(1.540	0.003	0.039	0.014	0.003	0.042) $\times 10^{0}$
2.67–2.97	(1.404	0.002	0.035	0.011	0.001	0.037) $\times 10^{0}$
2.97–3.29	(1.238	0.002	0.030	0.008	0.000	0.031) $\times 10^{0}$
3.29–3.64	(1.077	0.002	0.026	0.006	0.000	0.026) $\times 10^{0}$
3.64–4.02	(9.241	0.013	0.219	0.042	0.006	0.223) $\times 10^{-1}$
4.02–4.43	(7.897	0.011	0.185	0.031	0.008	0.188) $\times 10^{-1}$
4.43–4.88	(6.703	0.009	0.156	0.022	0.009	0.157) $\times 10^{-1}$
4.88–5.37	(5.653	0.007	0.130	0.016	0.009	0.132) $\times 10^{-1}$
5.37–5.90	(4.716	0.006	0.108	0.012	0.009	0.109) $\times 10^{-1}$
5.90–6.47	(3.931	0.005	0.090	0.009	0.009	0.091) $\times 10^{-1}$
6.47–7.09	(3.249	0.004	0.074	0.007	0.008	0.075) $\times 10^{-1}$
7.09–7.76	(2.670	0.003	0.061	0.005	0.007	0.061) $\times 10^{-1}$
7.76–8.48	(2.195	0.003	0.050	0.004	0.006	0.050) $\times 10^{-1}$
8.48–9.26	(1.795	0.002	0.041	0.003	0.005	0.041) $\times 10^{-1}$
9.26–10.1	(1.462	0.002	0.033	0.003	0.005	0.034) $\times 10^{-1}$
10.1–11.0	(1.193	0.002	0.027	0.002	0.004	0.027) $\times 10^{-1}$
11.0–12.0	(9.699	0.014	0.219	0.017	0.032	0.223) $\times 10^{-2}$
12.0–13.0	(7.906	0.013	0.179	0.015	0.027	0.182) $\times 10^{-2}$
13.0–14.1	(6.496	0.011	0.147	0.013	0.023	0.149) $\times 10^{-2}$
14.1–15.3	(5.303	0.009	0.120	0.011	0.019	0.122) $\times 10^{-2}$
15.3–16.6	(4.321	0.008	0.098	0.009	0.016	0.100) $\times 10^{-2}$
16.6–18.0	(3.521	0.007	0.080	0.008	0.013	0.081) $\times 10^{-2}$
18.0–19.5	(2.873	0.006	0.065	0.007	0.011	0.066) $\times 10^{-2}$
19.5–21.1	(2.351	0.005	0.053	0.006	0.009	0.055) $\times 10^{-2}$
21.1–22.8	(1.920	0.004	0.044	0.005	0.007	0.045) $\times 10^{-2}$
22.8–24.7	(1.566	0.003	0.036	0.005	0.006	0.037) $\times 10^{-2}$
24.7–26.7	(1.276	0.003	0.029	0.004	0.005	0.030) $\times 10^{-2}$
26.7–28.8	(1.043	0.002	0.024	0.003	0.004	0.024) $\times 10^{-2}$
28.8–31.1	(8.499	0.019	0.195	0.029	0.034	0.200) $\times 10^{-3}$
31.1–33.5	(6.989	0.017	0.161	0.025	0.028	0.165) $\times 10^{-3}$
33.5–36.1	(5.741	0.015	0.132	0.022	0.024	0.136) $\times 10^{-3}$
36.1–38.9	(4.718	0.013	0.109	0.019	0.020	0.112) $\times 10^{-3}$
38.9–41.9	(3.865	0.011	0.089	0.016	0.016	0.092) $\times 10^{-3}$
41.9–45.1	(3.160	0.010	0.073	0.014	0.013	0.076) $\times 10^{-3}$
45.1–48.5	(2.603	0.008	0.060	0.012	0.011	0.063) $\times 10^{-3}$
48.5–52.2	(2.154	0.007	0.050	0.010	0.009	0.052) $\times 10^{-3}$
52.2–56.1	(1.768	0.007	0.041	0.009	0.008	0.043) $\times 10^{-3}$
56.1–60.3	(1.459	0.006	0.034	0.007	0.007	0.035) $\times 10^{-3}$
60.3–64.8	(1.186	0.005	0.028	0.006	0.005	0.029) $\times 10^{-3}$
64.8–69.7	(9.799	0.043	0.230	0.053	0.046	0.240) $\times 10^{-4}$
69.7–74.9	(8.036	0.038	0.189	0.044	0.038	0.198) $\times 10^{-4}$
74.9–80.5	(6.630	0.033	0.156	0.037	0.032	0.164) $\times 10^{-4}$
80.5–86.5	(5.392	0.029	0.127	0.031	0.027	0.134) $\times 10^{-4}$
86.5–93.0	(4.475	0.025	0.106	0.026	0.023	0.111) $\times 10^{-4}$
93.0–100	(3.611	0.022	0.085	0.022	0.019	0.090) $\times 10^{-4}$
100–108	(2.990	0.019	0.071	0.018	0.016	0.075) $\times 10^{-4}$
108–116	(2.429	0.017	0.058	0.015	0.013	0.061) $\times 10^{-4}$
116–125	(1.992	0.014	0.047	0.012	0.011	0.050) $\times 10^{-4}$
125–135	(1.616	0.012	0.038	0.010	0.009	0.041) $\times 10^{-4}$
135–147	(1.299	0.010	0.031	0.008	0.008	0.033) $\times 10^{-4}$
147–160	(1.009	0.008	0.024	0.007	0.006	0.026) $\times 10^{-4}$
160–175	(7.979	0.070	0.191	0.054	0.051	0.205) $\times 10^{-5}$

(*continued on next page*)

Table 8 (*continued*).

Rigidity [GV]	Φ_C	σ_{stat}	σ_{acc}	σ_{unf}	σ_{scale}	σ_{syst}
175–192	(6.208	0.058	0.149	0.043	0.042	0.160) $\times 10^{-5}$
192–211	(4.918	0.049	0.118	0.036	0.035	0.128) $\times 10^{-5}$
211–233	(3.707	0.039	0.089	0.029	0.028	0.098) $\times 10^{-5}$
233–259	(2.892	0.032	0.070	0.024	0.024	0.077) $\times 10^{-5}$
259–291	(2.159	0.025	0.052	0.019	0.019	0.059) $\times 10^{-5}$
291–330	(1.535	0.019	0.037	0.015	0.015	0.043) $\times 10^{-5}$
330–379	(1.094	0.014	0.027	0.012	0.013	0.032) $\times 10^{-5}$
379–441	(7.205	0.103	0.177	0.096	0.099	0.225) $\times 10^{-6}$
441–525	(4.959	0.073	0.123	0.078	0.085	0.169) $\times 10^{-6}$
525–643	(2.982	0.048	0.075	0.057	0.066	0.115) $\times 10^{-6}$
643–822	(1.630	0.029	0.042	0.039	0.048	0.075) $\times 10^{-6}$
822–1130	(7.825	0.152	0.207	0.248	0.317	0.453) $\times 10^{-7}$
1130–1800	(3.014	0.145	0.100	0.072	0.132	0.181) $\times 10^{-7}$
1800–3000	(8.423	0.574	0.303	0.324	0.616	0.759) $\times 10^{-8}$

Table 9
The Oxygen flux Φ_O as a function of rigidity at the top of AMS in units of $[\mathrm{m}^2\,\mathrm{sr\,s\,GV}]^{-1}$ including errors due to statistics (σ_{stat}); contributions to the systematic error from the trigger, acceptance, and background (σ_{acc}); the rigidity resolution function and unfolding (σ_{unf}); the absolute rigidity scale (σ_{scale}); and the total systematic error (σ_{syst}). The contribution of individual sources to the systematic error are added in quadrature to arrive at the total systematic error.

Rigidity [GV]	Φ_O	σ_{stat}	σ_{acc}	σ_{unf}	σ_{scale}	σ_{syst}
2.15–2.40	(1.588	0.003	0.050	0.020	0.008	0.054) $\times 10^{0}$
2.40–2.67	(1.469	0.003	0.044	0.015	0.004	0.047) $\times 10^{0}$
2.67–2.97	(1.330	0.002	0.039	0.012	0.002	0.040) $\times 10^{0}$
2.97–3.29	(1.170	0.002	0.033	0.009	0.001	0.034) $\times 10^{0}$
3.29–3.64	(1.012	0.002	0.028	0.006	0.000	0.029) $\times 10^{0}$
3.64–4.02	(8.674	0.013	0.237	0.046	0.005	0.241) $\times 10^{-1}$
4.02–4.43	(7.370	0.011	0.199	0.033	0.007	0.202) $\times 10^{-1}$
4.43–4.88	(6.235	0.009	0.167	0.024	0.008	0.169) $\times 10^{-1}$
4.88–5.37	(5.260	0.007	0.140	0.018	0.008	0.142) $\times 10^{-1}$
5.37–5.90	(4.397	0.006	0.117	0.013	0.008	0.118) $\times 10^{-1}$
5.90–6.47	(3.660	0.005	0.097	0.010	0.008	0.098) $\times 10^{-1}$
6.47–7.09	(3.042	0.004	0.081	0.007	0.007	0.082) $\times 10^{-1}$
7.09–7.76	(2.510	0.003	0.067	0.005	0.006	0.067) $\times 10^{-1}$
7.76–8.48	(2.074	0.003	0.055	0.004	0.005	0.056) $\times 10^{-1}$
8.48–9.26	(1.708	0.002	0.046	0.003	0.005	0.046) $\times 10^{-1}$
9.26–10.1	(1.404	0.002	0.038	0.003	0.004	0.038) $\times 10^{-1}$
10.1–11.0	(1.148	0.002	0.031	0.002	0.003	0.031) $\times 10^{-1}$
11.0–12.0	(9.424	0.015	0.253	0.018	0.028	0.255) $\times 10^{-2}$
12.0–13.0	(7.750	0.013	0.208	0.015	0.024	0.210) $\times 10^{-2}$
13.0–14.1	(6.366	0.011	0.171	0.013	0.020	0.173) $\times 10^{-2}$
14.1–15.3	(5.204	0.009	0.140	0.011	0.017	0.141) $\times 10^{-2}$
15.3–16.6	(4.280	0.008	0.115	0.009	0.014	0.117) $\times 10^{-2}$
16.6–18.0	(3.498	0.007	0.094	0.008	0.012	0.095) $\times 10^{-2}$
18.0–19.5	(2.876	0.006	0.078	0.007	0.010	0.079) $\times 10^{-2}$
19.5–21.1	(2.359	0.005	0.064	0.006	0.008	0.065) $\times 10^{-2}$
21.1–22.8	(1.939	0.004	0.053	0.005	0.007	0.053) $\times 10^{-2}$
22.8–24.7	(1.586	0.003	0.043	0.004	0.006	0.044) $\times 10^{-2}$
24.7–26.7	(1.297	0.003	0.035	0.004	0.005	0.036) $\times 10^{-2}$
26.7–28.8	(1.064	0.002	0.029	0.003	0.004	0.029) $\times 10^{-2}$
28.8–31.1	(8.801	0.021	0.240	0.027	0.034	0.244) $\times 10^{-3}$
31.1–33.5	(7.256	0.018	0.199	0.024	0.028	0.202) $\times 10^{-3}$
33.5–36.1	(5.962	0.015	0.164	0.020	0.024	0.167) $\times 10^{-3}$
36.1–38.9	(4.933	0.014	0.136	0.018	0.020	0.138) $\times 10^{-3}$
38.9–41.9	(4.027	0.012	0.111	0.015	0.016	0.113) $\times 10^{-3}$

(*continued on next page*)

Table 9 (*continued*).

Rigidity [GV]	Φ_O	σ_{stat}	σ_{acc}	σ_{unf}	σ_{scale}	σ_{syst}
41.9–45.1	(3.336	0.010	0.092	0.013	0.014	0.094) $\times 10^{-3}$
45.1–48.5	(2.761	0.009	0.077	0.011	0.012	0.078) $\times 10^{-3}$
48.5–52.2	(2.280	0.008	0.064	0.010	0.010	0.065) $\times 10^{-3}$
52.2–56.1	(1.877	0.007	0.053	0.008	0.008	0.054) $\times 10^{-3}$
56.1–60.3	(1.538	0.006	0.043	0.007	0.007	0.044) $\times 10^{-3}$
60.3–64.8	(1.274	0.005	0.036	0.006	0.006	0.037) $\times 10^{-3}$
64.8–69.7	(1.045	0.005	0.030	0.005	0.005	0.030) $\times 10^{-3}$
69.7–74.9	(8.535	0.041	0.243	0.042	0.040	0.250) $\times 10^{-4}$
74.9–80.5	(7.059	0.036	0.202	0.035	0.034	0.208) $\times 10^{-4}$
80.5–86.5	(5.828	0.032	0.168	0.030	0.029	0.173) $\times 10^{-4}$
86.5–93.0	(4.780	0.027	0.138	0.025	0.024	0.143) $\times 10^{-4}$
93.0–100	(3.910	0.024	0.114	0.021	0.020	0.117) $\times 10^{-4}$
100–108	(3.214	0.020	0.094	0.017	0.017	0.097) $\times 10^{-4}$
108–116	(2.642	0.018	0.078	0.015	0.014	0.080) $\times 10^{-4}$
116–125	(2.174	0.016	0.064	0.012	0.012	0.067) $\times 10^{-4}$
125–135	(1.762	0.013	0.053	0.010	0.010	0.054) $\times 10^{-4}$
135–147	(1.415	0.011	0.042	0.008	0.009	0.044) $\times 10^{-4}$
147–160	(1.111	0.009	0.034	0.007	0.007	0.035) $\times 10^{-4}$
160–175	(8.817	0.077	0.269	0.054	0.059	0.281) $\times 10^{-5}$
175–192	(6.938	0.064	0.214	0.045	0.049	0.224) $\times 10^{-5}$
192–211	(5.436	0.054	0.169	0.037	0.041	0.178) $\times 10^{-5}$
211–233	(4.155	0.044	0.130	0.030	0.034	0.138) $\times 10^{-5}$
233–259	(3.142	0.035	0.100	0.025	0.028	0.106) $\times 10^{-5}$
259–291	(2.369	0.027	0.076	0.020	0.023	0.082) $\times 10^{-5}$
291–330	(1.701	0.021	0.055	0.017	0.019	0.061) $\times 10^{-5}$
330–379	(1.199	0.016	0.040	0.013	0.015	0.045) $\times 10^{-5}$
379–441	(8.082	0.115	0.273	0.107	0.119	0.317) $\times 10^{-6}$
441–525	(5.121	0.079	0.177	0.082	0.092	0.215) $\times 10^{-6}$
525–643	(3.175	0.052	0.113	0.064	0.071	0.148) $\times 10^{-6}$
643–822	(1.735	0.031	0.064	0.046	0.050	0.093) $\times 10^{-6}$
822–1130	(8.722	0.170	0.333	0.315	0.332	0.566) $\times 10^{-7}$
1130–1800	(3.224	0.165	0.148	0.077	0.128	0.210) $\times 10^{-7}$
1800–3000	(8.982	0.652	0.440	0.377	0.590	0.827) $\times 10^{-8}$

Table 10
The helium to oxygen flux ratio He/O as a function of rigidity including errors due to statistics (σ_{stat}); contributions to the systematic error from the trigger, acceptance, and background (σ_{acc}); the rigidity resolution function and unfolding (σ_{unf}); the absolute rigidity scale (σ_{scale}); and the total systematic error (σ_{syst}). The statistical errors are the sum in quadrature of the ratios of helium and oxygen fluxes statistical errors to the corresponding flux values, multiplied by the flux ratio. The systematic errors from the background subtraction, the trigger, and the event reconstruction and selection are likewise added in quadrature. The correlations in the systematic errors from the uncertainty in nuclear interaction cross sections, the unfolding and the absolute rigidity scale between the helium and oxygen fluxes have been taken into account in calculating the corresponding systematic errors of the flux ratio. The contribution of individual sources to the systematic error are added in quadrature to arrive at the total systematic uncertainty.

Rigidity [GV]	He/O	σ_{stat}	σ_{acc}	σ_{unf}	σ_{scale}	σ_{syst}
2.15–2.40	40.379	0.083	1.104	0.435	0.136	1.194
2.40–2.67	39.144	0.074	1.054	0.345	0.093	1.113
2.67–2.97	38.437	0.068	1.026	0.291	0.063	1.068
2.97–3.29	38.373	0.066	1.018	0.247	0.006	1.048
3.29–3.64	38.444	0.062	1.017	0.211	0.038	1.039
3.64–4.02	38.378	0.061	1.013	0.180	0.033	1.030
4.02–4.43	38.285	0.060	1.010	0.154	0.028	1.022
4.43–4.88	37.980	0.057	1.002	0.133	0.024	1.011
4.88–5.37	37.416	0.054	0.987	0.114	0.020	0.994
5.37–5.90	36.942	0.053	0.975	0.100	0.018	0.981

(*continued on next page*)

Table 10 (*continued*).

Rigidity [GV]	He/O	σ_{stat}	σ_{acc}	σ_{unf}	σ_{scale}	σ_{syst}
5.90–6.47	36.463	0.052	0.964	0.089	0.017	0.968
6.47–7.09	35.907	0.051	0.950	0.081	0.017	0.954
7.09–7.76	35.541	0.051	0.942	0.076	0.017	0.945
7.76–8.48	35.088	0.050	0.931	0.072	0.018	0.934
8.48–9.26	34.703	0.050	0.922	0.069	0.018	0.925
9.26–10.1	34.399	0.052	0.916	0.069	0.019	0.918
10.1–11.0	34.225	0.054	0.912	0.069	0.019	0.915
11.0–12.0	33.801	0.055	0.902	0.069	0.019	0.905
12.0–13.0	33.510	0.059	0.895	0.071	0.018	0.898
13.0–14.1	33.340	0.061	0.892	0.073	0.018	0.895
14.1–15.3	33.237	0.063	0.890	0.076	0.017	0.894
15.3–16.6	32.852	0.065	0.881	0.079	0.016	0.885
16.6–18.0	32.632	0.067	0.876	0.082	0.015	0.880
18.0–19.5	32.219	0.069	0.867	0.085	0.013	0.871
19.5–21.1	31.922	0.070	0.860	0.089	0.012	0.865
21.1–22.8	31.621	0.071	0.853	0.092	0.011	0.858
22.8–24.7	31.444	0.071	0.850	0.096	0.010	0.855
24.7–26.7	31.222	0.073	0.846	0.100	0.009	0.852
26.7–28.8	31.036	0.075	0.842	0.104	0.008	0.849
28.8–31.1	30.612	0.076	0.833	0.107	0.007	0.840
31.1–33.5	30.328	0.080	0.827	0.111	0.007	0.834
33.5–36.1	30.223	0.083	0.826	0.115	0.007	0.834
36.1–38.9	29.894	0.087	0.820	0.118	0.007	0.828
38.9–41.9	29.881	0.093	0.822	0.122	0.007	0.831
41.9–45.1	29.561	0.097	0.816	0.124	0.008	0.825
45.1–48.5	29.308	0.103	0.812	0.127	0.009	0.822
48.5–52.2	29.073	0.108	0.808	0.130	0.010	0.818
52.2–56.1	29.018	0.115	0.810	0.133	0.011	0.821
56.1–60.3	29.137	0.123	0.816	0.136	0.012	0.828
60.3–64.8	28.919	0.130	0.814	0.138	0.013	0.826
64.8–69.7	29.051	0.138	0.821	0.141	0.014	0.834
69.7–74.9	29.240	0.149	0.831	0.144	0.015	0.843
74.9–80.5	29.055	0.157	0.830	0.146	0.016	0.842
80.5–86.5	28.853	0.166	0.828	0.146	0.017	0.841
86.5–93.0	29.016	0.176	0.837	0.148	0.017	0.851
93.0–100	29.163	0.189	0.846	0.150	0.018	0.860
100–108	28.968	0.193	0.846	0.150	0.019	0.859
108–116	28.749	0.212	0.845	0.150	0.019	0.858
116–125	28.461	0.218	0.842	0.149	0.020	0.855
125–135	28.535	0.230	0.850	0.151	0.021	0.863
135–147	28.529	0.234	0.856	0.152	0.022	0.870
147–160	28.684	0.255	0.868	0.156	0.024	0.882
160–175	28.590	0.265	0.873	0.159	0.028	0.887
175–192	28.428	0.279	0.876	0.164	0.032	0.892
192–211	28.182	0.295	0.877	0.170	0.039	0.894
211–233	28.149	0.314	0.886	0.179	0.047	0.905
233–259	28.310	0.333	0.901	0.194	0.058	0.924
259–291	27.660	0.338	0.892	0.209	0.070	0.919
291–330	27.975	0.365	0.916	0.237	0.087	0.950
330–379	27.836	0.386	0.926	0.272	0.109	0.971
379–441	28.143	0.422	0.954	0.324	0.141	1.017
441–525	28.774	0.465	0.997	0.401	0.189	1.091
525–643	28.650	0.497	1.019	0.501	0.250	1.162
643–822	28.717	0.548	1.051	0.655	0.328	1.281
822–1130	27.652	0.569	1.044	0.866	0.401	1.415
1130–1800	27.390	1.415	1.222	0.663	0.078	1.393
1800–3000	28.030	2.054	1.297	1.153	0.037	1.736

Table 11
The carbon to oxygen flux ratio C/O as a function of rigidity including errors due to statistics (σ_{stat}); contributions to the systematic error from the trigger, acceptance, and background (σ_{acc}); the rigidity resolution function and unfolding (σ_{unf}); the absolute rigidity scale (σ_{scale}); and the total systematic error (σ_{syst}). The statistical errors are the sum in quadrature of the ratios of carbon and oxygen fluxes statistical errors to the corresponding flux values, multiplied by the flux ratio. The systematic errors from the background subtraction, the trigger, and the event reconstruction and selection are likewise added in quadrature. The correlations in the systematic errors from the uncertainty in nuclear interaction cross sections, the unfolding and the absolute rigidity scale between the carbon and oxygenfluxes have been taken into account in calculating the corresponding systematic errors of the flux ratio. The contribution of individual sources to the systematic error are added in quadrature to arrive at the total systematic uncertainty.

Rigidity [GV]	C/O	σ_{stat}	σ_{acc}	σ_{unf}	σ_{scale}	σ_{syst}
2.15–2.40	1.016	0.003	0.023	0.012	0.002	0.026
2.40–2.67	1.048	0.003	0.022	0.010	0.001	0.024
2.67–2.97	1.056	0.002	0.021	0.009	0.001	0.023
2.97–3.29	1.058	0.002	0.021	0.007	0.000	0.022
3.29–3.64	1.064	0.002	0.020	0.006	0.000	0.021
3.64–4.02	1.065	0.002	0.020	0.005	0.000	0.021
4.02–4.43	1.072	0.002	0.020	0.005	0.000	0.020
4.43–4.88	1.075	0.002	0.020	0.004	0.000	0.020
4.88–5.37	1.075	0.002	0.020	0.003	0.000	0.020
5.37–5.90	1.073	0.002	0.019	0.003	0.000	0.020
5.90–6.47	1.074	0.002	0.019	0.003	0.000	0.020
6.47–7.09	1.068	0.002	0.019	0.002	0.000	0.019
7.09–7.76	1.064	0.002	0.019	0.002	0.000	0.019
7.76–8.48	1.058	0.002	0.019	0.002	0.000	0.019
8.48–9.26	1.051	0.002	0.019	0.002	0.000	0.019
9.26–10.1	1.042	0.002	0.019	0.002	0.000	0.019
10.1–11.0	1.040	0.002	0.019	0.002	0.000	0.019
11.0–12.0	1.029	0.002	0.019	0.002	0.000	0.019
12.0–13.0	1.020	0.002	0.019	0.002	0.000	0.019
13.0–14.1	1.020	0.002	0.019	0.002	0.000	0.019
14.1–15.3	1.019	0.003	0.019	0.002	0.000	0.019
15.3–16.6	1.010	0.003	0.019	0.002	0.000	0.019
16.6–18.0	1.006	0.003	0.019	0.002	0.000	0.019
18.0–19.5	0.999	0.003	0.019	0.002	0.000	0.019
19.5–21.1	0.997	0.003	0.019	0.003	0.000	0.019
21.1–22.8	0.990	0.003	0.019	0.003	0.000	0.019
22.8–24.7	0.988	0.003	0.019	0.003	0.000	0.019
24.7–26.7	0.984	0.003	0.019	0.003	0.000	0.019
26.7–28.8	0.981	0.003	0.019	0.003	0.000	0.019
28.8–31.1	0.966	0.003	0.019	0.003	0.000	0.019
31.1–33.5	0.963	0.003	0.019	0.003	0.000	0.019
33.5–36.1	0.963	0.003	0.019	0.003	0.000	0.019
36.1–38.9	0.956	0.004	0.019	0.004	0.000	0.019
38.9–41.9	0.960	0.004	0.019	0.004	0.000	0.020
41.9–45.1	0.947	0.004	0.019	0.004	0.000	0.020
45.1–48.5	0.943	0.004	0.019	0.004	0.000	0.020
48.5–52.2	0.945	0.005	0.019	0.004	0.000	0.020
52.2–56.1	0.942	0.005	0.020	0.004	0.000	0.020
56.1–60.3	0.949	0.005	0.020	0.005	0.000	0.020
60.3–64.8	0.931	0.006	0.020	0.005	0.000	0.020
64.8–69.7	0.938	0.006	0.020	0.005	0.000	0.021
69.7–74.9	0.942	0.006	0.020	0.005	0.000	0.021
74.9–80.5	0.939	0.007	0.021	0.005	0.000	0.021
80.5–86.5	0.925	0.007	0.020	0.005	0.000	0.021
86.5–93.0	0.936	0.008	0.021	0.005	0.000	0.022
93.0–100	0.923	0.008	0.021	0.005	0.000	0.022
100–108	0.930	0.008	0.021	0.005	0.000	0.022
108–116	0.919	0.009	0.021	0.005	0.000	0.022
116–125	0.916	0.009	0.021	0.005	0.000	0.022
125–135	0.917	0.010	0.022	0.006	0.000	0.022
135–147	0.918	0.010	0.022	0.006	0.000	0.023
147–160	0.908	0.011	0.022	0.006	0.000	0.023
160–175	0.905	0.011	0.022	0.006	0.000	0.023
175–192	0.895	0.012	0.022	0.006	0.000	0.023
192–211	0.905	0.013	0.023	0.006	0.000	0.024

(*continued on next page*)

Table 11 (*continued*).

Rigidity [GV]	C/O	σ_{stat}	σ_{acc}	σ_{unf}	σ_{scale}	σ_{syst}
211–233	0.892	0.013	0.023	0.007	0.001	0.024
233–259	0.920	0.014	0.024	0.007	0.001	0.025
259–291	0.912	0.015	0.024	0.008	0.001	0.026
291–330	0.903	0.016	0.025	0.009	0.001	0.026
330–379	0.912	0.017	0.026	0.010	0.001	0.028
379–441	0.892	0.018	0.026	0.012	0.001	0.028
441–525	0.968	0.021	0.029	0.015	0.001	0.033
525–643	0.939	0.022	0.029	0.019	0.000	0.034
643–822	0.939	0.024	0.030	0.024	0.001	0.038
822–1130	0.897	0.025	0.030	0.031	0.002	0.043
1130–1800	0.935	0.066	0.041	0.022	0.004	0.047
1800–3000	0.938	0.093	0.044	0.038	0.007	0.058

Table 12
The proton to helium flux ratio p/He as a function of rigidity including errors due to statistics (σ_{stat}); contributions to the systematic error from the trigger, acceptance, and background (σ_{acc}); the rigidity resolution function and unfolding (σ_{unf}); the absolute rigidity scale (σ_{scale}); and the total systematic error (σ_{syst}). The statistical errors are the sum in quadrature of the ratios of proton and helium fluxes statistical errors to the corresponding flux values, multiplied by the flux ratio. The systematic errors from the background subtraction, the trigger, and the event reconstruction and selection are likewise added in quadrature. The correlations in the systematic errors from the uncertainty in nuclear interaction cross sections, the unfolding and the absolute rigidity scale between the proton and helium fluxes have been taken into account in calculating the corresponding systematic errors of the flux ratio. The contribution of individual sources to the systematic error are added in quadrature to arrive at the total systematic uncertainty.

Rigidity [GV]	p/He	σ_{stat}	σ_{acc}	σ_{unf}	σ_{scale}	σ_{syst}
1.92–2.15	8.164	0.005	0.155	0.122	0.018	0.198
2.15–2.40	7.694	0.005	0.134	0.051	0.005	0.144
2.40–2.67	7.386	0.004	0.122	0.038	0.004	0.128
2.67–2.97	7.080	0.004	0.115	0.032	0.010	0.119
2.97–3.29	6.819	0.004	0.111	0.028	0.008	0.115
3.29–3.64	6.609	0.003	0.109	0.025	0.006	0.112
3.64–4.02	6.442	0.003	0.108	0.023	0.005	0.110
4.02–4.43	6.304	0.003	0.106	0.021	0.004	0.108
4.43–4.88	6.188	0.003	0.105	0.020	0.004	0.107
4.88–5.37	6.080	0.003	0.102	0.019	0.003	0.104
5.37–5.90	5.990	0.003	0.100	0.019	0.003	0.102
5.90–6.47	5.908	0.003	0.098	0.018	0.002	0.099
6.47–7.09	5.833	0.003	0.095	0.018	0.002	0.097
7.09–7.76	5.760	0.003	0.092	0.018	0.002	0.094
7.76–8.48	5.687	0.003	0.090	0.018	0.001	0.091
8.48–9.26	5.620	0.003	0.087	0.017	0.001	0.089
9.26–10.1	5.549	0.003	0.085	0.017	0.001	0.087
10.1–11.0	5.488	0.003	0.083	0.017	0.001	0.085
11.0–12.0	5.433	0.003	0.081	0.017	0.001	0.083
12.0–13.0	5.373	0.003	0.079	0.017	0.000	0.081
13.0–14.1	5.335	0.003	0.078	0.018	0.000	0.080
14.1–15.3	5.285	0.003	0.076	0.018	0.000	0.078
15.3–16.6	5.237	0.004	0.075	0.018	0.001	0.077
16.6–18.0	5.195	0.004	0.073	0.019	0.001	0.076
18.0–19.5	5.151	0.004	0.072	0.019	0.001	0.074
19.5–21.1	5.113	0.004	0.071	0.019	0.001	0.074

(*continued on next page*)

Table 12 (*continued*).

Rigidity [GV]	p/He	σ_{stat}	σ_{acc}	σ_{unf}	σ_{scale}	σ_{syst}
21.1–22.8	5.074	0.004	0.071	0.020	0.001	0.073
22.8–24.7	5.026	0.004	0.070	0.020	0.001	0.073
24.7–26.7	4.971	0.004	0.069	0.021	0.001	0.072
26.7–28.8	4.929	0.004	0.069	0.021	0.002	0.072
28.8–31.1	4.883	0.004	0.068	0.022	0.002	0.071
31.1–33.5	4.844	0.005	0.068	0.022	0.002	0.071
33.5–36.1	4.800	0.005	0.067	0.023	0.002	0.071
36.1–38.9	4.759	0.005	0.066	0.023	0.002	0.070
38.9–41.9	4.738	0.005	0.066	0.024	0.002	0.070
41.9–45.1	4.703	0.006	0.066	0.025	0.002	0.070
45.1–48.5	4.665	0.006	0.065	0.025	0.002	0.070
48.5–52.2	4.639	0.006	0.065	0.026	0.003	0.070
52.2–56.1	4.605	0.007	0.064	0.026	0.003	0.070
56.1–60.3	4.570	0.007	0.064	0.027	0.003	0.069
60.3–64.8	4.543	0.007	0.064	0.027	0.003	0.069
64.8–69.7	4.508	0.008	0.063	0.028	0.003	0.069
69.7–74.9	4.474	0.008	0.063	0.028	0.003	0.069
74.9–80.5	4.448	0.009	0.063	0.029	0.002	0.069
80.5–86.5	4.428	0.009	0.062	0.029	0.002	0.069
86.5–93.0	4.375	0.010	0.062	0.029	0.002	0.068
93.0–100	4.342	0.010	0.061	0.030	0.002	0.068
100–108	4.305	0.010	0.061	0.030	0.003	0.068
108–116	4.283	0.011	0.061	0.031	0.003	0.069
116–125	4.278	0.012	0.061	0.032	0.003	0.069
125–135	4.251	0.012	0.061	0.032	0.004	0.069
135–147	4.217	0.012	0.061	0.033	0.004	0.070
147–160	4.208	0.013	0.062	0.034	0.005	0.071
160–175	4.175	0.014	0.062	0.036	0.005	0.072
175–192	4.140	0.015	0.062	0.037	0.005	0.073
192–211	4.093	0.015	0.063	0.038	0.006	0.074
211–233	4.095	0.016	0.064	0.041	0.006	0.076
233–259	4.077	0.017	0.065	0.043	0.007	0.078
259–291	4.082	0.018	0.066	0.047	0.008	0.082
291–330	4.023	0.019	0.067	0.050	0.009	0.084
330–379	4.023	0.020	0.070	0.055	0.010	0.089
379–441	3.938	0.021	0.071	0.060	0.011	0.094
441–525	3.904	0.022	0.073	0.066	0.012	0.099
525–643	3.774	0.023	0.074	0.071	0.012	0.104
643–822	3.822	0.026	0.079	0.079	0.012	0.113
822–1130	3.760	0.028	0.083	0.086	0.011	0.120
1130–1800	3.691	0.030	0.089	0.097	0.007	0.132

Table 13
The Lithium flux Φ_{Li} as a function of rigidity at the top of AMS in units of $[\mathrm{m}^2\,\mathrm{sr}\,\mathrm{s}\,\mathrm{GV}]^{-1}$ including errors due to statistics (σ_{stat}); contributions to the systematic error from the trigger, acceptance, and background (σ_{acc}); the rigidity resolution function and unfolding (σ_{unf}); the absolute rigidity scale (σ_{scale}); and the total systematic error (σ_{syst}). The contribution of individual sources to the systematic error are added in quadrature to arrive at the total systematic error.

Rigidity [GV]	Φ_{Li}	σ_{stat}	σ_{acc}	σ_{unf}	σ_{scale}	σ_{syst}
1.92–2.15	(2.827	0.014	0.086	0.020	0.013	0.089) $\times 10^{-1}$
2.15–2.40	(2.863	0.012	0.080	0.017	0.010	0.082) $\times 10^{-1}$
2.40–2.67	(2.835	0.011	0.077	0.014	0.007	0.078) $\times 10^{-1}$
2.67–2.97	(2.725	0.009	0.072	0.011	0.004	0.073) $\times 10^{-1}$
2.97–3.29	(2.524	0.008	0.066	0.009	0.002	0.067) $\times 10^{-1}$
3.29–3.64	(2.278	0.007	0.060	0.007	0.001	0.060) $\times 10^{-1}$
3.64–4.02	(1.996	0.006	0.052	0.006	0.001	0.052) $\times 10^{-1}$
4.02–4.43	(1.737	0.005	0.045	0.005	0.002	0.045) $\times 10^{-1}$
4.43–4.88	(1.484	0.004	0.038	0.004	0.002	0.039) $\times 10^{-1}$
4.88–5.37	(1.252	0.003	0.032	0.003	0.002	0.033) $\times 10^{-1}$
5.37–5.90	(1.049	0.003	0.027	0.003	0.002	0.027) $\times 10^{-1}$
5.90–6.47	(8.656	0.023	0.224	0.024	0.021	0.226) $\times 10^{-2}$
6.47–7.09	(7.115	0.019	0.184	0.021	0.020	0.186) $\times 10^{-2}$
7.09–7.76	(5.818	0.016	0.150	0.018	0.017	0.152) $\times 10^{-2}$
7.76–8.48	(4.703	0.013	0.122	0.015	0.015	0.123) $\times 10^{-2}$
8.48–9.26	(3.806	0.011	0.098	0.013	0.013	0.100) $\times 10^{-2}$
9.26–10.1	(3.070	0.009	0.079	0.011	0.011	0.081) $\times 10^{-2}$
10.1–11.0	(2.447	0.008	0.063	0.009	0.009	0.064) $\times 10^{-2}$
11.0–12.0	(1.953	0.006	0.050	0.007	0.007	0.052) $\times 10^{-2}$
12.0–13.0	(1.571	0.006	0.041	0.006	0.006	0.041) $\times 10^{-2}$
13.0–14.1	(1.263	0.005	0.033	0.005	0.005	0.033) $\times 10^{-2}$
14.1–15.3	(1.010	0.004	0.026	0.004	0.004	0.027) $\times 10^{-2}$
15.3–16.6	(8.063	0.033	0.209	0.031	0.035	0.214) $\times 10^{-3}$
16.6–18.0	(6.394	0.028	0.165	0.024	0.028	0.170) $\times 10^{-3}$
18.0–19.5	(5.101	0.023	0.132	0.019	0.023	0.135) $\times 10^{-3}$
19.5–21.1	(4.043	0.019	0.105	0.015	0.019	0.107) $\times 10^{-3}$
21.1–22.8	(3.220	0.016	0.083	0.012	0.015	0.086) $\times 10^{-3}$
22.8–24.7	(2.585	0.013	0.067	0.010	0.012	0.069) $\times 10^{-3}$
24.7–26.7	(2.046	0.011	0.053	0.008	0.010	0.054) $\times 10^{-3}$
26.7–28.8	(1.624	0.009	0.042	0.006	0.008	0.043) $\times 10^{-3}$
28.8–31.1	(1.299	0.007	0.034	0.005	0.006	0.035) $\times 10^{-3}$
31.1–33.5	(1.034	0.006	0.027	0.004	0.005	0.028) $\times 10^{-3}$
33.5–36.1	(8.206	0.054	0.213	0.031	0.042	0.219) $\times 10^{-4}$
36.1–38.9	(6.546	0.046	0.170	0.025	0.034	0.175) $\times 10^{-4}$
38.9–41.9	(5.249	0.040	0.137	0.020	0.028	0.141) $\times 10^{-4}$
41.9–45.1	(4.139	0.034	0.108	0.016	0.022	0.111) $\times 10^{-4}$
45.1–48.5	(3.421	0.030	0.089	0.014	0.019	0.092) $\times 10^{-4}$
48.5–52.2	(2.639	0.025	0.069	0.011	0.015	0.071) $\times 10^{-4}$
52.2–56.1	(2.122	0.022	0.056	0.009	0.012	0.058) $\times 10^{-4}$
56.1–60.3	(1.680	0.019	0.044	0.007	0.010	0.046) $\times 10^{-4}$
60.3–64.8	(1.355	0.016	0.036	0.006	0.008	0.037) $\times 10^{-4}$
64.8–69.7	(1.071	0.014	0.028	0.005	0.006	0.029) $\times 10^{-4}$
69.7–74.9	(8.747	0.122	0.231	0.042	0.054	0.241) $\times 10^{-5}$
74.9–80.5	(6.701	0.103	0.178	0.034	0.043	0.186) $\times 10^{-5}$
80.5–86.5	(5.409	0.089	0.144	0.029	0.036	0.151) $\times 10^{-5}$
86.5–93.0	(4.382	0.077	0.117	0.025	0.030	0.123) $\times 10^{-5}$
93.0–100	(3.441	0.066	0.092	0.020	0.024	0.097) $\times 10^{-5}$
100–108	(2.708	0.054	0.073	0.017	0.020	0.077) $\times 10^{-5}$
108–116	(2.066	0.048	0.056	0.014	0.015	0.059) $\times 10^{-5}$
116–125	(1.615	0.040	0.044	0.012	0.012	0.047) $\times 10^{-5}$
125–135	(1.329	0.034	0.036	0.010	0.011	0.039) $\times 10^{-5}$
135–147	(1.038	0.027	0.028	0.009	0.009	0.031) $\times 10^{-5}$

(*continued on next page*)

Table 13 (*continued*).

Rigidity [GV]	Φ_{Li}	σ_{stat}	σ_{acc}	σ_{unf}	σ_{scale}	σ_{syst}
147–160	(8.249	0.234	0.224	0.074	0.073	0.247) $\times 10^{-6}$
160–175	(6.182	0.188	0.169	0.061	0.057	0.188) $\times 10^{-6}$
175–192	(4.659	0.153	0.128	0.050	0.046	0.145) $\times 10^{-6}$
192–211	(3.554	0.126	0.098	0.042	0.037	0.113) $\times 10^{-6}$
211–233	(2.571	0.099	0.071	0.034	0.029	0.084) $\times 10^{-6}$
233–259	(2.009	0.081	0.056	0.029	0.024	0.068) $\times 10^{-6}$
259–291	(1.298	0.058	0.036	0.021	0.017	0.046) $\times 10^{-6}$
291–330	(9.327	0.446	0.263	0.173	0.136	0.343) $\times 10^{-7}$
330–379	(6.826	0.339	0.192	0.145	0.111	0.265) $\times 10^{-7}$
379–441	(4.744	0.251	0.134	0.117	0.088	0.199) $\times 10^{-7}$
441–525	(2.563	0.158	0.074	0.075	0.054	0.119) $\times 10^{-7}$
525–660	(1.525	0.096	0.044	0.056	0.039	0.081) $\times 10^{-7}$
660–880	(7.418	0.525	0.217	0.363	0.237	0.485) $\times 10^{-8}$
880–1300	(2.787	0.233	0.084	0.199	0.119	0.246) $\times 10^{-8}$
1300–3300	(0.575	0.103	0.024	0.048	0.029	0.061) $\times 10^{-8}$

Table 14
The Beryllium flux Φ_{Be} as a function of rigidity at the top of AMS in units of $[\mathrm{m}^2\,\mathrm{sr\,s\,GV}]^{-1}$ including errors due to statistics (σ_{stat}); contributions to the systematic error from the trigger, acceptance, and background (σ_{acc}); the rigidity resolution function and unfolding (σ_{unf}); the absolute rigidity scale (σ_{scale}); and the total systematic error (σ_{syst}). The contribution of individual sources to the systematic error are added in quadrature to arrive at the total systematic error.

Rigidity [GV]	Φ_{Be}	σ_{stat}	σ_{acc}	σ_{unf}	σ_{scale}	σ_{syst}
1.92–2.15	(1.572	0.010	0.051	0.012	0.005	0.053) $\times 10^{-1}$
2.15–2.40	(1.538	0.009	0.048	0.009	0.004	0.049) $\times 10^{-1}$
2.40–2.67	(1.437	0.008	0.044	0.008	0.003	0.045) $\times 10^{-1}$
2.67–2.97	(1.337	0.007	0.040	0.006	0.002	0.040) $\times 10^{-1}$
2.97–3.29	(1.241	0.006	0.036	0.005	0.001	0.036) $\times 10^{-1}$
3.29–3.64	(1.100	0.005	0.031	0.004	0.000	0.032) $\times 10^{-1}$
3.64–4.02	(9.659	0.042	0.271	0.034	0.006	0.274) $\times 10^{-2}$
4.02–4.43	(8.316	0.035	0.231	0.028	0.009	0.233) $\times 10^{-2}$
4.43–4.88	(7.078	0.029	0.195	0.023	0.011	0.197) $\times 10^{-2}$
4.88–5.37	(5.986	0.023	0.164	0.019	0.011	0.165) $\times 10^{-2}$
5.37–5.90	(4.945	0.019	0.135	0.016	0.011	0.136) $\times 10^{-2}$
5.90–6.47	(4.082	0.016	0.111	0.013	0.010	0.112) $\times 10^{-2}$
6.47–7.09	(3.336	0.013	0.091	0.011	0.009	0.092) $\times 10^{-2}$
7.09–7.76	(2.702	0.011	0.073	0.009	0.008	0.074) $\times 10^{-2}$
7.76–8.48	(2.169	0.009	0.059	0.007	0.007	0.060) $\times 10^{-2}$
8.48–9.26	(1.765	0.007	0.048	0.006	0.006	0.048) $\times 10^{-2}$
9.26–10.1	(1.422	0.006	0.038	0.005	0.005	0.039) $\times 10^{-2}$
10.1–11.0	(1.141	0.005	0.031	0.004	0.004	0.031) $\times 10^{-2}$
11.0–12.0	(9.017	0.043	0.244	0.030	0.034	0.248) $\times 10^{-3}$
12.0–13.0	(7.382	0.038	0.200	0.024	0.029	0.203) $\times 10^{-3}$
13.0–14.1	(5.935	0.032	0.161	0.019	0.024	0.164) $\times 10^{-3}$
14.1–15.3	(4.752	0.027	0.129	0.015	0.019	0.131) $\times 10^{-3}$
15.3–16.6	(3.812	0.023	0.103	0.012	0.016	0.105) $\times 10^{-3}$
16.6–18.0	(3.094	0.019	0.084	0.010	0.013	0.085) $\times 10^{-3}$
18.0–19.5	(2.425	0.016	0.066	0.007	0.011	0.067) $\times 10^{-3}$
19.5–21.1	(1.960	0.013	0.053	0.006	0.009	0.054) $\times 10^{-3}$
21.1–22.8	(1.563	0.011	0.043	0.005	0.007	0.043) $\times 10^{-3}$
22.8–24.7	(1.247	0.009	0.034	0.004	0.006	0.035) $\times 10^{-3}$
24.7–26.7	(9.884	0.075	0.271	0.029	0.046	0.276) $\times 10^{-4}$
26.7–28.8	(7.913	0.063	0.217	0.023	0.037	0.222) $\times 10^{-4}$
28.8–31.1	(6.324	0.052	0.174	0.018	0.030	0.178) $\times 10^{-4}$
31.1–33.5	(5.088	0.045	0.140	0.015	0.025	0.143) $\times 10^{-4}$
33.5–36.1	(4.066	0.038	0.113	0.012	0.020	0.115) $\times 10^{-4}$
36.1–38.9	(3.260	0.033	0.091	0.010	0.016	0.093) $\times 10^{-4}$
38.9–41.9	(2.643	0.028	0.074	0.008	0.014	0.075) $\times 10^{-4}$
41.9–45.1	(2.047	0.024	0.057	0.007	0.011	0.059) $\times 10^{-4}$
45.1–48.5	(1.674	0.021	0.047	0.006	0.009	0.048) $\times 10^{-4}$
48.5–52.2	(1.311	0.018	0.037	0.005	0.007	0.038) $\times 10^{-4}$
52.2–56.1	(1.074	0.016	0.031	0.004	0.006	0.031) $\times 10^{-4}$
56.1–60.3	(8.526	0.136	0.244	0.033	0.048	0.251) $\times 10^{-5}$
60.3–64.8	(6.956	0.119	0.200	0.028	0.041	0.206) $\times 10^{-5}$
64.8–69.7	(5.299	0.099	0.154	0.023	0.032	0.159) $\times 10^{-5}$
69.7–74.9	(4.453	0.088	0.130	0.021	0.028	0.134) $\times 10^{-5}$
74.9–80.5	(3.469	0.075	0.103	0.017	0.022	0.107) $\times 10^{-5}$
80.5–86.5	(2.865	0.066	0.085	0.015	0.019	0.088) $\times 10^{-5}$
86.5–93.0	(2.261	0.056	0.067	0.013	0.016	0.070) $\times 10^{-5}$
93.0–100	(1.833	0.049	0.055	0.011	0.013	0.058) $\times 10^{-5}$
100–108	(1.403	0.040	0.043	0.009	0.010	0.045) $\times 10^{-5}$
108–116	(1.169	0.036	0.036	0.008	0.009	0.038) $\times 10^{-5}$
116–125	(9.145	0.302	0.284	0.072	0.074	0.302) $\times 10^{-6}$
125–135	(6.700	0.245	0.213	0.057	0.056	0.228) $\times 10^{-6}$
135–147	(5.474	0.202	0.172	0.051	0.048	0.186) $\times 10^{-6}$
147–160	(4.021	0.166	0.129	0.042	0.037	0.141) $\times 10^{-6}$
160–175	(3.408	0.142	0.108	0.039	0.034	0.120) $\times 10^{-6}$
175–192	(2.300	0.110	0.076	0.029	0.024	0.085) $\times 10^{-6}$
192–211	(1.713	0.089	0.057	0.025	0.019	0.065) $\times 10^{-6}$

(*continued on next page*)

Table 14 (*continued*).

Rigidity [GV]	Φ_{Be}	σ_{stat}	σ_{acc}	σ_{unf}	σ_{scale}	σ_{syst}
211–233	(1.442	0.076	0.047	0.023	0.017	0.055) $\times 10^{-6}$
233–259	(9.505	0.566	0.314	0.174	0.125	0.380) $\times 10^{-7}$
259–291	(7.445	0.451	0.248	0.156	0.107	0.312) $\times 10^{-7}$
291–330	(4.686	0.324	0.159	0.113	0.075	0.209) $\times 10^{-7}$
330–379	(3.337	0.243	0.116	0.094	0.060	0.161) $\times 10^{-7}$
379–441	(2.325	0.180	0.078	0.078	0.047	0.120) $\times 10^{-7}$
441–525	(1.391	0.120	0.050	0.058	0.033	0.083) $\times 10^{-7}$
525–660	(8.464	0.737	0.299	0.457	0.240	0.596) $\times 10^{-8}$
660–880	(4.000	0.397	0.146	0.306	0.143	0.368) $\times 10^{-8}$
880–1300	(1.296	0.164	0.052	0.154	0.060	0.173) $\times 10^{-8}$
1300–3300	(0.153	0.056	0.010	0.017	0.009	0.022) $\times 10^{-8}$

Table 15
The Boron flux Φ_B as a function of rigidity at the top of AMS in units of $[\mathrm{m}^2\,\mathrm{sr\,s\,GV}]^{-1}$ including errors due to statistics (σ_{stat}); contributions to the systematic error from the trigger, acceptance, and background (σ_{acc}); the rigidity resolution function and unfolding (σ_{unf}); the absolute rigidity scale (σ_{scale}); and the total systematic error (σ_{syst}). The contribution of individual sources to the systematic error are added in quadrature to arrive at the total systematic error.

Rigidity [GV]	Φ_B	σ_{stat}	σ_{acc}	σ_{unf}	σ_{scale}	σ_{syst}
1.92–2.15	(4.852	0.019	0.268	0.061	0.023	0.276) $\times 10^{-1}$
2.15–2.40	(4.845	0.016	0.240	0.046	0.017	0.245) $\times 10^{-1}$
2.40–2.67	(4.703	0.014	0.210	0.037	0.011	0.214) $\times 10^{-1}$
2.67–2.97	(4.352	0.012	0.177	0.029	0.006	0.179) $\times 10^{-1}$
2.97–3.29	(3.921	0.010	0.146	0.022	0.002	0.148) $\times 10^{-1}$
3.29–3.64	(3.468	0.009	0.119	0.017	0.001	0.121) $\times 10^{-1}$
3.64–4.02	(3.024	0.007	0.097	0.013	0.002	0.098) $\times 10^{-1}$
4.02–4.43	(2.588	0.006	0.078	0.010	0.003	0.079) $\times 10^{-1}$
4.43–4.88	(2.170	0.005	0.062	0.007	0.003	0.063) $\times 10^{-1}$
4.88–5.37	(1.814	0.004	0.050	0.006	0.004	0.050) $\times 10^{-1}$
5.37–5.90	(1.494	0.003	0.040	0.005	0.003	0.040) $\times 10^{-1}$
5.90–6.47	(1.222	0.003	0.032	0.004	0.003	0.032) $\times 10^{-1}$
6.47–7.09	(9.973	0.023	0.252	0.029	0.028	0.255) $\times 10^{-2}$
7.09–7.76	(8.024	0.018	0.199	0.024	0.025	0.202) $\times 10^{-2}$
7.76–8.48	(6.488	0.015	0.159	0.019	0.021	0.161) $\times 10^{-2}$
8.48–9.26	(5.248	0.013	0.127	0.016	0.018	0.129) $\times 10^{-2}$
9.26–10.1	(4.199	0.011	0.101	0.013	0.015	0.103) $\times 10^{-2}$
10.1–11.0	(3.389	0.009	0.081	0.010	0.013	0.082) $\times 10^{-2}$
11.0–12.0	(2.701	0.007	0.064	0.008	0.010	0.065) $\times 10^{-2}$
12.0–13.0	(2.162	0.007	0.051	0.006	0.009	0.052) $\times 10^{-2}$
13.0–14.1	(1.731	0.006	0.041	0.005	0.007	0.042) $\times 10^{-2}$
14.1–15.3	(1.393	0.005	0.033	0.004	0.006	0.033) $\times 10^{-2}$
15.3–16.6	(1.113	0.004	0.026	0.003	0.005	0.027) $\times 10^{-2}$
16.6–18.0	(8.788	0.033	0.207	0.024	0.038	0.212) $\times 10^{-3}$
18.0–19.5	(7.075	0.028	0.166	0.019	0.032	0.170) $\times 10^{-3}$
19.5–21.1	(5.646	0.023	0.133	0.015	0.026	0.136) $\times 10^{-3}$
21.1–22.8	(4.486	0.019	0.106	0.012	0.021	0.109) $\times 10^{-3}$
22.8–24.7	(3.563	0.015	0.085	0.009	0.017	0.087) $\times 10^{-3}$
24.7–26.7	(2.841	0.013	0.068	0.007	0.014	0.069) $\times 10^{-3}$
26.7–28.8	(2.275	0.011	0.054	0.006	0.011	0.056) $\times 10^{-3}$
28.8–31.1	(1.802	0.009	0.043	0.004	0.009	0.044) $\times 10^{-3}$
31.1–33.5	(1.432	0.008	0.035	0.004	0.007	0.036) $\times 10^{-3}$
33.5–36.1	(1.159	0.006	0.028	0.003	0.006	0.029) $\times 10^{-3}$
36.1–38.9	(9.120	0.055	0.223	0.023	0.048	0.229) $\times 10^{-4}$
38.9–41.9	(7.194	0.047	0.178	0.019	0.038	0.183) $\times 10^{-4}$
41.9–45.1	(5.773	0.041	0.143	0.016	0.031	0.147) $\times 10^{-4}$
45.1–48.5	(4.701	0.036	0.117	0.013	0.026	0.121) $\times 10^{-4}$
48.5–52.2	(3.702	0.030	0.094	0.011	0.021	0.097) $\times 10^{-4}$
52.2–56.1	(2.990	0.027	0.076	0.009	0.017	0.079) $\times 10^{-4}$
56.1–60.3	(2.394	0.023	0.062	0.008	0.014	0.064) $\times 10^{-4}$
60.3–64.8	(1.910	0.020	0.050	0.007	0.011	0.051) $\times 10^{-4}$
64.8–69.7	(1.509	0.017	0.040	0.006	0.009	0.041) $\times 10^{-4}$
69.7–74.9	(1.212	0.015	0.032	0.005	0.008	0.033) $\times 10^{-4}$
74.9–80.5	(9.623	0.126	0.257	0.043	0.062	0.268) $\times 10^{-5}$
80.5–86.5	(7.739	0.109	0.209	0.037	0.051	0.218) $\times 10^{-5}$

(*continued on next page*)

Table 15 (*continued*).

Rigidity [GV]	Φ_B	σ_{stat}	σ_{acc}	σ_{unf}	σ_{scale}	σ_{syst}
86.5–93.0	(6.273	0.094	0.170	0.033	0.042	0.179) $\times 10^{-5}$
93.0–100	(4.879	0.080	0.135	0.028	0.034	0.142) $\times 10^{-5}$
100–108	(3.757	0.065	0.106	0.023	0.027	0.112) $\times 10^{-5}$
108–116	(3.068	0.059	0.088	0.021	0.023	0.093) $\times 10^{-5}$
116–125	(2.460	0.050	0.070	0.018	0.019	0.075) $\times 10^{-5}$
125–135	(1.874	0.041	0.055	0.015	0.015	0.059) $\times 10^{-5}$
135–147	(1.528	0.034	0.045	0.014	0.013	0.049) $\times 10^{-5}$
147–160	(1.158	0.028	0.035	0.011	0.010	0.038) $\times 10^{-5}$
160–175	(9.010	0.233	0.271	0.099	0.085	0.301) $\times 10^{-6}$
175–192	(6.788	0.189	0.203	0.083	0.069	0.229) $\times 10^{-6}$
192–211	(5.026	0.154	0.153	0.069	0.055	0.176) $\times 10^{-6}$
211–233	(3.845	0.125	0.119	0.059	0.045	0.140) $\times 10^{-6}$
233–259	(2.799	0.098	0.087	0.048	0.036	0.106) $\times 10^{-6}$
259–291	(2.001	0.075	0.066	0.039	0.029	0.082) $\times 10^{-6}$
291–330	(1.352	0.055	0.043	0.030	0.022	0.057) $\times 10^{-6}$
330–379	(9.053	0.404	0.302	0.233	0.167	0.416) $\times 10^{-7}$
379–441	(6.365	0.301	0.205	0.191	0.136	0.312) $\times 10^{-7}$
441–525	(3.879	0.202	0.127	0.139	0.097	0.212) $\times 10^{-7}$
525–660	(2.036	0.115	0.065	0.091	0.063	0.128) $\times 10^{-7}$
660–880	(1.043	0.065	0.035	0.062	0.042	0.082) $\times 10^{-7}$
880–1300	(4.361	0.303	0.142	0.366	0.235	0.457) $\times 10^{-8}$
1300–3300	(0.550	0.110	0.026	0.045	0.037	0.064) $\times 10^{-8}$

Table 16
The lithium to carbon flux ratio Li/C as a function of rigidity including errors due to statistics (σ_{stat}); contributions to the systematic error from the trigger, acceptance, and background (σ_{acc}); the rigidity resolution function and unfolding (σ_{unf}); the absolute rigidity scale (σ_{scale}); and the total systematic error (σ_{syst}). The statistical errors are the sum in quadrature of the ratios of lithium and carbon fluxes statistical errors to the corresponding flux values, multiplied by the flux ratio. The systematic errors from the background subtraction, the trigger, and the event reconstruction and selection are likewise added in quadrature. The correlations in the systematic errors from the uncertainty in nuclear interaction cross sections, the unfolding and the absolute rigidity scale between the lithium and carbon fluxes have been taken into account in calculating the corresponding systematic errors of the flux ratio. The contribution of individual sources to the systematic error are added in quadrature to arrive at the total systematic uncertainty.

Rigidity [GV]	Li/C	σ_{stat}	σ_{acc}	σ_{unf}	σ_{scale}	σ_{syst}
1.92–2.15	0.1670	0.0009	0.0041	0.0030	0.0000	0.0050
2.15–2.40	0.1723	0.0008	0.0044	0.0017	0.0001	0.0047
2.40–2.67	0.1805	0.0008	0.0045	0.0014	0.0001	0.0047
2.67–2.97	0.1917	0.0007	0.0047	0.0013	0.0001	0.0049
2.97–3.29	0.2023	0.0007	0.0048	0.0011	0.0001	0.0050
3.29–3.64	0.2102	0.0007	0.0049	0.0010	0.0000	0.0050
3.64–4.02	0.2145	0.0007	0.0050	0.0009	0.0001	0.0050
4.02–4.43	0.2183	0.0007	0.0050	0.0008	0.0000	0.0050
4.43–4.88	0.2197	0.0007	0.0050	0.0007	0.0000	0.0050
4.88–5.37	0.2201	0.0006	0.0049	0.0006	0.0001	0.0050
5.37–5.90	0.2211	0.0006	0.0049	0.0006	0.0001	0.0050
5.90–6.47	0.2191	0.0006	0.0049	0.0006	0.0001	0.0049
6.47–7.09	0.2180	0.0006	0.0048	0.0006	0.0001	0.0048
7.09–7.76	0.2170	0.0006	0.0048	0.0006	0.0001	0.0048
7.76–8.48	0.2134	0.0006	0.0047	0.0006	0.0001	0.0047
8.48–9.26	0.2111	0.0006	0.0046	0.0006	0.0001	0.0047
9.26–10.1	0.2089	0.0007	0.0046	0.0006	0.0001	0.0046
10.1–11.0	0.2038	0.0007	0.0045	0.0006	0.0001	0.0045
11.0–12.0	0.1999	0.0007	0.0044	0.0006	0.0001	0.0044
12.0–13.0	0.1971	0.0008	0.0043	0.0006	0.0001	0.0044
13.0–14.1	0.1925	0.0008	0.0042	0.0006	0.0001	0.0043
14.1–15.3	0.1884	0.0008	0.0041	0.0006	0.0001	0.0042
15.3–16.6	0.1842	0.0008	0.0041	0.0006	0.0001	0.0041
16.6–18.0	0.1790	0.0008	0.0040	0.0006	0.0001	0.0040
18.0–19.5	0.1748	0.0009	0.0039	0.0006	0.0001	0.0039
19.5–21.1	0.1692	0.0009	0.0037	0.0006	0.0001	0.0038
21.1–22.8	0.1649	0.0009	0.0037	0.0006	0.0001	0.0037
22.8–24.7	0.1624	0.0009	0.0036	0.0006	0.0002	0.0037
24.7–26.7	0.1577	0.0009	0.0035	0.0005	0.0002	0.0036
26.7–28.8	0.1531	0.0009	0.0034	0.0005	0.0002	0.0035
28.8–31.1	0.1504	0.0009	0.0034	0.0005	0.0002	0.0034
31.1–33.5	0.1456	0.0010	0.0033	0.0005	0.0002	0.0033
33.5–36.1	0.1407	0.0010	0.0032	0.0005	0.0002	0.0032
36.1–38.9	0.1367	0.0010	0.0031	0.0005	0.0002	0.0031
38.9–41.9	0.1338	0.0011	0.0030	0.0005	0.0002	0.0031
41.9–45.1	0.1291	0.0011	0.0029	0.0005	0.0002	0.0030
45.1–48.5	0.1296	0.0012	0.0030	0.0006	0.0002	0.0030
48.5–52.2	0.1207	0.0012	0.0028	0.0005	0.0001	0.0028
52.2–56.1	0.1184	0.0013	0.0027	0.0005	0.0002	0.0028
56.1–60.3	0.1135	0.0014	0.0026	0.0005	0.0002	0.0027
60.3–64.8	0.1127	0.0014	0.0026	0.0005	0.0002	0.0027

(*continued on next page*)

Table 16 (*continued*).

Rigidity [GV]	Li/C	σ_{stat}	σ_{acc}	σ_{unf}	σ_{scale}	σ_{syst}
64.8–69.7	0.1079	0.0015	0.0025	0.0005	0.0002	0.0026
69.7–74.9	0.1075	0.0016	0.0025	0.0006	0.0002	0.0026
74.9–80.5	0.0999	0.0016	0.0024	0.0005	0.0002	0.0024
80.5–86.5	0.0992	0.0017	0.0024	0.0006	0.0002	0.0024
86.5–93.0	0.0970	0.0018	0.0023	0.0006	0.0002	0.0024
93.0–100	0.0945	0.0019	0.0023	0.0006	0.0002	0.0023
100–108	0.0899	0.0019	0.0022	0.0006	0.0002	0.0022
108–116	0.0846	0.0020	0.0021	0.0005	0.0002	0.0021
116–125	0.0808	0.0021	0.0020	0.0005	0.0002	0.0021
125–135	0.0821	0.0022	0.0020	0.0006	0.0002	0.0021
135–147	0.0798	0.0022	0.0020	0.0006	0.0002	0.0021
147–160	0.0818	0.0024	0.0020	0.0007	0.0002	0.0021
160–175	0.0776	0.0025	0.0019	0.0007	0.0002	0.0021
175–192	0.0752	0.0026	0.0019	0.0007	0.0003	0.0020
192–211	0.0725	0.0027	0.0018	0.0008	0.0003	0.0020
211–233	0.0696	0.0028	0.0018	0.0008	0.0003	0.0020
233–259	0.0697	0.0029	0.0018	0.0009	0.0003	0.0020
259–291	0.0603	0.0028	0.0016	0.0009	0.0003	0.0018
291–330	0.0609	0.0030	0.0016	0.0010	0.0003	0.0019
330–379	0.0625	0.0032	0.0016	0.0012	0.0003	0.0020
379–441	0.0659	0.0036	0.0017	0.0014	0.0003	0.0023
441–525	0.0517	0.0033	0.0014	0.0013	0.0002	0.0019
525–660	0.0527	0.0034	0.0014	0.0017	0.0002	0.0022
660–880	0.0510	0.0037	0.0014	0.0022	0.0001	0.0026
880–1300	0.0469	0.0040	0.0013	0.0029	0.0001	0.0032
1300–3300	0.0486	0.0090	0.0020	0.0035	0.0003	0.0041

Table 17
The beryllium to carbon flux ratio Be/C as a function of rigidity including errors due to statistics (σ_{stat}); contributions to the systematic error from the trigger, acceptance, and background (σ_{acc}); the rigidity resolution function and unfolding (σ_{unf}); the absolute rigidity scale (σ_{scale}); and the total systematic error (σ_{syst}). The statistical errors are the sum in quadrature of the ratios of beryllium and carbon fluxes statistical errors to the corresponding flux values, multiplied by the flux ratio. The systematic errors from the background subtraction, the trigger, and the event reconstruction and selection are likewise added in quadrature. The correlations in the systematic errors from the uncertainty in nuclear interaction cross sections, the unfolding and the absolute rigidity scale between the beryllium and carbon fluxes have been taken into account in calculating the corresponding systematic errors of the flux ratio. The contribution of individual sources to the systematic error are added in quadrature to arrive at the total systematic uncertainty.

Rigidity [GV]	Be/C	σ_{stat}	σ_{acc}	σ_{unf}	σ_{scale}	σ_{syst}
1.92–2.15	0.0938	0.0006	0.0025	0.0017	0.0001	0.0030
2.15–2.40	0.0935	0.0006	0.0024	0.0009	0.0000	0.0026
2.40–2.67	0.0924	0.0005	0.0024	0.0007	0.0000	0.0025
2.67–2.97	0.0950	0.0005	0.0024	0.0006	0.0000	0.0025
2.97–3.29	0.1005	0.0005	0.0025	0.0006	0.0000	0.0025
3.29–3.64	0.1025	0.0005	0.0025	0.0005	0.0000	0.0025
3.64–4.02	0.1048	0.0005	0.0025	0.0004	0.0000	0.0025
4.02–4.43	0.1056	0.0005	0.0025	0.0004	0.0000	0.0025
4.43–4.88	0.1059	0.0004	0.0025	0.0003	0.0000	0.0025
4.88–5.37	0.1062	0.0004	0.0025	0.0003	0.0000	0.0025
5.37–5.90	0.1053	0.0004	0.0024	0.0003	0.0000	0.0025
5.90–6.47	0.1044	0.0004	0.0024	0.0003	0.0000	0.0024
6.47–7.09	0.1033	0.0004	0.0024	0.0003	0.0000	0.0024
7.09–7.76	0.1018	0.0004	0.0023	0.0003	0.0000	0.0024
7.76–8.48	0.0994	0.0004	0.0023	0.0003	0.0000	0.0023
8.48–9.26	0.0989	0.0004	0.0023	0.0003	0.0000	0.0023
9.26–10.1	0.0978	0.0004	0.0022	0.0003	0.0000	0.0023
10.1–11.0	0.0960	0.0005	0.0022	0.0003	0.0000	0.0022
11.0–12.0	0.0932	0.0005	0.0021	0.0003	0.0000	0.0022
12.0–13.0	0.0935	0.0005	0.0021	0.0003	0.0000	0.0022
13.0–14.1	0.0914	0.0005	0.0021	0.0003	0.0000	0.0021
14.1–15.3	0.0895	0.0005	0.0021	0.0002	0.0000	0.0021
15.3–16.6	0.0880	0.0006	0.0020	0.0002	0.0001	0.0020
16.6–18.0	0.0875	0.0006	0.0020	0.0002	0.0001	0.0020
18.0–19.5	0.0839	0.0006	0.0019	0.0002	0.0001	0.0020
19.5–21.1	0.0828	0.0006	0.0019	0.0002	0.0001	0.0019
21.1–22.8	0.0809	0.0006	0.0019	0.0002	0.0001	0.0019
22.8–24.7	0.0791	0.0006	0.0018	0.0002	0.0001	0.0019
24.7–26.7	0.0769	0.0006	0.0018	0.0002	0.0001	0.0018
26.7–28.8	0.0754	0.0006	0.0018	0.0002	0.0001	0.0018
28.8–31.1	0.0739	0.0006	0.0018	0.0002	0.0001	0.0018
31.1–33.5	0.0724	0.0007	0.0017	0.0002	0.0001	0.0017
33.5–36.1	0.0704	0.0007	0.0017	0.0002	0.0001	0.0017
36.1–38.9	0.0687	0.0007	0.0017	0.0002	0.0001	0.0017
38.9–41.9	0.0680	0.0008	0.0017	0.0003	0.0001	0.0017
41.9–45.1	0.0645	0.0008	0.0016	0.0003	0.0001	0.0016
45.1–48.5	0.0640	0.0008	0.0016	0.0003	0.0001	0.0016
48.5–52.2	0.0606	0.0009	0.0015	0.0003	0.0001	0.0015
52.2–56.1	0.0605	0.0009	0.0015	0.0003	0.0001	0.0015
56.1–60.3	0.0582	0.0010	0.0015	0.0003	0.0001	0.0015
60.3–64.8	0.0584	0.0010	0.0015	0.0003	0.0001	0.0015
64.8–69.7	0.0539	0.0010	0.0014	0.0003	0.0001	0.0014
69.7–74.9	0.0553	0.0011	0.0014	0.0003	0.0001	0.0015
74.9–80.5	0.0522	0.0012	0.0014	0.0003	0.0001	0.0014
80.5–86.5	0.0531	0.0013	0.0014	0.0003	0.0001	0.0014
86.5–93.0	0.0505	0.0013	0.0014	0.0003	0.0001	0.0014
93.0–100	0.0508	0.0014	0.0014	0.0003	0.0001	0.0014
100–108	0.0471	0.0014	0.0013	0.0003	0.0001	0.0013
108–116	0.0483	0.0015	0.0013	0.0003	0.0001	0.0014
116–125	0.0462	0.0016	0.0013	0.0003	0.0001	0.0014
125–135	0.0418	0.0016	0.0012	0.0003	0.0001	0.0013
135–147	0.0425	0.0016	0.0012	0.0004	0.0001	0.0013
147–160	0.0403	0.0017	0.0012	0.0004	0.0001	0.0013
160–175	0.0432	0.0018	0.0013	0.0004	0.0002	0.0014
175–192	0.0375	0.0018	0.0012	0.0004	0.0002	0.0012

(*continued on next page*)

Table 17 (*continued*).

Rigidity [GV]	Be/C	σ_{stat}	σ_{acc}	σ_{unf}	σ_{scale}	σ_{syst}
192–211	0.0353	0.0019	0.0011	0.0004	0.0002	0.0012
211–233	0.0394	0.0021	0.0012	0.0006	0.0002	0.0013
233–259	0.0333	0.0020	0.0010	0.0005	0.0002	0.0012
259–291	0.0349	0.0022	0.0011	0.0006	0.0002	0.0013
291–330	0.0309	0.0022	0.0010	0.0006	0.0002	0.0012
330–379	0.0309	0.0023	0.0010	0.0008	0.0002	0.0013
379–441	0.0326	0.0026	0.0010	0.0010	0.0002	0.0014
441–525	0.0283	0.0025	0.0010	0.0010	0.0002	0.0014
525–660	0.0295	0.0026	0.0010	0.0014	0.0002	0.0017
660–880	0.0278	0.0028	0.0010	0.0019	0.0001	0.0021
880–1300	0.0220	0.0028	0.0008	0.0023	0.0000	0.0025
1300–3300	0.0131	0.0048	0.0008	0.0013	0.0000	0.0016

Table 18
The boron to carbon flux ratio B/C as a function of rigidity including errors due to statistics (σ_{stat}); contributions to the systematic error from the trigger, acceptance, and background (σ_{acc}); the rigidity resolution function and unfolding (σ_{unf}); the absolute rigidity scale (σ_{scale}); and the total systematic error (σ_{syst}). The statistical errors are the sum in quadrature of the ratios of boron and carbon fluxes statistical errors to the corresponding flux values, multiplied by the flux ratio. The systematic errors from the background subtraction, the trigger, and the event reconstruction and selection are likewise added in quadrature. The correlations in the systematic errors from the uncertainty in nuclear interaction cross sections, the unfolding and the absolute rigidity scale between the boron and carbon fluxes have been taken into account in calculating the corresponding systematic errors of the flux ratio. The contribution of individual sources to the systematic error are added in quadrature to arrive at the total systematic uncertainty.

Rigidity [GV]	B/C	σ_{stat}	σ_{acc}	σ_{unf}	σ_{scale}	σ_{syst}
1.92–2.15	0.2867	0.0013	0.0150	0.0051	0.0002	0.0159
2.15–2.40	0.2915	0.0011	0.0137	0.0031	0.0002	0.0140
2.40–2.67	0.2995	0.0010	0.0127	0.0025	0.0002	0.0129
2.67–2.97	0.3061	0.0010	0.0117	0.0022	0.0002	0.0119
2.97–3.29	0.3142	0.0010	0.0110	0.0019	0.0001	0.0111
3.29–3.64	0.3199	0.0009	0.0102	0.0017	0.0001	0.0104
3.64–4.02	0.3250	0.0009	0.0096	0.0014	0.0000	0.0097
4.02–4.43	0.3253	0.0009	0.0090	0.0012	0.0001	0.0091
4.43–4.88	0.3213	0.0009	0.0084	0.0011	0.0001	0.0085
4.88–5.37	0.3188	0.0008	0.0079	0.0010	0.0001	0.0080
5.37–5.90	0.3149	0.0008	0.0075	0.0009	0.0002	0.0075
5.90–6.47	0.3093	0.0008	0.0071	0.0008	0.0002	0.0072
6.47–7.09	0.3056	0.0008	0.0068	0.0008	0.0002	0.0069
7.09–7.76	0.2993	0.0008	0.0065	0.0008	0.0001	0.0066
7.76–8.48	0.2943	0.0008	0.0063	0.0008	0.0001	0.0064
8.48–9.26	0.2910	0.0008	0.0062	0.0008	0.0001	0.0062
9.26–10.1	0.2857	0.0008	0.0060	0.0007	0.0001	0.0060
10.1–11.0	0.2823	0.0008	0.0058	0.0007	0.0001	0.0059
11.0–12.0	0.2765	0.0009	0.0057	0.0007	0.0001	0.0057
12.0–13.0	0.2712	0.0009	0.0055	0.0007	0.0001	0.0056
13.0–14.1	0.2639	0.0009	0.0054	0.0007	0.0001	0.0054
14.1–15.3	0.2597	0.0010	0.0053	0.0007	0.0002	0.0053
15.3–16.6	0.2543	0.0010	0.0052	0.0007	0.0002	0.0052
16.6–18.0	0.2461	0.0010	0.0050	0.0006	0.0002	0.0051
18.0–19.5	0.2425	0.0011	0.0050	0.0006	0.0002	0.0050
19.5–21.1	0.2363	0.0011	0.0049	0.0006	0.0002	0.0049
21.1–22.8	0.2298	0.0011	0.0047	0.0006	0.0002	0.0048
22.8–24.7	0.2238	0.0011	0.0047	0.0006	0.0002	0.0047
24.7–26.7	0.2190	0.0011	0.0046	0.0006	0.0002	0.0046
26.7–28.8	0.2145	0.0011	0.0045	0.0006	0.0002	0.0045
28.8–31.1	0.2086	0.0011	0.0044	0.0006	0.0002	0.0045
31.1–33.5	0.2017	0.0012	0.0043	0.0006	0.0002	0.0044
33.5–36.1	0.1988	0.0012	0.0043	0.0007	0.0002	0.0044
36.1–38.9	0.1904	0.0013	0.0042	0.0007	0.0002	0.0042
38.9–41.9	0.1834	0.0013	0.0041	0.0007	0.0002	0.0041
41.9–45.1	0.1800	0.0014	0.0040	0.0007	0.0002	0.0041
45.1–48.5	0.1780	0.0015	0.0040	0.0007	0.0002	0.0041
48.5–52.2	0.1694	0.0015	0.0039	0.0007	0.0002	0.0040
52.2–56.1	0.1668	0.0016	0.0039	0.0007	0.0002	0.0040
56.1–60.3	0.1618	0.0017	0.0038	0.0007	0.0002	0.0039
60.3–64.8	0.1589	0.0018	0.0038	0.0007	0.0002	0.0039
64.8–69.7	0.1519	0.0018	0.0037	0.0007	0.0002	0.0038
69.7–74.9	0.1489	0.0019	0.0037	0.0007	0.0002	0.0037
74.9–80.5	0.1434	0.0020	0.0036	0.0007	0.0002	0.0036
80.5–86.5	0.1420	0.0021	0.0036	0.0008	0.0002	0.0037
86.5–93.0	0.1388	0.0022	0.0035	0.0008	0.0003	0.0036
93.0–100	0.1340	0.0023	0.0035	0.0008	0.0003	0.0036
100–108	0.1247	0.0023	0.0033	0.0008	0.0003	0.0034
108–116	0.1256	0.0026	0.0034	0.0008	0.0003	0.0035
116–125	0.1230	0.0026	0.0033	0.0008	0.0003	0.0034
125–135	0.1157	0.0027	0.0032	0.0009	0.0003	0.0033
135–147	0.1176	0.0028	0.0033	0.0009	0.0003	0.0034
147–160	0.1148	0.0030	0.0033	0.0010	0.0003	0.0035
160–175	0.1131	0.0031	0.0033	0.0011	0.0004	0.0034
175–192	0.1096	0.0032	0.0031	0.0012	0.0004	0.0034

(*continued on next page*)

Table 18 (*continued*).

Rigidity [GV]	B/C	σ_{stat}	σ_{acc}	σ_{unf}	σ_{scale}	σ_{syst}
192–211	0.1025	0.0033	0.0030	0.0012	0.0004	0.0032
211–233	0.1040	0.0036	0.0031	0.0014	0.0004	0.0034
233–259	0.0970	0.0036	0.0029	0.0014	0.0004	0.0033
259–291	0.0929	0.0036	0.0030	0.0016	0.0005	0.0034
291–330	0.0883	0.0038	0.0027	0.0017	0.0005	0.0032
330–379	0.0829	0.0039	0.0027	0.0019	0.0005	0.0033
379–441	0.0884	0.0044	0.0028	0.0023	0.0006	0.0037
441–525	0.0782	0.0042	0.0025	0.0024	0.0006	0.0035
525–660	0.0703	0.0041	0.0022	0.0027	0.0006	0.0035
660–880	0.0717	0.0046	0.0023	0.0037	0.0007	0.0044
880–1300	0.0733	0.0053	0.0023	0.0054	0.0007	0.0059
1300–3300	0.0465	0.0095	0.0022	0.0033	0.0005	0.0040

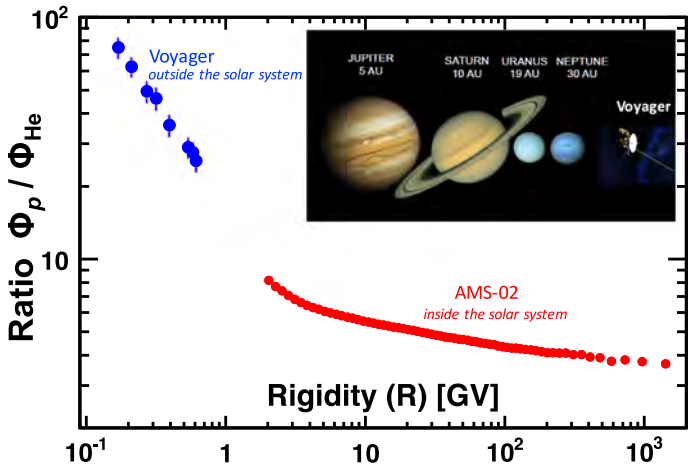

Fig. 79. The AMS rigidity dependence of the helium-to-proton flux ratio, measured in the solar system at 1 a.u. together with the Voyager data, measured outside the solar system at >100 a.u. (see insert).

The AMS data on the cosmic ray fluxes of protons and helium presented in Sections 4 and 8 provide an accurate measurement of the proton-to-helium ratio as shown in Fig. 80 (Table 12). As seen, the ratio is not constant, it decreases in the rigidity range 1.9–1800 GV, but the rate of decrease vanishes at high rigidities. Surprisingly, the observed ratio dependence above 3.5 GV can be fitted by the function $A + C(R/3.5\,GV)^{\Delta}$, where R is the rigidity and A, C and Δ are rigidity independent fit parameters. The beginning of the fit range (3.5 GV) is chosen such that the solar modulation effects are negligible (see Section 15). The fit yields

$$A = 3.15 \pm 0.07,$$
$$C = 3.30 \pm 0.07,$$
$$\Delta = -0.30 \pm 0.01,$$
$$\text{with } \chi^2/\text{d.o.f.} = 56/58.$$

Remarkably, the value of the parameter Δ is very close to the value of the spectral index of the Li/C, Be/C, B/C, Li/O, Be/O, and B/O ratios measured at high rigidities (-0.266 ± 0.022 above 192 GV, see Section 10).

An interpretation of this AMS result is that the proton flux has two components. One component has an identical rigidity dependence to the helium flux. Another component has a much softer dependence. This soft component is pronounced at low rigidities. At high rigidities, the hard component dominates and the proton-to-helium flux ratio gradually approaches a constant value of $A = 3.15$.

10. Secondary lithium, beryllium, boron fluxes and secondary to primary ratios

Lithium, beryllium, and boron nuclei in cosmic rays are thought to be produced by the collisions of the primary nuclei with the interstellar medium. They are called secondary cosmic rays. Precise knowledge of their spectra in the GV–TV rigidity region provides important information on the propagation of cosmic rays through the interstellar medium as well as the properties of the interstellar medium. Over the last 50 years, only a few experiments have measured the lithium and beryllium fluxes in cosmic rays above a few GV. Typically, these measurements have errors larger than 50%

Table 19
The lithium to oxygen flux ratio Li/O as a function of rigidity including errors due to statistics (σ_{stat}); contributions to the systematic error from the trigger, acceptance, and background (σ_{acc}); the rigidity resolution function and unfolding (σ_{unf}); the absolute rigidity scale (σ_{scale}); and the total systematic error (σ_{syst}). The statistical errors are the sum in quadrature of the ratios of lithium and oxygen fluxes statistical errors to the corresponding flux values, multiplied by the flux ratio. The systematic errors from the background subtraction, the trigger, and the event reconstruction and selection are likewise added in quadrature. The correlations in the systematic errors from the uncertainty in nuclear interaction cross sections, the unfolding and the absolute rigidity scale between the lithium and oxygen fluxes have been taken into account in calculating the corresponding systematic errors of the flux ratio. The contribution of individual sources to the systematic error are added in quadrature to arrive at the total systematic uncertainty.

Rigidity [GV]	Li/O	σ_{stat}	σ_{acc}	σ_{unf}	σ_{scale}	σ_{syst}
2.15–2.40	0.1835	0.0009	0.0050	0.0020	0.0001	0.0054
2.40–2.67	0.1971	0.0008	0.0052	0.0017	0.0001	0.0055
2.67–2.97	0.2087	0.0008	0.0052	0.0016	0.0001	0.0055
2.97–3.29	0.2178	0.0008	0.0053	0.0014	0.0001	0.0054
3.29–3.64	0.2247	0.0008	0.0053	0.0012	0.0000	0.0054
3.64–4.02	0.2272	0.0008	0.0052	0.0010	0.0000	0.0053
4.02–4.43	0.2310	0.0008	0.0052	0.0009	0.0000	0.0053
4.43–4.88	0.2326	0.0007	0.0052	0.0008	0.0001	0.0053
4.88–5.37	0.2327	0.0007	0.0052	0.0007	0.0001	0.0052
5.37–5.90	0.2327	0.0007	0.0052	0.0007	0.0001	0.0052
5.90–6.47	0.2301	0.0007	0.0051	0.0006	0.0001	0.0051
6.47–7.09	0.2279	0.0007	0.0050	0.0006	0.0001	0.0051
7.09–7.76	0.2262	0.0007	0.0050	0.0006	0.0001	0.0050
7.76–8.48	0.2216	0.0007	0.0049	0.0006	0.0001	0.0050
8.48–9.26	0.2181	0.0007	0.0048	0.0006	0.0001	0.0049
9.26–10.1	0.2143	0.0007	0.0048	0.0006	0.0001	0.0048
10.1–11.0	0.2091	0.0007	0.0047	0.0007	0.0001	0.0047
11.0–12.0	0.2033	0.0007	0.0045	0.0006	0.0002	0.0046
12.0–13.0	0.1989	0.0008	0.0045	0.0006	0.0002	0.0045
13.0–14.1	0.1945	0.0008	0.0044	0.0006	0.0002	0.0044
14.1–15.3	0.1903	0.0008	0.0043	0.0006	0.0002	0.0043
15.3–16.6	0.1845	0.0008	0.0042	0.0006	0.0002	0.0042
16.6–18.0	0.1788	0.0008	0.0040	0.0006	0.0002	0.0041
18.0–19.5	0.1734	0.0009	0.0039	0.0006	0.0002	0.0040
19.5–21.1	0.1676	0.0009	0.0038	0.0006	0.0002	0.0038
21.1–22.8	0.1624	0.0009	0.0037	0.0005	0.0002	0.0037
22.8–24.7	0.1595	0.0009	0.0036	0.0005	0.0002	0.0037
24.7–26.7	0.1545	0.0009	0.0035	0.0005	0.0002	0.0036
26.7–28.8	0.1496	0.0009	0.0034	0.0005	0.0002	0.0035
28.8–31.1	0.1448	0.0009	0.0033	0.0005	0.0002	0.0034
31.1–33.5	0.1399	0.0009	0.0032	0.0005	0.0002	0.0033
33.5–36.1	0.1352	0.0010	0.0031	0.0005	0.0002	0.0032
36.1–38.9	0.1305	0.0010	0.0031	0.0005	0.0002	0.0031
38.9–41.9	0.1283	0.0010	0.0030	0.0005	0.0002	0.0031
41.9–45.1	0.1222	0.0011	0.0029	0.0005	0.0002	0.0029
45.1–48.5	0.1221	0.0011	0.0029	0.0005	0.0002	0.0030
48.5–52.2	0.1141	0.0012	0.0027	0.0005	0.0002	0.0028
52.2–56.1	0.1114	0.0012	0.0027	0.0005	0.0002	0.0027
56.1–60.3	0.1076	0.0013	0.0026	0.0005	0.0002	0.0027
60.3–64.8	0.1047	0.0013	0.0026	0.0005	0.0002	0.0026
64.8–69.7	0.1008	0.0014	0.0025	0.0005	0.0002	0.0025
69.7–74.9	0.1008	0.0015	0.0025	0.0005	0.0002	0.0026
74.9–80.5	0.0933	0.0015	0.0024	0.0005	0.0002	0.0024
80.5–86.5	0.0912	0.0016	0.0023	0.0005	0.0002	0.0024
86.5–93.0	0.0901	0.0017	0.0023	0.0005	0.0002	0.0024
93.0–100	0.0866	0.0017	0.0023	0.0005	0.0002	0.0023
100–108	0.0829	0.0017	0.0022	0.0005	0.0002	0.0022
108–116	0.0770	0.0019	0.0020	0.0005	0.0002	0.0021
116–125	0.0733	0.0019	0.0020	0.0005	0.0002	0.0020

(*continued on next page*)

at 100 GV. For the boron flux, measurements have errors larger than 15% at 100 GV. Fig. 81 shows the measurements of lithium, beryllium and boron cosmic rays available before AMS [127–136].

We present precision measurements of the lithium, beryllium, and boron fluxes in cosmic rays in the rigidity range from 1.9 GV to 3.3 TV. These measurements are based on 3.0 million lithium, 1.7 million beryllium, and 4.2 million boron nuclei collected by AMS. The total error on each of the fluxes is 3% at 100 GV (Tables 13, 14, and 15). These new AMS results are consistent with earlier AMS measurements [137] but have smaller statistical and systematic errors.

Table 19 (*continued*).

Rigidity [GV]	Li/O	σ_{stat}	σ_{acc}	σ_{unf}	σ_{scale}	σ_{syst}
125–135	0.0744	0.0020	0.0020	0.0005	0.0002	0.0021
135–147	0.0724	0.0020	0.0020	0.0005	0.0002	0.0021
147–160	0.0734	0.0022	0.0020	0.0006	0.0002	0.0021
160–175	0.0693	0.0022	0.0019	0.0006	0.0002	0.0020
175–192	0.0664	0.0023	0.0019	0.0006	0.0002	0.0020
192–211	0.0646	0.0024	0.0019	0.0007	0.0002	0.0020
211–233	0.0611	0.0024	0.0018	0.0007	0.0002	0.0019
233–259	0.0632	0.0026	0.0019	0.0008	0.0002	0.0021
259–291	0.0541	0.0025	0.0017	0.0008	0.0002	0.0018
291–330	0.0541	0.0027	0.0017	0.0009	0.0002	0.0019
330–379	0.0561	0.0029	0.0018	0.0010	0.0002	0.0021
379–441	0.0577	0.0032	0.0019	0.0012	0.0002	0.0022
441–525	0.0491	0.0031	0.0016	0.0013	0.0002	0.0021
525–660	0.0493	0.0032	0.0017	0.0016	0.0001	0.0023
660–880	0.0464	0.0034	0.0016	0.0020	0.0001	0.0026
880–1300	0.0405	0.0035	0.0015	0.0025	0.0000	0.0029
1300–3300	0.0459	0.0085	0.0023	0.0033	0.0001	0.0041

Table 20
The beryllium to oxygen flux ratio Be/O as a function of rigidity including errors due to statistics (σ_{stat}); contributions to the systematic error from the trigger, acceptance, and background (σ_{acc}); the rigidity resolution function and unfolding (σ_{unf}); the absolute rigidity scale (σ_{scale}); and the total systematic error (σ_{syst}). The statistical errors are the sum in quadrature of the ratios of beryllium and oxygen fluxes statistical errors to the corresponding flux values, multiplied by the flux ratio. The systematic errors from the background subtraction, the trigger, and the event reconstruction and selection are likewise added in quadrature. The correlations in the systematic errors from the uncertainty in nuclear interaction cross sections, the unfolding and the absolute rigidity scale between the beryllium and oxygen fluxes have been taken into account in calculating the corresponding systematic errors of the flux ratio. The contribution of individual sources to the systematic error are added in quadrature to arrive at the total systematic uncertainty.

Rigidity [GV]	Be/O	σ_{stat}	σ_{acc}	σ_{unf}	σ_{scale}	σ_{syst}
2.15–2.40	0.0996	0.0006	0.0027	0.0011	0.0000	0.0029
2.40–2.67	0.1009	0.0006	0.0026	0.0009	0.0000	0.0027
2.67–2.97	0.1034	0.0005	0.0025	0.0008	0.0000	0.0026
2.97–3.29	0.1082	0.0005	0.0026	0.0007	0.0000	0.0027
3.29–3.64	0.1095	0.0005	0.0026	0.0006	0.0000	0.0027
3.64–4.02	0.1110	0.0005	0.0026	0.0005	0.0000	0.0027
4.02–4.43	0.1117	0.0005	0.0026	0.0005	0.0000	0.0027
4.43–4.88	0.1121	0.0005	0.0026	0.0004	0.0000	0.0027
4.88–5.37	0.1123	0.0005	0.0026	0.0004	0.0000	0.0027
5.37–5.90	0.1108	0.0005	0.0026	0.0003	0.0000	0.0026
5.90–6.47	0.1096	0.0005	0.0026	0.0003	0.0000	0.0026
6.47–7.09	0.1079	0.0004	0.0025	0.0003	0.0000	0.0026
7.09–7.76	0.1061	0.0004	0.0025	0.0003	0.0001	0.0025
7.76–8.48	0.1032	0.0004	0.0024	0.0003	0.0001	0.0025
8.48–9.26	0.1022	0.0004	0.0024	0.0003	0.0001	0.0024
9.26–10.1	0.1003	0.0005	0.0024	0.0003	0.0001	0.0024
10.1–11.0	0.0985	0.0005	0.0023	0.0003	0.0001	0.0024
11.0–12.0	0.0948	0.0005	0.0023	0.0003	0.0001	0.0023
12.0–13.0	0.0944	0.0005	0.0022	0.0003	0.0001	0.0023
13.0–14.1	0.0924	0.0005	0.0022	0.0003	0.0001	0.0022
14.1–15.3	0.0904	0.0005	0.0022	0.0003	0.0001	0.0022
15.3–16.6	0.0881	0.0006	0.0021	0.0002	0.0001	0.0021
16.6–18.0	0.0874	0.0006	0.0021	0.0002	0.0001	0.0021
18.0–19.5	0.0833	0.0006	0.0020	0.0002	0.0001	0.0020
19.5–21.1	0.0821	0.0006	0.0020	0.0002	0.0001	0.0020
21.1–22.8	0.0796	0.0006	0.0019	0.0002	0.0001	0.0019
22.8–24.7	0.0777	0.0006	0.0019	0.0002	0.0001	0.0019
24.7–26.7	0.0754	0.0006	0.0019	0.0002	0.0001	0.0019
26.7–28.8	0.0736	0.0006	0.0018	0.0002	0.0001	0.0018
28.8–31.1	0.0712	0.0006	0.0018	0.0002	0.0001	0.0018
31.1–33.5	0.0695	0.0006	0.0017	0.0002	0.0001	0.0018
33.5–36.1	0.0677	0.0007	0.0017	0.0002	0.0001	0.0017
36.1–38.9	0.0656	0.0007	0.0017	0.0002	0.0001	0.0017
38.9–41.9	0.0652	0.0007	0.0017	0.0002	0.0001	0.0017
41.9–45.1	0.0610	0.0007	0.0016	0.0002	0.0001	0.0016

(*continued on next page*)

Table 20 (*continued*).

Rigidity [GV]	Be/O	σ_{stat}	σ_{acc}	σ_{unf}	σ_{scale}	σ_{syst}
45.1–48.5	0.0604	0.0008	0.0016	0.0002	0.0001	0.0016
48.5–52.2	0.0573	0.0008	0.0015	0.0002	0.0001	0.0015
52.2–56.1	0.0569	0.0009	0.0015	0.0002	0.0001	0.0015
56.1–60.3	0.0552	0.0009	0.0015	0.0002	0.0001	0.0015
60.3–64.8	0.0543	0.0010	0.0015	0.0002	0.0001	0.0015
64.8–69.7	0.0504	0.0010	0.0014	0.0002	0.0001	0.0014
69.7–74.9	0.0518	0.0011	0.0014	0.0002	0.0001	0.0015
74.9–80.5	0.0488	0.0011	0.0014	0.0002	0.0001	0.0014
80.5–86.5	0.0488	0.0012	0.0014	0.0003	0.0001	0.0014
86.5–93.0	0.0470	0.0012	0.0014	0.0003	0.0001	0.0014
93.0–100	0.0466	0.0013	0.0014	0.0003	0.0001	0.0014
100–108	0.0434	0.0013	0.0013	0.0003	0.0001	0.0013
108–116	0.0440	0.0014	0.0013	0.0003	0.0001	0.0014
116–125	0.0419	0.0014	0.0013	0.0003	0.0001	0.0013
125–135	0.0379	0.0014	0.0012	0.0003	0.0001	0.0012
135–147	0.0386	0.0015	0.0012	0.0003	0.0001	0.0013
147–160	0.0361	0.0015	0.0012	0.0003	0.0001	0.0012
160–175	0.0386	0.0016	0.0013	0.0004	0.0001	0.0013
175–192	0.0331	0.0016	0.0011	0.0004	0.0001	0.0012
192–211	0.0315	0.0017	0.0011	0.0004	0.0001	0.0012
211–233	0.0346	0.0019	0.0012	0.0005	0.0001	0.0013
233–259	0.0302	0.0018	0.0011	0.0005	0.0001	0.0012
259–291	0.0313	0.0019	0.0011	0.0006	0.0002	0.0013
291–330	0.0275	0.0019	0.0010	0.0006	0.0001	0.0012
330–379	0.0277	0.0021	0.0010	0.0007	0.0002	0.0013
379–441	0.0286	0.0023	0.0011	0.0008	0.0002	0.0014
441–525	0.0269	0.0024	0.0011	0.0010	0.0002	0.0014
525–660	0.0276	0.0024	0.0011	0.0013	0.0002	0.0017
660–880	0.0253	0.0025	0.0010	0.0017	0.0001	0.0020
880–1300	0.0190	0.0024	0.0008	0.0020	0.0001	0.0022
1300–3300	0.0124	0.0046	0.0009	0.0012	0.0001	0.0015

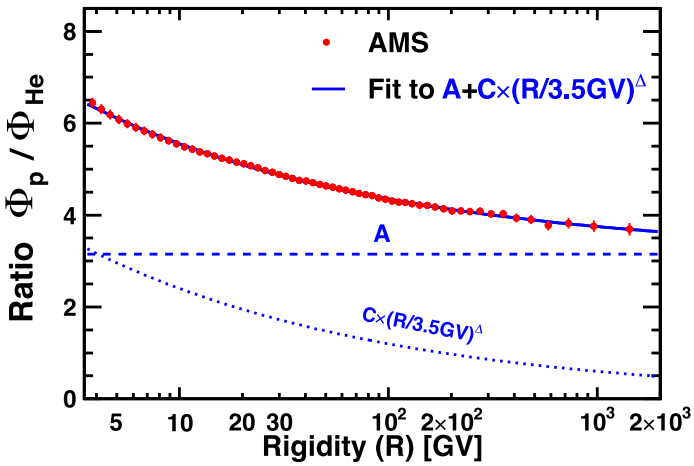

Fig. 80. The rigidity dependence of the proton-to-helium flux ratio together with a fit of the function $A + C(R/3.5\,GV)^{\Delta}$ (solid curve). The soft component, $C(R/3.5\,GV)^{\Delta}$ term (dotted curve), and the helium-like component, A term (dashed line), are also shown.

Fig. 82 shows the fluxes of lithium, beryllium and boron measured by AMS.

As seen, the Li and B fluxes have an identical rigidity dependence above ∼7 GV and all three secondary fluxes have an identical rigidity dependence above ∼30 GV, as shown in Fig. 83. Note that the different rigidity dependence of the Be flux and Li flux below 30 GV is most likely due to the significant presence of the radioactive ^{10}Be isotope, which has a half-life of 1.4 MY.

Most surprising is that the Li/Be flux ratio is 2.0 ± 0.1 over the rigidity range from 30 GV to 3.3 TV.

Precise AMS measurements of primary cosmic rays helium, carbon, and oxygen (see Section 8) show that they have identical rigidity dependence above 60 GV. In addition, the spectra of He, C, and O exhibit progressive hardening of the spectra above 200 GV. To understand the origin of the hardening in cosmic ray fluxes, the detailed knowledge of lithium, beryllium, and boron flux rigidity dependence is of crucial importance.

Table 21
The boron to oxygen flux ratio B/O as a function of rigidity including errors due to statistics (σ_{stat}); contributions to the systematic error from the trigger, acceptance, and background (σ_{acc}); the rigidity resolution function and unfolding (σ_{unf}); the absolute rigidity scale (σ_{scale}); and the total systematic error (σ_{syst}). The statistical errors are the sum in quadrature of the ratios of boron and oxygen fluxes statistical errors to the corresponding flux values, multiplied by the flux ratio. The systematic errors from the background subtraction, the trigger, and the event reconstruction and selection are likewise added in quadrature. The correlations in the systematic errors from the uncertainty in nuclear interaction cross sections, the unfolding and the absolute rigidity scale between the boron and oxygen fluxes have been taken into account in calculating the corresponding systematic errors of the flux ratio. The contribution of individual sources to the systematic error are added in quadrature to arrive at the total systematic uncertainty.

Rigidity [GV]	B/O	σ_{stat}	σ_{acc}	σ_{unf}	σ_{scale}	σ_{syst}
2.15–2.40	0.3106	0.0012	0.0144	0.0035	0.0003	0.0148
2.40–2.67	0.3270	0.0012	0.0137	0.0030	0.0002	0.0140
2.67–2.97	0.3333	0.0011	0.0127	0.0026	0.0001	0.0130
2.97–3.29	0.3384	0.0011	0.0118	0.0023	0.0001	0.0120
3.29–3.64	0.3420	0.0010	0.0110	0.0019	0.0000	0.0112
3.64–4.02	0.3442	0.0010	0.0103	0.0017	0.0001	0.0104
4.02–4.43	0.3442	0.0010	0.0097	0.0014	0.0001	0.0098
4.43–4.88	0.3401	0.0009	0.0091	0.0012	0.0002	0.0092
4.88–5.37	0.3371	0.0009	0.0086	0.0011	0.0002	0.0087
5.37–5.90	0.3314	0.0009	0.0082	0.0010	0.0002	0.0082
5.90–6.47	0.3248	0.0009	0.0078	0.0009	0.0002	0.0078
6.47–7.09	0.3194	0.0008	0.0075	0.0009	0.0002	0.0075
7.09–7.76	0.3119	0.0008	0.0072	0.0008	0.0002	0.0072
7.76–8.48	0.3056	0.0008	0.0070	0.0008	0.0002	0.0070
8.48–9.26	0.3007	0.0008	0.0068	0.0008	0.0002	0.0068
9.26–10.1	0.2931	0.0008	0.0065	0.0008	0.0002	0.0066
10.1–11.0	0.2896	0.0009	0.0064	0.0008	0.0002	0.0065
11.0–12.0	0.2812	0.0009	0.0062	0.0007	0.0002	0.0063
12.0–13.0	0.2738	0.0010	0.0060	0.0007	0.0002	0.0061
13.0–14.1	0.2668	0.0010	0.0059	0.0007	0.0002	0.0059
14.1–15.3	0.2623	0.0010	0.0058	0.0007	0.0002	0.0058
15.3–16.6	0.2547	0.0010	0.0056	0.0007	0.0002	0.0057
16.6–18.0	0.2458	0.0010	0.0054	0.0006	0.0002	0.0055
18.0–19.5	0.2405	0.0011	0.0053	0.0006	0.0002	0.0054
19.5–21.1	0.2340	0.0011	0.0052	0.0006	0.0002	0.0053
21.1–22.8	0.2262	0.0011	0.0051	0.0006	0.0002	0.0051
22.8–24.7	0.2199	0.0011	0.0050	0.0006	0.0002	0.0050
24.7–26.7	0.2145	0.0011	0.0049	0.0006	0.0002	0.0049
26.7–28.8	0.2095	0.0011	0.0048	0.0006	0.0002	0.0048
28.8–31.1	0.2009	0.0011	0.0046	0.0006	0.0002	0.0047
31.1–33.5	0.1938	0.0011	0.0045	0.0006	0.0002	0.0046
33.5–36.1	0.1911	0.0012	0.0045	0.0006	0.0002	0.0045
36.1–38.9	0.1818	0.0012	0.0043	0.0006	0.0002	0.0044
38.9–41.9	0.1758	0.0013	0.0043	0.0006	0.0002	0.0043
41.9–45.1	0.1704	0.0013	0.0042	0.0006	0.0002	0.0042
45.1–48.5	0.1678	0.0014	0.0041	0.0006	0.0002	0.0042
48.5–52.2	0.1600	0.0014	0.0040	0.0006	0.0002	0.0041
52.2–56.1	0.1570	0.0015	0.0040	0.0006	0.0002	0.0040
56.1–60.3	0.1534	0.0016	0.0040	0.0006	0.0002	0.0040
60.3–64.8	0.1476	0.0017	0.0039	0.0006	0.0002	0.0039
64.8–69.7	0.1420	0.0017	0.0038	0.0006	0.0002	0.0038
69.7–74.9	0.1397	0.0018	0.0038	0.0006	0.0002	0.0038
74.9–80.5	0.1340	0.0019	0.0037	0.0006	0.0002	0.0037
80.5–86.5	0.1305	0.0020	0.0036	0.0007	0.0002	0.0037
86.5–93.0	0.1291	0.0021	0.0036	0.0007	0.0002	0.0037
93.0–100	0.1228	0.0021	0.0035	0.0007	0.0002	0.0036
100–108	0.1151	0.0021	0.0034	0.0007	0.0002	0.0035
108–116	0.1144	0.0023	0.0034	0.0007	0.0002	0.0035
116–125	0.1116	0.0024	0.0033	0.0007	0.0003	0.0034
125–135	0.1050	0.0024	0.0032	0.0008	0.0003	0.0033
135–147	0.1066	0.0025	0.0033	0.0008	0.0003	0.0035
147–160	0.1030	0.0027	0.0033	0.0009	0.0003	0.0035
160–175	0.1010	0.0028	0.0033	0.0010	0.0003	0.0034
175–192	0.0967	0.0028	0.0031	0.0010	0.0003	0.0033
192–211	0.0914	0.0029	0.0030	0.0011	0.0003	0.0032
211–233	0.0914	0.0031	0.0031	0.0012	0.0003	0.0033

(*continued on next page*)

Table 21 (*continued*).

Rigidity [GV]	B/O	σ_{stat}	σ_{acc}	σ_{unf}	σ_{scale}	σ_{syst}
233–259	0.0880	0.0032	0.0030	0.0013	0.0004	0.0033
259–291	0.0834	0.0033	0.0030	0.0014	0.0004	0.0034
291–330	0.0784	0.0034	0.0028	0.0015	0.0004	0.0032
330–379	0.0744	0.0035	0.0028	0.0017	0.0004	0.0033
379–441	0.0775	0.0038	0.0029	0.0020	0.0005	0.0036
441–525	0.0743	0.0040	0.0028	0.0023	0.0005	0.0037
525–660	0.0658	0.0039	0.0025	0.0025	0.0005	0.0036
660–880	0.0653	0.0042	0.0026	0.0033	0.0006	0.0043
880–1300	0.0634	0.0046	0.0026	0.0046	0.0008	0.0053
1300–3300	0.0439	0.0090	0.0025	0.0031	0.0007	0.0041

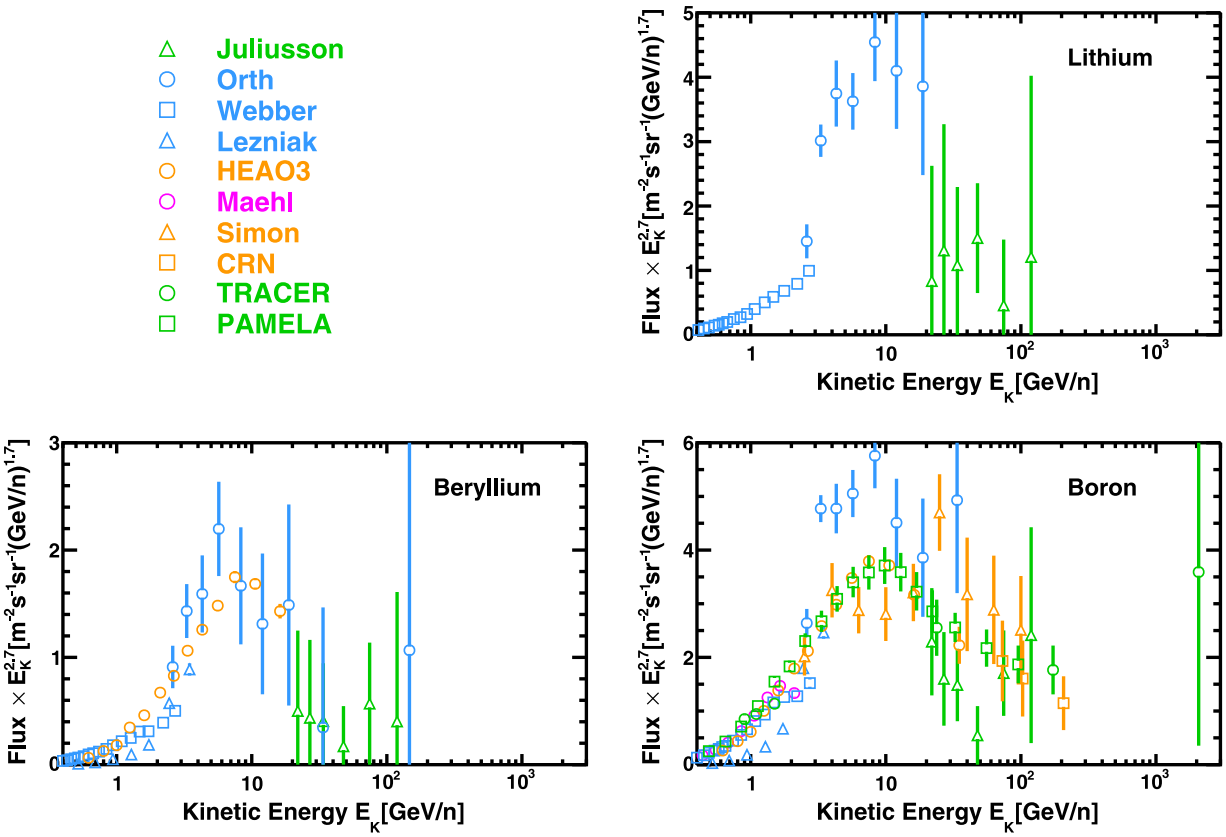

Fig. 81. The measurements of the lithium, beryllium, and boron fluxes [127–136] available before AMS as functions of kinetic energy per nucleon E_K multiplied by $E_K^{2.7}$.

There are many theoretical models describing the behavior of cosmic rays. For example, if the hardening in cosmic rays is related to the injected spectra at their source, then similar hardening is expected both for secondary and primary cosmic rays [138,139]. However, if the hardening is related to propagation properties in the Galaxy then a stronger hardening is expected for the secondary with respect to the primary cosmic rays [139]. The theoretical models have their limitations, as none of them predicted the AMS observed spectral behavior of the primary cosmic rays He, C, and O nor the secondary cosmic rays Li, Be, and B.

To examine the rigidity dependence of the secondary fluxes, detailed variations of the flux spectral indices with rigidity were obtained in a model-independent way. The lithium, beryllium and boron flux Φ spectral indices γ were calculated using Eq. (13) over rigidity intervals bounded by 7.09, 12.0, 16.6, 22.8, 41.9, 60.3, 192, and 3300 GV. The results are presented in Fig. 84 together with the spectral indices of helium, carbon, and oxygen. As seen, the magnitude and the rigidity dependence of the lithium, beryllium, and boron spectral indices are nearly identical, but distinctly different from the rigidity dependence of helium, carbon, and oxygen. In addition, above ∼200 GV, Li, Be, and B all harden more than He, C, and O.

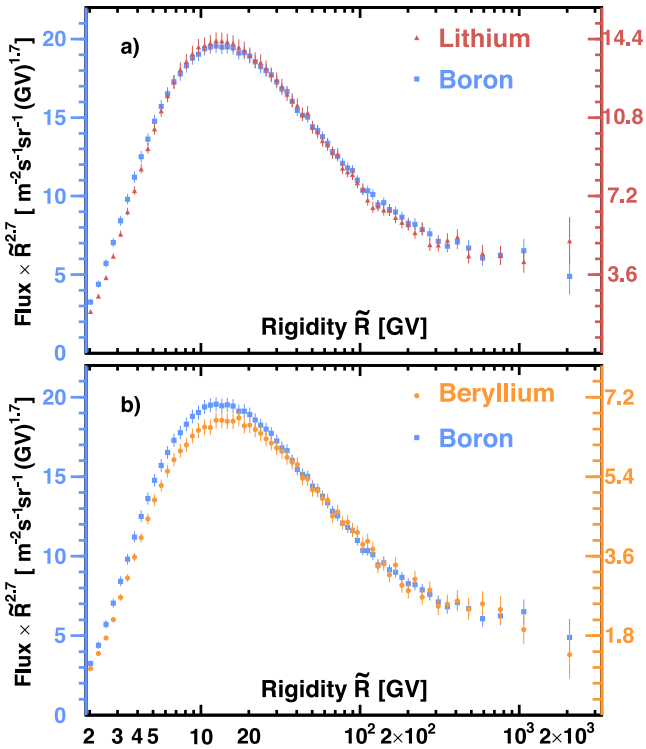

Fig. 82. The AMS (a) Li (red, right axis) and B (blue, left axis); and (b) Be (orange, right axis) and B (blue, left axis) fluxes multiplied by $\tilde{R}^{2.7}$ with their total errors as functions of rigidity.

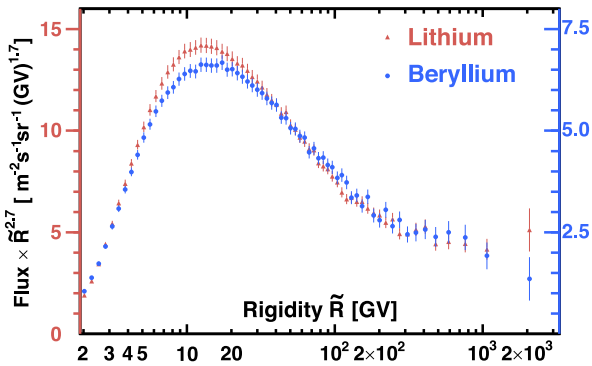

Fig. 83. The AMS Li (red, left axis) and Be (blue, right axis) fluxes multiplied by $\tilde{R}^{2.7}$ with their total errors as a function of rigidity. As seen, above 30 GV, the Li and Be fluxes have identical rigidity dependence and their ratio is 2.0 ± 0.1.

To examine the difference between the rigidity dependence of primary and secondary cosmic rays in detail, the ratios of the lithium, beryllium, and boron fluxes to the carbon and oxygen fluxes were computed (Tables 16, 17, 18, 19, 20, and 21). These results are illustrated in Figs. 85 and 86.

The detailed variations with rigidity of the spectral indices Δ of the secondary to primary flux ratios Φ_S/Φ_P (where Φ_S stands for $\Phi_{\mathrm{Li,Be,B}}$ and Φ_P for $\Phi_{\mathrm{C,O}}$) were obtained by fitting a single power law function ($\Phi_S/\Phi_P \propto R^{\Delta}$) to data in two non-overlapping rigidity intervals [60.3 − 192] and [192 − 3300] GV. Results of the fits are also presented in Figs. 85 and 86.

The detailed variations of the fitted spectral indices Δ corresponding to these two intervals are shown in Fig. 87. Above $\sim$ 200 GV these spectral indices exhibit an average hardening of

$$\Delta_{[192-3300]\,\mathrm{GV}} - \Delta_{[60.3-192]\,\mathrm{GV}} = 0.140 \pm 0.025.$$

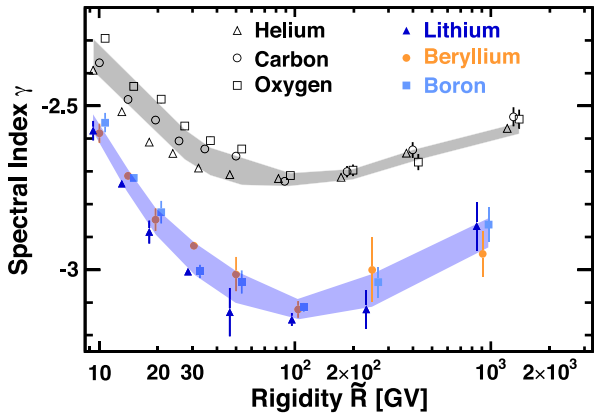

Fig. 84. The dependence of the Li, Be, and B spectral indices on rigidity together with the rigidity dependence of the He, C, and O spectral indices. For clarity, the Li, B, He, and O data points are displaced horizontally. The shaded regions are to guide the eye.

This shows that at high rigidities the secondary cosmic rays harden more than the primary cosmic rays. Significance of this hardening is found to exceed 5σ. This additional hardening of secondary cosmic rays is consistent with expectations when the hardening is due to the propagation in the Galaxy. This is a new and unexpected observation.

Fig. 88 shows a comparison of the secondary cosmic ray fluxes Li, Be and B with the primary cosmic ray fluxes He, C and O. As seen, the three secondary fluxes have an identical rigidity dependence above 30 GV, as do the three primary fluxes above 60 GV. The rigidity dependences of primary cosmic ray fluxes and of secondary cosmic ray fluxes are distinctly different.

In conclusion, the precise measurements of the lithium, beryllium, and boron fluxes from 1.9 GV to 3.3 TV show that the Li and B fluxes have identical rigidity dependence above 7 GV and all three fluxes have identical rigidity dependence above 30 GV with the Li/Be flux ratio of 2.0 ± 0.1. The three fluxes deviate from a single power law above 200 GV in an identical way. Independently, the primary cosmic rays He, C, and O also deviate from a single power law above 200 GV, but their rigidity dependence is distinctly different from the secondary cosmic rays. In particular, above 200 GV, the spectral indices of secondary cosmic rays harden by an average of 0.140 ± 0.025 more than the primaries (more than 5σ effect). These are new properties of high energy cosmic rays.

11. Properties of cosmic helium isotopes

Helium nuclei are the second most abundant cosmic ray. They consist of two isotopes, ^{4}He and ^{3}He. ^{4}He are thought to be mainly produced and accelerated in astrophysical sources, while ^{3}He are overwhelmingly produced by the collisions of ^{4}He with the interstellar medium. The precise knowledge of the rigidity dependences of the helium isotope fluxes and their ratio provides important information on the sources, acceleration, and propagation of cosmic rays [140].

Helium (^{3}He, ^{4}He) interaction cross sections with the interstellar medium (p, He) are significantly smaller than that of heavier nuclei (Li, Be, B, C, N, O, etc.). Therefore, helium travel larger distances, probing a larger galactic volume. Explicitly, the ^{3}He/^{4}He ratio probes the properties of diffusion at larger distances [141]. Moreover, ^{3}He is produced mainly by the fragmentation of ^{4}He with the interstellar medium, whereas Li, Be, and B are produced by multiple fragmentation channels of many heavier nuclei with the interstellar medium [142].

Therefore, the ^{3}He/^{4}He flux ratio provides unique input to cosmic ray propagation models [143], distinctly different from the commonly studied secondary/primary ratios of heavier elements such as B/C and B/O presented in Section 10.

The AMS measurements are based on 100 million ^{4}He nuclei in the rigidity range from 2.1 to 21 GV, and 18 million ^{3}He from 1.9 to 15 GV. The details of the analysis are presented in Ref. [144]. The measured ^{3}He and ^{4}He spectra exhibit nearly identical variations with time (per 4 Bartels rotations, where a Bartels rotation is 27 days [145]), as presented in Fig. 89. The observed variations together with those observed by AMS in the proton flux (see Section 15), and in the electron and positron fluxes (see Section 16) provide important insights on the dynamics of solar modulation.

Before AMS there were no measurements of ^{3}He and ^{4}He isotopes as functions of rigidity. To compare with previous experiments [146], the ^{3}He and ^{4}He fluxes and their ratio have also been measured as functions of the kinetic energy per nucleon, $E_K = M(\gamma - 1)/A$, where $\gamma = 1/\sqrt{1-\beta^2}$, and M and A are the ^{3}He or ^{4}He mass and atomic mass number [144]. The resulting ^{3}He/^{4}He flux ratio is shown in Fig. 90 together with earlier experiments and the GALPROP model [147] predictions. The AMS result provides a precision measurement and covers a larger energy range.

The time averaged ^{3}He/^{4}He flux ratio as a function of rigidity is shown in Fig. 91a. Above 4 GV, the ^{3}He/^{4}He flux ratio is time independent and is well described with a single power law, $C(R/4\text{GV})^{\Delta}$, where Δ is the spectral index of the flux ratio. A fit to the data yields

$$C = 0.1476 \pm 0.0004,$$

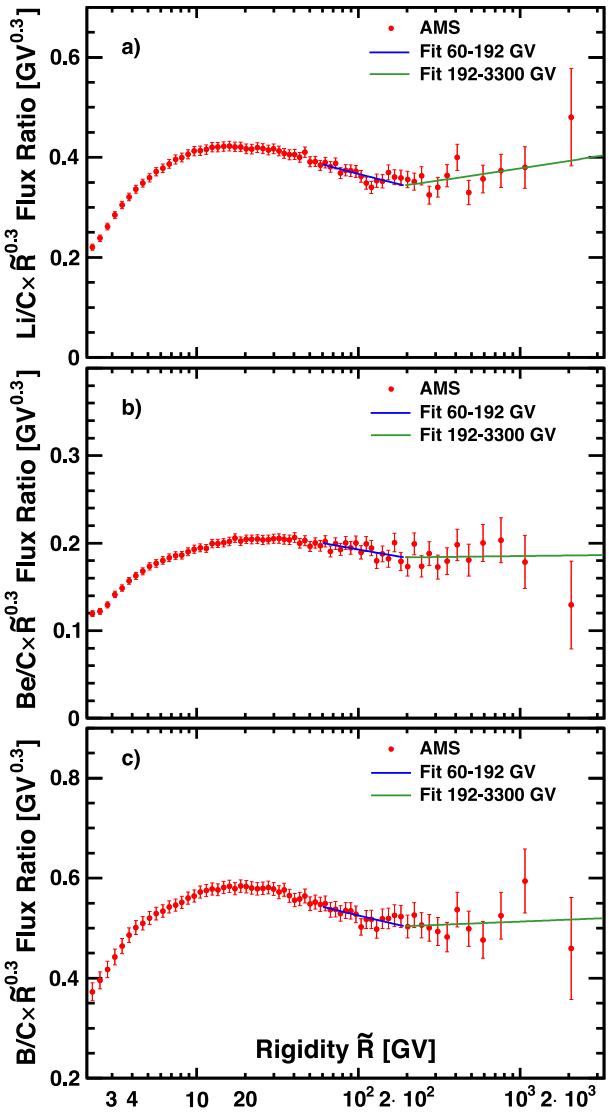

Fig. 85. The AMS secondary to primary flux ratios: (a) Li/C, (b) Be/C, and (c) B/C. Results of the fit of single power law function to data in two non-overlapping intervals $[60.3-192]$ and $[192-3300]$ GV are shown as blue and green lines, respectively. For display purposes, the ratios are scaled with $\tilde{R}^{0.3}$.

$$\Delta = -0.294 \pm 0.004,$$

with $\chi^2/\text{d.o.f.} = 15.7/13$.

Below 4 GV, to study the time and rigidity dependence of the ^{3}He/^{4}He flux ratio, fits to $C(R/4\text{GV})^\delta$ for each period of 4 Bartels rotations were performed. The 21 fit results, shown as a shaded band in Fig. 91a, yield an average δ of

$$\langle\delta\rangle = -0.21 \pm 0.02$$

with a time-variation of ± 0.05 corresponding to the 21 time intervals from May 2011 to November 2017. Different from the B/O and B/C flux ratios, which show a maximum around 4 GV, see Figs. 85c and 86c and Tables 18 and 21, the ^{3}He/^{4}He flux ratio is steadily decreasing with rigidity. Because of different propagation volumes and different inelastic interaction cross sections of He, B, C and O, the B/O and B/C flux ratio rigidity dependence can be different from the ^{3}He/^{4}He flux ratio rigidity dependence. This provides important information for different cosmic ray models [140–142].

Fig. 91b shows the ^{3}He/^{4}He flux ratio spectral index as a function of R for 4 independent rigidity bins. As seen, above 4 GV, the spectral index shows no dependence with rigidity with an average value of $\Delta = -0.294 \pm 0.004$. The extrapolation of Δ to higher energies is shown as a dotted line. The B/O and B/C flux ratio spectral indices (from Tables 18

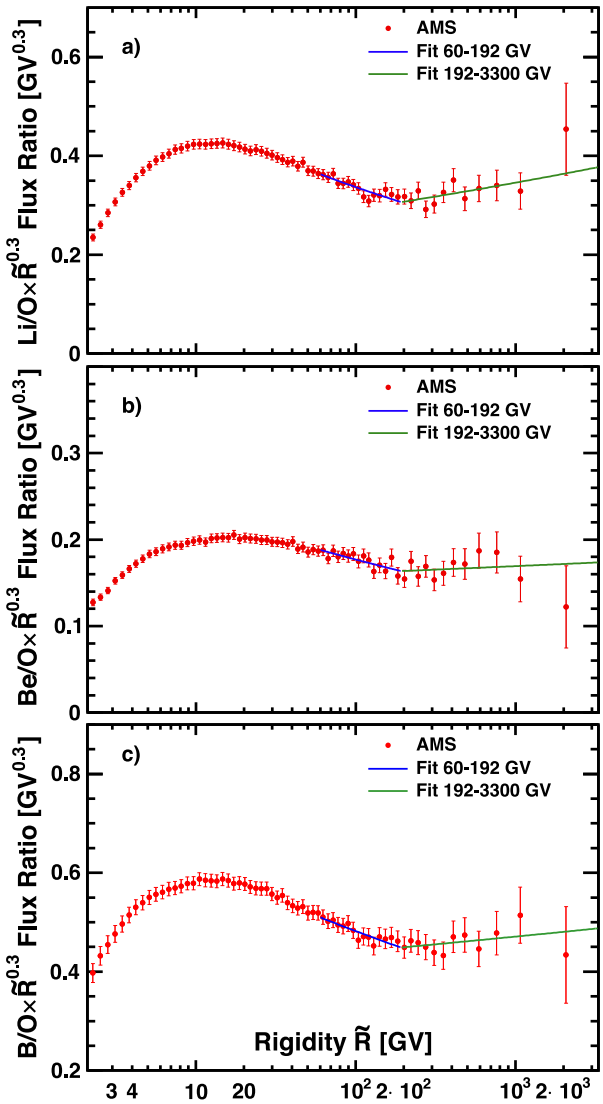

Fig. 86. The AMS secondary to primary flux ratios: (a) Li/O, (b) Be/O, and (c) B/O. Results of the fit of single power law function to data in two non-overlapping intervals [60.3 − 192] and [192 − 3300] GV are shown as blue and green lines, respectively. For display purposes, the ratios are scaled with $\tilde{R}^{0.3}$.

and 21) are shown as blue filled squares and blue open squares, respectively. As seen, the ^{3}He/^{4}He spectral index extrapolation to the highest energies is in agreement with the B/O and B/C spectral indices.

12. Cosmic nitrogen flux

Nitrogen nuclei in cosmic rays are thought to be produced both in astrophysical sources, mostly via the C-N-O cycle [148], and by the collisions of heavier nuclei with the interstellar medium. Therefore, the nitrogen flux Φ_N is expected to contain both primary and secondary components. Precise knowledge of the primary component of cosmic nitrogen provides important insights into the details of nitrogen production in astrophysical sources, while precise knowledge of the secondary component of the cosmic nitrogen provides insights into the details of propagation processes of cosmic rays in the Galaxy.

Over the last 50 years, a few experiments have measured the nitrogen flux as a function of kinetic energy [149–152]. Typically, these measurements have errors larger than 40%–50% above 100 GeV/n. There were no measurements of the nitrogen flux as a function of rigidity.

We present the precise measurement of the nitrogen flux in cosmic rays in the rigidity range from 2.2 GV to 3.3 TV based on 3.9 million nitrogen nuclei (see Table 22). The total flux error is 3.8% at 100 GV. The flux is shown in Fig. 92a as

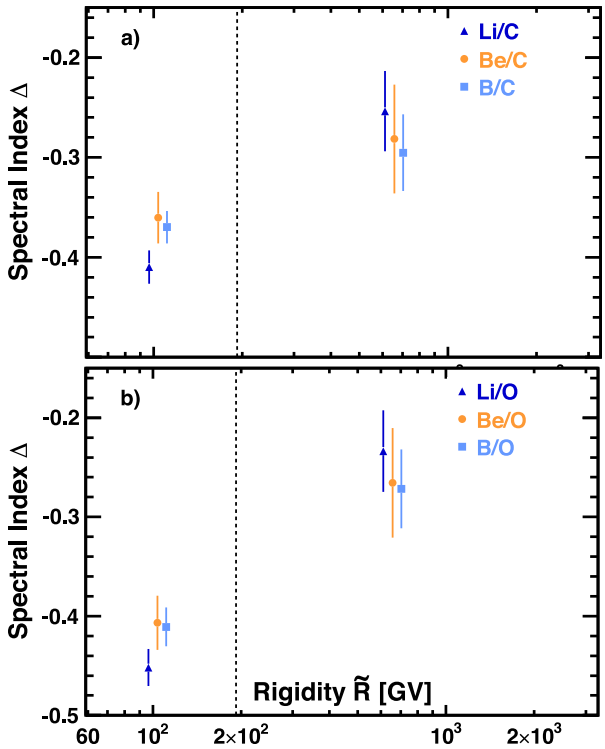

Fig. 87. The AMS secondary to primary flux ratio spectral indices Δ (defined from the fits of a single power law function $\Phi_S/\Phi_P \propto R^{\Delta}$ to data in the two non-overlapping rigidity intervals $[60.3 - 192]$ and $[192 - 3300]$ GV) for (a) Li/C, Be/C, and B/C, and (b) Li/O, Be/O, and B/O. For (a) and (b) the vertical dashed line shows the interval boundary. The spectral indices of Li/C, Be/C, B/C, Li/O, Be/O, and B/O in the range $[192 - 3300]$ GV exhibit an average hardening of 0.140 ± 0.025 compared to the spectral indices in the range $[60.3 - 192]$ GV. Significance of this change is found to exceed 5σ.

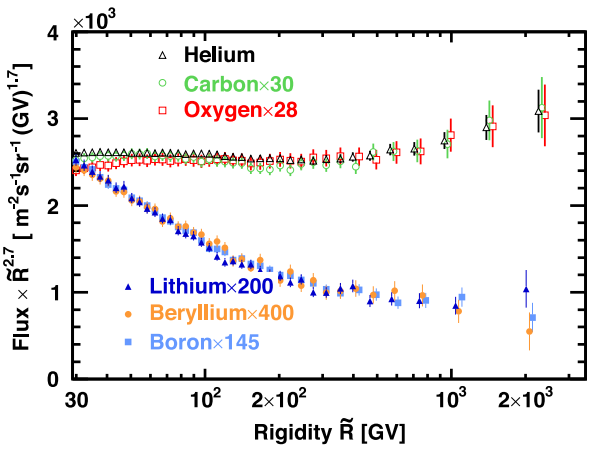

Fig. 88. Comparison of the secondary cosmic ray fluxes with the AMS primary cosmic ray fluxes multiplied by $\tilde{R}^{2.7}$ with their total error as a function of rigidity above 30 GV. For display purposes only, the C, O, Li, Be, and B fluxes were rescaled as indicated. For clarity, the He, O, Li, and B data points above 400 GV are displaced horizontally.

a function of rigidity with the total errors, the quadratic sum of statistical and systematic errors. These new AMS results are consistent with the published AMS results [153] but have smaller statistical and systematic errors.

To examine the rigidity dependence of the flux, the detailed variation of the flux spectral index γ with rigidity was calculated in a model independent way. The flux spectral indices γ were calculated using Eq. (13) over non-overlapping rigidity intervals above 8.48 GV. The intervals have a variable width to have sufficient sensitivity to determine γ. The results are presented in Fig. 92b together with the spectral indices of primary cosmic rays He, C, and O (see Section 8) and of secondary cosmic rays Li, Be, and B (see Section 10). As seen in Figs. 92a and 92b, the nitrogen spectral index

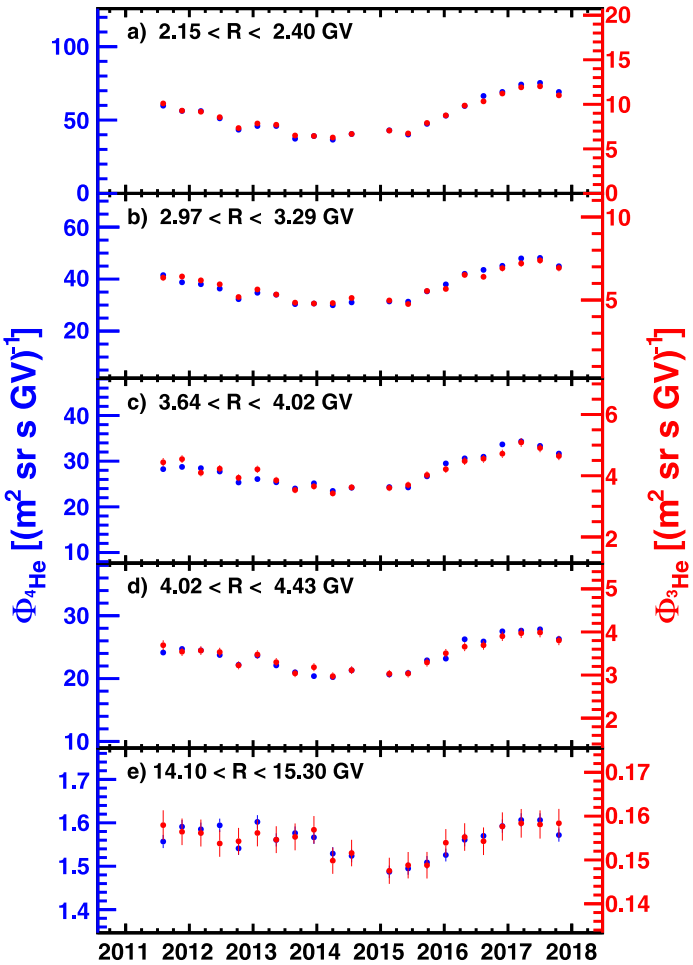

Fig. 89. The AMS ^{3}He (red points, right scale) and ^{4}He (blue points, left scale) fluxes as functions of time (one data point per 4 Bartels rotations) (a) from 2.15 to 2.40 GV, (b) from 2.97 to 3.29 GV, (c) from 3.64 to 4.02 GV, (d) from 4.02 to 4.43 GV, and (e) from 14.10 to 15.30 GV. The errors are the quadratic sum of the statistical and time dependent systematic errors.

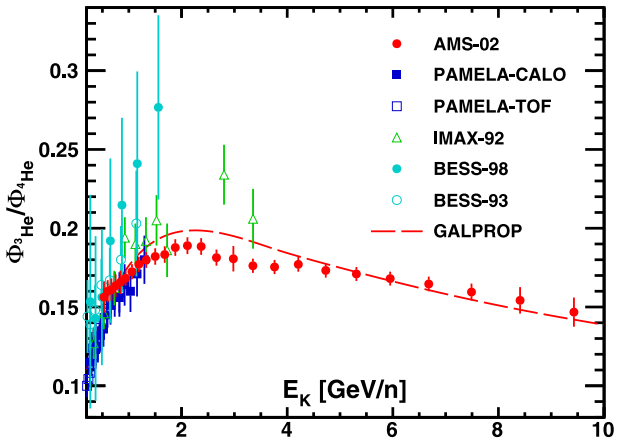

Fig. 90. The AMS ^{3}He/^{4}He flux ratio with total errors as a function of kinetic energy per nucleon, together with earlier experiments [146]. The dashed line shows the prediction of the GALPROP model [147].

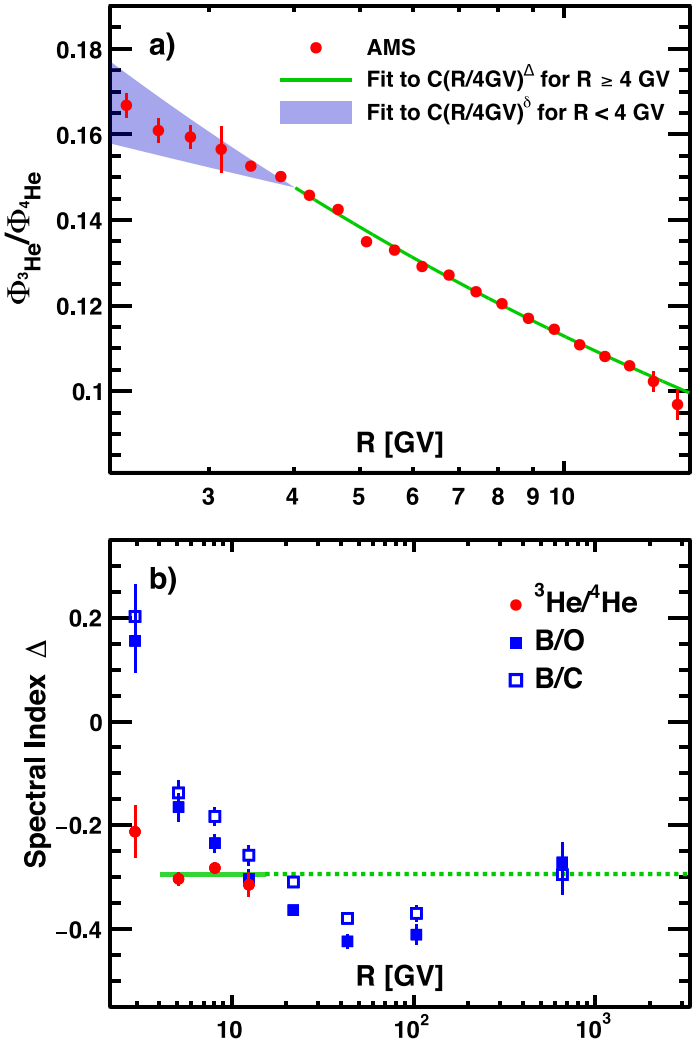

Fig. 91. (a) The time-averaged ^{3}He/^{4}He flux ratio as a function of rigidity R (red points) with statistical and uncorrelated systematic errors added in quadrature. The solid green curve shows a single power law fit $C(R/4\,\mathrm{GV})^{\Delta}$ above 4 GV. The shaded blue area indicates the results of single power law fits to $C(R/4\mathrm{GV})^{\delta}$ below 4 GV for each of the 21 time periods. (b) The ^{3}He/^{4}He flux ratio spectral index (red points) as a function of R. As seen, above 4 GV, the spectral index shows no dependence with rigidity (green band). The extrapolation of Δ to higher energies is shown (green dotted line). The B/O (blue filled squares) and B/C (blue open squares) flux ratio spectral indices (from Tables 18 and 21) are also shown. As seen, the ^{3}He/^{4}He spectral index extrapolated to the highest energies is in good agreement with the B/O and B/C spectral indices.

behavior is not consistent with a single power law. Its rigidity behavior is situated between the primary and secondary cosmic ray spectral indices, and it hardens rapidly with rigidity above ∼100 GV and becomes identical to the spectral indices of primary cosmic ray He, C, and O above ∼700 GV.

The converted AMS measurement as a function of kinetic energy is presented in Fig. 93 together with earlier experiments [149–152]. For the conversion, we use $E_K = \left(\sqrt{Z^2\tilde{R}^2 + M^2} - M\right)/A$ where Z, M, and A are the nitrogen charge, mass, and atomic mass number, respectively. For comparison with other measurements the atomic mass number of 14.5 was used. Predictions of the latest cosmic ray propagation model GALPROP-HELMOD [154] based on the AMS data are also shown in the figure.

To determine the primary and secondary components in the nitrogen flux, we have chosen the rigidity dependence of the oxygen flux as characteristic of primary fluxes and the rigidity dependence of the boron flux as characteristic of secondary fluxes. The secondary component of the oxygen flux is the lowest among He, C, and O. The boron flux has no primary contribution and is mostly produced from the interactions of primary cosmic rays C and O with interstellar medium [155]. To obtain the fractions of the primary Φ_N^P and secondary Φ_N^S components in the nitrogen flux $\Phi_N = \Phi_N^P + \Phi_N^S$, a fit of Φ_N to the weighted sum of a characteristic primary cosmic ray flux, namely, oxygen Φ_O (see Section 8) and of a characteristic secondary cosmic ray flux, namely, boron Φ_B (see Section 10) was performed over the entire rigidity

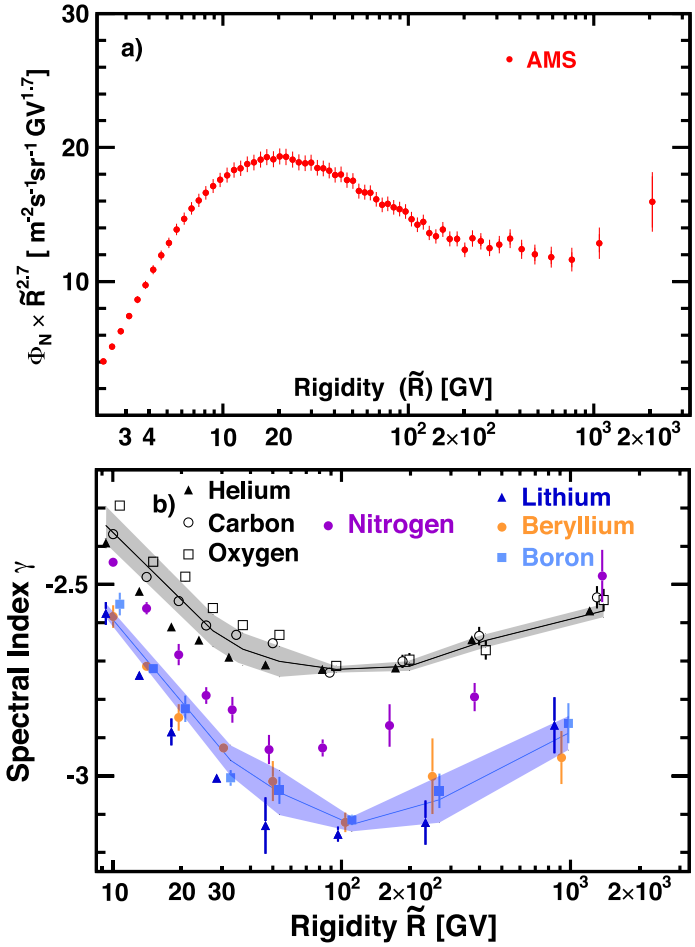

Fig. 92. (a) The AMS nitrogen flux Φ_N multiplied by $\tilde{R}^{2.7}$ with total errors as a function of rigidity. (b) The dependence of the nitrogen spectral index on rigidity together with the rigidity dependence of the spectral indices of primary He, C, and O cosmic rays and secondary Li, Be, and B cosmic rays. For clarity, the horizontal positions of the Li and B data points and He and O data points are displaced with respect to the Be and C data points, respectively. The shaded regions are to guide the eye. As seen, the nitrogen spectral index is situated between the primary and secondary cosmic ray spectral indices, hardens rapidly with rigidity above ∼100 GV and becomes identical to the spectral indices of the primary cosmic rays above ∼700 GV.

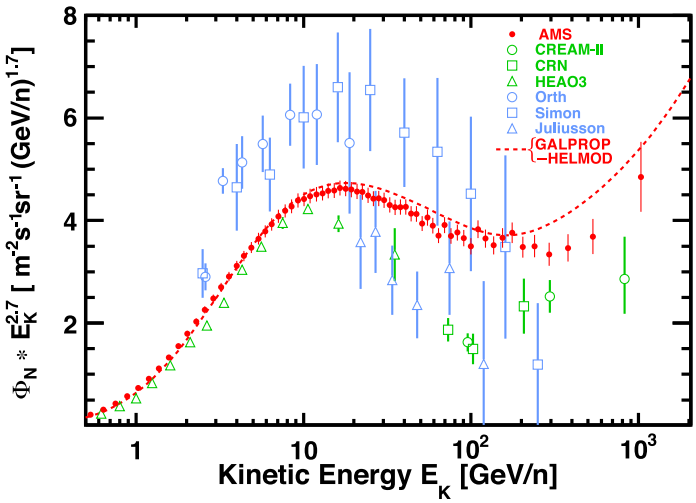

Fig. 93. The AMS nitrogen flux Φ_N as a function of kinetic energy per nucleon E_K multiplied by $E_K^{2.7}$ together with earlier experiments and with the predictions of the latest cosmic ray propagation model GALPROP-HELMOD [154] (dashed red curve).

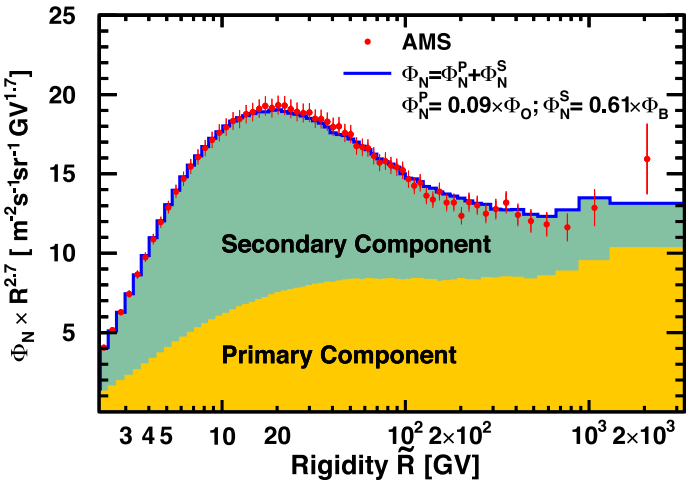

Fig. 94. The AMS nitrogen flux Φ_N together with the fit of the weighted sum of the oxygen flux Φ_O and the boron flux Φ_B over the entire rigidity range. The contributions of the primary and secondary components are indicated by the yellow and green shading, respectively.

range, as shown in Fig. 94. The fit yields

$$\Phi_N^P = (0.092 \pm 0.002) \times \Phi_O,$$
$$\Phi_N^S = (0.61 \pm 0.02) \times \Phi_B$$
$$\text{with } \chi^2/\text{d.o.f.} = 59/64.$$

It is important to note the excellent agreement between the data and the assumption that the nitrogen flux can be described by the sum of a primary and a secondary component in the entire rigidity range from 2.2 GV to 3.3 TV.

The oxygen flux, Φ_O, is mostly primary, whereas the boron flux, Φ_B, is mostly secondary. Fig. 95 shows the nitrogen to oxygen (N/O) flux ratio and nitrogen to boron (N/B) flux ratio as functions of rigidity (see also Tables 23 and 24) with the breakdown of the Φ_N spectrum into the primary, $\Phi_N^P = 0.092 \times \Phi_O$ (yellow shading), and secondary, $\Phi_N^S = 0.61 \times \Phi_B$ (green shading), components. As seen, the contribution of the secondary component in the nitrogen flux decreases, and the contribution of the primary component correspondingly increases, with rigidity.

The observation that the nitrogen flux can be fitted over a wide rigidity range as the simple linear combination of primary and secondary fluxes is a new result, which permits the determination of the N/O abundance ratio at the source without the need to consider the galactic propagation of cosmic rays. The measured value of N/O abundance at the source of 0.092 ± 0.002 is to be compared to the measured N/O abundance in the Solar System of $0.135^{+0.051}_{-0.047}$ [156]. These values are consistent with each other. Note that the accuracy of the AMS measurement exceeds by an order of magnitude the accuracy of the measured N/O abundance in the Solar System.

Finally, Fig. 96 shows the three distinctly different rigidity dependencies above 30 GV of the primary He, C, and O cosmic ray fluxes, the secondary Li, Be, and B fluxes, and the N flux. As seen, the rigidity dependence of the nitrogen flux is different from the dependences of both the primary fluxes and the secondary fluxes.

In conclusion, the precision measurement of the nitrogen flux in cosmic rays from 2.2 GV to 3.3 TV shows that, the flux deviates from a single power law. Its spectral index rapidly hardens at high rigidities starting from ∼100 GV and becomes identical to the spectral indices of primary cosmic rays He, C, and O above ∼700 GV. Remarkably, the nitrogen flux is well described over the entire rigidity range by the sum of the primary flux equal to 9.2% of the oxygen flux and the secondary flux equal to 61% of the boron flux.

13. Primary neon, magnesium, and silicon fluxes

Primary cosmic rays Ne, Mg, and Si are thought to be mainly produced and accelerated in astrophysical sources. Precise knowledge of their spectra in the GV - TV rigidity range provides important information on the origin, acceleration, and propagation processes of cosmic rays in the Galaxy. The precision measurement of the primary cosmic rays He, C, and O fluxes has been reported in Section 8 revealing an identical rigidity dependence of these three fluxes above 60 GV, including the unexpected deviation from a single power law (hardening) of their spectra above ∼200 GV. Precision study of differences in the rigidity dependence of Ne, Mg, and Si compared to He, C, and O provides new insights into the origin and propagation of cosmic rays [121] probing the existence of non-homogeneous diffusion, since heavier cosmic rays propagate shorter distances [157].

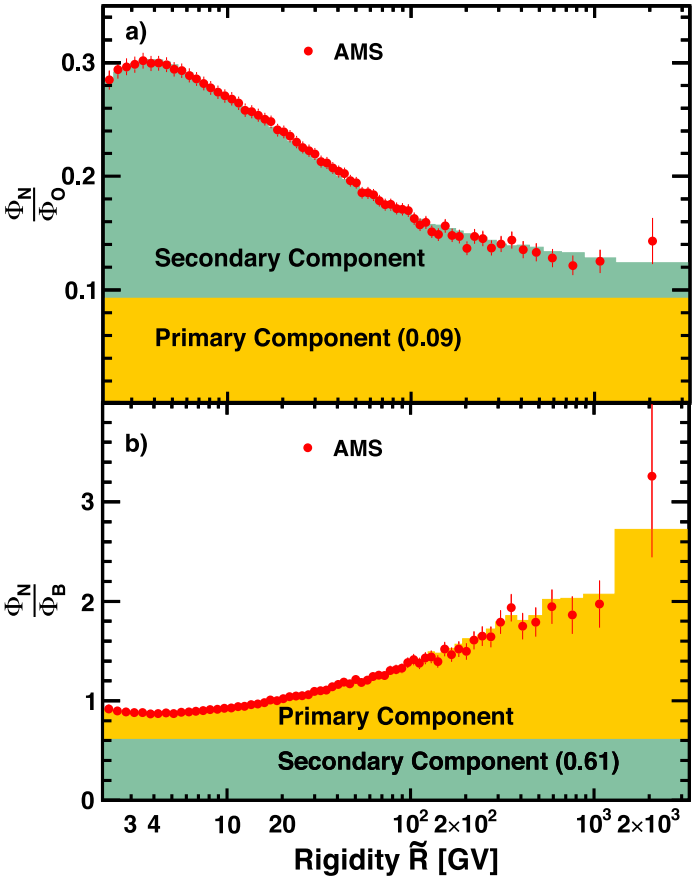

Fig. 95. (a) The AMS Φ_N/Φ_O ratio as a function of rigidity. (b) The AMS Φ_N/Φ_B ratio as a function of rigidity. The contributions of the primary and secondary components are indicated by the yellow and green shading, respectively. As seen from (a) and (b), the contribution of the secondary component in the nitrogen flux decreases, and the contribution of the primary component correspondingly increases, with rigidity.

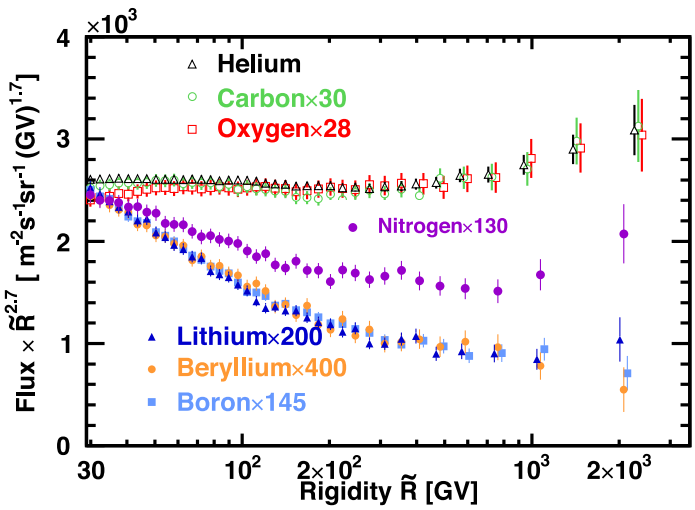

Fig. 96. Comparison of the AMS measurements of the primary and the secondary cosmic ray fluxes with the nitrogen flux multiplied by $\tilde{R}^{2.7}$ with their total errors as functions of rigidity above 30 GV. For display purposes only, the C, O, Li, Be, B, and N fluxes were rescaled as indicated. For clarity, the horizontal positions of the He, O, Li, and B data points above 400 GV are displaced while C, Be, and N are not.

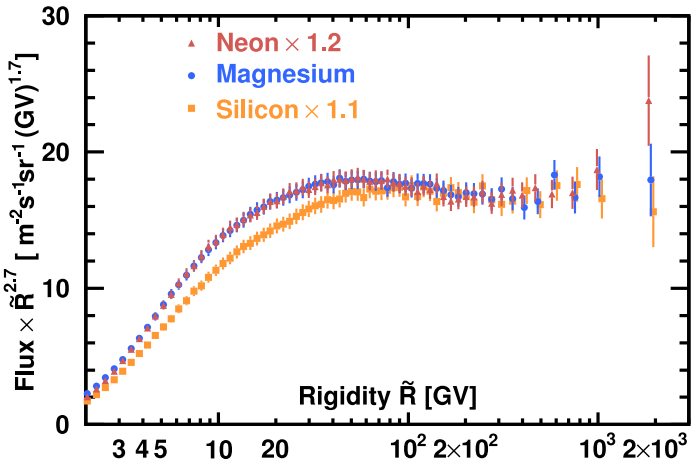

Fig. 97. Ne, Mg, and Si fluxes multiplied by $\tilde{R}^{2.7}$ with their total errors as functions of rigidity.

There have been no measurements of Ne, Mg, and Si fluxes as functions of rigidity, and over the last 30 years only few measurements exist in kinetic energy per nucleon [150–152,158–161]. Typically these measurements have errors larger than 20% at 50 GeV/n.

We present the precision measurements of the Ne, Mg, and Si fluxes in the rigidity range from 2.15 GV to 3.0 TV based on 1.8 million Ne, 2.2 million Mg, and 1.6 million Si nuclei [162]. Fig. 97 shows the rigidity dependence of the Ne, Mg, and Si fluxes with the total errors, the sum in quadrature of statistical and systematic errors. As seen, the total error is ∼5% at 100 GV for each flux (corresponding to kinetic energy of ∼50 GeV/n).

Fig. 98a shows the Ne and Mg fluxes and Ne/Mg flux ratio, and Fig. 98b the Si and Mg fluxes and Si/Mg flux ratio, as functions of rigidity $\tilde{R}$.

To establish the rigidity intervals where the Ne, Mg, and Si fluxes have identical rigidity dependence, the fits of Ne/Mg and Si/Mg ratios have been performed to

$$\frac{\Phi_{\mathrm{Ne,Si}}}{\Phi_{\mathrm{Mg}}} = \begin{cases} k\,(R/R_0)^{\Delta}, & R \le R_0, \\ k\,, & R > R_0. \end{cases} \tag{14}$$

For the Ne/Mg ratio, the fit yields

$$k^{\mathrm{Ne/Mg}} = 0.84 \pm 0.02,$$
$$R_0^{\mathrm{Ne/Mg}} = 3.65 \pm 0.5\,\mathrm{GV},$$
$$\Delta^{\mathrm{Ne/Mg}} = 0.19 \pm 0.08,$$

with $\chi^2/\mathrm{d.o.f.} = 42/64$ over the entire rigidity range.

From the fit results we found that the Ne and Mg fluxes have an identical rigidity dependence above 3.65 GV. Note that AMS has also observed an identical rigidity dependence above 7 GV between secondary cosmic ray Li and B fluxes (see Fig. 82a).

For the Si/Mg ratio, the fit yields

$$k^{\mathrm{Si/Mg}} = 0.89 \pm 0.02,$$
$$R_0^{\mathrm{Si/Mg}} = 86.5 \pm 13\,\mathrm{GV},$$
$$\Delta^{\mathrm{Si/Mg}} = 0.069 \pm 0.005,$$

with $\chi^2/\mathrm{d.o.f.} = 29/53$ above 6 GV.

From the fits results we conclude that all three fluxes have an identical rigidity dependence above 86.5 GV.

To examine the rigidity dependence of the fluxes, the variation of the flux spectral indices γ with rigidity was obtained in a model independent way using Eq. (13) over non-overlapping rigidity intervals bounded by 7.09, 12.0, 16.6, 28.8, 45.1, 86.5, 192.0, 441.0 and 3000.0 GV. The results are presented in Fig. 99. As seen, the Ne and Mg spectral indices are identical in this rigidity range and the three flux spectral indices harden identically with rigidity above ∼200 GV.

To compare the rigidity dependence of the Ne, Mg, and Si fluxes with lighter primary cosmic ray fluxes of He, C, and O, Φ_{O} was used as a reference (Table 9). The He, C, and O fluxes have identical rigidity dependence above 60 GV (see Section 8). The flux ratios of the neon, magnesium, and silicon to oxygen were fitted to the double power law for

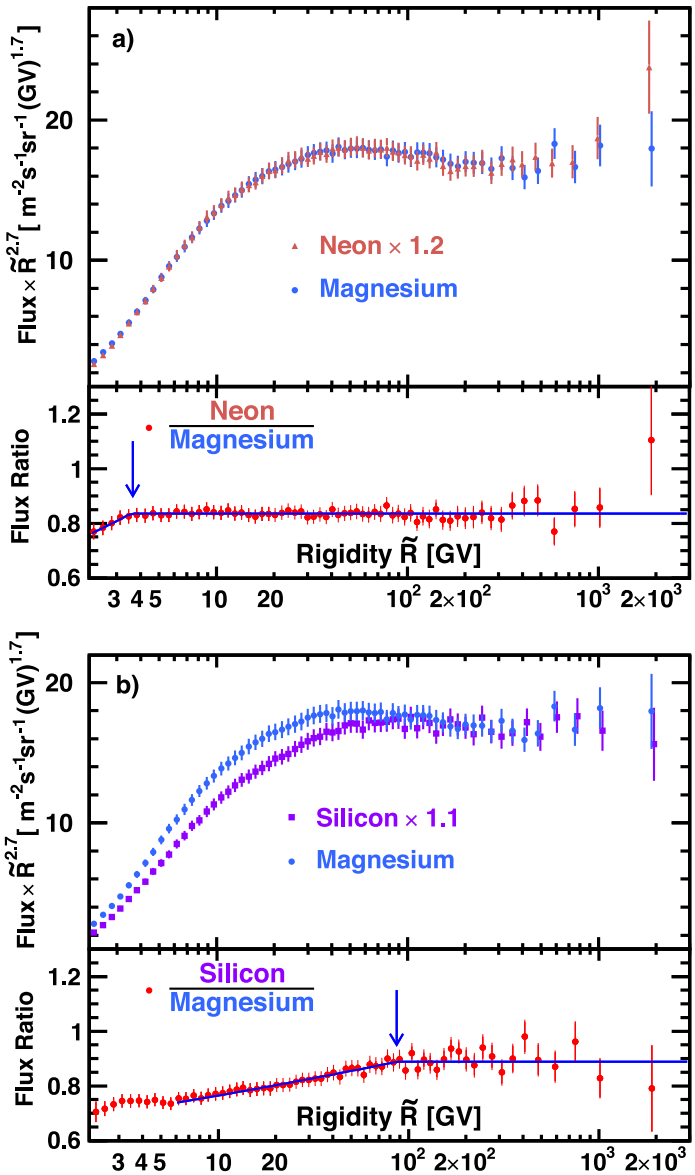

Fig. 98. (a) Ne and Mg fluxes multiplied by $\tilde{R}^{2.7}$ and Ne/Mg flux ratio, and (b) Si and Mg fluxes multiplied by $\tilde{R}^{2.7}$ and Si/Mg flux ratio with their total errors as functions of rigidity. For display purposes only, the Ne and Si fluxes were rescaled as indicated. For clarity, Ne and Si data points above 400 GV are displaced horizontally. The solid curves show the fit results with Eq. (14). As seen, the Ne and Mg fluxes have identical rigidity dependence above 3.65 GV and the three fluxes have identical rigidity dependence above 86.5 GV, as indicated by the location of the arrows.

rigidities above 20 GV

$$\frac{\Phi_{\mathrm{Ne,Mg,Si}}}{\Phi_{\mathrm{O}}} = \begin{cases} C\,(R/86.5\mathrm{GV})^{\Delta}, & R \leq 86.5\ \mathrm{GV}, \\ C\,(R/86.5\mathrm{GV})^{\delta}, & R > 86.5\ \mathrm{GV}, \end{cases} \tag{15}$$

where C is a constant (see Figure S4 of Ref. [162]).

Fig. 100 shows the rigidity dependence of the spectral indices Ne/O, Mg/O, and Si/O obtained from the fits. As seen, above 86.5 GV the spectral indices are

$$\delta^{\mathrm{Ne/O}} = -0.046 \pm 0.010,$$
$$\delta^{\mathrm{Mg/O}} = -0.049 \pm 0.011,$$
$$\delta^{\mathrm{Si/O}} = -0.040 \pm 0.011,$$

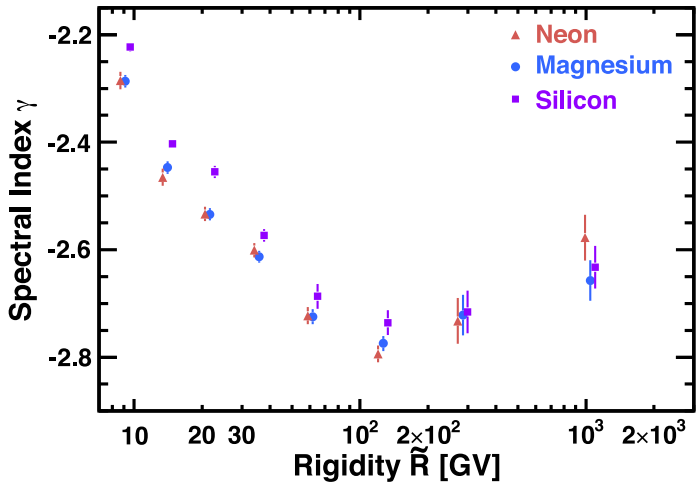

Fig. 99. The dependence of the Ne, Mg, and Si spectral indices on rigidity. For clarity, the Ne and Si data points are displaced horizontally. As seen, the Ne and Mg spectral indices are identical in this rigidity range and the three flux spectral indices harden identically with rigidity above ∼200 GV.

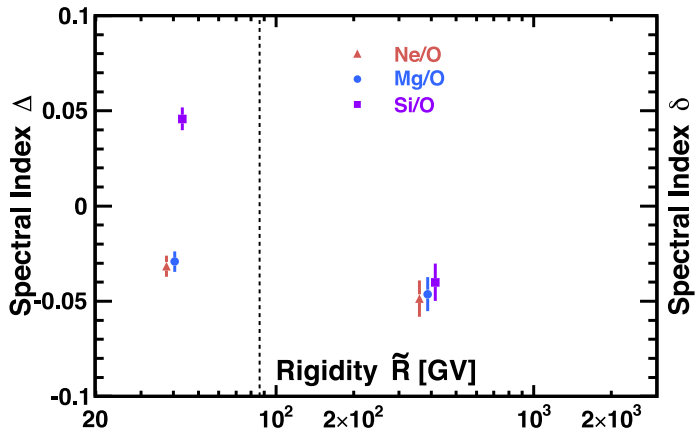

Fig. 100. The AMS Ne/O, Mg/O and Si/O flux ratio spectral indices obtained with fits of Eq. (15) as a function of rigidity. For clarity, Ne/O and Si/O spectral indices data points are displaced horizontally. The vertical dashed line shows the interval boundary of 86.5 GV.

fully compatible with each other. Their average value is

$$\langle\delta\rangle = -0.045 \pm 0.008.$$

The difference of $\langle\delta\rangle$ from zero by more than 5σ shows that the Ne, Mg, and Si is a different class of primary cosmic rays than He, C, and O [162].

This is illustrated in Fig. 101, which shows the rigidity dependence of the Ne, Mg, and Si fluxes compared to rigidity dependence of the He, C, and O fluxes (Tables 7, 8, 9).

Fitting the He, C and O fluxes over the rigidity range 60 GV to 3 TV with Eq. (12) simultaneously with common parameters γ, $\Delta\gamma$, s, and R_0 yields

$$\begin{aligned}
C_{\mathrm{He}} &= (950 \pm 10) \times 10^{-4}\ \mathrm{m^{-2}sr^{-1}s^{-1}\,GV^{-1}},\\
C_{\mathrm{C}} &= (31 \pm 1) \times 10^{-4}\ \mathrm{m^{-2}sr^{-1}s^{-1}\,GV^{-1}},\\
C_{\mathrm{O}} &= (33 \pm 1) \times 10^{-4}\ \mathrm{m^{-2}sr^{-1}s^{-1}\,GV^{-1}},\\
\gamma_{\mathrm{HeCO}} &= -2.756 \pm 0.002,\\
\Delta\gamma &= 0.170 \pm 0.015,\\
s &= 0.05 \pm 0.015,\\
R_0 &= 340^{+40}_{-30}\,\mathrm{GV}.
\end{aligned}$$

The fit result for He, C, and O fluxes together with the 68% C.L. band are shown in Fig. 101.

Table 22
The Nitrogen flux Φ_N as a function of rigidity at the top of AMS in units of $[\mathrm{m}^2\,\mathrm{sr\,s\,GV}]^{-1}$ including errors due to statistics (σ_{stat}); contributions to the systematic error from the trigger, acceptance, and background (σ_{acc}); the rigidity resolution function and unfolding (σ_{unf}); the absolute rigidity scale (σ_{scale}); and the total systematic error (σ_{syst}). The contribution of individual sources to the systematic error are added in quadrature to arrive at the total systematic error.

Rigidity [GV]	Φ_N	σ_{stat}	σ_{acc}	σ_{unf}	σ_{scale}	σ_{syst}
2.15–2.40	(4.396	0.016	0.142	0.054	0.018	0.153) $\times 10^{-1}$
2.40–2.67	(4.185	0.014	0.133	0.037	0.010	0.139) $\times 10^{-1}$
2.67–2.97	(3.832	0.012	0.121	0.029	0.005	0.124) $\times 10^{-1}$
2.97–3.29	(3.422	0.010	0.107	0.023	0.002	0.109) $\times 10^{-1}$
3.29–3.64	(3.028	0.008	0.094	0.018	0.000	0.096) $\times 10^{-1}$
3.64–4.02	(2.604	0.007	0.081	0.014	0.002	0.082) $\times 10^{-1}$
4.02–4.43	(2.229	0.006	0.069	0.011	0.002	0.070) $\times 10^{-1}$
4.43–4.88	(1.884	0.005	0.058	0.008	0.003	0.059) $\times 10^{-1}$
4.88–5.37	(1.568	0.004	0.049	0.006	0.003	0.049) $\times 10^{-1}$
5.37–5.90	(1.307	0.003	0.040	0.005	0.003	0.041) $\times 10^{-1}$
5.90–6.47	(1.075	0.003	0.033	0.003	0.003	0.034) $\times 10^{-1}$
6.47–7.09	(8.833	0.022	0.274	0.026	0.023	0.276) $\times 10^{-2}$
7.09–7.76	(7.177	0.018	0.223	0.020	0.020	0.225) $\times 10^{-2}$
7.76–8.48	(5.836	0.015	0.181	0.016	0.017	0.183) $\times 10^{-2}$
8.48–9.26	(4.736	0.012	0.147	0.012	0.015	0.149) $\times 10^{-2}$
9.26–10.1	(3.839	0.010	0.120	0.010	0.013	0.121) $\times 10^{-2}$
10.1–11.0	(3.105	0.009	0.097	0.008	0.011	0.098) $\times 10^{-2}$
11.0–12.0	(2.513	0.007	0.078	0.006	0.009	0.079) $\times 10^{-2}$
12.0–13.0	(2.019	0.007	0.063	0.005	0.007	0.064) $\times 10^{-2}$
13.0–14.1	(1.651	0.006	0.052	0.004	0.006	0.052) $\times 10^{-2}$
14.1–15.3	(1.335	0.005	0.042	0.003	0.005	0.042) $\times 10^{-2}$
15.3–16.6	(1.083	0.004	0.034	0.003	0.004	0.034) $\times 10^{-2}$
16.6–18.0	(8.774	0.034	0.276	0.023	0.035	0.279) $\times 10^{-3}$
18.0–19.5	(7.010	0.028	0.221	0.019	0.028	0.224) $\times 10^{-3}$
19.5–21.1	(5.714	0.024	0.180	0.016	0.024	0.183) $\times 10^{-3}$
21.1–22.8	(4.618	0.020	0.146	0.013	0.019	0.148) $\times 10^{-3}$
22.8–24.7	(3.694	0.016	0.117	0.011	0.016	0.119) $\times 10^{-3}$
24.7–26.7	(2.955	0.013	0.094	0.009	0.013	0.095) $\times 10^{-3}$
26.7–28.8	(2.392	0.011	0.076	0.008	0.011	0.077) $\times 10^{-3}$
28.8–31.1	(1.950	0.010	0.062	0.007	0.009	0.063) $\times 10^{-3}$
31.1–33.5	(1.558	0.008	0.050	0.006	0.007	0.051) $\times 10^{-3}$
33.5–36.1	(1.272	0.007	0.041	0.005	0.006	0.042) $\times 10^{-3}$
36.1–38.9	(1.030	0.006	0.033	0.004	0.005	0.034) $\times 10^{-3}$
38.9–41.9	(8.277	0.053	0.268	0.035	0.039	0.273) $\times 10^{-4}$
41.9–45.1	(6.791	0.046	0.220	0.030	0.033	0.225) $\times 10^{-4}$
45.1–48.5	(5.445	0.040	0.177	0.025	0.027	0.181) $\times 10^{-4}$
48.5–52.2	(4.451	0.035	0.145	0.022	0.022	0.149) $\times 10^{-4}$
52.2–56.1	(3.500	0.030	0.115	0.018	0.018	0.118) $\times 10^{-4}$
56.1–60.3	(2.866	0.026	0.095	0.016	0.015	0.097) $\times 10^{-4}$
60.3–64.8	(2.353	0.023	0.078	0.013	0.013	0.080) $\times 10^{-4}$
64.8–69.7	(1.878	0.020	0.062	0.011	0.010	0.064) $\times 10^{-4}$
69.7–74.9	(1.504	0.017	0.050	0.009	0.008	0.052) $\times 10^{-4}$
74.9–80.5	(1.245	0.015	0.042	0.008	0.007	0.043) $\times 10^{-4}$
80.5–86.5	(1.008	0.013	0.034	0.007	0.006	0.035) $\times 10^{-4}$

(*continued on next page*)

The fit of the normalization parameters C_{Ne}, C_{Mg}, and C_{Si} was performed on the Ne, Mg, and Si fluxes together with Eq. (12) above 86.5 GV fixing the γ_{NeMgSi}, $\Delta\gamma$, s, and R_0 parameters. We used the $\Delta\gamma$, s, and R_0 values obtained from the simultaneous fit to the He, C, and O fluxes and $\gamma_{\mathrm{NeMgSi}} = \gamma_{\mathrm{HeCO}} + \langle\delta\rangle$, where $\langle\delta\rangle = -0.045$ is the average spectral index of Ne/O, Mg/O and Si/O flux ratios above 86.5 GV, see Eq. (15). The fit yields

$$C_{\mathrm{Ne}} = (5.6 \pm 0.2) \times 10^{-4}\ \mathrm{m}^{-2}\mathrm{sr}^{-1}\mathrm{s}^{-1}\,\mathrm{GV}^{-1},$$
$$C_{\mathrm{Mg}} = (6.7 \pm 0.3) \times 10^{-4}\ \mathrm{m}^{-2}\mathrm{sr}^{-1}\mathrm{s}^{-1}\,\mathrm{GV}^{-1},$$
$$C_{\mathrm{Si}} = (6.0 \pm 0.3) \times 10^{-4}\ \mathrm{m}^{-2}\mathrm{sr}^{-1}\mathrm{s}^{-1}\,\mathrm{GV}^{-1}.$$

The fit result for Ne, Mg, and Si fluxes together with the 68% C.L. band are also shown in Fig. 101.

As seen, the rigidity dependences of Ne, Mg, and Si and He, C, and O are distinctly different.

The previous AMS results on primary cosmic rays He, C, and O show, unexpectedly, that they have identical rigidity dependence above 60 GV and that they deviate from a single power law above 200 GV, whereas the secondary cosmic rays Li, Be, and B also have identical rigidity dependence above 30 GV and deviate from a single power law above 200

Table 22 (*continued*).

Rigidity [GV]	Φ_N	σ_{stat}	σ_{acc}	σ_{unf}	σ_{scale}	σ_{syst}
86.5–93.0	(8.229	0.112	0.277	0.060	0.049	0.288) $\times 10^{-5}$
93.0–100	(6.684	0.097	0.226	0.051	0.041	0.236) $\times 10^{-5}$
100–108	(5.259	0.081	0.178	0.042	0.033	0.186) $\times 10^{-5}$
108–116	(4.182	0.072	0.144	0.035	0.027	0.150) $\times 10^{-5}$
116–125	(3.480	0.062	0.120	0.030	0.023	0.125) $\times 10^{-5}$
125–135	(2.674	0.051	0.092	0.024	0.018	0.097) $\times 10^{-5}$
135–147	(2.110	0.042	0.073	0.020	0.015	0.077) $\times 10^{-5}$
147–160	(1.742	0.036	0.061	0.018	0.013	0.064) $\times 10^{-5}$
160–175	(1.307	0.029	0.046	0.014	0.010	0.049) $\times 10^{-5}$
175–192	(1.021	0.024	0.036	0.012	0.009	0.039) $\times 10^{-5}$
192–211	(7.442	0.195	0.266	0.090	0.066	0.289) $\times 10^{-6}$
211–233	(6.127	0.165	0.216	0.079	0.058	0.238) $\times 10^{-6}$
233–259	(4.576	0.131	0.163	0.064	0.047	0.181) $\times 10^{-6}$
259–291	(3.256	0.099	0.116	0.049	0.037	0.131) $\times 10^{-6}$
291–330	(2.398	0.077	0.086	0.040	0.030	0.099) $\times 10^{-6}$
330–379	(1.735	0.059	0.062	0.032	0.025	0.074) $\times 10^{-6}$
379–441	(1.103	0.041	0.040	0.023	0.018	0.050) $\times 10^{-6}$
441–525	(6.883	0.281	0.251	0.163	0.133	0.328) $\times 10^{-7}$
525–660	(3.925	0.168	0.144	0.112	0.093	0.205) $\times 10^{-7}$
660–880	(1.924	0.092	0.071	0.070	0.058	0.116) $\times 10^{-7}$
880–1300	(8.520	0.445	0.325	0.429	0.344	0.639) $\times 10^{-8}$
1300–3300	(1.773	0.213	0.080	0.052	0.085	0.128) $\times 10^{-8}$

Table 23
The nitrogen to oxygen flux ratio N/O as a function of rigidity including errors due to statistics (σ_{stat}); contributions to the systematic error from the trigger, acceptance, and background (σ_{acc}); the rigidity resolution function and unfolding (σ_{unf}); the absolute rigidity scale (σ_{scale}); and the total systematic error (σ_{syst}). The statistical errors are the sum in quadrature of the ratios of nitrogen and oxygen fluxes statistical errors to the corresponding flux values, multiplied by the flux ratio. The systematic errors from the background subtraction, the trigger, and the event reconstruction and selection are likewise added in quadrature. The correlations in the systematic errors from the uncertainty in nuclear interaction cross sections, the unfolding and the absolute rigidity scale between the nitrogen and oxygen fluxes have been taken into account in calculating the corresponding systematic errors of the flux ratio. The contribution of individual sources to the systematic error are added in quadrature to arrive at the total systematic uncertainty.

Rigidity [GV]	N/O	σ_{stat}	σ_{acc}	σ_{unf}	σ_{scale}	σ_{syst}
2.15–2.40	0.2846	0.0012	0.0073	0.0035	0.0003	0.0081
2.40–2.67	0.2938	0.0011	0.0071	0.0028	0.0002	0.0077
2.67–2.97	0.2964	0.0010	0.0069	0.0024	0.0001	0.0073
2.97–3.29	0.2983	0.0010	0.0067	0.0021	0.0000	0.0070
3.29–3.64	0.3016	0.0010	0.0066	0.0018	0.0000	0.0069
3.64–4.02	0.2993	0.0009	0.0065	0.0016	0.0001	0.0067
4.02–4.43	0.2995	0.0009	0.0064	0.0014	0.0001	0.0065
4.43–4.88	0.2982	0.0009	0.0063	0.0012	0.0001	0.0064
4.88–5.37	0.2943	0.0008	0.0062	0.0011	0.0001	0.0063
5.37–5.90	0.2929	0.0008	0.0062	0.0009	0.0001	0.0063
5.90–6.47	0.2887	0.0008	0.0061	0.0008	0.0001	0.0062
6.47–7.09	0.2857	0.0008	0.0061	0.0008	0.0001	0.0061
7.09–7.76	0.2818	0.0008	0.0060	0.0007	0.0001	0.0060
7.76–8.48	0.2777	0.0008	0.0059	0.0007	0.0001	0.0060
8.48–9.26	0.2741	0.0008	0.0059	0.0006	0.0001	0.0059
9.26–10.1	0.2707	0.0008	0.0058	0.0006	0.0001	0.0059
10.1–11.0	0.2681	0.0009	0.0058	0.0006	0.0001	0.0059
11.0–12.0	0.2643	0.0009	0.0058	0.0006	0.0001	0.0058
12.0–13.0	0.2582	0.0009	0.0057	0.0006	0.0001	0.0057
13.0–14.1	0.2570	0.0010	0.0057	0.0006	0.0001	0.0057
14.1–15.3	0.2539	0.0010	0.0056	0.0006	0.0001	0.0056
15.3–16.6	0.2503	0.0010	0.0056	0.0006	0.0001	0.0056
16.6–18.0	0.2479	0.0011	0.0055	0.0006	0.0001	0.0056
18.0–19.5	0.2407	0.0011	0.0054	0.0006	0.0001	0.0055
19.5–21.1	0.2392	0.0011	0.0054	0.0006	0.0001	0.0054
21.1–22.8	0.2353	0.0011	0.0053	0.0006	0.0001	0.0054
22.8–24.7	0.2302	0.0011	0.0053	0.0007	0.0001	0.0053
24.7–26.7	0.2254	0.0011	0.0052	0.0007	0.0001	0.0053

(*continued on next page*)

Table 23 (*continued*).

Rigidity [GV]	N/O	σ_{stat}	σ_{acc}	σ_{unf}	σ_{scale}	σ_{syst}
26.7–28.8	0.2225	0.0012	0.0052	0.0007	0.0002	0.0052
28.8–31.1	0.2196	0.0012	0.0051	0.0007	0.0002	0.0052
31.1–33.5	0.2130	0.0012	0.0050	0.0007	0.0002	0.0051
33.5–36.1	0.2117	0.0013	0.0051	0.0008	0.0002	0.0051
36.1–38.9	0.2074	0.0013	0.0050	0.0008	0.0002	0.0051
38.9–41.9	0.2043	0.0014	0.0050	0.0008	0.0002	0.0050
41.9–45.1	0.2025	0.0015	0.0050	0.0008	0.0002	0.0050
45.1–48.5	0.1963	0.0016	0.0049	0.0009	0.0002	0.0049
48.5–52.2	0.1944	0.0017	0.0049	0.0009	0.0002	0.0049
52.2–56.1	0.1856	0.0017	0.0047	0.0009	0.0002	0.0048
56.1–60.3	0.1854	0.0018	0.0048	0.0009	0.0002	0.0049
60.3–64.8	0.1836	0.0019	0.0048	0.0010	0.0002	0.0049
64.8–69.7	0.1786	0.0020	0.0047	0.0010	0.0002	0.0048
69.7–74.9	0.1750	0.0021	0.0047	0.0010	0.0002	0.0048
74.9–80.5	0.1751	0.0023	0.0047	0.0010	0.0002	0.0048
80.5–86.5	0.1717	0.0024	0.0047	0.0011	0.0002	0.0048
86.5–93.0	0.1710	0.0025	0.0047	0.0011	0.0002	0.0048
93.0–100	0.1699	0.0027	0.0047	0.0011	0.0002	0.0049
100–108	0.1627	0.0027	0.0046	0.0011	0.0002	0.0047
108–116	0.1575	0.0029	0.0045	0.0012	0.0002	0.0047
116–125	0.1595	0.0031	0.0046	0.0012	0.0002	0.0048
125–135	0.1513	0.0031	0.0044	0.0012	0.0002	0.0046
135–147	0.1488	0.0031	0.0044	0.0012	0.0002	0.0046
147–160	0.1564	0.0035	0.0047	0.0014	0.0002	0.0049
160–175	0.1479	0.0036	0.0045	0.0014	0.0002	0.0047
175–192	0.1469	0.0037	0.0046	0.0014	0.0002	0.0048
192–211	0.1367	0.0038	0.0044	0.0014	0.0002	0.0046
211–233	0.1472	0.0042	0.0047	0.0017	0.0002	0.0050
233–259	0.1453	0.0045	0.0047	0.0018	0.0002	0.0050
259–291	0.1371	0.0045	0.0045	0.0018	0.0002	0.0048
291–330	0.1405	0.0048	0.0047	0.0020	0.0002	0.0051
330–379	0.1439	0.0052	0.0049	0.0023	0.0003	0.0054
379–441	0.1356	0.0054	0.0047	0.0025	0.0002	0.0053
441–525	0.1332	0.0058	0.0047	0.0028	0.0002	0.0055
525–660	0.1281	0.0058	0.0047	0.0033	0.0001	0.0057
660–880	0.1216	0.0062	0.0046	0.0040	0.0000	0.0061
880–1300	0.1252	0.0070	0.0048	0.0058	0.0002	0.0076
1300–3300	0.1430	0.0185	0.0070	0.0049	0.0004	0.0086

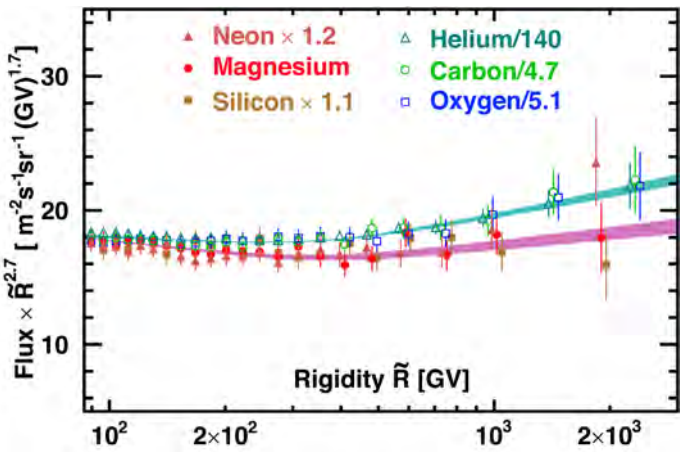

Fig. 101. The rigidity dependence of the Ne, Mg, and Si fluxes compared to rigidity dependence of the He, C, and O fluxes (Section 8) above 86.5 GV. For display purposes only, the He, C, O, Ne and Si fluxes were rescaled as indicated. For clarity, He, O, Ne and Si data points above 400 GV are displaced horizontally. The green shaded area shows the fit result of He, C, and O fluxes with Eq. (12) together with fit errors. The magenta shaded area shows the fit result of Ne, Mg and Si fluxes with Eq. (12) when varying $\gamma_{NeMgSi} = \gamma_{HeCO} + \langle\delta\rangle$, by ± 0.008, from the value of $\langle\delta\rangle = -0.045 \pm 0.008$.

Table 24
The nitrogen to boron flux ratio N/B as a function of rigidity including errors due to statistics (σ_{stat}); contributions to the systematic error from the trigger, acceptance, and background acceptance (σ_{acc}); the rigidity resolution function and unfolding (σ_{unf}); the absolute rigidity scale (σ_{scale}); and the total systematic error (σ_{syst}). The statistical errors are the sum in quadrature of the ratios of nitrogen and boron fluxes statistical errors to the corresponding flux values, multiplied by the flux ratio. The systematic errors from the background subtraction, the trigger, and the event reconstruction and selection are likewise added in quadrature. The correlations in the systematic errors from the uncertainty in nuclear interaction cross sections, the unfolding and the absolute rigidity scale between the nitrogen and boron fluxes have been taken into account in calculating the corresponding systematic errors of the flux ratio. The contribution of individual sources to the systematic error are added in quadrature to arrive at the total systematic uncertainty.

Rigidity [GV]	N/B	σ_{stat}	σ_{acc}	σ_{unf}	σ_{scale}	σ_{syst}
2.15–2.40	0.9164	0.0045	0.0448	0.0102	0.0003	0.0460
2.40–2.67	0.8986	0.0040	0.0397	0.0075	0.0001	0.0404
2.67–2.97	0.8894	0.0037	0.0358	0.0064	0.0002	0.0364
2.97–3.29	0.8815	0.0035	0.0326	0.0055	0.0002	0.0330
3.29–3.64	0.8819	0.0033	0.0301	0.0048	0.0001	0.0305
3.64–4.02	0.8696	0.0032	0.0278	0.0042	0.0000	0.0281
4.02–4.43	0.8701	0.0031	0.0262	0.0038	0.0001	0.0265
4.43–4.88	0.8768	0.0030	0.0251	0.0034	0.0002	0.0254
4.88–5.37	0.8730	0.0029	0.0240	0.0031	0.0002	0.0242
5.37–5.90	0.8838	0.0029	0.0235	0.0029	0.0003	0.0237
5.90–6.47	0.8890	0.0030	0.0231	0.0027	0.0003	0.0232
6.47–7.09	0.8945	0.0030	0.0227	0.0026	0.0003	0.0229
7.09–7.76	0.9034	0.0031	0.0226	0.0026	0.0003	0.0228
7.76–8.48	0.9086	0.0031	0.0225	0.0026	0.0002	0.0226
8.48–9.26	0.9115	0.0032	0.0223	0.0026	0.0002	0.0225
9.26–10.1	0.9235	0.0034	0.0225	0.0026	0.0002	0.0226
10.1–11.0	0.9255	0.0036	0.0224	0.0026	0.0002	0.0226
11.0–12.0	0.9399	0.0038	0.0227	0.0026	0.0003	0.0229
12.0–13.0	0.9432	0.0042	0.0228	0.0026	0.0003	0.0229
13.0–14.1	0.9632	0.0045	0.0233	0.0026	0.0003	0.0234
14.1–15.3	0.9678	0.0047	0.0234	0.0026	0.0003	0.0235
15.3–16.6	0.9827	0.0050	0.0238	0.0026	0.0004	0.0239
16.6–18.0	1.0084	0.0054	0.0245	0.0027	0.0004	0.0247
18.0–19.5	1.0008	0.0056	0.0244	0.0027	0.0004	0.0246
19.5–21.1	1.0220	0.0060	0.0251	0.0028	0.0004	0.0252
21.1–22.8	1.0399	0.0063	0.0257	0.0028	0.0005	0.0258
22.8–24.7	1.0471	0.0064	0.0261	0.0029	0.0005	0.0262
24.7–26.7	1.0506	0.0067	0.0263	0.0030	0.0005	0.0265
26.7–28.8	1.0620	0.0071	0.0267	0.0031	0.0005	0.0269
28.8–31.1	1.0931	0.0076	0.0278	0.0034	0.0005	0.0280
31.1–33.5	1.0990	0.0082	0.0283	0.0035	0.0006	0.0285
33.5–36.1	1.1080	0.0087	0.0287	0.0037	0.0006	0.0290
36.1–38.9	1.1409	0.0096	0.0299	0.0040	0.0006	0.0302
38.9–41.9	1.1621	0.0106	0.0310	0.0043	0.0007	0.0313
41.9–45.1	1.1883	0.0117	0.0319	0.0046	0.0007	0.0322
45.1–48.5	1.1698	0.0124	0.0316	0.0048	0.0007	0.0320
48.5–52.2	1.2144	0.0138	0.0335	0.0052	0.0008	0.0339
52.2–56.1	1.1820	0.0146	0.0330	0.0053	0.0008	0.0335
56.1–60.3	1.2089	0.0160	0.0342	0.0057	0.0008	0.0347
60.3–64.8	1.2442	0.0177	0.0356	0.0062	0.0009	0.0362
64.8–69.7	1.2575	0.0192	0.0365	0.0066	0.0009	0.0371
69.7–74.9	1.2531	0.0207	0.0370	0.0069	0.0010	0.0376
74.9–80.5	1.3066	0.0231	0.0389	0.0076	0.0010	0.0396
80.5–86.5	1.3152	0.0250	0.0396	0.0081	0.0011	0.0405
86.5–93.0	1.3249	0.0268	0.0403	0.0086	0.0011	0.0412
93.0–100	1.3836	0.0303	0.0430	0.0094	0.0013	0.0440
100–108	1.4139	0.0328	0.0447	0.0102	0.0014	0.0459
108–116	1.3765	0.0355	0.0446	0.0105	0.0014	0.0459
116–125	1.4290	0.0385	0.0461	0.0116	0.0016	0.0475
125–135	1.4411	0.0420	0.0477	0.0125	0.0017	0.0493
135–147	1.3951	0.0414	0.0468	0.0129	0.0018	0.0486
147–160	1.5191	0.0488	0.0521	0.0152	0.0022	0.0544

(*continued on next page*)

Table 24 (*continued*).

Rigidity [GV]	N/B	σ_{stat}	σ_{acc}	σ_{unf}	σ_{scale}	σ_{syst}
160–175	1.4651	0.0500	0.0502	0.0159	0.0023	0.0527
175–192	1.5199	0.0557	0.0522	0.0180	0.0027	0.0552
192–211	1.4957	0.0604	0.0529	0.0194	0.0031	0.0564
211–233	1.6093	0.0679	0.0569	0.0230	0.0037	0.0615
233–259	1.6514	0.0746	0.0590	0.0261	0.0044	0.0647
259–291	1.6433	0.0792	0.0615	0.0291	0.0051	0.0682
291–330	1.7911	0.0934	0.0651	0.0359	0.0064	0.0747
330–379	1.9353	0.1083	0.0735	0.0444	0.0081	0.0863
379–441	1.7499	0.1057	0.0655	0.0466	0.0086	0.0809
441–525	1.7919	0.1185	0.0677	0.0565	0.0103	0.0888
525–660	1.9468	0.1381	0.0725	0.0761	0.0139	0.1060
660–880	1.8625	0.1459	0.0710	0.0960	0.0177	0.1207
880–1300	1.9732	0.1715	0.0743	0.1444	0.0265	0.1645
1300–3300	3.2571	0.7594	0.1719	0.2339	0.0605	0.2965

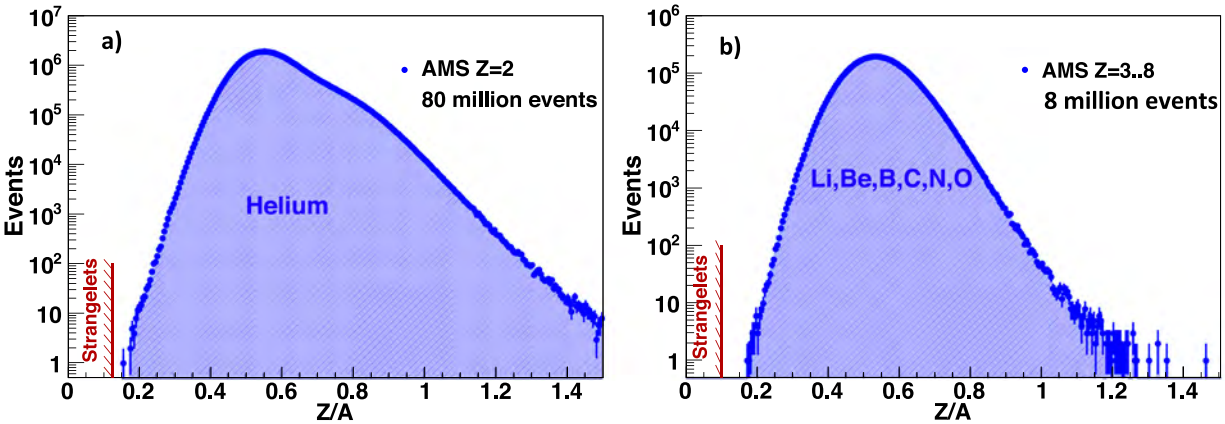

Fig. 102. The Z/A distribution for (a) $Z = 2$ and (b) $Z = 3 - 8$ nuclei. As seen, no strangelet candidate ($Z/A < 0.1$) was found.

GV. The rigidity dependence of primary cosmic rays He, C, and O is distinctly different from secondary cosmic rays Li, Be, and B [137]. These results indicate there are two kinds of cosmic ray rigidity dependences. These observations have generated new developments in cosmic ray models [121,122]. The theoretical models have their limitations, as none of them predicted the observed spectral behavior of the cosmic rays. The results on heavier primary cosmic rays Ne, Mg, and Si show that primary cosmic rays have at least two distinct classes of rigidity dependence. These unexpected results together with ongoing measurements of heavier elements in cosmic rays will enable us to determine how many classes of rigidity dependence exist in both primary and secondary cosmic rays and provide important information for the development of the theoretical models.

14. Strangelets

Strangelets are a proposed new form of matter made out of u, d, and s quarks instead of known nuclei which are made of u and d quarks [163]. J. Sandweiss and his group pioneered the experimental search for strangelets using accelerators [164] and lunar soil [165]. The search for strangelets has been a major activity in ground-based experiments [164–167] and satellite experiments [168]. The unique characteristic of strangelets is $Z/A < 0.1$ [163,164]. To search for strangelets we used inner tracker L2 to L8 to measure the rigidity and the TOF to measure the velocity. Due to the finite velocity resolution of the TOF ($0.01 < \Delta\beta/\beta^2 < 0.02$), the search was limited to events with measured velocity $\beta < 0.8$. Fig. 102 shows the measured Z/A distribution for $Z = 2$ and $Z = 3 - 8$ nuclei. No events with $Z/A < 0.1$ have been found.

Assuming the rigidity dependence of the strangelet flux is similar to that of the primary cosmic rays and taking into account the different acceptance for strangelets estimated with the Monte Carlo simulation we have calculated the 95% C.L. upper limits of the stranglelet flux for $Z = 2$ to $Z = 8$. Fig. 103 shows that the sensitivity of the AMS results for the search for strangelets with $Z = 2$ is improved by two orders of magnitude compared to the earlier results from PAMELA [168] and by many orders of magnitude compared to the searches at accelerators [164,166]. Note that the AMS limit for strangelets with $Z = 2$ is nine orders of magnitude lower than the value of the helium flux.

In Fig. 104 the AMS results on the search for strangelets with $Z = 6, 7, 8$ are compared with the results of the search using the lunar soil [165]. As seen, the AMS sensitivity for $Z = 6, 8$ strangelets is improved by an order of magnitude.

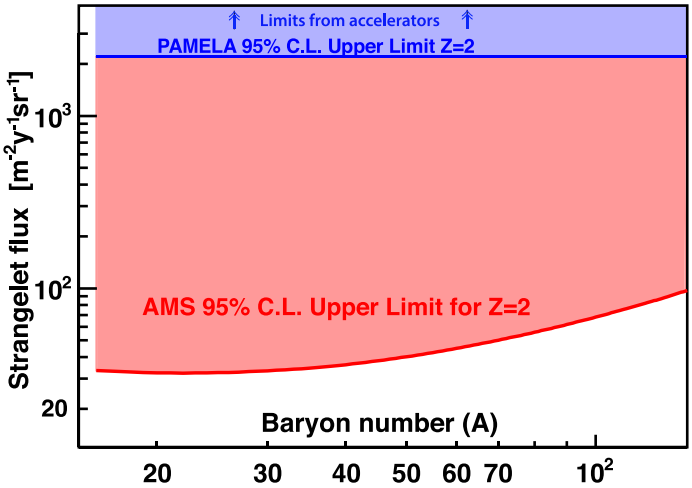

Fig. 103. AMS results on the search for strangelets together with results of the PAMELA experiment [168] and accelerator experiments [166] for $Z = 2$.

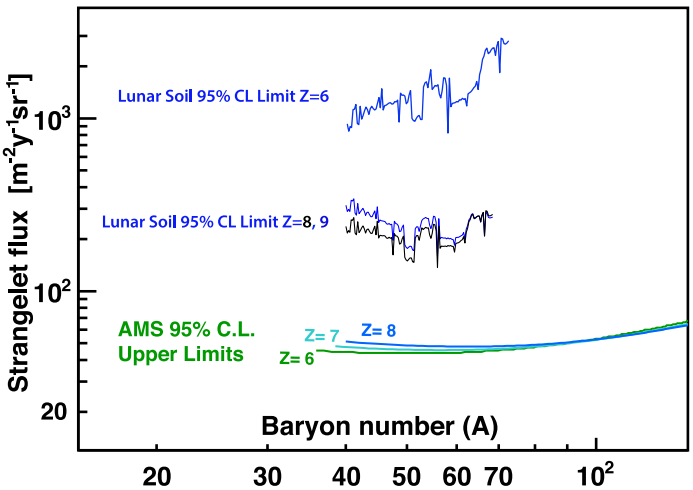

Fig. 104. AMS results on the search for strangelets together with results of the lunar soil experiments [165] for $Z = 6, 7, 8$.

Summary of the AMS results on the search for strangelets with $Z = 2, 3, 4, 5, 6, 7, 8$ is presented in Fig. 105 together with the theoretical prediction [169]. As seen, cosmic-ray strangelets with $2 \leq Z \leq 8$ are excluded by AMS well below the model prediction.

AMS will continue collecting data to improve the sensitivity of this important study and to explore a new territory for strangelets with $Z > 8$.

15. Time-dependent proton and helium fluxes

Cosmic rays entering the heliosphere are subject to diffusion, convection, adiabatic energy losses, and magnetic drift. The temporal evolution of these processes leads to cosmic ray intensity variation at Earth's orbit around the Sun. These variations correlate with solar activity, which has several cycles. The most significant is the 11-year solar cycle during which the number of sunspots changes from minimum to maximum and then back to a minimum. Another is the 22-year cycle of the Sun's magnetic field polarity, which reverses every 11 years during the maxima of the solar cycle. Cosmic ray spectra may also have temporary reductions due to the interactions of cosmic rays with strong disturbances in the magnetic field, especially during solar maxima, that can last from days to months. Time correlations at low rigidity among different particle spectra (p, He) due to solar modulation are expected by models of cosmic ray transport based on the Parker equation. This is because the time-dependent cosmic ray transport in the heliosphere is rigidity dependent and related to changes in solar activity. Numerous models of the propagation of charged particles in the heliosphere exist that predict different flux variations with time. The large acceptance and high precision of AMS allow us to perform accurate

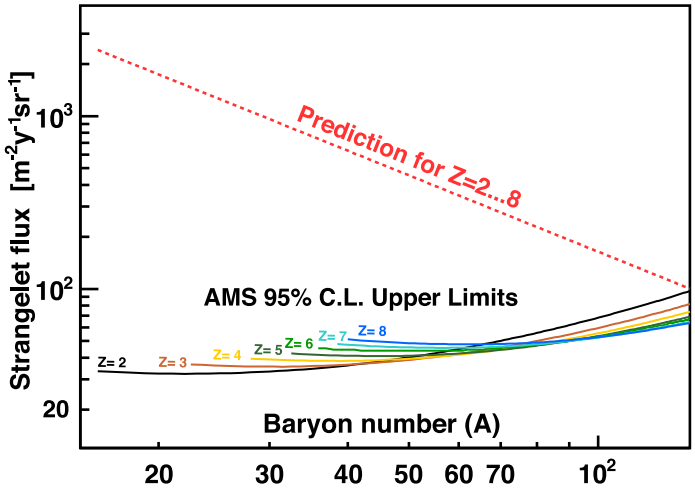

Fig. 105. Summary of the AMS results on the search for strangelets for $Z = 2, 3, 4, 5, 6, 7, 8$. A model prediction for $Z = 2-8$ [169] is shown by the red dashed line.

measurements of the fluxes as functions of time and energy. This provides unique information to probe the dynamics of solar modulation, to allow the improvement of constraints for dark matter searches, to investigate the processes of galactic cosmic ray propagation, and to reduce the uncertainties in radiation dose predictions for deep space human exploration.

We present the time evolution of the proton flux from 1 to 60 GV based on 846 million events and the helium flux from 1.9 to 60 GV based on 112 million events. The proton flux and the helium flux are measured for the 79 Bartels rotations (each 27 days) from May 2011 to May 2017. For the first time, proton and helium fluxes are simultaneously measured with the same precision instrument for an extended period of time [170].

Fig. 106 shows the detailed behavior of the proton flux and the helium flux as functions of time and of rigidity from 1 to 10 GV and from 1.9 to 10 GV, respectively.

The time dependence of the proton and helium fluxes are shown in Fig. 107 for 8 characteristic rigidity bins. As seen, both the proton and helium fluxes have fine time structures each with maxima and minima. The structures in the proton flux and the helium flux are nearly identical in both time and relative amplitude. In general, the amplitudes of the structures decrease progressively with rigidity. The precision of AMS enables us to observe these structures up to 40 GV. The amplitudes of the structures are reduced during the time period, which started one year after solar maximum (i.e. starting March 2015), when the proton and helium fluxes steadily increase. It is interesting to note that the structures in the proton and helium fluxes observed before the solar polarity change around July 2013 [171,172] coincide with the structures observed in the electron and positron fluxes (see Section 16). They are marked with red vertical dashed lines in Fig. 107.

Fig. 108 shows the AMS p/He flux ratio as a function of time for 9 rigidity bins. As seen, depending on the rigidity range, the p/He flux ratio shows two different behaviors in time. Above $\sim$3 GV the ratio is time independent. Below $\sim$3 GV the ratio has a long-term time dependence. To assess the transition between these two behaviors, we performed a fit of the p/He flux ratio r_i for each rigidity bin i as a function of time t, with

$$r_i(t) = \begin{cases} a_i, & t \le t_i; \\ a_i + b_i(t - t_i), & t > t_i. \end{cases} \tag{16}$$

where a_i is the average p/He flux ratio from May 2011 to t_i, t_i is the time when the p/He flux ratio deviates from the average a_i, and b_i is the slope of the time variation. Above 3.29 GV, the p/He flux ratio is consistent with a constant value at the 95% confidence level. This shows the universality of the solar modulation of cosmic ray nuclei at relativistic rigidities. Below 3.29 GV, the observed p/He flux ratio is steadily decreasing with time after t_i. In the first five rigidity bins, the best fit values of t_i are in agreement with each other. Their average value is equal to February 28, 2015 with an accuracy of $\pm$42 days, consistent with boundary VII of Fig. 107, after which the proton and helium fluxes start to increase. This last observation shows a new and important feature regarding the propagation of lower energy cosmic rays in the heliosphere. The precision of the AMS data provides information for the development of refined solar modulation models [173,174].

In conclusion, the precision proton flux and the helium flux observed by AMS have nearly identical fine structures both in time and in relative amplitude. The amplitudes of the flux structures decrease with increasing rigidity and vanish above 40 GV. The amplitudes of the structures are reduced during the time period, which started one year after solar maximum, when the proton and helium fluxes steadily increase. In addition, above $\sim$3 GV the p/He flux ratio is time independent. Below $\sim$3 GV the ratio has a long-term decrease coinciding with the period during which the fluxes start to rise.

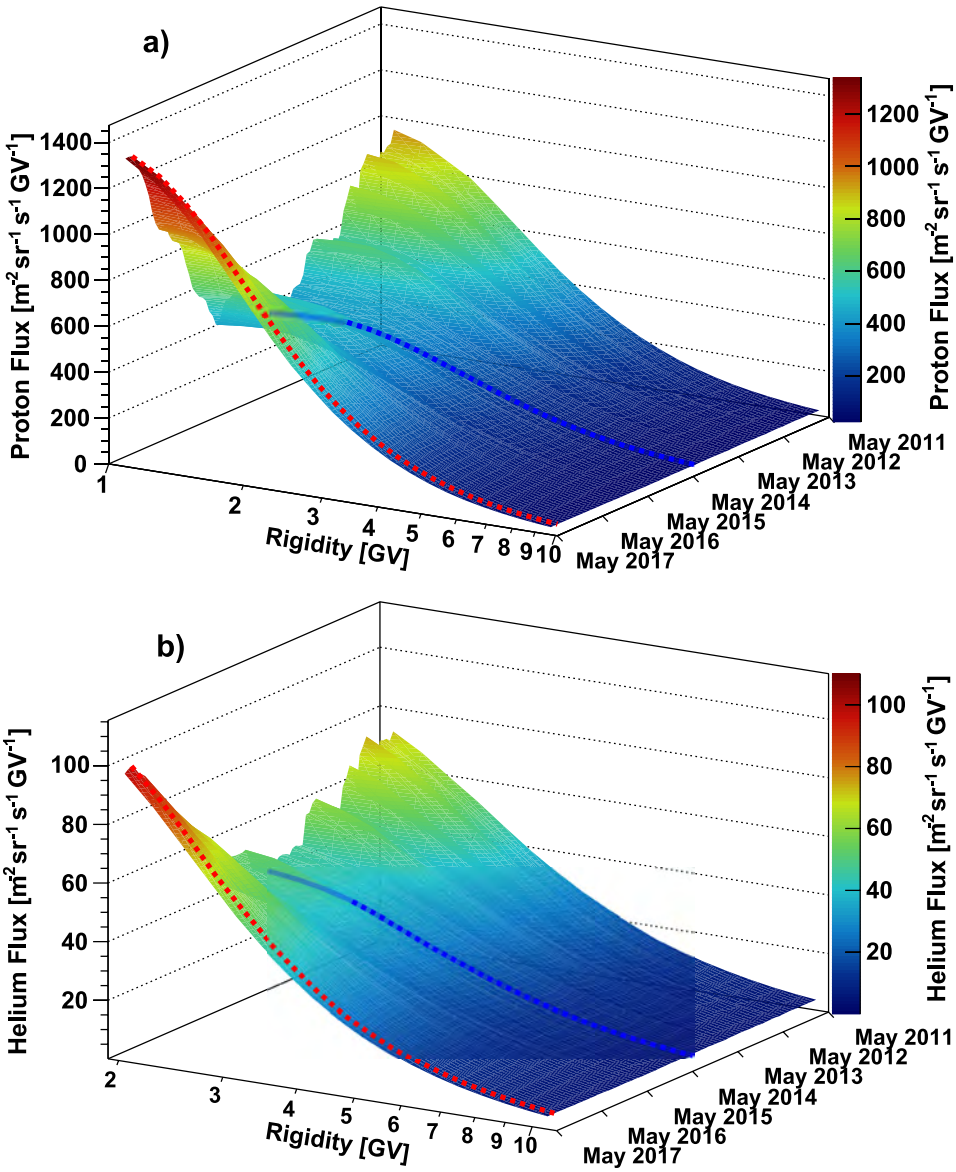

Fig. 106. The three-dimensional detailed behavior of the AMS (a) proton and (b) helium fluxes as functions of time and rigidity. The rigidity range for protons is from 1 to 10 GV and for helium from 1.9 to 10 GV. The color code indicates the flux intensity in units of [$m^{-2}\,sr^{-1}\,s^{-1}\,GV^{-1}$]. During the period of observation, both fluxes have a distinct minimum in February 2014 (blue dashed line) and a maximum in February 2017 (red dashed line).

16. Time-dependent electron and positron fluxes

We present high-statistics, precision measurements of the detailed time and energy dependence of the cosmic-ray electron flux and positron flux over 79 Bartels rotations from May 2011 to May 2017 in the energy range from 1 to 50 GeV. These data allow comprehensive studies of the energy and charge-sign dependence of short-term effects on the time scale of months, related to solar activity [175,176], and long-term effects on the time scale of years, related to the 22-year cycle of the solar magnetic field polarity.

Time-dependent structures in the energy spectra are expected from the solar modulation of interstellar cosmic rays when they enter the heliosphere. Solar modulation involves convective, diffusive, particle drift, and adiabatic energy loss processes. Only particle drift induces a dependence of solar modulation on the particle charge sign. Since electrons and positrons differ only in charge sign, their simultaneous measurement offers a unique way to study charge-sign dependent solar modulation effects.

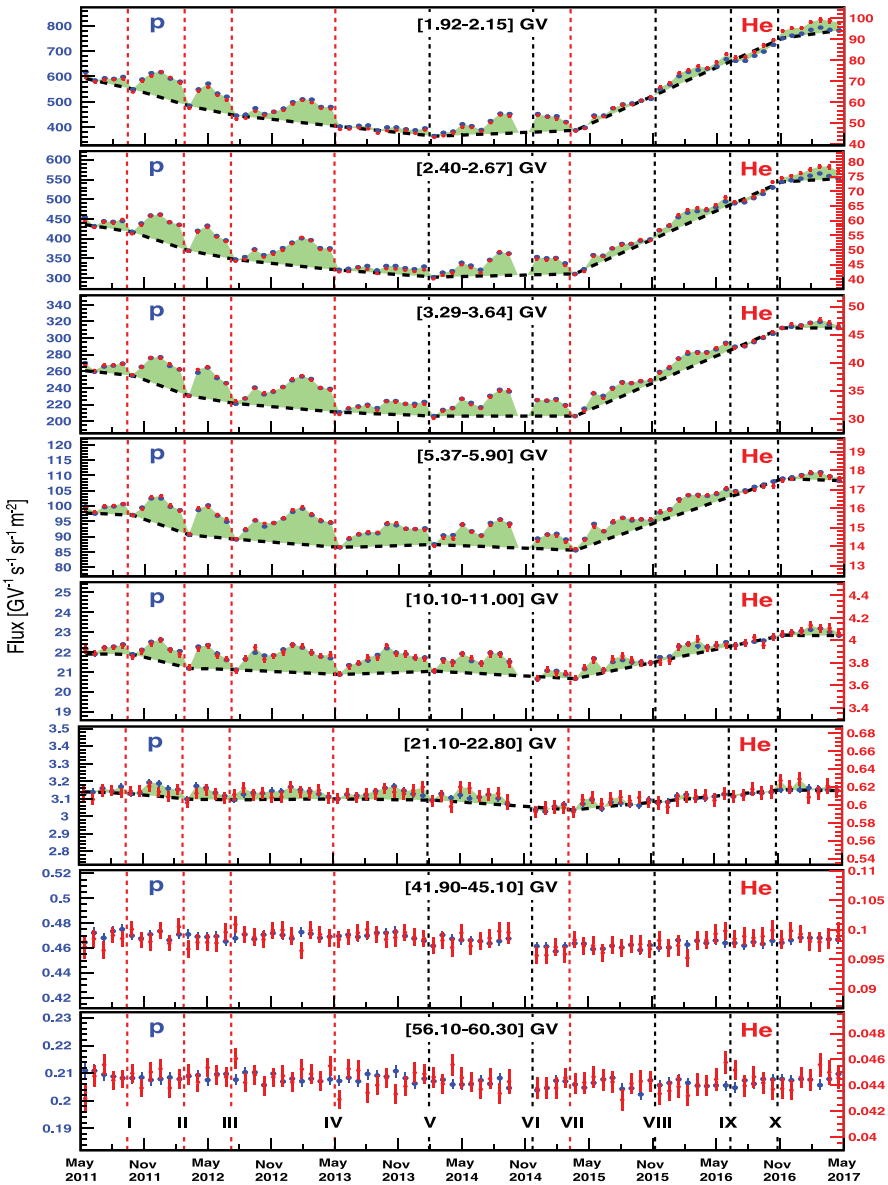

Fig. 107. The AMS proton (blue, left axis) and helium (red, right axis) fluxes as functions of time for 8 rigidity bins. The error bars are the quadratic sum of the statistical and time dependent systematic errors. Detailed structures (green shading and dashed lines to guide the eye) are clearly present below 40 GV. The vertical dashed lines denote boundaries between these structures at (I) September 27, 2011; II) March 7, 2012; (III) July 20, 2012; (IV) May 13, 2013; (V) February 7, 2014; (VI) December 1, 2014; (VII) March 19, 2015; (VIII) November 17, 2015; (IX) June 20, 2016; (X) November 28, 2016. The red vertical dashed lines denote structures that have also been observed by AMS in the electron flux and the positron flux, see Section 16. They fully coincide during the time period preceding the solar polarity change around July 2013.

For the first time, the charge-sign dependent modulation during solar maximum has been investigated in detail by leptons alone by AMS [177]. Based on 23.5 million events, we observed short-time structures, on the time scale of months, coincident in both the electron flux and the positron flux. The fluxes are shown in Fig. 109 as a function of time for five characteristic energy bins. We find a clear evolution of the fluxes with time at low energies that gradually diminishes towards high energies. At the lowest energies, the amplitudes of both the electron flux and the positron flux change by a factor of 3. Both fluxes exhibit profound short- and long-term variations. The short-term variations occur simultaneously in both fluxes with approximately the same relative amplitude. Several prominent and distinct structures are observed. They are characterized by minima, visible in both the electron flux and the positron flux across the energy range below $E < 10$ GeV. These are marked by dashed vertical lines in Fig. 109. At energies above 20 GeV, neither the electron flux nor the positron flux exhibits significant time dependence.

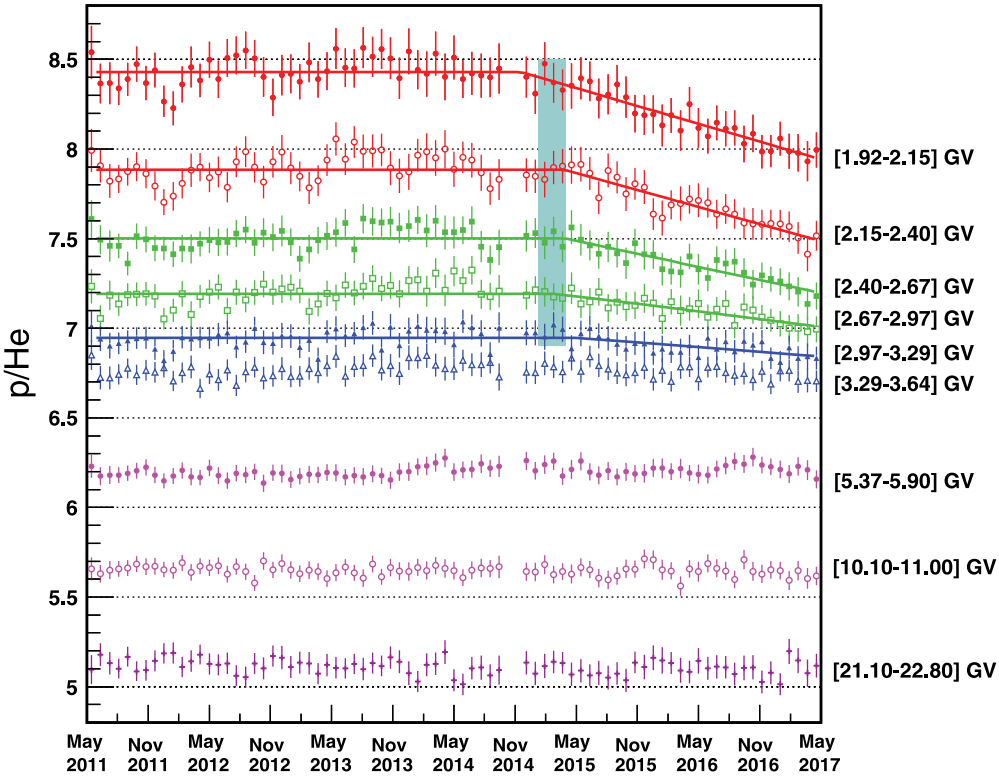

Fig. 108. The AMS p/He flux ratio as a function of time for 9 characteristic rigidity bins. The errors are the quadratic sum of the statistical and time dependent systematic errors. The solid lines are the best fit of Eq. (16), for the first 5 rigidity bins from [1.92–2.15] GV to [2.97–3.29] GV. The blue vertical band (February 28, 2015 ± 42 days) is the average of the best fit values of the transition time for these rigidity bins.

The long-term time structure of the data in Fig. 109 shows that the changes in relative amplitude are different for electrons and positrons. To quantify this effect, we use the ratio $R_e = \Phi_{e^+}/\Phi_{e^-}$, shown in Fig. 110 for one energy bin. In R_e, the important short-term variations in the fluxes largely cancel, and a clear overall long-term trend appears. At low energies, R_e is flat at first, then smoothly increases after the time of the solar magnetic field reversal, to reach a plateau at a higher amplitude.

We use a model independent approach to extract the energy dependence of the quantities that characterize the observed transition in R_e. With a set of four parameters, the 3871 independent R_e measurements as a function of energy and time can be described well with a logistic function:

$$R_e(t, E) = R_0(E)\left[1 + \frac{C(E)}{\exp\left(-\frac{t-t_{1/2}(E)}{\Delta t(E)/\Delta_{80}}\right) + 1}\right]. \tag{17}$$

At a given energy, the time-dependence is related to three parameters: the amplitude of the transition C; the midpoint of the transition $t_{1/2}(E)$; and the duration of the transition Δt. We choose $\Delta_{80} = 4.39$, such that Δt is the time it takes for the transition to proceed from 10% to 90% of the change in magnitude. The behavior of the logistic function is illustrated in Fig. 110 using the fit to data in the energy range [1.01–1.22] GeV.

The results of fitting in several energy bins from 1 to 21 GeV are shown in Fig. 111. We obtain $\chi^2/\text{d.o.f.} \approx 1$ for all fits.

The parameters $t_{1/2}(E)$ and $\Delta t(E)$ can only be determined at low energies, where the amplitude of the transition is large, see Fig. 112, where the energy dependences of these parameters are shown. As seen in Fig. 112a, the transition duration $\Delta t(E)$ is independent of energy and we obtain a value

$$\Delta t(E) = 830 \pm 30 \text{ days}.$$

Fig. 112b shows an energy-dependent time delay of $t_{1/2}(E)$, which is well parametrized using

$$t_{1/2}(E) - t_{\text{rev}} = \tau \cdot (E/\text{GeV})^{\rho}, \tag{18}$$

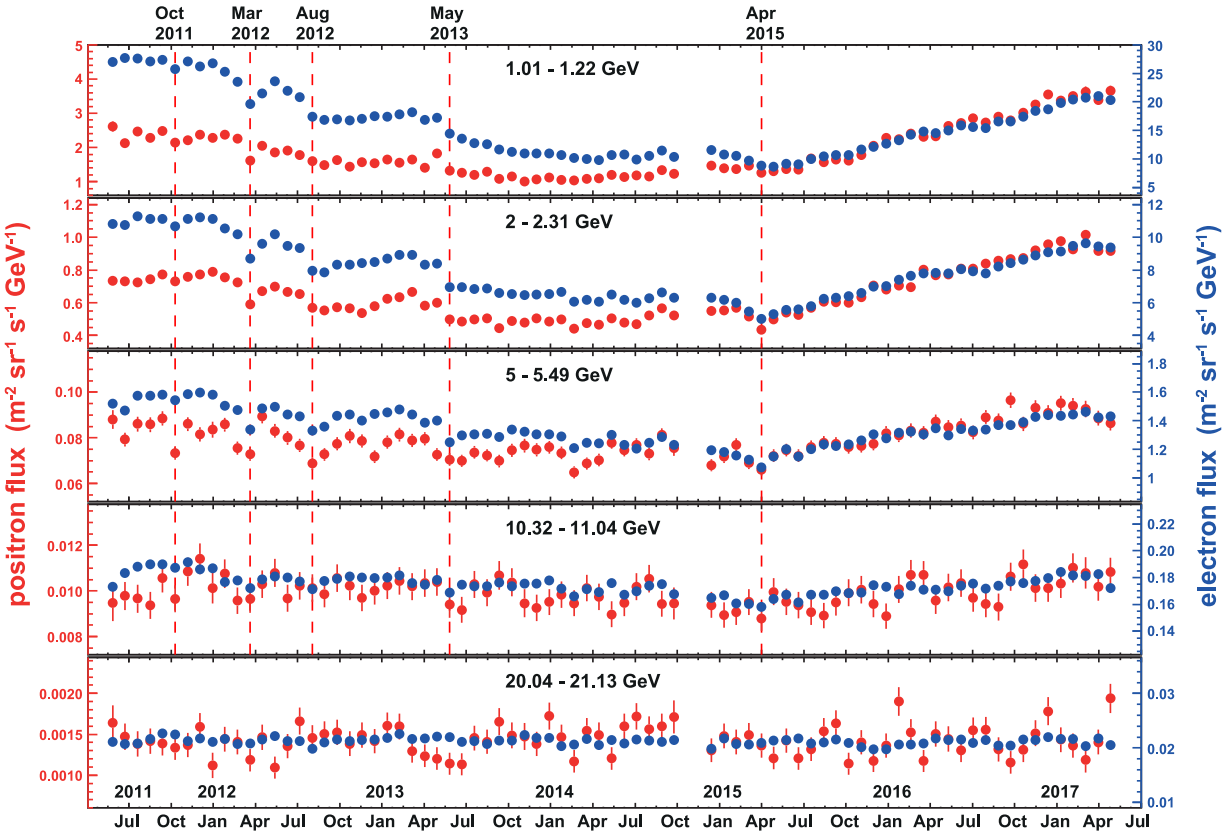

Fig. 109. Fluxes of cosmic-ray positrons (red, left axis) and electrons (blue, right axis) as functions of time, for five of the 49 energy bins. The error bars are the statistical uncertainties. Prominent and distinct time structures visible in both the positron spectrum and the electron spectrum and at different energies are marked by red dashed vertical lines (the same as red dashed vertical lines in Fig. 107).

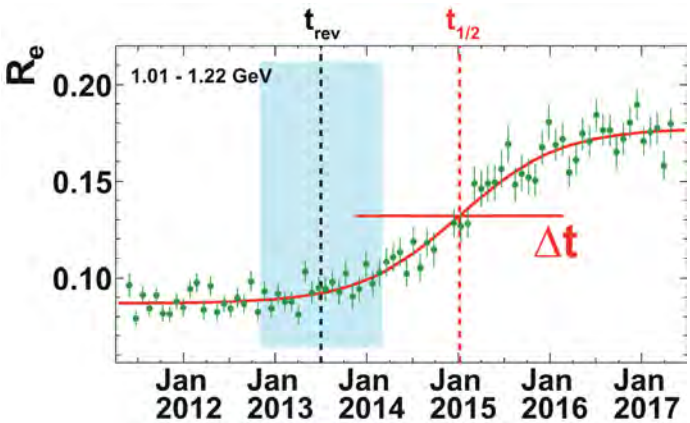

Fig. 110. Illustration of the logistic function parameters (Eq. (17)) in describing the time and energy dependence of R_e, using the fit in the energy bin [1.01–1.22] GeV as an example. The fit result is shown by the red curve. The data show that important short-term structures in the fluxes seen in Fig. 109 cancel in the flux ratio. The period without well-defined solar polarity is marked by the shaded area. Our choice for the effective time of the reversal of the solar magnetic field t_{rev} is marked by a black dashed vertical line. The fit result for the midpoint of the transition $t_{1/2}$ is marked by a red dashed vertical line. The width of the red horizontal bar indicates the duration of the transition Δt. It takes time Δt for the transition to proceed from 10% to 90% of the change in magnitude.

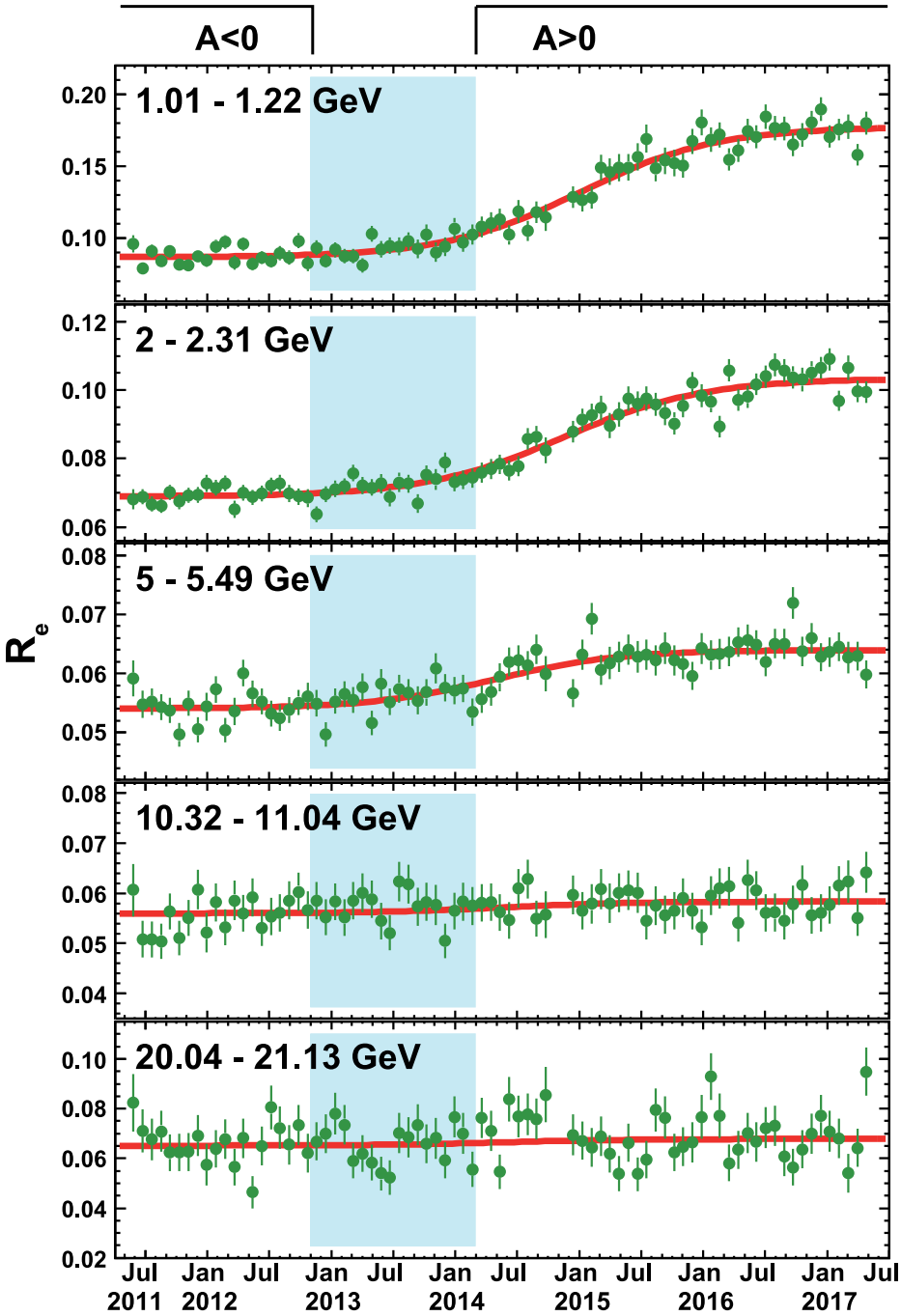

Fig. 111. The ratio R_e of the positron flux to the electron flux as a function of time. The error bars are statistical. The best-fit parametrization of a logistic function, Eq. (17), is shown by red curves. The polarity of the heliospheric magnetic field is denoted by $A < 0$ and $A > 0$. The period without well-defined polarity is marked by the shaded area.

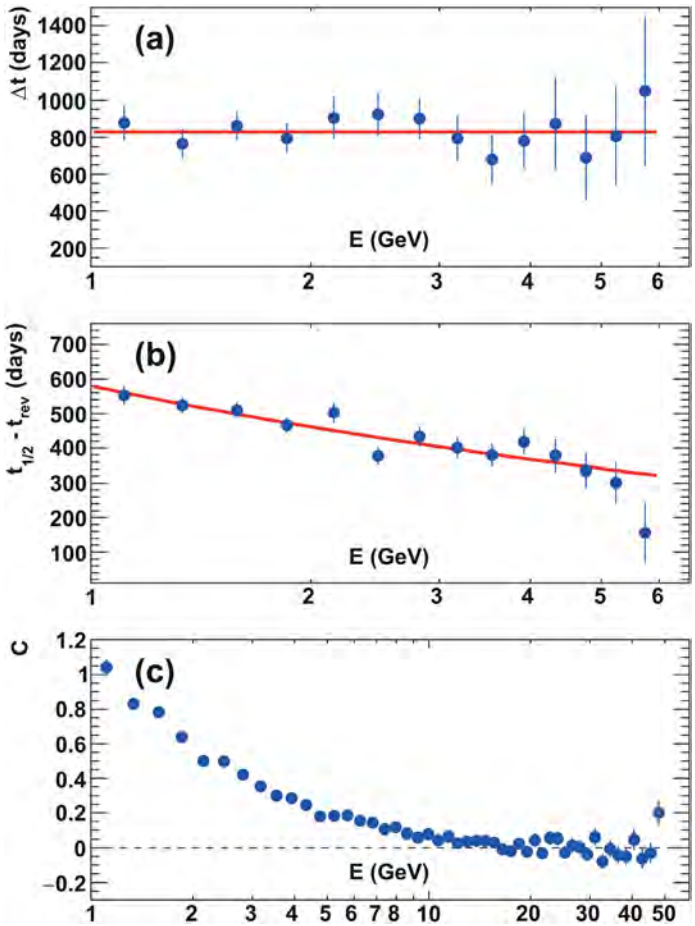

Fig. 112. Results of the logistic function fit to the ratio R_e as a function of energy (blue data points): (a) Δt and the best fit constant value of 830 days (red line); (b) $t_{1/2} - t_{\rm rev}$ with its parametrization (red curve, Eq. (18)), note that the fit value of $t_{1/2}(E)$ changes by 260 ± 30 days from 1 GeV to 6 GeV; (c) amplitude of the transition C with a dashed line at zero to guide the eye.

where we choose $t_{\rm rev}$ to be the effective time of the reversal of the solar magnetic field. For the value of $t_{\rm rev}$, we use 1 July 2013, the center of the period without well defined polarity [172]. A fit of Eq. (18) yields

$$\rho = -0.33 \pm 0.04\,(\text{stat})\,^{+0.08}_{-0.15}\,(\text{syst}),$$
$$\tau = 580 \pm 19\,(\text{stat}) \pm 136\,(\text{syst})\ \text{days},$$

and the value of $t_{1/2}(E)$ changes by 260 ± 30 days from 1 GeV to 6 GeV, as seen in Fig. 112b.

To study the amplitude of the transition C in Fig. 112c, we have fixed $\Delta t(E)$ to its average value of 830 days and we use the value of $t_{1/2}(E)$ calculated from Eq. (17) for energies above 6 GeV. At high energies, the fit result for the amplitude depends only weakly on the choice of the values for $\Delta t(E)$ and $t_{1/2}(E)$. As seen in Fig. 112c, C is close to 1 at $E = 1$ GeV and decreases smoothly with energy. This is in qualitative agreement with the expectation from solar modulation models including drift effects [178]. Above 20 GeV, the amplitude of the transition is consistent with zero.

In conclusion, for the first time, the charge-sign dependent modulation during solar maximum has been investigated in detail by leptons alone. We observe prominent, distinct, and coincident structures in both the positron flux and the electron flux on a time scale of months. These structures are not visible in the e^+/e^- flux ratio. We also observe the existence of a long-term feature in the e^+/e^- flux ratio, namely, a smooth transition from one value to another, after the polarity reversal of the solar magnetic field. The duration of the transition is measured to be 830 ± 30 days, independent of energy. The transition magnitude is decreasing as a function of energy. The midpoint of the transition relative to the polarity reversal of the solar magnetic field changes by 260 ± 30 days from 1 to 6 GeV. These high-statistics, precision data on positrons and electrons provide accurate input to the understanding of solar modulation.

17. Summary

Since the discovery of cosmic rays in 1912, cosmic ray experiments have provided fundamentally important information for particle physics, such as discovery of e^+, $\pi^\pm$, $K^\pm$, etc., and on the nature of the cosmos.

Based on the cosmic ray studies over the past century important models of cosmic rays have been developed (Leaky Box, galprop, dragon, usine, etc.).

The precision and characteristics of the AMS data, simultaneously for many different types of cosmic rays, provide unique input to the understanding of cosmic ray production and propagation. This requires a new and comprehensive model.

AMS will continue collecting data through the life of the ISS exploring the physics of complex anti-matter (anti-He, anti-C, etc.), the physics of dark matter (anti-deuterons, anti-protons, and positrons), the physics of cosmic-ray nuclei across the periodic table, and study solar physics over the entire solar cycle.

Declaration of competing interest

The authors declare that they have no known competing financial interests or personal relationships that could have appeared to influence the work reported in this paper.

Acknowledgments

We thank former NASA Administrator Daniel S. Goldin for his dedication to the legacy of the ISS as a scientific laboratory and his decision for NASA to fly AMS as a DOE payload. We particularly want to acknowledge the continuous strong support and guidance of the former NASA, USA Associate Administrator William H. Gerstenmaier, whose enthusiasm to use the ISS to explore frontier science has made AMS a reality.

We also want to acknowledge the support, dedication and guidance of the AMS Program Office at JSC, USA as well as the MSFC, USA flight control teams which has allowed AMS to operate continuously and optimally on the ISS.

We are grateful for the support of Jim Siegrist and Glen Crawford and their staff of the DOE, USA including resources from the National Energy Research Scientific Computing Center under Contract No. DE-AC02-05CH11231.

We gratefully acknowledge the strong support from CERN, Switzerland including Fabiola Gianotti, Rolf Heuer, Robert Aymar, Dieter Schinzel, Bernd Panzer-Steindel, and Andrzej Siemko.

We gratefully acknowledge the strong support from the European Space Agency including Johann-Dietrich Wörner and Simonetta Di Pippo.

We also acknowledge the continuous support from MIT, USA and its School of Science, Michael Sipser, Robert Silbey, Robert Birgeneau, and the Laboratory for Nuclear Science Boleslaw Wyslouch, Richard Milner, June Mathews, and Robert Redwine. We dedicate this paper to the memory of our long-term colleagues Ulrich Becker and Fred Eppling.

We acknowledge the continuous and strong support of Chinese Academy of Sciences, China, Institute of High Energy Physics, China, Institute of Electrical Engineering, China, China Academy of Space Technology, China, National Natural Science Foundation, and Ministry of Science and Technology, the China Scholarship Council, China, the provincial governments of Shandong, Jiangsu, Guangdong, Shandong University, Shandong Institute of Advanced Technology, China.

AMS research is supported by: the Academy of Finland, Finland, Project No. 321882, Finland; CNRS/IN2P3, France and CNES, France, France; Pascale Ehrenfreund, DLR, Germany under Grants No. 50OO1403 and No. 50OO1803 and JARA-HPC, Germany under Project No. JARA0052, Germany; INFN, Italy and ASI, Italy under ASI-INFN Agreements No. 2019-19-HH.0 and No. 2014-037-R.0, and ASI-University of Perugia, Italy Agreement No. 2019-2-HH.0, Italy; CHEP, Republic of Korea and NRF, Republic of Korea under Grant No. NRF-2018R1A6A1A06024970 at Kyungpook National University, Korea; the Consejo Nacional de Ciencia y Tecnología, Mexico and UNAM, Mexico, Mexico; NWO, Netherlands under Grant. No. 680-1-004, the Netherlands; FCT, Portugal under Grant No. CERN/FIS-PAR/0013/2019, Portugal; CIEMAT, Spain, IAC, Spain, CDTI, Spain, and SEIDI-MINECO, Spain under Grants No. ESP2017-87055-C2-1-P, No. SEV-2015-0548, No. MDM-2015-0509, and No. RyC-2013-14660, Spain; the Swiss National Science Foundation (SNSF), Switzerland, federal and cantonal authorities, and the Fondation Dr. Manfred Steuer, Switzerland; Academia Sinica, Taiwan and the Ministry of Science and Technology (MOST), Taiwan under Grants No. 103-2112-M-006-018-MY3, No. 105-2112-M-001-003, and No. CDA-105-M06, former Presidents of Academia Sinica Yuan-Tseh Lee and Chi-Huey Wong and former Ministers of MOST Maw-Kuen Wu and Luo-Chuan Lee, Taiwan; the Turkish Atomic Energy Authority, Turkey under Grants No. 2017TAEK(CERN)A5.H6.F2-15, Turkey; and NSF, United States Grants No. 14255202 and No. 1551980, Wyle Laboratories, United States Grant No. 2014/T72497, and NASA NESSF, United States Grant No. HELIO15F-0005, USA. We are grateful for important physics discussions with Pasquale Blasi, Fiorenza Donato, Jonathan Ellis, Jonathan Feng, Tim Linden, Igor Moskalenko, Subir Sarkar, and Steven Weinberg.

References

[1] M. Aguilar, et al., Phys. Rep. 366 (2002) 331.
[2] N.W. Boggess, et al., Astrophys. J. 397 (1992) 420.
[3] C. Fichtel, Astron. Astrophys. Suppl. Ser 120 (1996) 23.
[4] C.L. Bennett, et al., Astrophys. J. Suppl. Ser. 208 (2013) 20.
[5] N. Aghanim, et al., Astron. Astrophys. 641 (2020) A1.
[6] H.U. Zimmermann, Data Analysis in Astronomy IV, in: Ettore Majorana International Science Series, vol 59, Springer, Boston, MA, 1992.
[7] J. Leibee, M. Seidleck, J. McEnery, 2009 IEEE Aerospace conference, 2009.
[8] M. Tavani, et al., Astron. Astrophys. 502 (2009) 995.
[9] M.C. Weisskopf, et al., Exp. Astrophys. 16 (2003) 1.
[10] C. Winkler, et al., Astron. Astrophys. 411 (2003) L1.
[11] J.J. Dalcanton, et al., Nature 457 (2009) 41.
[12] M. Greenhouse, 2009 IEEE Aerospace conference, 2009.
[13] G. Aielli, et al., Nucl. Instrum. Methods Phys. Res. A 661 (2012) S50.
[14] A.J. Smith, PoS ICRC 2015, 2016, p. 966.
[15] H. Prokoph, PoS ICRC 2019, 2019, p. 656.
[16] D. Masin, AIP Conf. Proc. 1505 (2012) 186.
[17] F. Halzen1, S.R. Klein, Rev. Sc. Instr. 81 (2010) 081101.
[18] M. Takita, et al., PoS ICRC2017, 2017, p. 831.
[19] C. Zhen, et al., Chin. Astron. Astrophys. 43 (2019) 457.
[20] T.G. Guzik, et al., Adv. Space Res. 33 (2004) 1763.
[21] Y. Ajima, et al., Nucl. Instrum. Methods Phys. Res. A 443 (2000) 71.
[22] M. Circella, et al., Nuclear Phys. A 85 (2000) 355.
[23] E.S. Seo, et al., Adv. Space Res. 33 (2004) 1777.
[24] E. Stone, et al., Space Sc. Rev. 86 (1998) 285.
[25] M. Bouffard, J.J. Engelmann, L. Koch, A. Soutoul, N. Lund, B. Peters, I.L. Rasmussen, Astrophys. Space Sc. 84 (1982) 3.
[26] P. Picozza, et al., Astropart. Phys. 27 (2007) 296.
[27] Y. Asaoka, PoS ICRC2019, 2019, p. 1.
[28] E.S. Seo, et al., PoS ICRC 2019, 2019, p. 137.
[29] J. Chang, et al., Astropart. Phys. 95 (2017) 6.
[30] L. Wiencke, A. Olinto, PoS ICRC 2017, 2017, p. 1097;
L. Wiencke, PoS ICRC 2019, 2019, p. 466.
[31] A. Olinto, et al., PoS ICRC2019, 2019, p. 378.
[32] A. Castellina, PoS ICRC 2019, 2019, p. 004.
[33] W.D. Apel, et al., Nucl. Instrum. Methods Phys. Res. A 620 (2010) 202.
[34] S. Ogio, PoS ICRC 2019, 2019, p. 013.
[35] U. Barres de Almeida, PoS ICRC 2019, 2019, p. 627.
[36] A. Kounine, Internat. J. Modern Phys. E 21 (2012) 1230005;
S. Rosier-Lees, Proceedings of the 19th Symposium on Astroparticle Physics in the Netherlands, Beekbergen, 2014, unpublished;
S.C.C. Ting, Nucl. Phys. B Proc. Suppl. 244 (2013) 12;
S.C. Lee, Proceedings of the 20th International Conference on Supersymmetry and Unification of Fundamental Interactions (SUSY 2012), Beijing, 2012, unpublished;
M. Aguilar, Proceedings of the XL International Meeting on Fundamental Physics, Centro de Ciencias de Benasque Pedro Pascual, 2012, unpublished;
S. Schael, Proceedings of the 10th Symposium on Sources and Detection of Dark Matter and Dark Energy in the Universe, Los Angeles, 2012, unpublished;
B. Bertucci, Proc. Sci., EPS-HEP, 2011, p. 67;
M. Incagli, AIP Conf. Proc. 1223 (2010) 43;
R. Battiston, Nucl. Instrum. Methods Phys. Res. A 588 (2008) 227.
[37] J. Allison, et al., Nucl. Instrum. Methods Phys. Res. A 835 (2016) 186;
J. Allison, et al., IEEE Trans. Nucl. Sci. 53 (2006) 270;
S. Agostinelli, et al., Nucl. Instrum. Methods Phys. Res. A 506 (2003) 250.
[38] K. Lübelsmeyer, et al., Nucl. Instrum. Methods Phys. Res. A 654 (2011) 639.
[39] B. Alpat, et al., Nucl. Instrum. Methods Phys. Res. A 613 (2010) 207.
[40] G. Ambrosi, V. Choutko, C. Delgado, A. Oliva, Q. Yan, Y. Li, Nucl. Instrum. Methods Phys. Res. A 869 (2017) 29.
[41] Zh. Qu, S. Haino, P. Zuccon, M. Zhao, Nucl. Instrum. Methods Phys. Res. A 869 (2017) 135.
[42] C. Höppner, S. Neubert, B. Ketzer, S. Paul, Nucl. Instrum. Methods Phys. Res. A 620 (2010) 580.
[43] J. Berdugo, V. Choutko, C. Delgado, Q. Yan, Nucl. Instrum. Methods Phys. Res. A 869 (2017) 10.
[44] M. Aguilar, et al., Phys. Rev. Lett. 117 (2016) 091103.
[45] M. Aguilar, et al., Phys. Rev. Lett. 122 (2019) 041102.
[46] Y. Jia, Q. Yan, V. Choutko, H. Liu, A. Oliva, Nucl. Instrum. Methods Phys. Res. A 972 (2020) 164169.
[47] F. Hauler, et al., IEEE Trans. Nucl. Sci. 51 (2004) 1365;
Ph. Doetinchem, et al., Nucl. Instrum. Methods Phys. Res. A 558 (2006) 526;
Th. Kirn, Nucl. Instrum. Methods Phys. Res. A 706 (2013) 43.
[48] T. Räihä, A. Bachlechner, B. Beischer, C.H. Chung, H. Gast, S. Schael, T. Siedenburg, Nucl. Instrum. Methods Phys. Res. A 868 (2017) 10.
[49] V. Bindi, et al., Nucl. Instrum. Methods Phys. Res. A 743 (2014) 22, and references therein.
[50] Ph. von Doetinchem, W. Karpinski, Th. Kirn, K. Lübelsmeyer, St. Schael, M. Wlochal, Nucl. Phys. B Proc. Suppl. 197 (2009) 15.
[51] M. Aguilar-Benitez, et al., Nucl. Instrum. Methods Phys. Res. A 614 (2010) 237;
F. Giovacchini, Nucl. Instrum. Methods Phys. Res. A 766 (2014) 57.
[52] C. Adloff, et al., Nucl. Instrum. Methods Phys. Res. A 714 (2013) 147.
[53] A. Kounine, Z. Weng, W. Xu, C. Zhang, Nucl. Instrum. Methods Phys. Res. A 869 (2017) 110.
[54] M. Tanabashi, et al., (Particle Data Group), Phys. Rev. D 98 (2018) 030001.
[55] M. Aguilar, et al., Phys. Rev. Lett. 110 (2013) 141102;
L. Accardo, et al., Phys. Rev. Lett. 113 (2014) 121101.

[56] M. Aguilar, et al., Phys. Rev. Lett. 113 (2014) 121102;
M. Aguilar, et al., Phys. Rev. Lett. 113 (2014) 221102.
[57] P. Lipari, Phys. Rev. D 95 (2017) 063009;
R. Cowsik, B. Burch, T. Madziwa-Nussinov, Astrophys. J. 786 (2014) 124;
K. Blum, B. Katz, E. Waxman, Phys. Rev. Lett. 111 (2013) 211101.
[58] P.D. Serpico, Astropart. Phys. 39–40 (2012) 2;
T. Linden, S. Profumo, Astrophys. J. 772 (2013) 18;
P. Mertsch , S. Sarkar, Phys. Rev. D 90 (2014) 061301;
N. Tomassetti, F. Donato, Astrophys. J. Lett. 803 (2015) L15;
D. Hooper, I. Cholis, T. Linden, K. Fang , Phys. Rev. D 96 (2017) 103013;
W. Liu, X.J. Bi, S.J. Lin, B.B. Wang, P.F. Yin, Phys. Rev. D 96 (2017) 023006;
M. Kachelrieß, A. Neronov, D.V. Semikoz, Phys. Rev. D 97 (2018) 063011;
S. Profumo, J. Reynoso-Cordova, N. Kaaz, M. Silverman, Phys. Rev. D 97 (2018) 123008.
[59] T. Linden, S. Profumo, Astrophys. J. 772 (2013) 18;
D. Hooper, P. Blasi, P.D. Serpico, JCAP (2009) 0901;
JCAP 01 (2009) 025.
[60] K. Ioka, Progr. Theoret. Phys. 123 (2010) 743.
[61] M.S. Turner, F. Wilczek, Phys. Rev. D 42 (1990) 1001;
J. Ellis, AIP Conf. Proc. 516 (2000) 21;
H. Cheng, J. Feng, K. Matchev, Phys. Rev. Lett. 89 (2002) 211301;
G. Kane, R. Lu, S. Watson, Phys. Lett. B 681 (2009) 151;
J. Feng, Ann. Rev. Astron. Astrophys. 48 (2010) 495;
C.H. Chen, C.W. Chiang, T. Nomura, Phys. Lett. B 747 (2015) 495;
H.C. Cheng, W.C. Huang, X. Huang, I. Low, Y.L. Sming Tsia, Q. Yuan , JCAP 03 (2017) 041;
Y. Bai, J. Berger, S. Lu, Phys. Rev. D 97 (2018) 115012.
[62] J. Kopp, Phys. Rev. D 88 (2013) 076013.
[63] M. Aguilar, et al., Phys. Rev. Lett. 114 (2015) 171103.
[64] G.D. Lafferty, T.R. Wyatt, Nucl. Instrum. Methods Phys. Res. A 355 (1995) 541, We have used Eq. (6) with $\tilde{E}(\tilde{R}) \equiv x_{lw}$.
[65] O. Adriani, et al., Phys. Rev. Lett. 111 (2013) 081102.
[66] M. Ackermann, et al., Phys. Rev. Lett. 108 (2012) 011103.
[67] C. Grimani, et al., Astron. Astrophys. 392 (2002) 287.
[68] M. Boezio, et al., Adv. Space Res. 27 (2001) 669.
[69] M. Aguilar, et al., Phys. Lett. B 646 (2007) 145.
[70] S.W. Barwick, et al., Astrophys. J. 498 (1998) 779;
M.A. DuVernois, et al., Astrophys. J. 559 (2001) 296;
J.J. Beatty, et al., Phys. Rev. Lett. 93 (2004) 241102.
[71] I.V. Moskalenko, A.W. Strong, Astrophys. J. 493 (1998) 694;
A.E. Vladimirov, S.W. Digela, G. Jóhannesson, P.F. Michelson, I.V. Moskalenko, P.L. Nolan, E. Orlando, T.A. Porter, A.W. Strong, Comput. Phys. Commun. 182 (2011) 1156.
[72] R. Trotta, G. Johannesson, I. Moskalenko, T. Porter, R. Ruiz de Austri, A. Strong, Astrophys. J. 729 (2011) 106.
[73] T. Delahaye, J. Lavalle, R. Lineros, F. Donato, N. Fornengo, Astron. Astroph 524 (2010) A51.
[74] C. Evoli, D. Gaggero, D. Grasso, L. Maccione, J. Cosmol. Astropart. Phys. 10 (2008) 018.
[75] D. Maurin, Comput. Phys. Comm. 247 (2020) 106942.
[76] R. Kissmann, J. Phys. Conf. Ser. 837 (2017) 012003.
[77] R.A. Caballero-Lopez, H. Moraal, J. GeoPhys. Res. A 109 (2004) 01101;
L. Gleeson, W. Axford, Astrophys. J. 154 (1968) 1011, We have also used recent data from theUniversity of Oulu website and varied the solar potential ϕ from 0.50 to 0.62 GV in the fit.
[78] I.G. Usoskin, A. Gil, G.A. Kovaltsov, A. Mishev, V.V. Mikhailov, J. Geophys. Res. Space Phys. 122 (2017) 3875, Recent data are taken from the University of Oulu website.
[79] M.A. Velasco, Ph. D. Thesis, Universidad Complutense de Madrid, 2018;
S. Zeissler, Ph. D. Thesis, Karlsruhe Institute of Technology, 2018.
[80] M. Aguilar, et al., Phys. Rev. Lett. 122 (2019) 101101.
[81] J. Alcaraz, et al., Phys. Lett. B 484 (2000) 10.
[82] O. Adriani, et al., Phys. Rev. Lett. 106 (2011) 201101.
[83] A.M. Hillas, J. Phys. G: Nucl. Part. Phys. R 31 (2005) 95;
Y.Z. Fan, B. Zhang, J. Chang, Int. J. Mod. Phys. D 19 (2010) 2011.
[84] T. Kobayashi, Y. Komori, K. Yoshida, J. Nishimura, Astrophys. J. 601 (2004) 340.
[85] Ł. Stawarz, V. Petrosian, R.D. Blandford, Astrophys. J. 710 (2010) 236.
[86] A.W. Strong, E. Orlando, T.R. Jaffe, Astron. Astrophys. A 534 (2011) 54.
[87] M. Aguilar, et al., Phys. Rev. Lett. 121 (2018) 051102.
[88] J. Chang, et al., Nature 456 (2008) 362.
[89] F. Aharonian, et al., Astron. Astrophys. 508 (2008) 561;
F. Aharonian, et al., Phys. Rev. Lett. 101 (2008) 261104;
D. Kerszberg, M. Kraus, D. Kolitzus, K. Egberts, S. Funk, P. J.-Lenain, O. Reimer, P. Vincent, The cosmic-ray electron spectrum measured with H.E.S.S., CRI215, proceedings of the 35th International Cosmic Ray Conference (ICRC-2017), Busan, 2017, unpublished.
[90] S. Abdollahi, et al., Phys. Rev. D 95 (2017) 082007.
[91] G. Ambrosi, et al., Nature 552 (2017) 63.
[92] O. Adriani, et al., Phys. Rev. Lett. 120 (2018) 261102.
[93] M. Aguilar, et al., Phys. Rev. Lett. 113 (2014) 221102.
[94] See, for example, P. Blasi, Braz. J. Phys. 44 (2014) 426;
also, P. Blasi, Astron. Astrophys. Rev. 21 (2013) 70.

[95] M. Ackermann, et al., Phys. Rev. Lett. 112 (2014) 151103;
M. Hareyama, et al., J. Phys. Conf. 31 (2006) 159;
M. Boezio, et al., Astropart. Phys. 19 (2003) 583;
E. Diehl, D. Ellithorpe, D. Muller, S.P. Swordy, Astropart. Phys. 18 (2003) 487;
J. Alcaraz, et al., Phys. Lett. B 490 (2000) 27;
W. Menn, et al., Astrophys. J. 533 (2000) 281;
R. Bellotti, et al., Phys. Rev. D 60 (1999) 052002;
M. Boezio, et al., Astrophys. J. 518 (1999) 457;
K. Asakimori, et al., Astrophys. J. 502 (1998) 278;
M. Ichimura, et al., Phys. Rev. D 48 (1993) 1949;
I.P. Ivanenko, et al., Proceedings of the 23rd International Cosmic Ray Conference, Calgary, 1993, p. 17.
[96] A.D. Panov, et al., Bull. Russian Acad. Sci. 73 (2009) 564.
[97] We are grateful to the BESS-Polar Collaboration for providing the BESS-Polar II proton spectrum,measured during a 25-day Antarctic balloon flight in December 2007 and January 2008. Statistical and systematic errors are combined. A publication detailing these measurements is in preparation. For a description of the BESS-Polar experiment see, K. Abe, et al., Phys. Rev. Lett. 108 (2012) 051102;
For the BESS experiment see, Y. Shikaze, et al., Astropart. Phys. 28 (2007) 154;
S. Haino, et al., Phys. Lett. B 594 (2004) 35;
T. Sanuki, et al., Astrophys. J. 545 (2000) 1135.
[98] For the CREAM experiment see, Y.S. Yoon, et al., Astrophys. J. 728 (2011) 122.
[99] For the PAMELA experiment see, O. Adriani, et al., Astrophys. J. 765 (2013) 91;
O. Adriani, et al., Science 332 (2011) 69.
[100] O. Adriani, et al., Phys. Rev. Lett. 122 (2019) 181102.
[101] Q. An, et al., Sc. Adv. 5 (9) (2019) eaax3793.
[102] See, for example, G. Bernard, T. Delahaye, P. Salati, R. Taillet, Astronon. Astrophys. A 555 (2013) 48;
V.S. Ptuskin, V. Zirakashvili, E.S. Seo, Astrophys. J. 47 (2013) 763;
N. Tomassetti, Astrophys. J. Lett. 752 (2012) L13;
P. Blasi, E. Amato, P.D. Serpico, Phys. Rev. Lett. 109 (2012) 061101;
A.E. Vladimirov, G. Jóhannesson, I.V. Moskalenko, T.A. Porter, Astrophys. J. 752 (2012) 68.
[103] D. Maurin, F. Melot, R. Taillet, Astron. Astrophys. A 569 (2014) 32, (this reference describes a database used to extract data from other experiments).
[104] G.F. Smoot, A. Buffington, C.D. Orth, Phys. Rev. Lett. 35 (1975) 258;
E.A. Bogomolov, et al., Proceedings of the 16th International Cosmic Ray Conference, Vol. 1 , University of Tokio, Tokio, Japan , 1979, p. 330;
R.L. Golden, S. Horan, B.G. Mauger, G.D. Badhwar, J.L. Lacy, S.A. Stephens, R., R. Daniel, J.E. Zipse, Phys. Rev. Lett. 43 (1979) 1196;
A. Buffington, S.M. Shindler, Astrophys. J. 247 (1981) L105.
[105] K. Yoshimura, et al., Phys. Rev. Lett. 75 (1995) 3792;
S. Orito, et al., Phys. Rev. Lett. 84 (2000) 1078;
Y. Asaoka, et al., Phys. Rev. Lett. 88 (2002) 051101;
K. Abe, et al., Phys. Lett. B 670 (2008) 103;
K. Abe, et al., Phys. Rev. Lett. 108 (2012) 051102;
K. Abe, et al., Astrophys. J. 882 (2016) 65.
[106] M. Boezio, et al., Astrophys. J. 487 (1997) 415;
M. Boezio, et al., Astrophys. J. 561 (2001) 787.
[107] A.S. Beach, et al., Phys. Rev. Lett. 87 (2001) 271101.
[108] M. Aguilar, et al., Phys. Rep. 366 (2002) 331.
[109] O. Adriani, et al., Phys. Rev. Lett. 102 (2009) 051101;
O. Adriani, et al., Phys. Rev. Lett. 105 (2010) 121101;
O. Adriani, et al., JETP Lett. 96 (2013) 621.
[110] K. Hamaguchi, T. Moroi, K. Nakayama, Phys. Lett. B 747 (2015) 523;
Y.-H. Chen, K. Cheung, P.-Y. Tseng, Phys. Rev. D 93 (2016) 015015.
[111] R. Kappl, M.W. Winkler, J. Cosmol. Astropart. Phys. 09 (2014) 051;
G. Giesen, Others JCAP 09 (2015) 023;
C. Evoli, D. Gaggero, D. Grasso, JCAP 12 (2015) 039;
Q. Yuan, S.-J. Lin, K. Fang, X.-J. Bi , Phys. Rev. D 95 (2017) 083007;
M. Kachelriess, I.V. Moskalenko, S.S. Ostapchenko, Astrophys. J. 803 (2015) 54;
M.W. Winkler, JCAP 02 (2017) 048.
[112] P. Lipari, Phys. Rev. D 95 (2017) 063009.
[113] V. Bresci, E. Amato, P. Blasi, G. Morlino, Mon. Not. R. Astron. Soc. 488 (2019) 2068.
[114] A. Cuoco, M. Krämer, M. Korsmeier, Phys. Rev. Lett. 118 (2017) 191102;
A. Reinert, M.W. Winkler, JCAP 01 (2018) 055;
I. Cholis, T. Linden, D. Hooper, Phys. Rev. D 99 (2019) 103026.
[115] M.Y. Cui, Q. Yuan, Y.L.S. Tsai, Y.Z. Fan, Phys. Rev. Lett. 118 (2017) 191101.
[116] A. Cuoco, J. Heisig, L. Klamt, M. Korsmeier, M. Krämer, Phys. Rev. D 99 (2019) 103014;
M. Carena, J. Osborne, N.R. Shah, E.M., C. Wagner, Phys. Rev. D 100 (2019) 055002.
[117] F.C. Jones, Phys. Rev. B 137 (1965) 1306;
G.R. Blumenthal, R.J. Gould, Rev. Mod. Phys. 42 (1970) 237;
R. Cowsik, M.A. Lee, Astrophys. J. 228 (1979) 297.
[118] J. Jaros, et al., Phys. Rev. C 18 (1978) 2273;
A. Ozawa, et al., Nucl. Phys. a 691 (2001) 599;
I. Tanihata, et al., Phys. Lett. B 160 (1985) 380;
V.G. Ableev, et al., ACTA Physica Polonica B 16 (1985) 913.
[119] Q. Yan, V. Choutko, A. Oliva, M. Paniccia, Nuclear Phys. A 996 (2020) 121712.
[120] M. Aguilar, et al., Phys. Rev. Lett. 119 (2017) 251101.

[121] M.J. Boschini, et al., Astrophys. J. 840 (2017) 115;
M.J. Boschini, et al., Astrophys. J. 858 (2018) 61, In the 2018 paper, for each individual primary cosmic ray He, C, and O a set of distinct parameters are chosen so that, with their model, they can describe our measured data. We thank Professor I. Moskalenko for the illuminating discussions on these important papers.
[122] C. Evoli, R. Aloisio, P. Blasi, Phys. Rev. D 99 (2019) 103023;
M.J. Boschini, et al., Astrophys. J. 889 (2020) 167;
N. Weinrich, Y. Génolini, M. Boudaud, L. Derome, D. Maurin, Astron. Astrophys. A 639 (2020) 131.
[123] B. Schwarzschild, Phys. Today 64 (5) (2011) 10;
P.D. Serpico, Proc. 34th ICRC PoS(ICRC2015), 2015, p. 009.
[124] A.D. Erlykin, A.W. Wolfendale, J. Phys. G: Nucl. Part. Phys. 42 (2015) 075201;
M.A. Malkov, P.H. Diamond, R.Z. Sagdeev , Phys. Rev. Lett. 108 (2012) 081104;
L.A. Fisk and, G. Gloeckler, Astrophys. J. 744 (2012) 127.
[125] N. Tomassetti, Adv. Sp. Res. 60 (2017) 815;
N. Tomassetti, Astrophys. J. Lett. 815 (2015) L1.
[126] A.C. Cummings, et al., Astrophys. J. 831 (2016) 18, The Voyager data are converted from kinetic energy per nucleon to rigidity, assuming pure p and ^{4}He for proton and helium samples, respectively. The Voyager p/He ratio as a function of rigidity is computed by interpolating He flux linearly to the corresponding values of the proton rigidity bins.
[127] E. Juliusson, Astrophys. J. 191 (1974) 331.
[128] C.D. Orth, A. Buffington, G.F. Smoot, T.S. Mast, Astrophys. J. 226 (1978) 1147.
[129] W.R. Webber, S.M. Yushak, Proceedings of 16th International Cosmic Ray Conference, vol. 12, Tokyo 1979, p. 51.
[130] J.A. Lezniak, W.R. Webber, Astrophys. J. 223 (1978) 676.
[131] R.C. Maehl, J.F. Ormes, A.J. Fisher, F.A. Hagen, Astrophys. Space Sci. 47 (1977) 163.
[132] M. Simon, H. Spiegelhauer, W.K.H. Schmidt, F. Siohan, J.F. Ormes, V.K. Balasubrahmanyan, J.F. Arens, Astrophys. J. 239 (1980) 712.
[133] S.P. Swordy, D. Müller, P. Meyer, J. L'Heureux, J.M. Grunsfeld, Astrophys. J. 349 (1990) 625.
[134] J.J. Engelmann, P. Ferrando, A. Soutoul, P. Goret, E. Juliusson, Astron. Astrophys. 233 (1990) 96.
[135] A. Obermeier, M. Ave, P. Boyle, Ch. Höppner, J. Hörandel, D. Müller, Astrophys. J. 724 (2011) 14.
[136] O. Adriani, et al., Astrophys. J. 791 (2014) 93.
[137] M. Aguilar, et al., Phys. Rev. Lett. 120 (2018) 021101.
[138] S. Thoudam, J.R. Hörandel, Mon. Not. R. Astron. Soc. 435 (2013) 2532.
[139] A.E. Vladimirov, et al., Astrophys. J. 752 (2012) 68.
[140] I.A. Grenier, J.H. Black, A.W. Strong, Annu. Rev. Astron. Astrophys. 53 (2015) 199;
P. Blasi, Astron. Astrophys. Rev. 21 (2013) 70;
A.W. Strong, I.V. Moskalenko, V.S. Ptuskin, Annu. Rev. Nucl. Part. Sci. 57 (2007) 285.
[141] G. Jóhannesson, et al., Astroph. J. 824 (2016) 16.
[142] Y. Génolini, D. Maurin, I.V. Moskalenko, M. Unger, Phys. Rev. C 98 (2018) 034611.
[143] B. Coste, et al., Astron. & Astroph. A 539 (2012) 88;
N. Tomassetti, Astroph. Space Sci. 342 (2012) 131.
[144] M. Aguilar, et al., Phys. Rev. Lett. 123 (2019) 181102.
[145] J. Bartels, Terr. Magn. Atm. El. 39 (1934) 201.
[146] O. Reimer, et al., Astroph. J. 496 (1998) 490;
J.Z. Wang, et al., Astroph. J. 564 (2002) 244;
Z.D. Myers, et al., Proc. of the 28th Int. Cosmic Rays Conf. (ICRC 2003), 1805, Tokyo, Japan, 2003;
E. Mocchiutti, for the WIZARD/Caprice Coll., Proc. of the 28th Int. Cosmic Rays Conf. (ICRC 2003), 1809, Tokyo, Japan, 2003;
O. Adriani, et al., Astroph. J. 818 (2016) 68.
[147] We used Galprop WebRun, A.E. Vladimirov, S.W. Digel, G. Jóhannesson, P.F. Michelson, I.V. Moskalenko, P.L. Nolan, E. Orlando, T.A. Porter, A.W. Strong, Comput. Phys. Comm. 182 (2011) 1156;
with parametrization from, R. Trotta, G. Jóhannesson, I.V. Moskalenko, T.A. Porter, R. Ruiz de Austri, A.W. Strong, Astrophys. J. 729 (2011) 106.
[148] H.A. Bethe, Phys. Rev. 55 (1939) 434.
[149] M. Simon, et al., Astrophys. J. 239 (1980) 712;
C.D. Orth, et al., Astrophys. J. 226 (1978) 1147;
E. Juliusson, Astrophys. J. 191 (1974) 331.
[150] J.J. Engelmann, et al., Astron. Astrophys. 233 (1990) 96.
[151] S. Swordy, et al., Astrophys. J. 349 (1990) 625.
[152] H.S. Ahn, et al., Astrophys. J. 715 (2010) 1400;
H.S. Ahn, et al., Astrophys. J. 714 (2010) 89;
H.S. Ahn, et al., Astrophys. J. 707 (2009) 593.
[153] M. Aguilar, et al., Phys. Rev. Lett. 121 (2018) 051103.
[154] M.J. Boschini, et al., astro-ph.HE.
[155] E. Vangioni-Flam, M. Casse, J. Audouze, Phys. Rep. 333–334 (2000) 365.
[156] Synthesis of Elements in Stars, Springer-Verlag, Berlin Heidelberg, 2010, pp. 379–417.
[157] G. Jóhannesson, et al., Astrophys. J. 824 (2016) 16.
[158] K.A. Lave, et al., Astrophys. J. 770 (2013) 117;
J.A. Esposito, et al., Astroparticle Physics 1 (1992) 33;
M. Ichimura, et al., Phys. Rev. D 48 (1993) 1949.
[159] A.D. Panov, et al., Bull. Russian Acad. Sci. 73 (2009) 564.
[160] F. Gahbauer, G. Hermann, J.R. Hörandel, D. Müller, A.A. Radu, Astrophys. J. 607 (2004) 333.
[161] M. Ave, P.J. Boyle, F. Gahbauer, C. Höppner, J.R. Hörandel, M. Ichimura, D. Müller, A. Romero-Wolf, Astrophys. J. 678 (2008) 262.
[162] M. Aguilar, et al., Phys. Rev. Lett. 124 (2020) 211102.
[163] E. Witten, Phys. Rev. D 30 (1984) 272.
[164] T.A. Armstrong, et al., Phys. Rev. C 61 (2000) 064908;
T.A. Armstrong, et al., Phys. Rev. Lett. 83 (1999) 5431.
[165] K. Han, et al., Phys. Rev. Lett. 103 (2009) 092302.

[166] R. Arsenescu, et al., J. Phys. G: Nucl. Part. Phys. 27 (2002) 487;
M.C. Isaac, et al., Phys. Rev. Lett. 81 (1998) 2416;
T.K. Hemmick, et al., Phys. Rev. D 41 (1990) 2074;
A. Turkevich, K. Wielgoz, T.E. Economou, Phys. Rev. D 30 (1984) 1876;
R. Middleton, R.W. Zurmühle, J. Klein, R.V. Kollarits, Phys. Rev. Lett. 43 (1979) 429.
[167] P. Mueller, L.B. Wang, R.J. Holt, Z.T. Lu, T.P. O'Connor, J.P. Schiffer, Phys. Rev. Lett. 92 (2004) 022501.
[168] O. Adriani, et al., Phys. Rev. Lett. 115 (2015) 111101.
[169] J. Madsen, Phys. Rev. D 71 (2005) 014026.
[170] M. Aguilar, et al., Phys. Rev. Lett. 121 (2018) 051101.
[171] Sunspot data from the World Data Center SILSO, Royal Observatory of Belgium, Brussels at http://www.sidc.be/silso/datafiles.
[172] X. Sun, J.T. Hoeksema, Y. Liu, J. Zhao, Astrophys. J. 798 (2015) 114.
[173] L.F. Burlaga, J. Perko, J. Pirraglia, Astrophys. J. 407 (1993) 347.
[174] G. Newkirk Jr, A.J. Hundhausen, V. Pizzo, J. Geophys. Res. Space Phys. 86 (1981) 5387.
[175] H.V. Cane, Space Sci. Rev. 93 (2000) 55.
[176] M.S. Potgieter, J.A. Le Roux, L.F. Burlaga, F.B. McDonald, Astrophys. J. 403 (1993) 760.
[177] M. Aguilar, et al., Phys. Rev. Lett. 121 (2018) 051102.
[178] M.S. Potgieter, Adv. Space Res. 53 (2014) 1415;
M.S. Potgieter, Adv. Space Res. 13 (1993) 239.